TUNING THE ELECTRONIC PROPERTIES OF COORDINATION COMPLEXES WITH SULFUR-BRIDGED LIGANDS

by

Christopher M. Brown

M.Chem., The University *of* Newcastle upon Tyne, 2011

A Thesis Submitted *in* Partial Fulfilment *of*

the Requirements *for* the Degree *of*

DOCTOR *of* PHILOSOPHY

in

The Faculty *of* Graduate and Postdoctoral Studies

(Chemistry)

The University *of* British Columbia

(Vancouver)

October 2018

The following individuals certify that they have read, and recommend to the Faculty of Graduate and Postdoctoral Studies for acceptance, the dissertation entitled:

Tuning the Electronic Properties of Coordination Complexes with Sulfur-Bridged Ligands

submitted by Christopher Mark Brown in partial fulfillment of the requirements for

the degree of Ph.D.

in Chemistry

Examining Committee:

Michael Wolf

Supervisor

Mark MacLachlan

Supervisory Committee Member

Dan Bizzotto

Supervisory Committee Member

Zachary Hudson

University Examiner

Keng Chou

University Examiner

Additional Supervisory Committee Members:

Sarah Burke

Supervisory Committee Member

Supervisory Committee Member

ABSTRACT

By altering the oxidation state at the sulfur atom of sulfur-bridged ligands we have shown that photophysical properties of coordination complexes can be changed. A new class of sulfur-bridged dipyridyl ligand has been developed for effective "two-level" tuning of the emission colour of Ir(III) complexes. Tuning can occur *via* the classical method of altering substituents at the pyridyl ring, and/or through oxidizing the sulfur. Changing the oxidation state of the sulfur atom serves as a switch to alter the emissive state from that of mainly ^{3}LC character (blue-green emission) to one of ^{3}MLCT/^{3}LLCT character (yellow emission), evidenced from photophysical characterization and DFT calculations.

The larger bite angle of the sulfur-bridged dipyridyl ligands, in conjunction with additional coordination sites afforded by the oxygen atoms at the sulfur, has led to interesting binding modes when bound to copper(I) in heteroleptic diimine-diphosphine species. On increasing steric constraints about the copper(I) center, bimetallic adducts are isolated, with thermally activated delayed fluorescence the mechanism of photoluminescence.

Of the copper(I) species reported in this body of work, one was found to exhibit remarkable thermochromic properties not-before seen in a monometallic copper(I) complex. When isolated as an amorphous powder, **Cu-Me-DPSO** shows a yellow solid state emission, however when heated to 180 ºC a crystalline powder is formed which shows an orange luminescence. This crystalline powder displays a reversible thermochromic solid state emission, from orange at room temperature to yellow at low temperatures. Using solid state variable temperature excitation and absorption data, this phenomenon is attributed to a change in coordination geometry about the copper atom in the excited-state.

With a view to further understanding the impact of sulfur oxidation state on the excited-state properties of coordination complexes, two new Ru(II)-Re(I) dyads were synthesized, for use as CO_2 photocatalysts. Connected by a sulfur-bridged bisphenanthroline bridge, oxidation state at the sulfur can be changed which could modulate the electron transfer from the photo-excited Ru(II) to the catalytic Re(I) center. The synthesis, characterization and preliminary photocatalytic results are discussed.

LAY SUMMARY

The control of light is of great value to the human race, both in utilizing the sun's rays or generating our own light using electricity. In this work, the manipulation of light is afforded with "coordination complexes", which consist of building blocks (called ligands) bound to a specific metal. Some of these complexes can emit light, and ligands are used to finely-tune the colour of this light radiated by these species. The ligands herein contain sulfur, a versatile element to which oxygen atoms can be added, but so far an underutilized handle in the chemistry of coordination complexes. This thesis demonstrates that the number of oxygen atoms bonded to the sulfur can have a large impact on the properties of a complex, in particular regarding the colour of light emitted, opening a new avenue of control for chemists to explore.

PREFACE

In all chapters I am the principle author of the work, carried out under the supervision of Prof. Michael O. Wolf. I performed all the experiments, with additional contributions and collaborations noted below.

A version of **Chapter 2** has been previously published as a full paper[†] written by myself with contributions of M. O. Wolf. Complexes **Ir-DPS**, **Ir-DPSO** and **Ir-DPSO$_2$** were synthesized by Mitchell J. Kitt. DFT calculations were performed by Zhen (Allen) Xu and the crystallographic data collected and solved by Duane Hean. NMR characterization for complex **Ir-4,4'-Me-DPS** was assigned by Dr. Maria B. Ezhova.

The contents of **Chapter 3** are included in a manuscript in preparation, written by myself with contributions from M. O. Wolf. The project involves a collaboration with Dr. Eli Zysman-Colman and Prof. Ifor D. W. Samuel at the University of St. Andrews, Scotland. DFT calculations were performed by Zhen (Allen) Xu, crystallographic data collected and solved by Veronica Carta and time-resolved emission studies performed by Chenfei Li at the University of St. Andrews.

A version of **Chapter 4** has been accepted for publication,[‡] authored by myself with contributions from M. O. Wolf. Single-crystal X-ray data was collected and solved by Veronica Carta, and pXRD data collected by Anita Lam.

All experiments in **Chapter 5** were conducted by myself, with the exceptions of electrochemical data, which was collected by Emile E. DeLuca, and NMR characterization for **Ru-PSO$_2$P-Re** which was assigned by Dr. Maria B. Ezhova.

[†] **Brown, C. M.**; Kitt, M. J.; Xu, Z.; Hean, D.; Ezhova, M. B.; Wolf, M. O. *Inorg. Chem.* **2017**, *56*, 15110–15118.

[‡] **Brown, C. M.**; Carta, V.; Wolf, M. O. *Chem. Mater.* **2018**, *30*, 5786–5795.

TABLE *of* CONTENTS

LIST *of* TABLES

LIST *of* FIGURES

LIST *of* SCHEMES

LIST *of* SYMBOLS *and* ABBREVIATIONS

^{1}MLCT	singlet metal-to-ligand charge transfer
^{3}MLCT	triplet metal-to-ligand charge transfer
^{3}LLCT	triplet ligand-to-ligand charge transfer
^{1}H	proton
^{13}C	carbon-13
^{31}P	phosphorus-31
4,4′-Me-DPS	bis(4-methylpyridin-2-yl)sulfane
4,4′-Me-DPSO	2,2′-sulfinylbis(4-methylpyridine)
4,4′-Me-DPSO$_2$	2,2′-sulfonylbis(4-methylpyridine)
Å	Angström (10^{-10} m)
AC	alternating current
ATR	attenuated total reflection
a.u.	arbitrary units
bpy	2,2′-bipyridine
BNAH	1-benzyl-1,4-dihydronicotinamide
Δ	crystal field splitting
ºC	degrees Celsius
C^N	cyclometallating ligand
CCD	charge-coupled device
cm	centimeter
cm^{-1}	wavenumber

COSY	correlation spectroscopy
CRT	cathode ray tube
CS	charge-separated
CT	charge transfer
CV	cyclic voltammetry
Δ	difference
d	doublet
dbp	2,9-dibutyl-1,10-phenanthroline
DC	direct current
D–C–A	donor–chromophore–acceptor
dfppy	2-(2,4-difluorophenyl)pyridine)
DFT	density functional theory
dma	dimethylamine
dmbpy	4,4′-dimethyl-2,2′-biyridyl
dmgH	dimethylglyoxime (anionic form)
dmp	2,9-dimethyl-1,10-phenanthroline
DMT	*N*,*N*-dimethyl-*p*-toluidine
dnpp	2,9-dineopentyl-1,10-phenanthroline
dop	2,9-dioctyl-1,10-phenanthroline
DPS	di(priding-2-yl)sulfane
DPSO	2,2′-sulfinyldipyridine
$DPSO_2$	2,2′-sulfonyldipyridine
dsbp	2,9-di(*sec*-butyl)-1,10-phenanthroline

dsbtmp	2,9-di(*sec*-butyl)-3,4,7,8-tetramethyl-1,10-phenanthroline
DSSC	dye-sensitized solar cell
E_{0-0}	zero–zero energy
E_{em}	emission energy
E_{HOMO}	HOMO energy
E_{LUMO}	LUMO energy
E_{ox}^*	excited-state oxidation potential
E_{red}^*	excited-state reduction potential
$\Delta E(S_1–T_1)$	energy gap between S_1 and T_1 states
EDG	electron-donating group
ESI-MS	electrospray ionization mass spectrometry
Et_2O	diethyl ether
EtOH	ethanol
eq.	equivalent
eV	electron volts
EWG	electron-withdrawing group
Exciplex	excited-state complex
f	oscillator strength
fac	facial
Fc	ferrocene
fs	femtosecond (10^{-15} s)
FT-IR	Fourier transform infrared spectroscopy
FWHM	full width at half maximum

g	grams
GC	gas chromatography
GC-MS	gas chromatography-mass spectrometry
h	hours
HOMO	highest occupied molecular orbital
HMBC	heteronuclear multiple-bond correlation spectroscopy
HR-ESI MS	high resolution electrospray ionization mass spectrometry
HSQC	heteronuclear single-quantum correlation spectroscopy
Hz	hertz
IC	internal conversion
IQE	internal quantum efficiency
IR	infrared
ISC	intersystem crossing
J–T	Jahn–Teller
K	Kelvin
k_{ISC}	rate of intersystem crossing
k_{nr}	rate of non-radiative decay
k_r	rate of radiative decay
kHz	kilohertz (10^3 Hz)
λ	wavelength
λ_{em}	wavelength of emission
λ_{ex}	wavelength of excitation
λ_{max}	wavelength at peak maximum

L^X	ancillary ligand
LC	ligand-centered
LCD	liquid crystal display
LED	light-emitting diode
LEEC	light-emitting electrochemical cell
LLCT	ligand-to-ligand charge transfer
LMCT	ligand-to-metal charge transfer
LUMO	lowest unoccupied molecular orbital
µs	microsecond
m	multiplet
m/z	mass-to-charge ratio
M	molar
MC	metal-centered
Me-DPS	bis(6-methylpyridin-2-yl)sulfane
Me-DPSO	6,6′-sulfinylbis(2-methylpyridine)
Me-DPSO$_2$	6,6′-sulfonylbis(2-methylpyridine)
MeCN	acetonitrile
MeOH	methanol
MHz	megahertz (10^6 Hz)
min	minutes
mL	milliliter
MLCT	metal-to-ligand charge transfer
mol	mole

MS	mass spectrometry
mV	millivolts
N^N	diimine ligand
N^P	imine-phosphine ligand
nm	nanometer
NMR	nuclear magnetic resonance
NOESY	nuclear Overhauser effect spectroscopy
ns	nanosecond (10^{-9} s)
OERS	one-electron reduced species
OLED	organic light-emitting diode
ORTEP	Oak Ridge Thermal Ellipsoid Plot
P^P	diphosphine ligand
PDT	photodynamic therapy
phen	1,10-phenanthroline
PLQY	photoluminescence quantum yield
POP	bis(2-(diphenylphospanyl)phenyl) ether
ppy	2-phenylpyridine
ps	picosecond (10^{-12} s)
PS	photosensitizer
PSP	di(1,10-phenanthrolin-5-yl)sulfane
PSO_2P	5,5′-sulfonylbis(1,10-phenanthroline)
PTI	Photon Technology International
pXRD	powder X-ray diffraction

py	pyridine
pz_2BH_2	bis(pyrazol-1-yl)borohydrate
pz_2Bph_2	bis-(pyrazol-1-yl)biphenylborate)
Φ_{CO}	quantum yield of CO
q	quintet
RISC	reverse intersystem crossing
ROESY	rotating frame nuclear Overhauser effect spectroscopy
rpm	revolutions per minute
S_0	ground-state
S_1	first excited singlet state
S_2	second excited singlet state
s	seconds
S	sulfide
SCXRD	single crystal X-ray diffraction
SO	sulfoxide
SO_2	sulfone
SOC	spin-orbit coupling
SWV	squarewave voltammetry
t	triplet
T	Tesla
T_1	first excited triplet state
TADF	thermally activated delayed fluorescence
TCI	Tokyo Chemical Industry Co., Ltd.

TCSPC	time-correlated single photon counting
TD-DFT	time-dependent density functional theory
T_g	glass transition temperature
TEOA	triethanolamine
TLC	thin layer chromatography
tmbpy	4,4′,6,6′-tetramethyl-2,2′-biyridyl
TOF	turn over frequency
TON	turn over number
TON_{CO}	turnover number for carbon monoxide
UBC	University of British Columbia
UV	ultraviolet
V	volts
v/v	volume/volume
Vis	visible
W	watts
XRD	X-ray difraction

ACKNOWLEDGEMENTS

Firstly I would like to thank my boss, Mike Wolf, for his support and guidance during this endeavor. The trust you put in me, in addition to the creative freedom afforded with my work, has helped me grow not just as a scientist, but as a person. From the bottom of my heart, thank you.

I have been fortunate to work with a number of great collaborators to whom I am very grateful. In particular I would like to thank Dr. Saeid Kamal at LASIR his vital help regarding excited-state lifetimes; Milan Coschizza, whose electrical engineering talents babied the fluorimeter through some tough times; Veronica Carta, for always enthusiastically running my (sometimes) crystalline species; and of course Dr. Maria Ezhova, whose patience and tremendous talent has shown me that NMR is not as scary as it seems. During my fifth year I had the pleasure of working with an undergraduate student, Mitchell Kitt, whose unrelenting drive and determination laid the foundation for the work in Chapter 2. Thank you.

I'd like to thank all the members of the Wolf group (past and present) for making this such an enjoyable period of my life. Special thanks to Marek Majewski, Ashlee Howarth and Yang Cao for your guidance when I started, and for continuing to support me in the years after your graduation. To the lads of the office (BRFL), thanks for the good times in and out of the lab. Janet, Emile, Duane, Allen, Cathrin, Val, Kyle, Lev, Damon, Amber and Mitch, it's been a blast.

To Rebecca, without you these last few years in Vancouver would not have been the same. You are an inspiration to me, and your unwavering support has been invaluable. I can't wait for what the future holds for us.

And finally, my greatest appreciation goes out to my family. Who would have thought after dropping me off in Newcastle on a damp day in 2006 I would still be at university and half-way around the world? Thank you for your support, I love you all dearly.

Mum, Dad, Ellie

and

Libby

CHAPTER 1: Introduction

1.1 Light

In the fifth century BC, Greek philosopher Empedocles proposed that four elements – fire, earth, air and water – made up the composition of everything in the universe. He suggested that the goddess Aphrodite crafted the human eye out of these four elements.[1] She then lit the fire, causing it to radiate from the eye, allowing us to see. While this view was at the time generally accepted, in ~ 50 BC Lucretius wrote in *On the Nature of Things*:[2]

"The light and heat of the sun; these are composed of minute atoms which, when they are shoved off, lose no time in shooting right across the interspace of air in the direction imparted by the shove."

This surprisingly accurate interpretation was derided until around 1000 years later, when al-Haytham argued that sight is due to a light beam from the sun reflecting off an object and entering our eyes.[3] Pioneering work by Gassendi, Newton, Hooke and Huygens – to name but a few – advanced our understanding, but it is the modern day view of Maxwell's theory of electromagnetic radiation that is now widely accepted.[4,5] Light is intertwined intimately with the natural world and the human race. From the day-night cycle that is linked to our circadian rhythm, to the photosynthetic machinery of plants, algae and cyanobacteria, to the Aurora Borealis; light is not just a vital source of energy, but also a thought-provoking and emotive entity.

At the onset of the Information Age, a broad range of applications for light are helping to drive civilization: harnessing solar irradiation is seen to be an alternative to reduce our dependence

on fossil fuels;[6] luminescence-based bioimaging can help detect tumours;[7] quantum computing could perform calculations much quicker than binary digital computers based on transistors.[8] Of particular interest are photofunctional materials for illumination applications. In recent decades display technologies have advanced from cathode ray tube (CRT) devices to liquid-crystal displays (LCD),[9] to electroluminescent materials such as light-emitting diodes (LEDs), organic light-emitting diodes (OLEDs)[10] or light-emitting electrochemical cells (LEECs).[11]

OLEDs in particular, have been successfully commercialized, with a market predicted to be valued at 49 billion US$ by 2023.[12] The advantage for these newer technologies is that the sub-pixels themselves emit light, negating the need for a backlight and thus forming thinner devices that are more energy-efficient. Iridium(III) complexes have been prepared for uses in both OLEDs and LEECs due to their high photoluminescence quantum yields (PLQY) and highly tuneable emission colour.[13,14] Iridium however is a precious metal with low Earth abundance and so cheaper, more sustainable alternatives are sought, such as emitters based on copper(I) complexes. The properties of these materials are dictated by their excited-state dynamics, which for a chosen metal center can be tuned by altering the electronics at the chelating ligands. In this work a number of new complexes with sulfur-functionalized ligands are reported, illustrating that subtle electronic changes can greatly impact the photophysical properties of a coordination complex.

1.2 Photophysical Processes

Photophysical processes occur following excitation of a system by electromagnetic radiation (photons). The subsequent events induce a change of states through radiative and non-radiative transitions, resulting in a physical outcome with no chemical change. These

photophysical processes were illustrated by Polish physicist Aleksander Jablonski in 1933, with a simplified Jablonski diagram given in Figure 1-1.[15] The diagram depicts the different electronic states of a system and their relative energies. Singlet electronic states are denoted by S_0, S_1, S_2 etc. and triplet states as T_1, T_2, etc. and within each of these states are vibrational levels which are expressed in order of increasing energy by v = 0, v =1, v = 2, etc. Radiative and non-radiative transitions can occur between these energy levels and are depicted in Figure 1-1 as solid and dashed lines, respectively.

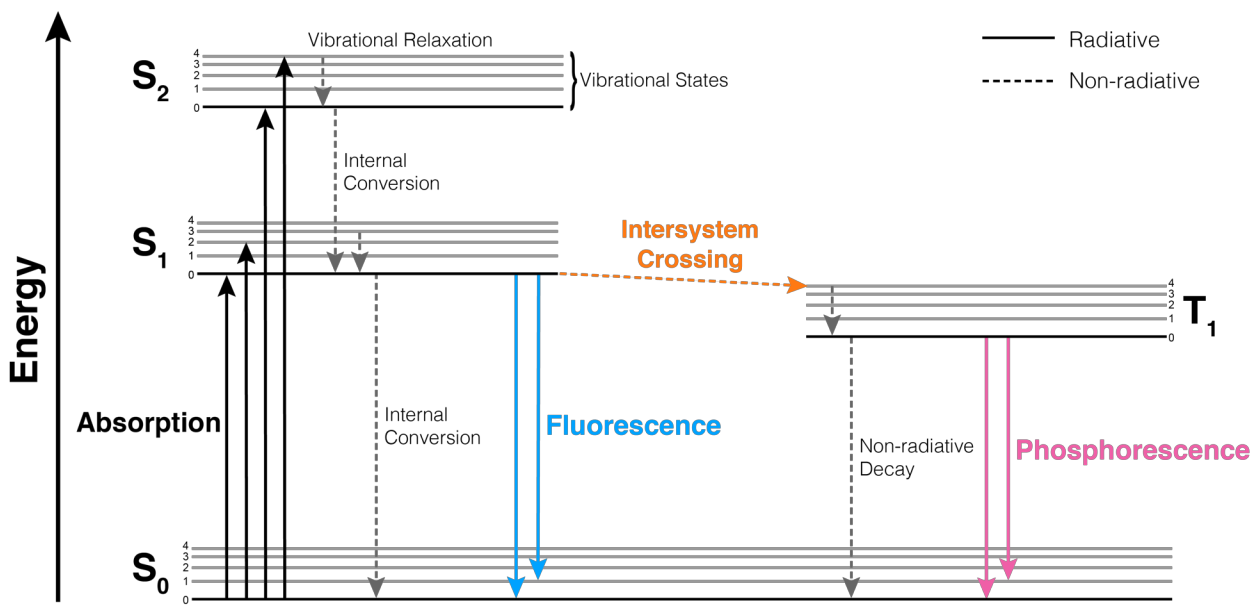

Figure 1-1 Depiction of a simplified Jablonski diagram. Adapted from reference.[16]

In order to absorb light and induce an electronically-excited state, the incoming photon must have an energy equal to the difference between the two electronic states to be able to promote an electron from the ground-state (S_0) to the higher energy level (S_1, S_2, etc.). This absorption

process occurs on a very fast timescale of 10^{-15} s. The resultant excited-state is inherently unstable and thus will relax back to the ground-state *via* a number of possible relaxation processes:[17]

- *Vibrational relaxation* (10^{-14} to 10^{-11} s): occurs within an electronic state between a vibrationally-excited state ($v \geq 1$) and $v = 0$. Excess energy is dissipated as heat.
- *Internal conversion (IC)* (10^{-14} to 10^{-11} s): occurs between isoenergetic states of the same spin multiplicity, with IC between excited states (e.g. $S_2 \rightarrow S_1$) occurring much faster than IC between S_1 and S_0. Excess energy is dissipated as heat.
- *Intersystem Crossing (ISC)* (10^{-8} to 10^{-3} s): the spin-forbidden transition between two electronic states with different spin multiplicity, such as $S_1 \rightarrow T_1$.
- *Fluorescence* (10^{-9} to 10^{-7} s): the spin-allowed radiative transition between states of the same multiplicity to the ground-state (e.g. $S_1 \rightarrow S_0$). Results in the emission of a photon.
- *Phosphorescence* (10^{-3} to 10^{2} s): the spin-forbidden radiative transition between states of different multiplicity to the ground-state (e.g. $T_1 \rightarrow S_0$). Results in the emission of a photon. Generally only observed in organic molecules at low temperatures where non-radiative decay is minimized; or when utilizing a heavy atom to induce spin-orbit coupling (SOC) promotes the spin-forbidden transition.

As discussed above, the electronic processes involved occur on a very fast timescale and can be considered as vertical transitions and explained in terms of the Franck-Condon principle. The efficiency of the absorption and radiative processes are therefore dependent on the overlap between the square of the wavefunctions of the excited-state and the ground-state.

1.3 Photophysics of Transition Metal Complexes

Luminescent transition metal complexes have applications in a wide variety of fields, such as solar energy conversion,[6] light-emitting devices,[14] photocatalysis,[18] molecular electronics[19] and as bioimaging probes,[20] to name a few. This is due to the high photostability, long luminescence lifetimes and large Stokes shifts exhibited by transition metal complexes, in addition to the high degree of tunability that can be afforded with these materials. In this section, the photophysical properties of the metals utilized in this work, namely copper, iridium and ruthenium, are discussed.

1.3.1 Photophysics of d^6 Metal Complexes

Transition metal complexes with a d^6 electronic configuration, such as Ir(III) and Ru(II) give a bright phosphorescence at room temperature both in solution and in the solid state due to fast intersystem crossing that is promoted by the strong SOC induced by the heavy-atom. These d^6 complexes adopt an octahedral geometry (Figure 1-2(a)) and the photophysical processes involved can be understood using a molecular orbital diagram (Figure 1-2(b)).

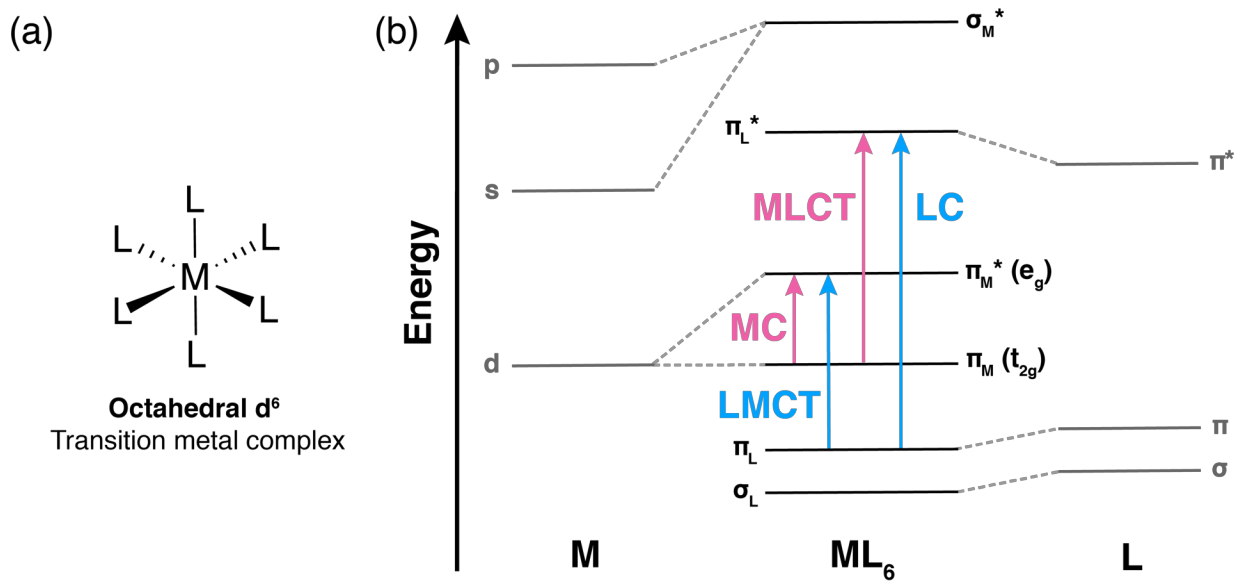

Figure 1-2 (a) Octahedral structure of a ML_6 transition metal complex. (b) Molecular orbital diagram showing the absorptive transitions for an octahedral transition metal complex. Adapted from reference.[17]

In a free transition metal ion, the five d-orbitals are degenerate. However, once the metal is bound as an octahedral complex the crystal field of the ligands splits these into triply degenerate t_{2g} (non-bonding) and doubly degenerate e_g* molecular orbitals (Figure 1-2(b)).[21] The extent of this splitting (Δ) is determined by the crystal field strength of the ligands and the central metal ion, and thus changes at the ligand, the geometry or the metal ion can have a substantial impact on the luminescence properties.[22] The distribution of electrons between the t_{2g} and e_g energy levels is dictated by the magnitude of Δ. In a system with a large Δ (low spin), according to Hund's rule it is energetically more favourable to pair the electrons in the t_{2g} level. If the magnitude of Δ is less than that of the pairing energy then the electrons are distributed to give the maximum number of unpaired electrons, resulting in a high spin system. High spin systems however are not favourable

for emission, and so only low spin metal complexes where all six d electrons are paired in the t_{2g} orbitals (for a d^6 system) are discussed below.

The classification for the excited-states is derived from the various orbital configurations and the transitions which occur between them, and are visualized in Figure 1-2(b). In a d^6 strong field complex all spins are paired in its non-excited-state, denoted as a ground-state singlet (S_0). Upon irradiating with light of sufficient energy one of these paired electrons is promoted to an empty orbital of a higher energy to give an excited-state. Three different types of excited-state are seen: metal-centered (MC) states resulting from a d–d transition; ligand-centered states (LC) arising from a π–π* transition; and charge transfer (CT) states. The CT states can occur from either the promotion of a d electron to the π* antibonding orbital of the ligand to give a metal-to-ligand charge transfer (MLCT), or from promotion of a π bonding orbital electron from the ligand to an empty d orbital on the metal, yielding a ligand-to-metal charge transfer (LMCT) state.[22] In each instance the excited-state can be singlet or triplet in nature, with the triplet state lower in energy than its corresponding singlet state. The MC d–d states are very weakly absorbing because, even if spin-allowed, they are Laporte forbidden ($t_{2g} \rightarrow e_g$). As such they are often too weak to be seen in comparison to the more intense CT transitions, which are more strongly allowed and have favourable characteristics such as higher molar extinction coefficients and shorter emission lifetimes.[17]

Emission from d^6 complexes always occurs from the lowest excited-state and, because of efficient SOC due to the heavy metal center, the dominant emission is from a triplet state. Thus when designing a luminescent transition complex a number of factors must be considered:[22]

1. *Avoid d–d excited states*. These transitions are inherently unstable and so CT or LC excited-states are preferable.

2. *Lowest d–d states should be higher in energy than the emitting state*. This prevents thermal population from the emitting state.
3. *Have a high degree of SOC*. This increases the probability of emission and allows the radiative decay to be competitive with non-radiative decay.
4. *Encourage mixing between LC states and CT states.* Purely π–π* phosphorescence is too long-lived to be efficient, and so mixing with the more-allowed CT state increases the emission probability.
5. *The emitting state should not be too low in energy.* The energy gap law dictates that radiationless processes are more efficient as the emitting state approaches the ground-state.[23] Though of course when designing an emitter the desired colour dictates the energy required.

1.3.2 Iridium(III) Luminescent Complexes

Phosphorescent emitters have been intensively researched due to their ability to harvest both the electrogenerated singlet and triplet excitons in an electroluminescent device, leading to a theoretical internal quantum efficiency (IQE) of 100%.[24] The study of iridium systems is a relatively mature field and Ir(III) complexes fall into one of two categories: tris- cyclometallated neutral complexes; and bis-cyclometallated ionic complexes bearing an ancillary ligand. In 1985, King *et al.* described the synthesis of *fac*-Ir(ppy)$_3$ (**1,** ppy = 2-phenylpyridine, Figure 1-3(a)),[25] a neutral cyclometallated complex which, in 1999, was used as a green phosphorescent dopant in an OLED that still retains the highest IQE of an electroluminescent material using an Ir(III) complex.[26]

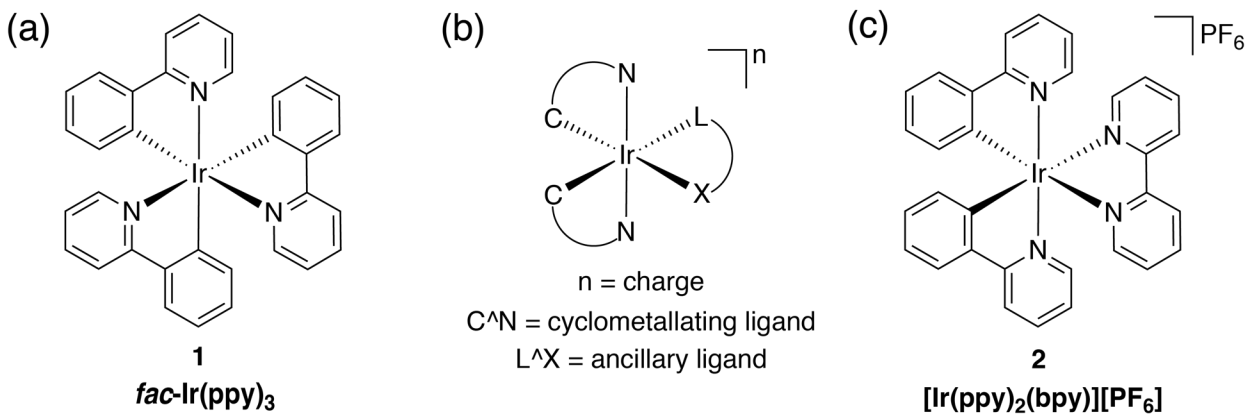

Figure 1-3 (a) *fac*-Ir(ppy)$_3$ (**1**) as reported by King *et al*.[25] (b) Structure of a bis-cylometallated Ir(III) species. (c) Structure of [Ir(ppy)$_2$(bpy)][PF$_6$] (**2**).

Unlike neutral iridium(III) species, ionic complexes feature desirable characteristics due to their charged nature, such as enhanced solubility, in addition to ease of design, synthesis and purification, which has piqued interest industrially with some complexes showing promise in LEECs.[11,27] In this section, bis-cyclometallated Ir(III) complexes of the structure [Ir(C^N)$_2$(L^X)]^n (Figure 1-3(b)) will be discussed, whereby C^N is a cyclometallating ligand and L^X is the ancillary ligand. The charge of the complex can be modulated with the choice of ancillary ligand by choosing neutral, monoanionic or dianionic species (N^N, O^O or C^C, respectively).[27]

Of the transitions discussed in Section 1.3.1, those seen in Ir(III) complexes are predominantly of mixed MLCT/LLCT and LC character. Once in the singlet excited-state, ISC can occur due to the strong SOC enabled by the heavy iridium atom, yielding a mixed triplet excited-state of ^{3}MLCT and ^{3}LC nature.[28] Commonly in bis-cyclometallated Ir(III) complexes the cyclometallating ligand is linked to the ^{3}LC state and the ancillary ligand with the ^{3}MLCT state. In a typical cationic complex such as [Ir(ppy)$_2$(bpy)][PF$_6$] (**2**, bpy = 2,2′-bipyridine, Figure 1-3(c)), its highest occupied molecular orbital (HOMO) is a mixture of Ir dπ orbitals and phenyl π orbitals

of the cyclometallating ppy ligands, while the lowest unoccupied molecular orbital (LUMO) lies on the ancillary bpy ligand.[13] As the HOMO and LUMO are often located on different ligands in cationic Ir(III) complexes, it is therefore possible to finely-tune the emission colour by independently modifying the C^N and L^X ligands.[29]

1.3.3 Tuning the Emission of Bis-cyclometallated Ir(III) Complexes

As discussed above, altering the electronics of the cyclometallating or ancillary ligands can result in a rational tuning of emission colour of bis-cyclometallated Ir(III) complexes to cover the visible spectrum. Of the C^N ligands used, ppy and its various derivatives are amongst the most common, and the effects of altering these ligands is highlighted in Figure 1-4. On the introduction of an electron-withdrawing group (EWG), such as fluorine, it is possible to stabilize the HOMO and thus blueshift the emission. For example, $[Ir(ppy)_2(bpy)][PF_6]$ (**2**) gives yellow emission at 585 nm in acetonitrile solution;[13] however, Park *et al.* showed that on fluorinating the phenyl ring of the ppy ligands in $[Ir(dfppy)_2(bpy)][PF_6]$ (**3**, dfppy = 2-(2,4-difluorophenyl)pyridine)) a blue-shift of the emission maximum of over 30 nm is seen.[30] Conversely, the emission can be bathochromically shifted through the addition of electron-donating groups (EDG) to the ppy ligands. Hasan and co-workers demonstrated that when substituting the phenyl ring of ppy with methoxy groups in the 3- and 4-positions (**4**) gives a strongly red-shifted emission with a maximum of 730 nm in acetonitrile solution.[31]

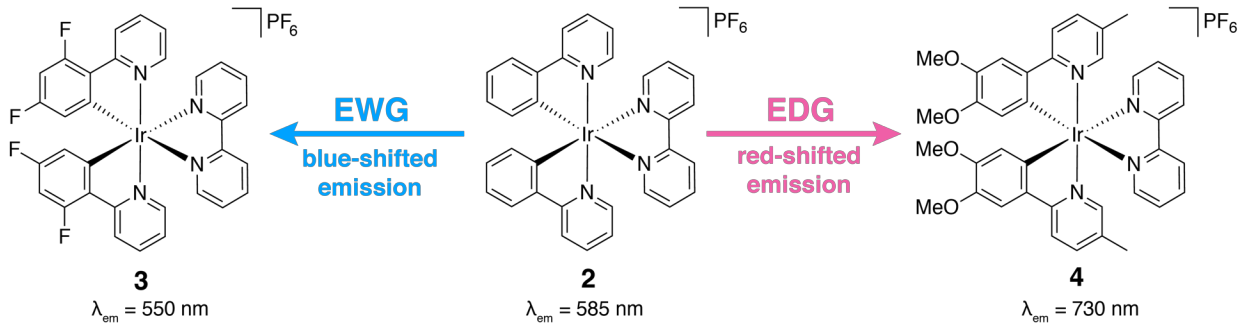

Figure 1-4 The electronic effects of substitution at the cyclometallating ligands on luminescence colour.[13,30,31]

In comparison to modification at the C^N ligands, altering the electronics at the L^X offers a more convenient and flexible approach to altering the luminescence colours of cationic Ir(III) complexes because the LUMO exclusively lies on the ancillary ligand. In Figure 1-5 $[Ir(ppy)_2(bpy)][PF_6]$ (**2**) is again used as the standard. In substituting the bpy with EDGs such as dimethylamino (dma) groups to give $[Ir(ppy)_2(dma\text{-}bpy)][PF_6]$ (**5**) it is possible to blue-shift the emission by destabilizing the LUMO.[32] Using the same rationale, employing EWGs will stabilize the LUMO and red-shift the luminescence. Rodriquez-Redono *et al.* introduced carboxylate groups to the 4- and 4′-positions of the bpy in complex **6** and were able to achieve deep-red emission with a maximum at 687 nm.[33]

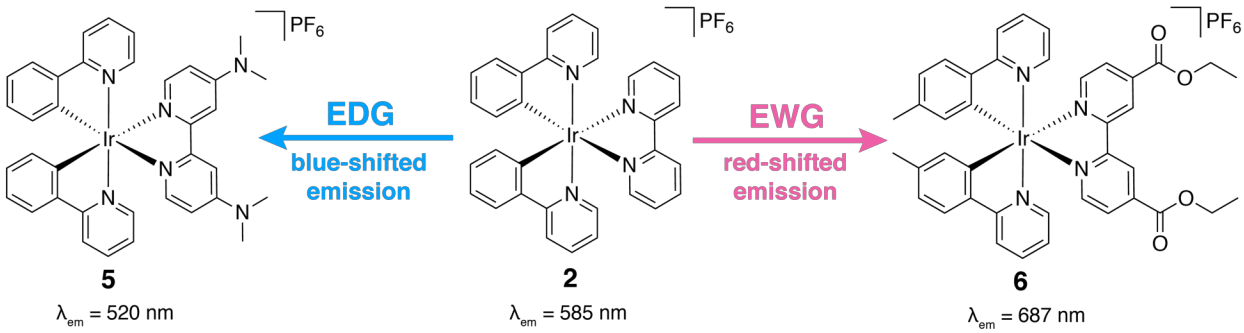

Figure 1-5 The electronic effects of substitution at the ancillary ligands on luminescence colour.[13,32,33]

1.3.4 Luminescent Ruthenium(II) Complexes

Over the last 50 years, ruthenium-based coordination compounds have garnered a great deal of research interest due to their desirable photophysical properties. Ruthenium complexes have been synthesized for numerous applications including: the study of light-induced electron and energy transfer (such as artificial photosynthesis);[34,35] bioimaging;[36] photodynamic therapy (PDT);[37] and as sensitizers for dye-sensitized solar cells (DSSCs).[38]

Ru(II) polypyridyl complexes, in particular $[Ru(bpy)_3]^{2+}$ (**7**, Figure 1-6(a)) and its many derivatives, have been the focus of many photophysical studies,[38-40] due to their strong absorption in the visible spectrum, high luminescence, and only small changes in geometry following excitation. $[Ru(bpy)_3]^{2+}$ undergoes the same transitions as discussed in Section 1.3.1 and highlighted in Figure 1-2(b). A ^{1}MLCT state is formed when the complex is irradiated with light at λ_{max} = 452 nm, with the photoexcited electron localized on one of the bpy ligands.[41] Using ultrafast time-resolved absorption anisotropy measurements, McCusker *et al*. reported that the excited electron is initially delocalized between all three ligands, but quickly localizes to only one of the ligands in ~60 fs in acetonitrile solution.[42] Following excitation to the ^{1}MLCT, a fast ($\tau \approx$ 100 fs) ISC to a ^{3}MLCT excited-state occurs with a near-unity quantum yield of formation.[43] Deactivation of this excited-state can then occur radiatively with the emission of a photon, or through a non-radiative pathway.[40] This deactivation shows both solvent[44] and temperature dependence.[39] In H_2O the emission quantum yield is 0.04 with an excited-state lifetime of 0.6 μs, but the lifetime increases to 5 μs at 77 K. The temperature dependence is due to a thermal population of a MC excited-state that then proceeds to decay non-radiatively. The excited-state lifetime is therefore a sum of the radiative rate of decay (k_r), non-radiative decay (k_{nr}) and the rate

of the population of the MC state (k_{MC}). A simplified Jablonski diagram illustrating this process is shown in Figure 1-6(b).

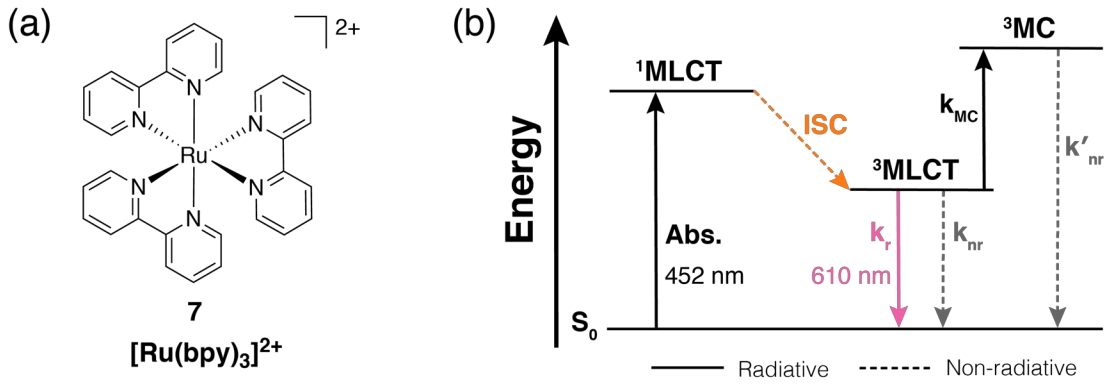

Figure 1-6 (a) Structure of $[Ru(bpy)_3]^{2+}$ (**7**). (b) Simplified Jablonski diagram illustrating the excited-state processes in $[Ru(bpy)_3]^{2+}$ (**7**). Adapted from references.[39,40]

The excited-state energy of Ru(II)-polypyridyl complexes can be altered by varying the electronics at the ligands. Substituents that affect the electron density utilizing EDGs, EWGs or altering the degree of conjugation can tune the π^* acceptor levels of the ligands and give systematic alterations to both the redox and photophysical properties of the complexes.[45]

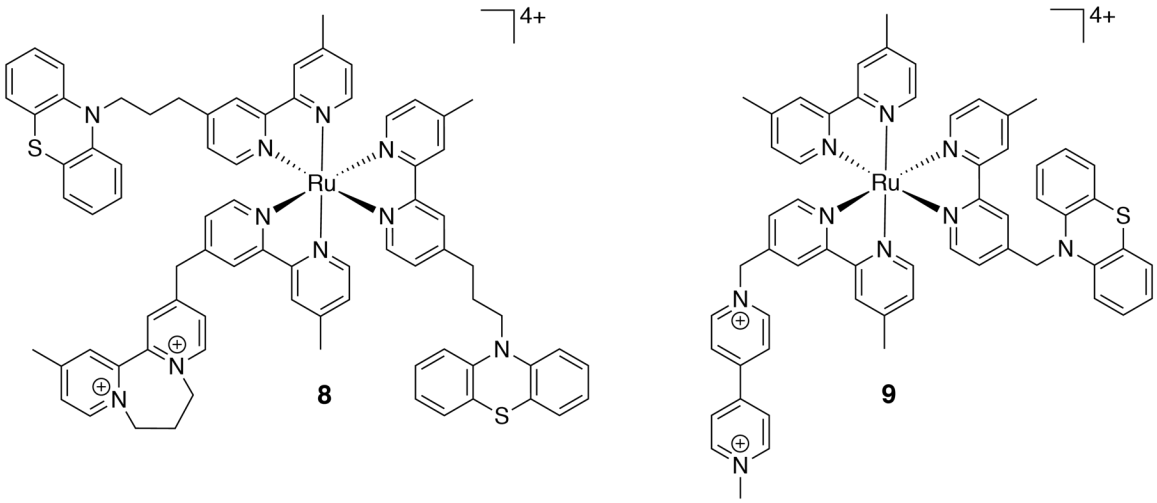

Figure 1-7 Donor–acceptor–chromophore triads based on $[Ru(bpy)_3]^{2+}$ by Meyer *et al*.[46,47]

This highly tuneable nature, in addition to well-established excited-state properties has led ruthenium complexes to become integral in the study of charge-separated (CS) states. The use of donor–chromophore–acceptor (D–C–A) triads based on $[Ru(bpy)_3]^{2+}$ triads has been instrumental in the understanding of artificial photosynthesis.[48,49] Meyer *et al*. have shown that D–C–A triads (**8** and **9**) can undergo a photoinduced, intramolecular electron transfer and generate CS states (Figure 1-7).[46,47] The transfer of electrons involved is qualitatively analogous to the electron cascade in Photosystem II, the first protein complex involved in the light-dependent reactions of oxygenic photosynthesis.

1.3.5 Photophysics of Cu(I) d^{10} Metal Complexes

While iridium and ruthenium complexes make excellent candidates for the study of fundamental photophysical processes, they are both precious metals and therefore more abundant

alternatives are sought. Thanks to the pioneering work by the McMillin group in the 1970s,[50] copper(I) complexes have emerged as promising candidates due to the ability to finely-tune their photophysical properties, in addition to a greater abundance, lower toxicity and lower cost.[51] The potential for Cu(I) complexes in commercial applications is high, such as use in electroluminescent materials like OLEDs[52] and LEECs,[53] as temperature sensors[54] or as photocatalysts.[55]

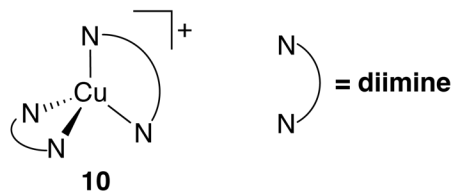

Tetrahedral Cu(I) Species

Figure 1-8 Tetrahedral geometry of $[Cu(N^{\wedge}N)_2]^+$ species.

$[Cu(N^{\wedge}N)_2]^+$ complexes (N^N = diimine ligand) have been seen as an alternative to extensively researched $[Ru(bpy)_3]^{2+}$ (**10**) due to MLCT absorptions bands located in the visible region, in addition to emission in the red region of the spectrum. Three MLCT bands are seen in the visible spectral region.[56] Band I is seen as a shoulder above 500 nm ($S_1 \leftarrow S_0$), the most prominent band, Band II, has a maximum between 430–480 nm ($S_2 \leftarrow S_0$) and Band III around 390–420 nm, though it is often hidden by the onset of Band II. The summation of these bands defines the shape of the visible absorptions and the spectral intensities are related to the symmetry of the complex.[57] Typically the coordination number about the copper atom is lower than the d^6 complexes discussed earlier in this chapter with a pseudo-tetrahedral ligating environment (**10**, Figure 1-8), though a range of distortions can exist in the ground-state from nearly-tetrahedral (D_{2d}) symmetry to flattened-tetrahedral (D_2) depending on the steric constraints imposed by the

ligands.[58] An additional distortion is also attained in the excited-state due to changes in electronic distribution upon irradiation.

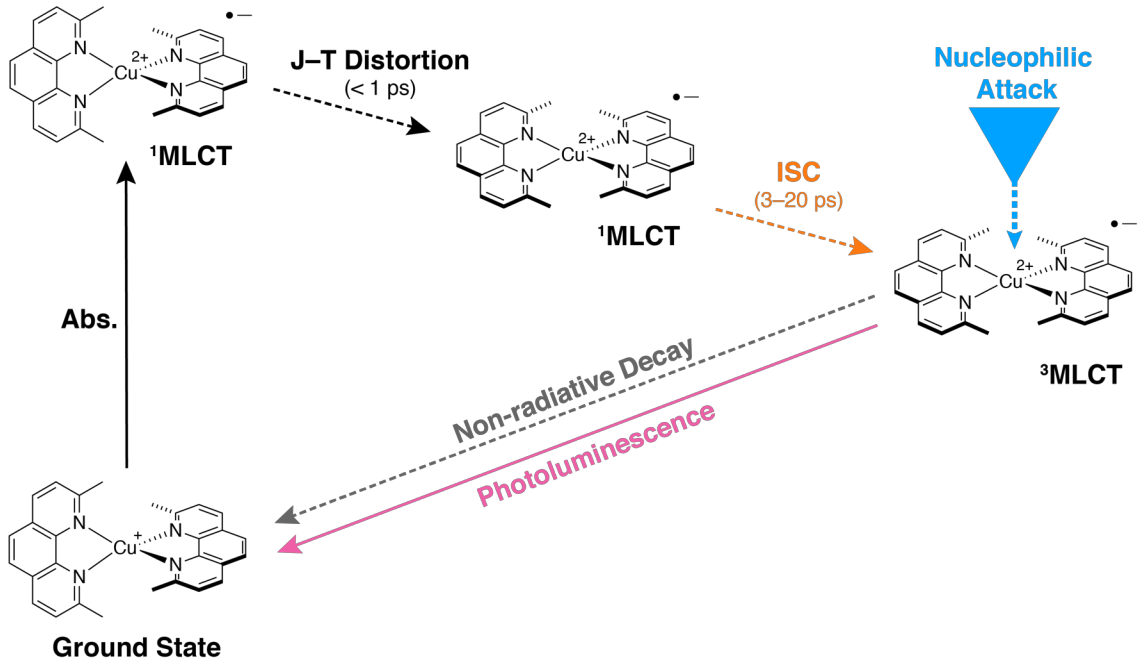

Figure 1-9 Simplified excited-state pathways of Cu(I) diimine complexes. After undergoing excitation, a Jahn-Teller distortion occurs, leaving an open site available for exciplex formation, following which the complex can relax radiatively or non-radiatively. Adapted from references.[57,58]

The excited-state dynamics of Cu(I) diimine complexes are illustrated in Figure 1-9. Upon photoexcitation one electron is transferred from the Cu(I) center to one of the diimine ligands, oxidizing the metal to a transient Cu(II) species and reducing the ligand to a radical-anion species.[59] The excitation process alters the complex from a closed shell $3d^{10}$ configuration in the ground-state to an open shell $3d^{9}$ configuration in the excited-state. The molecule then undergoes a Jahn–Teller distortion whereby a fast structural rearrangement, in which the pseudo-tetrahedral geometry observed in the ground-state is flattened, decreasing the angle between the two ligand

planes.[60,61] Singlet–triplet ISC then occurs on a picosecond timescale to give the ^{3}MLCT state. In this flattened geometry, an additional axial coordination site is opened up that is available for nucleophilic attack by solvent, counteranion, or Lewis bases present in solution, resulting in a 5-coordinate structure. Increased coordination number at the copper center is known to quench the excited-state. McMillin *et al*. have shown in a number of reports that the addition of a Lewis base yields a 5-coordinate exciplex (excited-state complex)[59,62-64] where the excited-state is stabilized, thus leading to a decrease in the energy gap between the ground- and excited-states which in turn promotes non-radiative decay and reduces the emissivity of the complex.

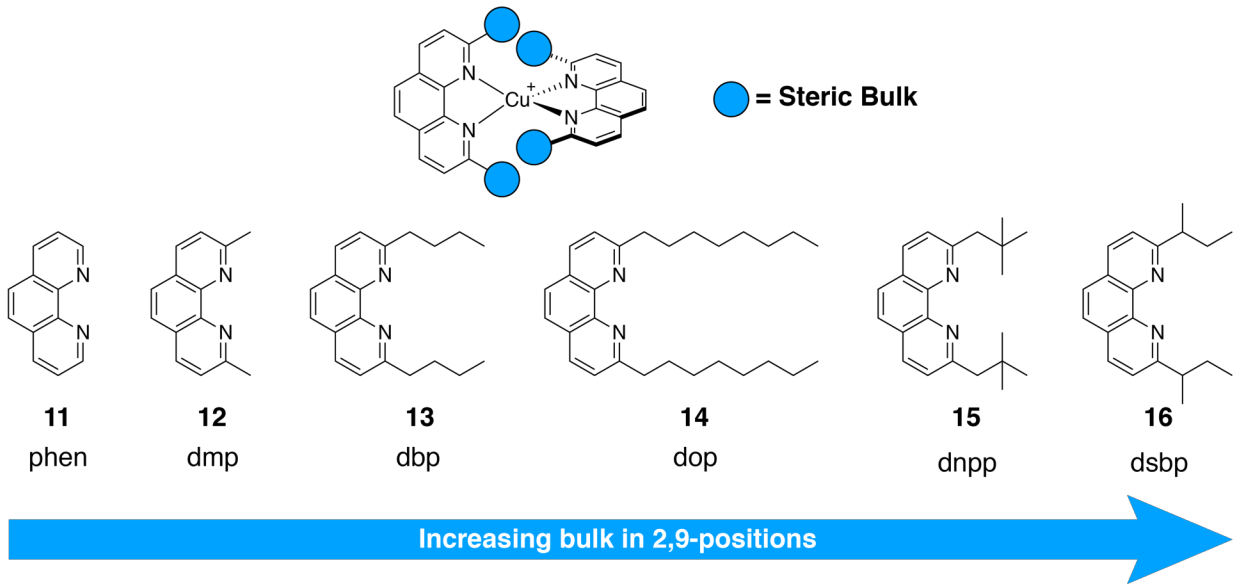

Figure 1-10 Increasing the steric bulk in the 2,9-positions of phen restricts the Jahn-Teller distortion at the Cu(I) center in the excited-state and increases emission intensity.[65]

The geometry of $[Cu(N^\wedge N)_2]^+$ can be altered by modulating the sterical hindrance at the ligand, which is often a variation of 1,10-phenanthroline (phen, **11**). Altering the bulk at the 2,9-positions of the phen can limit the degree of distortion in the excited-state and thus decrease the

exciplex formation and increase the emission intensity. McMillin and co-workers found that the addition of alkyl groups at these positions restricted the Jahn-Teller distortion and increase the photoluminescence quantum yield (PLQY) and emission lifetimes (Figure 1-10).[65] $[Cu(phen)_2]^+$ (**11**) shows virtually no emission in CH_2Cl_2 solution,[66] but the series $[Cu(dmp)_2]^+$ (**12,** dmp = 2,9-dimethyl-1,10-phenanthroline), $[Cu(dbp)_2]^+$ (**13,** dbp = 2,9-dibutyl-1,10-phenanthroline) and $[Cu(dop)_2]^+$ (**14,** dop = 2,9-dioctyl-1,10-phenanthroline) have PLQYs of 4×10^{-4}, 9×10^{-4} and 10×10^{-4}, and emission lifetimes of 90, 150 and 155 ns, respectively. Introducing even more steric bulk with branching chains further inhibits the Jahn-Teller distortion. For $[Cu(dnpp)_2]^+$ (**15,** dnpp = 2,9-dineopentyl-1,10-phenanthroline) and $[Cu(dsbp)_2]^+$ (**16,** dsbp = 2,9-di(*sec*-butyl)-1,10-phenanthroline) PLQYs and emission lifetimes were increased to 16×10^4 and 260 ns, and 45×10^4 and 400 ns, respectively.

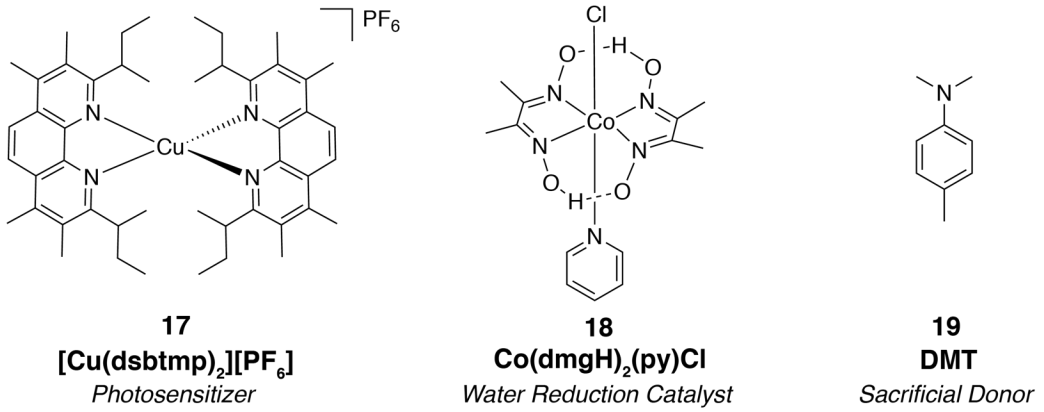

Figure 1-11 A sterically congested Cu(I) photosensitizer used for hydrogen photocatalysis by Castellano *et al*.[67]

In 2013, Castellano *et al*. designed a Cu(I) photosensitizer for use as a hydrogen evolution catalyst (Figure 1-11).[67] $[Cu(dsbtmp)_2][PF_6]$ (**17**, dsbtmp = 2,9-di(*sec*-butyl)-3,4,7,8-tetramethyl-

1,10-phenanthroline) was used together with the $Co(dmgH)_2(py)Cl$ (**18**) water reduction catalyst and a *N*,*N*-dimethyl-*p*-toluidine (**19**, DMT) sacrificial donor in 1:1 H_2O:CH_3CN, and the photosensitizer was found to be stable after 5 days of visible light irradiation, due to the inhibited Jahn-Teller distortion about the copper center. Turnover number (TON) was 35 (H_2/Co) on average and turnover frequency (TOF) was 5 h^{-1}, though it was found that the catalyst, not the photosensitizer limited the performance as with other systems utilizing a Co-dmg platform.

1.3.6 Thermally Activated Delayed Fluorescence (TADF)

In an OLED device the excitons generated are of 25% singlet character and 75% triplet character. In order to have high efficiencies it is key that all singlet and triplet excited-states generated are harvested and utilized for luminescence.[68] Third row transition metals, such as Ir(III), are well suited for these applications due to the efficient SOC that they possess between the lowest triplet state and higher-lying singlet states, as discussed in Section 1.2. These triplet emitters, however, are high-cost precious metals which may not be industrially scalable and so cheaper, more abundant alternatives are sought.[69] As mentioned above, copper(I) species are possible alternatives for electroluminescent materials, but initially it appears as if they were not very suitable candidates. As a first row transition metal, copper suffers from a much weaker SOC and thus transitions between the excited triplet state and singlet ground state are principally forbidden. This leads to long phosphorescence decay times (>100 μs)[10] which in a device can lead to strong saturation effects and side reactions which reduce the device stability,[70] in addition to the structural non-radiative deactivation of the excited-state discussed in Section 1.3.5. However, these deficiencies may be overcome by the thermally activated delayed fluorescence (TADF) properties that Cu(I) complexes can possess.

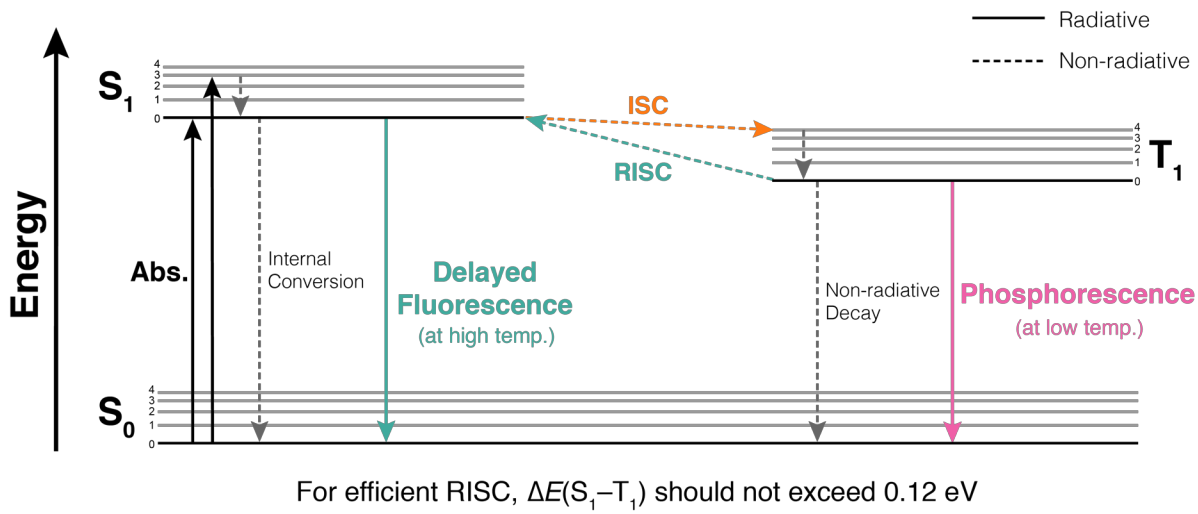

Figure 1-12 Jablonski diagram illustrating the process of thermally activated delayed fluorescence (TADF). Adapted from reference.[71]

At its heart, TADF is a process in which otherwise "wasted" triplets can be harvested thermally to give a delayed fluorescence, thus increasing the efficiency of a system. A simplified Jablonski diagram illustrating the photophysical processes of TADF is given in Figure 1-12. First, one can imagine the system at a very low temperature, such as 4 K. Following irradiation with light, the Cu(I) complex is excited to a higher energy singlet state which then very quickly undergoes a fast IC to the S_1 excited-state. An efficient ISC ($S_1 \rightarrow T_1$) then occurs with relatively short lifetimes of ~10 ps,[61,72] followed by a bright, long-lived phosphorescence ($T_1 \rightarrow S_0$). Consequently, a prompt fluorescence ($S_1 \rightarrow S_0$) is not seen.[71,73]

As the temperature is increased, the S_1 state can be re-populated depending on both the thermal energy available and the energy separation between the lowest energy singlet and triplet states, $\Delta E(S_1–T_1)$. The re-population occurs *via* a reverse intersystem crossing (RISC) and while TADF has been detected with a $\Delta E(S_1–T_1)$ of ≈ 0.43 eV in the red fluorescent dye eosin,[74] for practical applications this value should not exceed 0.12 eV.[71] Following the RISC, a strong S_1-

based fluorescence is observed with a long lifetime due to the population and depopulation of the T_1 state.

In order to design a successful TADF emitter, there are three parameters that must be addressed:[71]

1. $\Delta E(S_1–T_1)$: the energy gap between the lowest energy singlet and triplet states should be as small as possible. Cu(I) complexes are well suited as they possess MLCT states resulting in discrete charge separation between excited and non-excited electrons causing a small singlet-triplet splitting.
2. $\tau(S_1)$: the fluorescence decay time $\tau(S_1)$ should be as short as possible. Unfortunately, a short $\tau(S_1)$ is often related to a large $\Delta E(S_1–T_1)$.
3. $\tau(T_1)$: the phosphorescence decay time $\tau(T_1)$ should also be as short as possible in order to utilize an effective decay pathway in addition to the TADF.

1.3.7 Copper(I) TADF Emitters

Heteroleptic copper(I) complexes bearing diphosphine and diimine ligands, of the structure $[Cu(P^P)(N^N)]^n$ (where P^P = diphosphine and n = 0 or 1), have been shown to be effective TADF emitters. As discussed in Section 1.3.5, Cu(I) complexes undergo a significant geometric reorganization upon excitation and that with a judicious use of sterically demanding ligands the distortion can be minimized, reducing the excited-state quenching and thus increasing the efficiency of the radiative decay. This also holds true for the design of copper(I) TADF emitters.

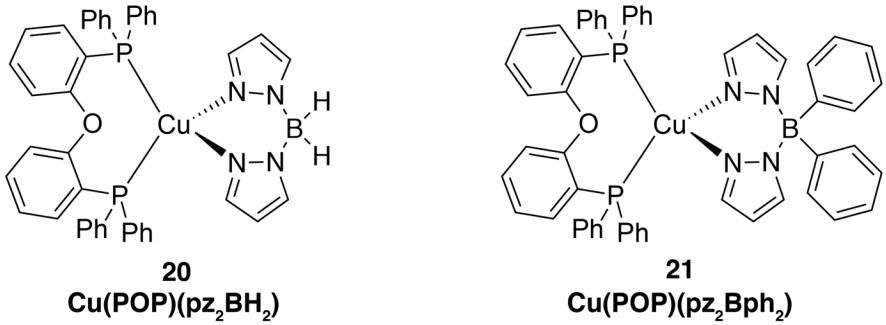

Figure 1-13 Neutral Cu(P^P)(N^N) emitters reported by Yersin *et al*.[75]

In 2011, Czerwieniec, Yu and Yersin reported strongly blue/white luminescent neutral Cu(I) complexes utilizing POP (bis(2-(diphenylphospanyl)phenyl) ether) as the diphosphine and bis(pyrazol-1-yl)borate ligands as the diimine ligands (Figure 1-13).[75] At room temperature the emission of the complexes was nearly completely fluorescence from the $S_1 \rightarrow S_0$ transition with the S_1 state thermally populated from the T_1 state, as determined from emission lifetime measurements. In CH_2Cl_2 solutions, Cu(POP)(pz_2BH_2) (**20**) and Cu(POP)(pz_2Bph_2) (**21**) (where pz_2BH_2 = bis(pyrazol-1-yl)borohydrate and pz_2Bph_2 = bis-(pyrazol-1-yl)biphenylborate) showed emission maxima at 525 nm and 498 nm, and PLQYs of 0.09 and 0.08, respectively. The low emission quantum yields are attributed to the greater rearrangement of molecular geometry afforded in solution. As a neat crystalline powder, however, where molecular distortion is disfavoured, λ_{max} values of 436 and 464 nm were seen in addition to much higher PLQYs of 0.45 and 0.90, respectively.

Introducing steric constraints, in a similar vein to the work by McMillin[65] highlighted in Figure 1-14, can aid the emissivity of a Cu(I) TADF luminophore. In 2014, Linfoot, Robertson and Yersin reported a Cu(I) system where adding steric bulk to a dmbpy (4,4′-dimethyl-2,2′-biyridyl) diimine ligand in complex **22** to give a tmbpy (4,4′,6,6′-tetramethyl-2,2′-biyridyl) diimine

ligand in **23** not only increased the PLQY in the solid state from 0.09 to 0.74, but also in EtOH solutions from <0.01 to 0.06.

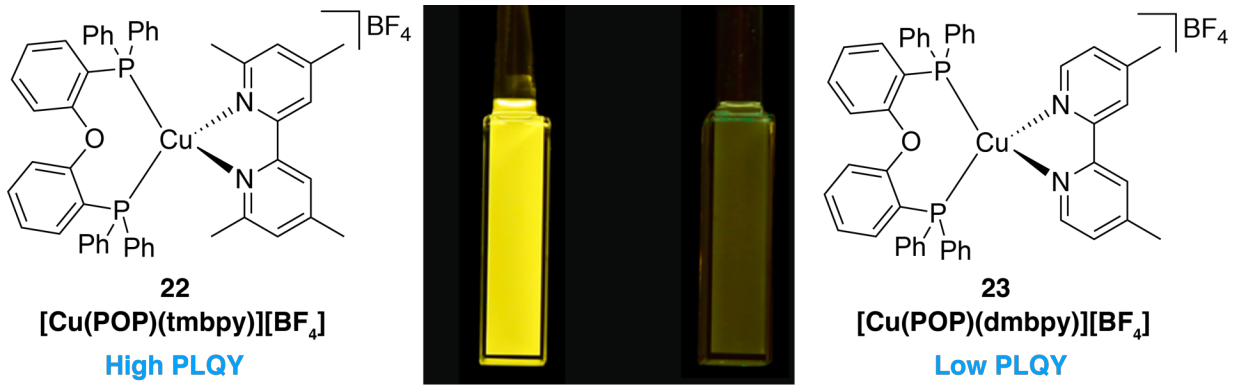

Figure 1-14 Adding steric bulk can decrease the degree of geometric distortion in the excited-state and can increase the emission intensity in Cu(I) TADF emitters in solution, as reported by Linfoot, Robertson and Yersin.[76] Image reproduced with permission from the American Chemical Society, Copyright © 2014.

1.4 Sulfur Oxidation States Alter Photophysical Processes

In recent years, our group has shown that electronic coupling between two identical molecules can be controlled by altering the oxidation state at a sulfur-bridge linking the two molecules. In 2013, we reported a system in which two identical chromophores bridged by a sulfur atom can undergo a systematic increase in PLQY by oxidizing the sulfur from sulfide (S), to sulfoxide (SO) and to sulfone (SO_2) (Figure 1-15).[77] In the case of bridged terthiophene dimer **T3S**, oxidizing to sulfone compound **T3SO$_2$** increased the emission intensity by an order of magnitude. In addition, a solvent dependence of the PL spectra, whereby a bathochromic shift was seen in more polar solvents, hinted towards an increase in CT character.

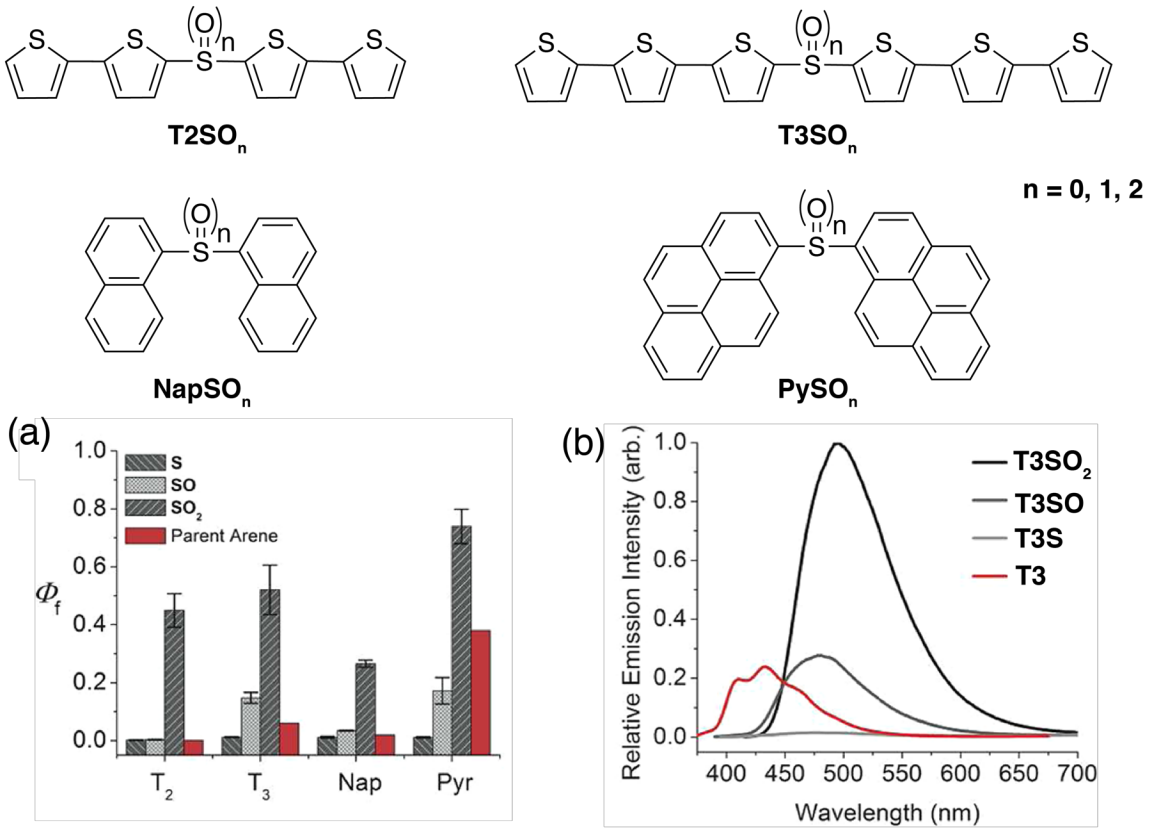

Figure 1-15 Structures of sulfur-bridged dimers synthesized by our group[77] showing (a) increased PLQY as the oxidation state at sulfur is increased. (b) Emission spectra in CH_2Cl_2 solutions for **T3SO$_n$** in comparison to the parent arene, terthiophene (**T3**). Image reproduced with permission from the American Chemical Society, Copyright © 2013.

Further study of the **T3** system by our group, in conjunction with the Bardeen group at University of California Riverside, elucidated the cause of this phenomenon through the use of femtosecond transient absorption in tandem with computational calculations.[78] In changing the oxidation state of the bridging sulfur, the electronic coupling of the chromophoric system is tuned. Electron lone pairs in the S and SO bridges of **T3S** and **T3SO** screen the interaction between the π electrons of the two terthiophene chromophores. Full oxidation to SO_2 in **T3SO**, however, leads to polarized bonds that decrease the screening, thus stabilizing the CT contributions. We have

further demonstrated this oxidation-dependent intramolecular charge transfer in anthracene-containing donor–acceptor–donor systems[79] and oligothiophenes.[80]

1.5 Goals of Thesis

Photo-active organometallic complexes have applications as emissive materials and in photocatalysis. By modifying the electronics of the ligands using substituent control one can affect the HOMO and LUMO energies and alter the excited-state properties, such as luminescence colour. The primary focus of this thesis lies on the synthesis and spectroscopic characterization of organometallic complexes bearing diimine sulfur-bridged ligands. In addition to substituent control, the sulfur center provides a convenient approach to adjust the electron density with chemical oxidation. By varying the oxidation state of the sulfur atom (S, SO, SO_2) the excited-state electronics of the complex can be altered, adding a degree of "two-level tuning" that can be achieved with a number of inexpensive, easy-to-handle oxidants.

In **Chapter 2** a series of new sulfur-bridged ligands is introduced. These ligands are analogous to 2,2′-bipyridine with the two pyridyl rings bound in the 2,2′-positions by a sulfur atom. Both the pyridyl and 4-methylpyridyl derivatives are prepared as sulfide, sulfoxide and sulfone derivatives. The spectroscopic properties of these compounds are investigated, both as pro-ligands and as ligands in a series of bis-cyclometallated Ir(III) complexes. The effect of these ligands on the excited-state is quantified using a combination of ground-state and excited-state spectroscopic techniques, in addition to computational calculations. It is found that complexes featuring the S- and SO-bridged ligands emit from a ^{3}LC state, but, on ligand oxidation to SO_2, the emission is

dominated by a ^{3}LLCT/^{3}MLCT state, therefore demonstrating an oxidation state-sensitive luminescence.

Chapter 3 highlights a series of heteroleptic Cu(I) complexes ligated by sulfur-bridged dipyridyl ligands of S and SO_2 oxidation states with steric bulk in the 6,6′-positions, designed as possible TADF emitters. A combination of increased diimine bite angle and additional coordination sites at the S=O oxygen afforded interesting bimetallic species when bulkier substituents were used, with excited-state properties probed at ambient temperature and at 77 K, including time-resolved spectroscopy.

Chapter 4 discusses Cu(I) sulfoxide species which illustrate how very subtle changes in ligand design can greatly impact the excited-state properties. A reversible, solid state thermochromic emission is observed in one of the complexes, in addition to phase-specific luminescence as a powder. A correlation between the structural properties (*via* crystallographic data) and the temperature-dependent excited-state behaviour is discussed.

The modulation of electron transfer in a bimetallic system is addressed in **Chapter 5**. Ru(II)-Re(I) supramolecular photocatalysts can be used in the reduction of CO_2 to more useful products, and the nature of the electron transfer from the Ru(II) photosensitizer to the Re(I) catalyst is imperative to the process. Here the two metallic centers are bound *via* a sulfur-linked bisphenanthroline bridge, with the photocatalytic properties of the S and SO_2 oxidation states explored.

CHAPTER 2: Tunable Emission of Iridium(III) Complexes Bearing Sulfur-Bridged Dipyridyl Ligands

2.1 Introduction

Since the discovery of the incandescent carbon filament lamp by Thomas Edison in 1879, artificial light has had a great impact on the human race, releasing us from the light-dark cycle our ancestors were bound by. The global electricity consumption for grid-based lighting sits at roughly 19%[81] and thus there has been a recent push to increase the efficiency of modern-day lighting as efficiency gains in this sector would greatly contribute to decreasing worldwide energy use.[82] Over the past two decades solid state lighting (SSL) has emerged as the source for higher efficiency light generation with reduced heat output.[83] Widely used SSL is based on inorganic light-emitting diodes (LEDs), with organic light-emitting diodes (OLEDs)[84,85] and, more recently, light-emitting electrochemical cells (LECs)[86,87] showing promise for the future.

Iridium(III) complexes are known for their high efficiency and wide scope of tunability in both OLEDs[27,88-90] and LECs,[91-94] yet there remains a lack of wide band-gap blue emitters for both these purposes.[27] Blue emission typically requires the addition of fluorine substituents on the cyclometallated C^N ligands, but these groups are often unstable under bias, leading to degradation and lower device longevity.[95] In $[Ir(C^N)_2(N^N)]^+$ complexes the HOMO contains contributions from the Ir(III) dπ orbitals and the phenyl π-orbitals of the C^N cyclometallating ligand, and the LUMO is usually localized on the N^N ancillary ligands.[94] This localized nature leads to effective colour tuning of the HOMO–LUMO gap. Adding electron-donating substituents

to the N^N ligand destabilizes the LUMO and blue-shifts the emission. Additionally, altering the N^N ligands can help stabilize the HOMO to increase the HOMO–LUMO gap even further.

Our group has previously reported that the degree of sulfur oxidation in sulfur-bridged conjugated organic molecules has significant effects on the electronic properties of these systems.[77,78] It has been shown that by increasing the oxidation state of a bridging sulfur in a thiophene-based system from sulfide (S), to sulfoxide (SO), to sulfone (SO_2) it is possible to influence intramolecular charge transfer and emission intensity. In this body of work it is shown that the emission colour of an Ir(III) complex can be tuned through altering the oxidation state at the sulfur of the N^N ancillary ligands. This approach is advantageous as only one parent ligand is needed, with simple oxidation yielding the other two variants, considerably simplifying synthesis.

2.2 Ligand Synthesis and Characterization

The symmetrical sulfide-bridged pro-ligands **DPS** and **4,4'-Me-DPS** were prepared *via* a nucleophilic aromatic substitution reaction using thiourea,[96] starting with either 2-bromopyridine or 2-chloro-4-(methyl)pyridine (Scheme 2-1). The desired sulfoxide and sulfone compounds were then obtained by oxidation of the corresponding diaryl sulfides. Oxidation to the sulfoxide products was performed using one of two different pathways:[97,98] Compound **DPSO** was prepared through the addition of 30% H_2O_2 to **DPS** dissolved in glacial acetic acid, while **4,4'-Me-DPSO** was formed by the addition of *m*-CPBA to **4,4'-Me-DPS** at 0 ºC. Sulfone pro-ligands **DPSO$_2$** and **4,4'-Me-DPSO$_2$** were synthesized through oxidation of the appropriate diaryl sulfide with 30% H_2O_2 using a NbC catalyst.[99] Moderate to high yields of the desired products were obtained in all synthetic steps and the six pro-ligands were characterized using NMR spectroscopy, mass

spectrometry and infrared spectroscopy. ^{1}H and ^{13}C signals were assigned using COSY, NOESY, HSQC and HMBC experiments.

Scheme 2-1 Synthesis of Iridium(III) Complexes **Ir-DPSO*n*** and **Ir-4,4'-Me-DPSO*n*** (where *n* = 0, 1 or 2).

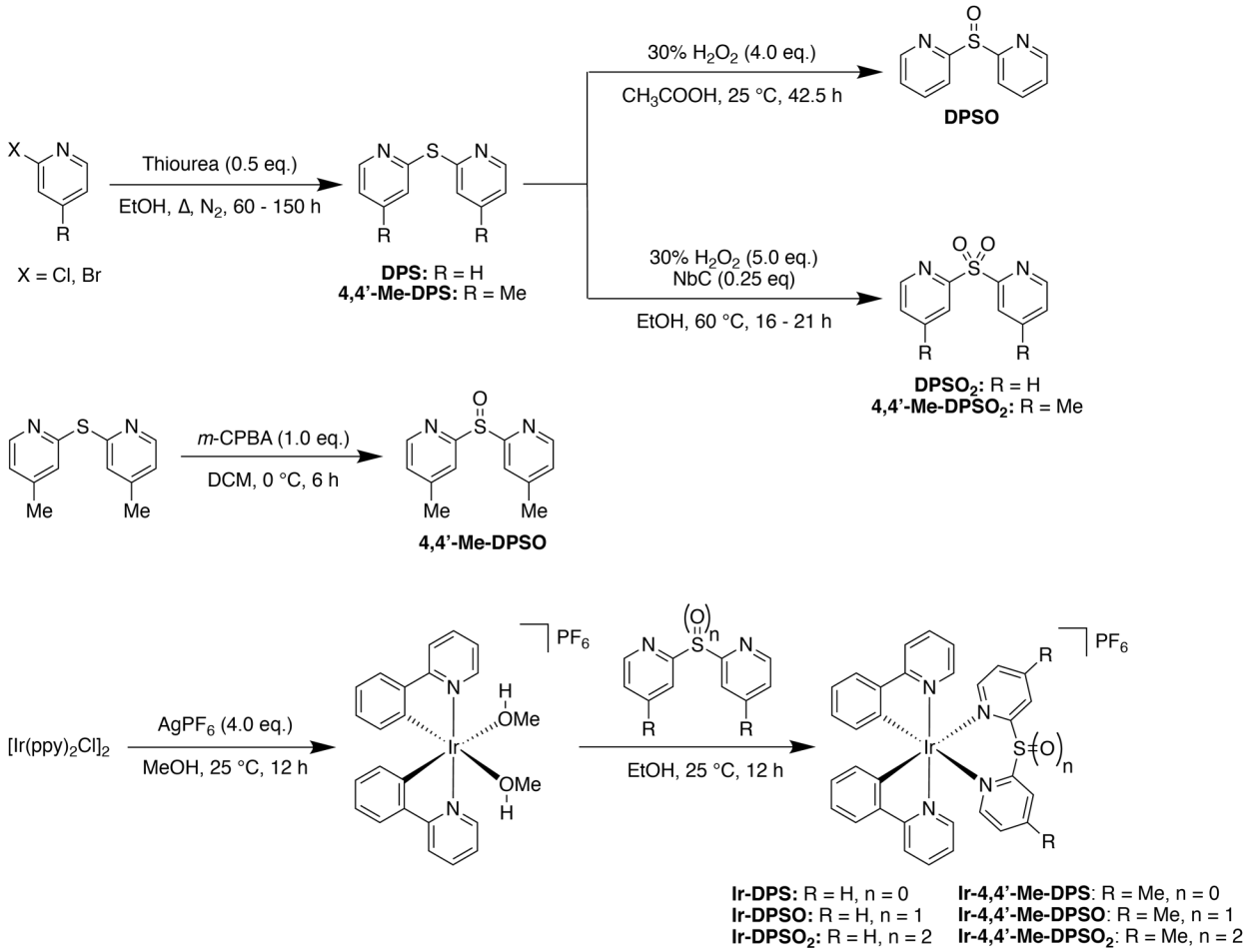

2.3 Synthesis of $[Ir(ppy)_2(N^{\wedge}N)][PF_6]$ Complexes

The $[Ir(ppy)_2Cl]_2$ dimer was prepared by a microwave-assisted reaction of $IrCl_3 \cdot xH_2O$ with 2-phenylpyridine.[100] The dimer was isolated as a yellow solid in high yield, requiring no further purification. Complexes $[Ir(ppy)_2(N^{\wedge}N)][PF_6]$ (N^N = **DPSO*n*** or **4,4'-Me-DPSO*n***, where *n* = 0, 1

or 2) were synthesized *via* an intermediate solvento complex, formed by the reaction of the iridium dimer with $AgPF_6$ in MeOH, followed by the addition of the appropriate N^N ligand yielding the desired compounds as yellow powders in all cases (Scheme 2-1).[11] The HR-ESI mass spectra show a product peak corresponding to $[M-PF_6]^+$ exhibiting a characteristic iridium isotope pattern.

2.3.1 Nuclear Magnetic Resonance (NMR)

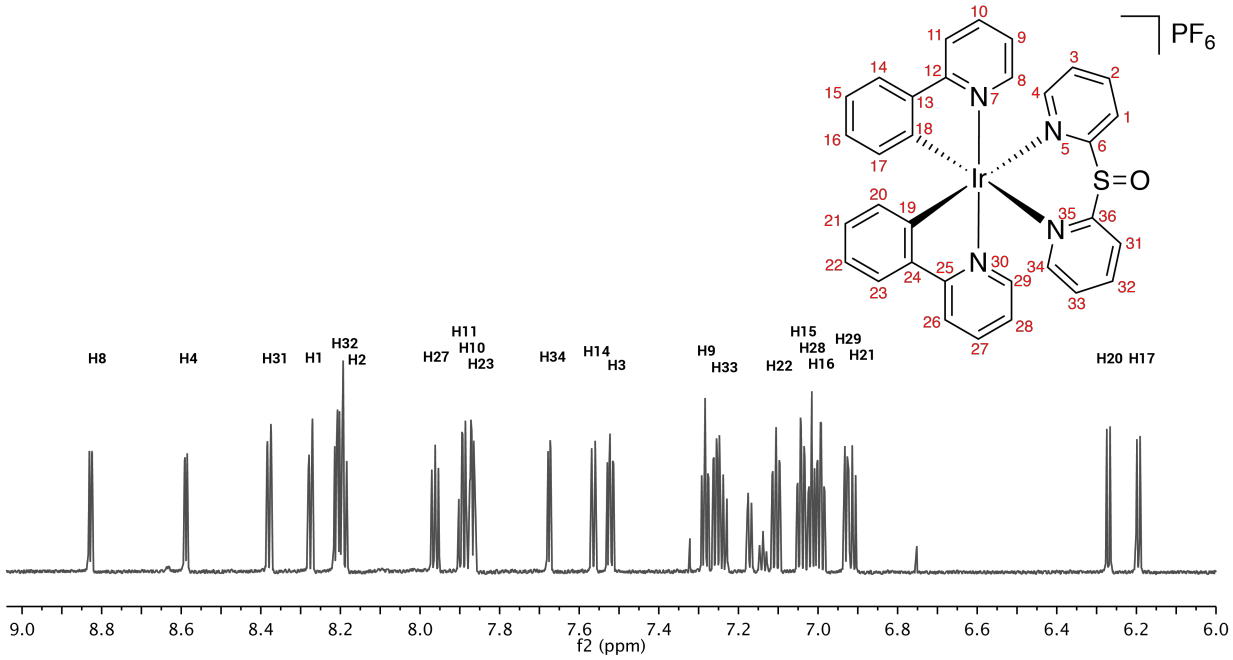

Figure 2-1 Expanded NMR spectrum of **Ir-DPSO** in CD_2Cl_2 at 25 ºC (850 MHz).

^{1}H and ^{13}C NMR spectra of the Ir(III) complexes were assigned using COSY, NOESY, HSQC and HMBC experiments. The sulfoxide component of complexes **Ir-DPSO** and **Ir-4,4'-Me-DPSO** causes the two cyclometallating ligands, and thus the two pyridyl rings of the ancillary ligand, to become inequivalent. This is due to the proximity of the sulfoxide oxygen to one of the ppy ligands, changing its environment relative to the other ppy. The NMR spectrum for **Ir-DPSO**

exhibiting this inequivalence is shown in Figure 2-1. The two different phenylpyridine ligands were distinguished through NOESY cross peaks. Due to the presence of a chiral sulfur center and a chiral metal center it would be expected to see a mixture of diastereomers in the NMR spectrum, however only one species is seen. It is postulated that hydrogen bonding between the oxygen atom and H_8 could be providing a stabilizing interaction that preferentially forms one stereoisomer.

The room temperature NMR spectra of all six complexes have clear, defined peaks with no evidence for exchange or dissociation occurring in CD_2Cl_2; however, in CD_3CN, a stronger coordinating NMR solvent, it was observed for complexes **Ir-DPSO**, **Ir-DPSO$_2$** and **Ir-4,4'-Me-DPSO**, **Ir-4,4'-Me-DPSO$_2$** that the ancillary ligand is replaced by solvent, resulting in $Ir(ppy)_2(CD_3CN)_2][PF_6]$. It is known that upon increasing the oxidation state at the sulfur from sulfide to sulfoxide to sulfone, the electron withdrawing strength of the substituent increases.[101] It is likely that the increased electron-withdrawing character reduces the σ-donating ability of the pyridyl moieties. This may also explain the lower isolated yields found in the complexes with ligands of higher sulfur oxidation state.

Complexes **Ir-DPSO** and **Ir-4,4'-Me-DPSO** both have the possibility of *N,N* coordination through both pyridyl moieties and *N,O* binding through one pyridyl group and the oxygen of the sulfoxide. NMR experiments show that in both cases the ancillary ligand is bound *N,N* as there are no NOE cross peaks observed between protons H_4 and H_{34}, the presence of which would indicate free rotation of a pendant pyridyl ring.

2.3.2 Single Crystal X-Ray Diffraction

Single crystals of **Ir-DPS** were grown by vapour diffusion of hexanes into a CH_2Cl_2 solution of the complex. **Ir-DPS** crystallizes in the space group P-1 with the asymmetric unit

containing two complex molecules and their respective counter-anions (Figure 2-2). The hexane solvent molecule contained within the structure is disordered and has been removed using the SQUEEZE method.[102]

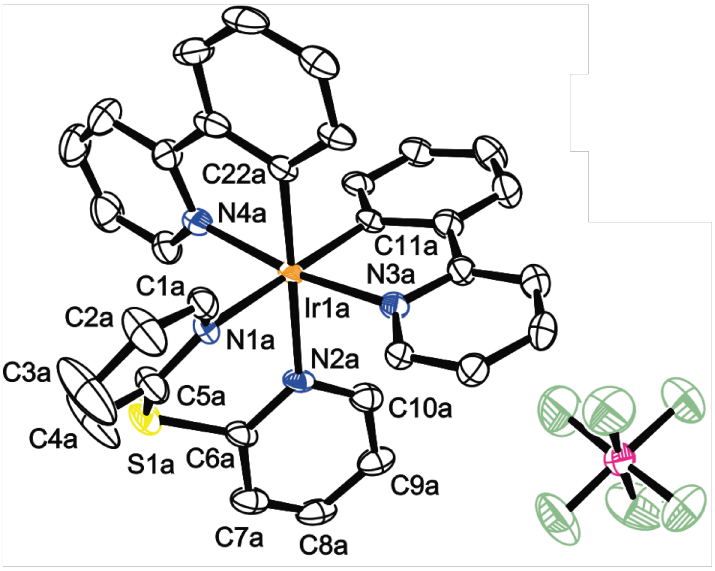

Figure 2-2 Crystal structure of **Ir-DPS** (Λ conformer). Ellipsoids plotted at 50% probability and H atoms and hexane molecules removed for clarity.

As shown in Figure 2-2, coordination occurs through the pyridyl nitrogen atoms of the diimine ligand (**DPS**), each adopting a *trans* configuration with respect to the corresponding coordinating carbon atom of the cyclometallating phenyl ring. Bond angles and lengths discussed in this section are in respect to the Λ conformation of **Ir-DPS**. The complex exists in an octahedral geometry with both ppy cyclometallating ligands showing deviation from planarity between the rings (angles between ring planes are 5.8 and 13.15º respectively). The tetrahedral geometry about the sulfur atom results in non-planarity of the **DPS** ligand pyridyl rings with an angle of 40.3º between each ring plane and results in a N1–Ir–N2 bite angle of 89.99º. This allows the complex

to adopt a more perfect octahedron when compared to $[Ir(ppy)_2(bpy)][PF_6]$[13] which has a smaller bite angle for the bpy ligand of 76.20º. The bond Ir–N bond lengths are comparable between the two species, with **Ir-DPS** having slightly longer bond lengths (Ir–N1, Ir–N2 = 2.198, 2.173 Å, respectively) than $[Ir(ppy)_2(bpy)][PF_6]$ (Ir–N1, Ir–N2 = 2.129, 2.136 Å respectively), indicating a slight reduction in σ-donation from the ancillary ligand in **Ir-DPS**. Complexes containing ligand **DPS** have previously been synthesized, with crystal structures reported for species containing ruthenium,[103-105] rhodium[106] and platinum and palladium.[107,108] In the case of $[Ru(\mathbf{DPS})_2(N,S\text{-}\mathbf{DPS})][PF_6]$,[105] a homoleptic Ru(II) complex chelated with ligand **DPS**, two ligands bind *N*,*N* while the third binds *N*,*S* resulting in a pendant pyridyl ring. This is not observed in **Ir-DPS**, likely due to the cyclometalling ppy ligands having less bulk than **DPS**.

2.4 Photophysical Properties

2.4.1 Absorption Spectroscopy

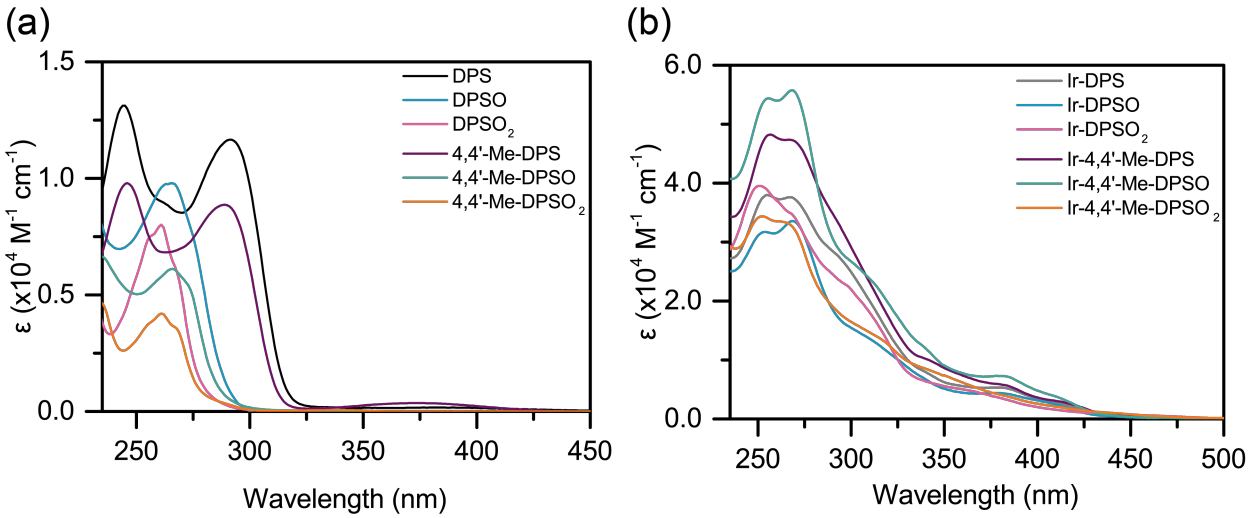

Figure 2-3 Absorption spectra of (a) Pro-ligands **DPSO*n*** and **4,4'-Me-DPSO*n*** and (b) complexes **Ir-DPSO*n*** and **Ir-4,4'-Me-DPSO*n***. All spectra were recorded in ~ 2×10^{-5} M CH_2Cl_2 solutions at room temperature.

The absorption spectra of sulfide, sulfoxide and sulfone pro-ligands **DPSO$_n$** and **4,4'-Me-DPSO$_n$** (n = 0, 1 or 2) are shown in Figure 2-3(a). Features at higher energies than 325 nm in all pro-ligands correspond to π–π* transitions. The spectra of the sulfide compounds **DPS** and **4,4'-Me-DPS** contain a weak low energy feature at 375 nm. Absorption spectra of all six Ir(III) complexes were recorded in CH_2Cl_2 with concentrations of ~2 × 10^{-5} M (Figure 2-3(b)). The spectra are similar with all complexes showing intense absorption bands lying in the UV region with maxima in the range 250–270 nm, which are assigned to spin-allowed π–π* transitions of the ligands. Lower intensity bands are observed between 350 and 450 nm which correspond to spin-allowed metal-to-ligand (^{1}MLCT) and ligand-to-ligand (^{1}LLCT) transitions. Weaker intensity tails above 450 nm comprise spin-forbidden ^{3}MLCT, ^{3}LLCT and ligand centered (^{3}LC) transitions.[94]

2.4.2 Photoluminescence Spectroscopy

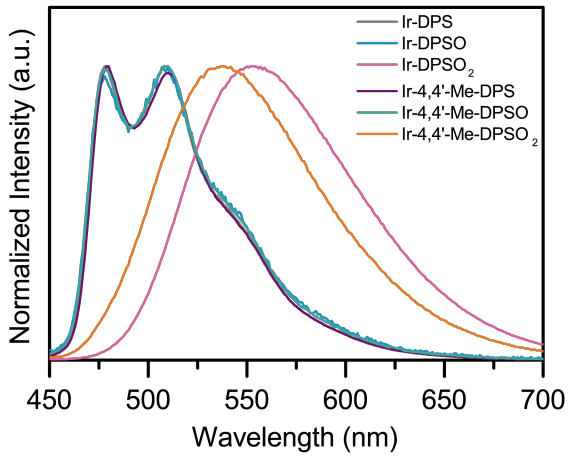

Figure 2-4 Photoluminescence spectra of Ir(III) complexes (λ_{ex} = 390 nm). All spectra were recorded in ~2 × 10^{-5} M CH_2Cl_2 solutions at room temperature and sparged with Ar for 25 min.

The normalized photoluminescence spectra of all six Ir(III) complexes were recorded in CH_2Cl_2 solution after deaerating with Ar for 25 min and are shown in Figure 2-4(c). Emission maxima are summarized in Table 2-1. Emission of Ir(III) complexes with the general structure $[Ir(N^N)_2(N^N)][PF_6]$ occurs from the lowest-lying triplet state (T_1), which due to the heavy atom effect, typically contains a mixture of contributions from ^{3}MLCT, ^{3}LLCT and ^{3}LC states.[109] In general, when the contribution is higher in charge-transfer character, the emission profile becomes broader and less structured.

Table 2-1 Photophysical data of Ir(III) complexes in ~2×10^{-5} M CH_2Cl_2 solutions at room temperature.

	λ_{em} [nm] [a]	τ_{em} [μs] [b]	PLQY [a]	k_r [10^6 s^{-1}]	k_{nr} [10^6 s^{-1}]
Ir-DPS	478, 510, 548	0.360	0.04	0.10	2.7
Ir-DPSO	478, 510, 548	0.163 (3.6%), 0.024 (93.2%), 0.001 (3.2%)	<0.01	0.25 [c]	41.4 [c]
Ir-DPSO$_2$	552	0.231	0.03	0.14	4.2
Ir-4,4'-Me-DPS	478, 510, 548	0.828	0.08	0.10	1.1
Ir-4,4'-Me-DPSO	478, 510, 548	0.898 (13.2%) , 0.060 (83.9%), 0.044 (2.9%)	0.03	0.43 [c]	16.2 [c]
Ir-4,4'-Me-DPSO$_2$	537	0.065	0.04	0.66	14.7

[a] λ_{ex} = 390 nm. [b] λ_{ex} = 370 nm. [c] k_r and k_{nr} for sulfoxide complexes calculated using the major lifetime component.

Sulfide (**Ir-DPS**, **Ir-4,4'-Me-DPS**) and sulfoxide (**Ir-DPSO**, **Ir-4,4'-Me-DPSO**) complexes show identical, fine-structured luminescence profiles with maxima at 478, 510 and 548

nm, indicating a large ^{3}LC character of the emissive state. This emission is independent of excitation wavelength. Solvents with higher polarity can often stabilize charge transfer states resulting in broadened, red-shifted emission, hence photo-luminescence spectra of **Ir-DPS** were obtained in solvents of increasing polarity (CH_2Cl_2, MeOH and CH_3CN) to probe the nature of the emission. No change in emission profile was observed in these experiments with the fine structure intact, supporting the assignment of an emitting ^{3}LC state of π–π* character, localized on the ppy cyclometallating ligands. This shape also bears a distinct resemblance to the emission band of $[Ir(ppy)_2(CO)(Cl)]$[110], further suggesting a dominant ^{3}LC contribution to the emissive triplet state.

In contrast, sulfone complexes **Ir-DPSO$_2$** and **Ir-4,4'-Me-DPSO$_2$** show broad, featureless photoluminescence spectra indicative of ^{3}MLCT character with both species exhibiting bathochromically shifted emission bands compared to their sulfide and sulfoxide counterparts. A small blue-shift of 15 nm is observed on going from **Ir-DPSO$_2$** (552 nm) to **Ir-4,4'-Me-DPSO$_2$** (537 nm) which is attributed to the methyl substituents in the 4- and 4′-positions of the ancillary ligand in **Ir-4,4'-Me-DPSO$_2$**, resulting in destabilization of the LUMO due to the higher electron density on the N^N ligand.[111]

2.4.3 Photoluminescence Quantum Yields (PLQY)

Photoluminescence quantum yields (PLQY, Table 2-1) in deaerated CH_2Cl_2 are in the range ~0.01–0.08, slightly lower than that of $[Ir(ppy)_2(bpy)][PF_6]$ in deaerated CH_3CN (0.14).[112] These low values are attributed to the increased ligand flexibility of the ancillary ligands about the sulfur atom. The excited-state energy can presumably be dissipated more readily through ligand motion when compared to more rigid ancillary ligands such as 2,2'-bipyridine. The low PLQYs for sulfoxide-containing complexes **Ir-DPSO** and **Ir-4,4'-Me-DPSO** (<0.01 and 0.03,

respectively) could be due to a deactivating pathway opened up by excited-state sulfoxide inversion. The general trend of higher PLQY for the methyl-functionalized complexes **Ir-4,4'-Me-DPSO*n*** relative to **Ir-DPSO*n*** is attributed to the increased σ-donation caused by this methyl substitution destabilizing a short-lived, non-emissive triplet metal-centered state (^{3}MC) and increases the energy separation between this ^{3}MC state and the emissive ^{3}LC state based on the cyclometalling ligands.[113,114]

2.4.4 Photoluminescence Lifetimes

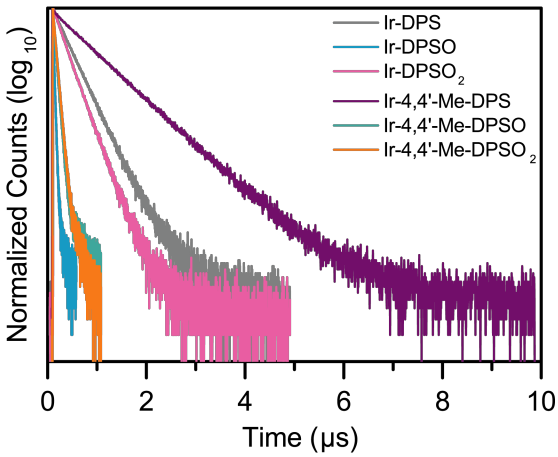

Figure 2-5 Photoluminescence lifetimes of Ir(III) complexes (λ_{ex} = 370 nm). All spectra were recorded in ~2×10^{-5} M CH_2Cl_2 solutions at room temperature and sparged with Ar for 25 min.

Excited-state lifetimes (τ) in deaerated CH_2Cl_2 are less than 1 μs for all complexes (Figure 2-5 and Table 2-1). The sulfone complexes **Ir-DPSO$_2$** and **Ir-4,4'-Me-DPSO$_2$** each display a mono-exponential decay. The lifetimes are shorter than those of sulfide complexes **Ir-DPS** and **Ir-4,4'-Me-DPS**, consistent with an emission attributed to ^{3}MLCT/^{3}LLCT states rather than from a ^{3}LC state.[115-117] This is further supported as a lower ^{3}LC character is indicated by a higher k_r.[94,117]

Both sulfoxide complexes **Ir-DPSO** and **Ir-4,4'-Me-DPSO** display a tri-exponential decay with the major component of each emission residing in the 10's of nanoseconds range. The presence of the sulfoxide group breaks the symmetry in the complex (see 2.3.1) and it is thought that this break in symmetry causes the multi-exponential emission lifetimes.

2.5 Electrochemical Properties

Cyclic voltammetric data for $[Ir(N^N)(N^N)]^+$ (N^N = **DPSO*n*** or **4,4'-Me-DPSO*n***, where *n* = 0, 1 or 2) are visualized in Figure 2-6 and summarized in Table 2-2. All complexes show irreversible oxidation processes. For both series, upon increasing sulfur oxidation state from sulfide through sulfone, the first oxidation of the complex is shifted to higher potential. This is attributed to the electron-withdrawing nature of the sulfoxide and sulfone groups reducing the electron density on the iridium center, thereby stabilizing the HOMO. Additional peaks may be due to oxidation at the sulfur center on the ancillary ligand.

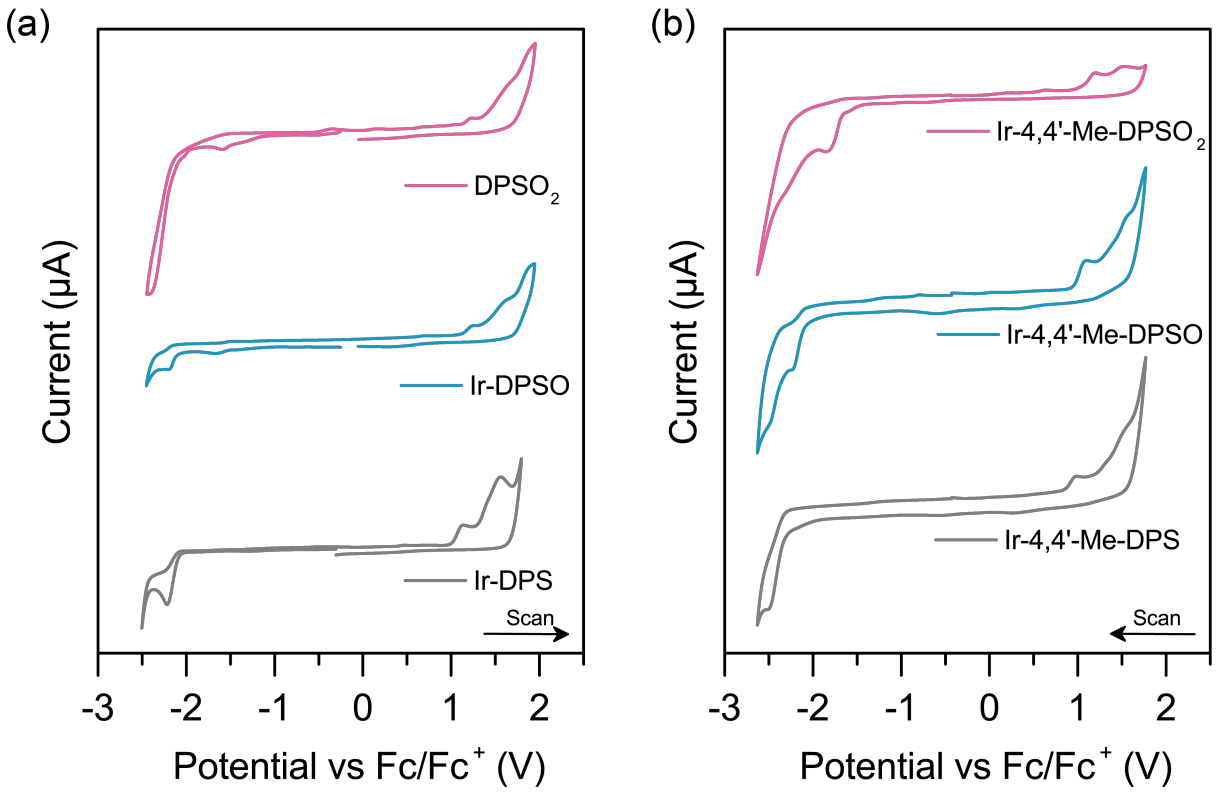

Figure 2-6 Cyclic voltammograms of Ir(III) in dry, N_2-sparged CH_2Cl_2 at room temperature. (a) **Ir-DPSO*n*** complexes. (b) **Ir-4,4'-Me-DPSO*n*** complexes.

As the sulfur oxidation state is increased, the first reduction occurs at a more positive potential when measured against the sulfide complexes (–1.26 V, –1.73 V for **Ir-DPSO$_2$** and **Ir-4,4'-Me-DPSO$_2$** respectively compared to –2.16 V, –2.07 V for **Ir-DPS** and **Ir-4,4'-Me-DPS** respectively), consistent with stabilization of the LUMO. Additional reductive peaks seen in **Ir-DPSO**, **Ir-DPSO$_2$**, **Ir-4,4'-Me-DPSO** and **Ir-4,4'-Me-DPSO$_2$** are attributed to reduction of the respective sulfoxide and sulfone gap. The smaller electrochemical ΔE for sulfone complexes **Ir-DPSO$_2$** and **Ir-4,4'-Me-DPSO$_2$** is consistent with the red-shift of the emission compared to the respective sulfide and sulfoxide complexes.

Table 2-2 Electrochemical data of Ir(III) complexes in deaerated CH_2Cl_2 solutions and referenced to Fc/Fc^+.

Complex	$E_{1/2}^{ox}$ [V]	$E_{1/2}^{red}$ [V]	$\Delta E_{1/2}$ [V] [a]
Ir-DPS	1.06	–2.16	3.22
Ir-DPSO	1.16	–1.59	2.75
Ir-DPSO$_2$	1.17	–1.26	2.43
Ir-4,4'-Me-DPS	0.92	–2.40	3.32
Ir-4,4'-Me-DPSO	1.02	–2.16	3.18
Ir-4,4'-Me-DPSO$_2$	1.13	–1.73	2.86

[a] $\Delta E = E_{1/2}^{ox} - E_{1/2}^{red}$

2.6 Theoretical Calculations

The energy and electron density contours were calculated for the HOMO and lowest unoccupied molecular orbitals (LUMO, LUMO+1 and LUMO+2) for all six Ir(III) complexes and are shown in Table 2-3, with frontier orbital diagrams illustrated in Appendix Chapter 6:Listing A.1Chapter 6:Listing A.2.

Table 2-3 Ground-state frontier orbital energies for Ir(III) complexes.

	Energy [eV]					
	Ir-DPS	**Ir-DPSO**	**Ir-DPSO$_2$**	**Ir-4,4'-Me-DPS**	**Ir-4,4'-Me-DPSO**	**Ir-4,4'-Me-DPSO$_2$**
HOMO	–5.90	–6.00	–6.05	–5.86	–5.95	–6.01
LUMO	–2.07	–2.25	–2.70	–1.97	–2.11	–2.53
LUMO+1	–2.01	–2.14	–2.24	–1.94	–2.06	–2.11
LUMO+2	–1.99	–2.04	–2.08	–1.92	–1.94	–2.01

It was found that both increasing the oxidation state of sulfur and introducing methyl groups have a negligible impact on the HOMO energy and electron density distribution of the complexes. The HOMO is mainly located at the iridium and ppy ligands, with functionalization at the ancillary N^N ligand not contributing to this orbital. These trends are also consistent with the oxidation potentials of these complexes. The LUMOs of these complexes are located at the ancillary N^N ligand with a small contribution from iridium (except in **Ir-4,4'-Me-DPS**), and oxidation of the sulfur stabilizes the orbitals centered on the N^N ligand. In the case of the unsubstituted series, the LUMO energy of **Ir-DPSO$_2$** is 0.63 eV lower than **Ir-DPS**. The addition of methyl groups in the 4- and 4'- positions of the ancillary ligand destabilizes the LUMO by 0.1–0.17 eV. The LUMO, LUMO+1 and LUMO+2 of **Ir-4,4'-Me-DPS** all have similar energies and contributions from both the ppy ligands and the N^N ligand. The combination of these effects leads to HOMO–LUMO energy gaps that decrease on oxidation of sulfur, and increase with the introduction of methyl groups. These trends follow those seen in the electrochemical data, however they contradict the experimental emission data. To gain more insight into the emitting states, the geometry of the lowest-energy triplet excited state (T_1) must be probed.

Table 2-4 The calculated adiabatic energy differences of Ir(III) complexes with regard to the experimental emission energies.

	Ir-DPS	**Ir-DPSO**	**Ir-DPSO$_2$**	**Ir-4,4'-Me-DPS**	**Ir-4,4'-Me-DPSO**	**Ir-4,4'-Me-DPSO$_2$**
ΔE [eV]	2.66	2.65	2.58	2.66	2.65	2.66
E_{em} [eV]	2.35	2.34	2.24	2.35	2.34	2.28
λ_{em} calc. [nm]	528	530	554	528	530	543

To elucidate the emitting state, the geometry of the T_1 state was optimized using the spin-unrestricted UB3LYP method. Table 2-4 summarizes the adiabatic energy difference between S_0 and T_1 and emission energy (E_{em}) calculated as the vertical energy difference between T_1 and S_0 at the optimized geometry of T_1 (Figure 2-7(a)). The calculations find almost identical emission energies for **Ir-DPS**, **Ir-DPSO**, **Ir-4,4'-Me-DPS** and **Ir-4,4'-Me-DPSO**. This is in accordance with the experimental data that on oxidizing the ligands from sulfide to sulfoxide (in addition to the introduction of methyl groups in the case of **Ir-4,4'-Me-DPS** and **Ir-4,4'-Me-DPSO**) the emission energy is unaffected since the emitting state is centered on the ppy ligands. The calculations also correctly predict the red-shifted emission on full oxidation to sulfone, in addition to the blue-shifted emission of **Ir-4,4'-Me-DPSO$_2$** relative to **Ir-DPSO$_2$** after substitution of methyl groups in the 4- and 4'- positions of the ancillary ligand.

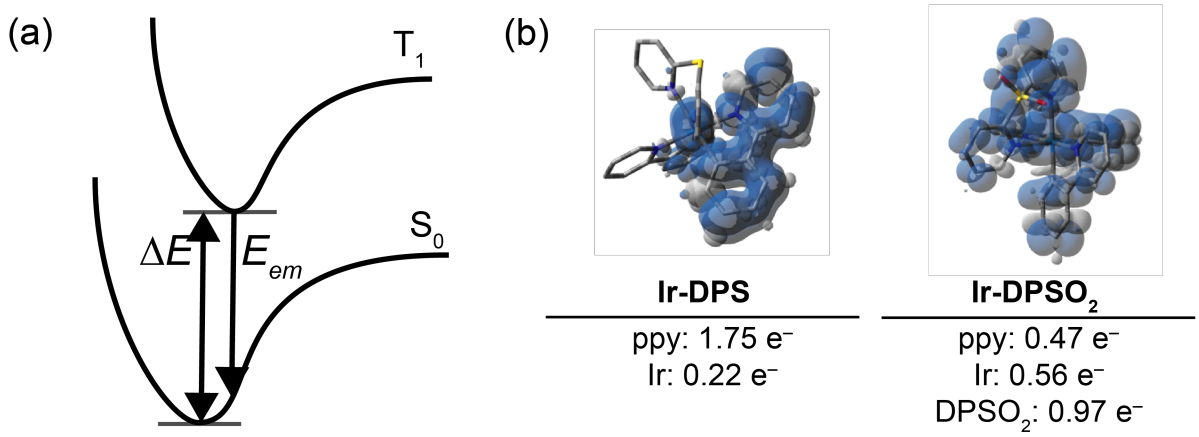

Figure 2-7 (a) Schematic diagram of the adiabatic energy difference (ΔE) between S_0 and T_1, and the emission energy (E_{em}) from T_1. (b) Unpaired-electron spin density contours for **Ir-DPS** and **Ir-DPSO$_2$**.

The unpaired-electron spin density plots for T_1 of each complex are shown in Appendix A.3. Unpaired-electron spin density plots comparing complexes **Ir-DPS** and **Ir-DPSO$_2$** are shown

in Figure 2-7(b). The sulfide and sulfoxide complexes exhibit similar spin density distributions which are mainly centered on one of the ppy ligands, with some contribution from the iridium center. This indicates that the T_1 states of the sulfide and sulfoxide complexes are mainly ligand-centered, with a small contribution of MLCT character. The unpaired electron spin density of **Ir-DPSO$_2$** and **Ir-4,4'-Me-DPSO$_2$** is spread over the complex, with ~0.5 e^- on the iridium, 0.5 e^- on the ppy ligands and 1 e^- on the ancillary ligand, which matches the topology of MLCT transitions, supporting the assigned MLCT emitting state of sulfone complexes.

To further understand the nature of the lowest-energy triplet state, time-dependent DFT (TD-DFT) calculations were employed for all six complexes at the optimized geometry of S_0 (Appendix A.4). The first triplet states of **Ir-DPS**, **Ir-DPSO**, **Ir-4,4'-Me-DPS** and **Ir-4,4'-Me-DPSO** result from the mono-excitation of the HOMO to the first orbital centered on the ppy ligands; the LUMO for **Ir-4,4'-Me-DPS**, the LUMO+1 for **Ir-4,4'-Me-DPSO** and the LUMO+2 for **Ir-DPS** and **Ir-DPSO**. The first T_1 states of **Ir-DPSO$_2$** and **Ir-4,4'-Me-DPSO$_2$** are mainly contributed from HOMO–LUMO excitation and have MLCT character. The addition of methyl groups to the ancillary ligand decreases the contribution of the MLCT transition. These results again demonstrate the LC emitting nature of the sulfide and sulfoxide complexes and the MLCT emitting nature of the sulfone complexes.

2.7 Conclusions

Six new $[Ir(N^N)(N^N)]^+$ cationic complexes have been synthesized consisting of 2-phenylpyridine cyclometallating ligands (N^N) and sulfur-bridged ancillary ligands (N^N). Pro-ligands **DPSO$_n$** (n = 0, 1 or 2) contain two pyridyl rings connected in the 2,2'- positions by a sulfide (**DPS**; S), sulfoxide (**DPSO**; SO) and sulfone (**DPSO$_2$**; SO_2), and pro-ligands **4,4'-Me-DPSO$_n$** (n

= 0, 1 or 2) retained a similar structure, except with methyl substituents in the 4 and 4'-positions. These ligands were designed to gradually red-shift the emission upon increasing sulfur oxidation state.

The complexes were characterized by spectroscopic and mass spectrometry techniques, along with the single crystal structure of **Ir-DPS**. The sulfide (**Ir-DPS**, **Ir-4,4'-Me-DPS**) and sulfoxide complexes (**Ir-DPSO**, **Ir-4,4'-Me-DPSO**) show blue-green emission with identical, fine-structured profiles (maxima at 478, 510 and 548 nm). The vibrational structure indicates significant ^{3}LC contributions to the lowest lying triplet state, and the absence of a red-shifted broadening in solvents of increasing polarity confirms a lack of charge transfer nature. Sulfone complexes (**Ir-DPSO$_2$, Ir-4,4'-Me-DPSO$_2$**) exhibit broad, red-shifted emission bands, indicative of a pronounced ^{3}MLCT/^{3}LLCT state. Complex **Ir-4,4'-Me-DPSO$_2$**, with methyl substituents in the 4,4'-positions, shows a slight blue-shift (15 nm) compared to **Ir-DPSO$_2$**. PLQYs in deaerated CH_2Cl_2 were low (<0.01–0.08), slightly slower than that of $[Ir(ppy)_2(bpy)][PF_6]$ (0.14) in deaerated CH_3CN.

Here we have shown a new "two-level" method to tuning the emission colour of Ir(III) complexes utilizing methyl- substitution of a sulfur-bridged ancillary ligand, coupled with varying oxidation state at the sulfur center. Increasing the substituents' electron-donating ability at the 4,4'-positions of the sulfide-bridged ancillary ligand, coupled with the addition of electron-withdrawing groups at the cyclometallating 2-phenylpyridine ligands could result in a desired blue-shift of the emission colour.

2.8 Experimental Details

2.8.1 General

All experiments were conducted in an inert atmosphere using standard Schlenk techniques unless otherwise stated. Solvents used were of reagent grade and used without any further purification. HPLC grade solvents were used for analyses. Thiourea was purchased from TCI and 2-bromopyridine and 2-chloro-4-(methyl)pyridine purchased from Sigma Aldrich. All compounds were used as received. $[Ir(ppy)_2Cl]_2$ was prepared as per the literature.[100]

2.8.2 Spectroscopy

^{1}H NMR and ^{13}C NMR spectra were collected using either a Bruker AV-400 or AV-850 spectrometer and referenced to the residual protonated solvent peak. NMR solvents (from either Cambridge Isotope Laboratories or Aldrich) were used as received. Electrospray ionization mass spectrometry data was obtained using a Bruker Esquire LC ion trap mass spectrometer. Infrared spectroscopy was performed on an attenuated total reflection (ATR) crystal using a Perkin-Elmer Frontier FT-IR spectrometer. Electronic absorption spectra were recorded on a Varian-Cary 5000 UV-Vis-near-IR spectrophotometer. Fluorescence data were collected on a Photon Technology International (PTI) QuantaMaster 50 fluorimeter fitted with an integrating sphere, double excitation monochrometer and utilizing a 75 W Xe arc lamp as the source. Emission lifetime data were collected using a Horiba Yvon Fluorocube TCSPC apparatus. A 370 nm NanoLED source pulsing at a repetition rate of 50–100 kHz was used for excitation. Broadband emission was monitored by a CCD detector at wavelengths >450 nm using a low pass filter. Data were fitted using the DAS6 Data Analysis software package. All measurements were recorded at room

temperature. Sample solutions were maintained under a blanket of Ar for the duration of the measurements in 1 cm^2 quartz cells (Starna Cells) fitted with a rubber septum.

2.8.3 X-ray Crystallography

Single crystal X-ray data was collected using a Bruker APEX DUO diffractometer with graphite monochromated Mo Kα radiation (λ = 0.71073 Å) at 90 K. Raw frame data were processed using APEX2.[118] The program SAINT+, version 6.02[118] was used to reduce the data and the program SADABS was used to make corrections to the empirical absorptions. Space group assignments were made using XPREP[118] on all compounds. In all cases, the structures were solved in the WinGX Suite[119] of programs by direct methods using SHELXS-97[120] and refined using full-matrix least-squares/difference Fourier techniques on F using SHELXL-97[120] All non-hydrogen atoms were refined anisotropically. Diagrams and publication material were generated using ORTEP-3,[121] and PLATON.[122]

2.8.4 Electrochemistry

Solution state electrochemical data was collected on a CHI660D potentiostat with a 3-electrode configuration using a glassy carbon working electrode, Ag/AgCl reference electrode and Pt wire counter electrode. 0.1 M $[NBu_4][PF_6]$ in CH_2Cl_2 was degassed with N_2 and used as the electrolyte. 0.3 mM solutions of each complex were prepared and a scan rate of 100 mV/s was applied in all cases. Potentials were referenced to Fc/Fc^+ with the addition of ferrocene at the end of each experiment.

2.8.5 Computational Details

Density functional theory (DFT) calculations were carried out using the Gaussian 09 Rev.D01 suite of programs. The B3LYP functional with 6-31G** basis set (for C, H, S and O atoms)[123,124] and the LANL2DZ effective-core pseudopotential (for iridium)[125] were employed to optimize the geometry of the ground states (S_0) and lowest-energy triplet states (T_1) of all complexes, with no symmetry restrictions. Phosphorescence energy is estimated as the energy difference the minimum of T_1 and the energy of S_0 at the T_1 optimized geometry. All calculations were performed in the presence of the solvent (CH_2Cl_2). Solvent effects were considered within the self-consistent reaction field (SCRF) theory using the polarized continuum model (PCM) approach.[126,127] Time-dependent DFT (TD-DFT) calculations were also performed to understand the nature of T1 states.[128,129]

2.8.6 Synthesis

di(pyridin-2-yl)sulfane (DPS)

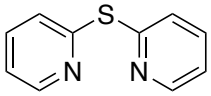

Synthesis of **DPS** was adapted from the literature.[96] 2-bromopyridine (0.5 mL, 0.154 mol, 1.0 eq.) and thiourea (5.86 g, 0.077 mol, 0.5 eq.) were placed under a N_2 atmosphere and then dissolved in EtOH (500 mL). The resulting solution was heated at reflux for 60 h, cooled and the EtOH removed. The crude product was dissolved in CH_2Cl_2 (20 mL), washed with water (3 × 20 mL), brine (20 mL) and then dried using $MgSO_4$. The solution was filtered and solvent removed under reduced pressure. The resulting solid was purified by column chromatography (silica, 100% CH_2Cl_2 followed by 9:1 CH_2Cl_2:MeOH) yielding a yellow oil (11.6 g, 0.062 mol, 80%). NMR spectroscopic data agree with the literature values.[105,130] ^{1}H NMR (400

MHz, CD_2Cl_2) δ 8.50 (ddd, J = 4.8, 2.0, 0.9 Hz, 1H), 7.63 (ddd, J = 7.9, 7.5, 2.0 Hz, 1H), 7.43 (dt, J = 8.0, 1.0 Hz, 1H), 7.17 (ddd, J = 7.5, 4.8, 1.1 Hz, 1H).

2,2'-sulfinyldipyridine (DPSO)

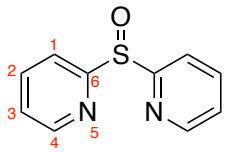

DPS (0.173 g, 0.919 mmol, 1.0 eq.) was dissolved in 2 mL glacial acetic acid, to which a 30% solution of H_2O_2 (0.35 mL, 3.68 mmol, 15.0 eq.) was added dropwise. The reaction mixture was stirred at 25 ºC for 42.5 h, followed by basification with 6 M NaOH, forming a yellow suspension which turned white after stirring for 30 min. Brine (50 mL) was added and the crude product extracted with CH_2Cl_2 (3 × 10 mL) followed by drying of the combined organics over $MgSO_4$ and removal of the CH_2Cl_2 *in vacuo*. Purification was performed by column chromatography (silica, 95:5 CH_2Cl_2:MeOH), resulting in an off-white powder (0.107 g, 0.524 mmol, 57%). ^{1}H NMR (400 MHz, CD_2Cl_2) δ 8.57 (d, J = 4.6 Hz, 2H, H_4), 7.97 (d, J = 7.9 Hz, 2H, H_1), 7.88 (td, J = 7.7, 1.6 Hz, 2H, H_2), 7.39 – 7.31 (m, 2H, H_3). ^{13}C{^{1}H} NMR (CD_2Cl_2, 100 MHz) δ 164.84 (C_6), 150.23 (C_4), 138.40 (C_2), 125.47 (C_3), 119.96 (C_1). HR-ESI MS: *m/z* calcd. for $C_{10}H_8N_2ONaS$: 227.0255; Found: 227.0255 $[M+Na]^+$. IR (neat): $\tilde{\nu}$ (σ SO) 1037 cm^{-1}.

2,2'-sulfonyldipyridine ($DPSO_2$)

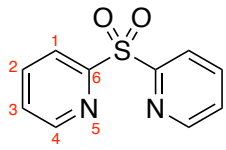

DPS (0.743 g, 3.95 mmol, 1.0 eq.) was dissolved in 12 mL EtOH, to which NbC (0.048 g, 0.460 mmol, 0.25 eq.) was added, followed by a 30% solution of H_2O_2 (2.85 mL, 28.5 mmol, 5.0 eq.). The reaction mixture was heated at 60 ºC for 21 h. The mixture was cooled to room temperature, saturated $Na_2S_2O_3$ solution (50 mL) added to quench any unreacted peroxides and the product extracted with CH_2Cl_2 (3 × 15 mL). The

combined organics were washed with brine (20 mL), dried over $MgSO_4$ and the solvent evaporated, yielding a white powder that required no further purification (0.730 g, 3.31 mmol, 84%). ^{1}H NMR (400 MHz, CD_2Cl_2) δ 8.63 (ddd, J = 4.7, 1.8, 0.9 Hz, 2H, H_4), 8.29 (d, J = 7.9 Hz, 2H, H_1), 8.00 (td, J = 7.8, 1.7 Hz, 2H, H_2), 7.52 (ddd, J = 7.7, 4.7, 1.0 Hz, 2H, H_3). ^{13}C{^{1}H} NMR (CD_2Cl_2, 100 MHz) δ 157.46 (C_6), 150.73 (C_4), 138.47 (C_2), 127.77 (C_3), 124.18 (C_1). HR-ESI MS: *m/z* calcd. for $C_{10}H_8N_2O_2S$: 220.0306; Found: 220.0307 $[M]^+$. IR (neat): $\tilde{\nu}$ (σ SO_2) 1170 and 1309 cm^{-1}.

bis(4-methylpyridin-2-yl)sulfane (4,4'-Me-DPS)

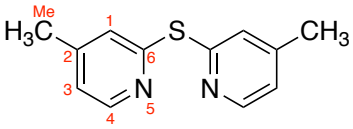

2-Chloro-4-(methyl)pyridine (5.71 g, 44.8 mmol, 2.0 eq.) and thiourea (1.618 g, 23.3 mmol, 0.95 eq.) were dissolved in EtOH (500 mL) under a N_2 atmosphere and heated to reflux for 150 h. After cooling to room temperature, the EtOH was removed, the crude product dissolved in CH_2Cl_2 (10 mL) and washed using water (3 × 10 mL), brine (10 mL), dried with $MgSO_4$ and filtered. Purification was performed by column chromatography (silica, 100% CH_2Cl_2 then 9:1 CH_2Cl_2:MeOH) and after removal of the solvents *in vacuo* a yellow oil was isolated (2.32 g, 10.7 mmol, 48%). ^{1}H NMR (400 MHz, CD_2Cl_2) δ 8.37 – 8.30 (m, 2H, H_4), 7.23 (dt, J = 1.6, 0.8 Hz, 2H, H_1), 6.98 (ddd, J = 5.1, 1.6, 0.8 Hz, 2H, H_3), 2.29 (d, J = 0.8 Hz, 6H, H_{Me}). ^{13}C{^{1}H} NMR (101 MHz, CD_2Cl_2) δ 156.62 (C_2), 149.71 (C_4), 148.51 (C_6), 126.45 (C_1), 122.87 (C_3), 20.69 (C_{Me}). HR-ESI MS: *m/z* calcd. for $C_{12}H_{12}N_2S$: 216.0721; Found: 217.0797 $[M+H]^+$.

2,2'-sulfinylbis(4-methylpyridine) (4,4'-Me-DPSO)

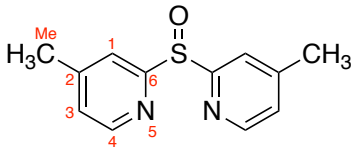

4,4'-Me-DPS (0.300 g, 1.39 mmol, 1.0 eq.) was dissolved in CH_2Cl_2 (7 mL) at 0 ºC. A solution of *m*-CPBA (0.264 g, 1.40 mmol, 1.0 eq.) in CH_2Cl_2 (6 mL) was cooled to 0 ºC and added dropwise over 30 min to the diaryl sulfide. The reaction mixture was stirred at 0 ºC for 6 h and then extracted with 10% NaOH (2 × 20 mL), 5% HCl (2 × 20 mL) and 10% $NaHCO_3$ (20 mL). The organic layer was dried over $MgSO_4$, filtered and the solvent removed under reduced pressure yielding a white solid that required no further purification (0.249 g, 1.07 mmol, 77%). ^{1}H NMR (400 MHz, CD_2Cl_2) δ 8.41 (d, J = 4.9 Hz, 2H, H_4), 7.78 (dt, J = 1.8, 0.8 Hz, 2H, H_1), 7.18 – 7.11 (m, 2H, H_3), 2.41 (s, 6H, H_{Me}). ^{13}C{^{1}H} NMR (101 MHz, CD_2Cl_2) δ 164.85 (C_6), 150.57 (C_2), 150.08 (C_4), 126.58 (C_3), 120.69 (C_1), 21.60 (C_{Me}). HR-ESI MS: *m/z* calcd. for $C_{12}H_{12}N_2ONaS$: 255.0568; Found: 255.0575 $[M+Na]^+$. IR (neat): $\tilde{\nu}$ (σ SO) 1045 cm^{-1}.

2,2'-sulfonylbis(4-methylpyridine) (4,4'-Me-DPSO$_2$)

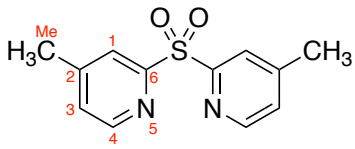

4,4'-Me-DPS (0.590 g, 0.273 mmol, 1.0 eq.) was dissolved in 25 mL EtOH, to which NbC (0.077 g, 0.683 mmol, 0.25 eq.) was suspended and 30% H_2O_2 (4.1 mL, 40.9 mmol, 5.0 eq.) was added dropwise. The reaction mixture was heated to 60 ºC and stirred for 16 h. After cooling to room temperature saturated $Na_2S_2O_3$ solution (80 mL) was added, the product extracted with CH_2Cl_2 (3 × 25 mL), the organics combined, dried over $MgSO_4$ and filtered. After removing the solvent *in vacuo* a white powder was isolated that required no further purification (0.566 g, 2.28 mmol, 83%). ^{1}H NMR (400 MHz, CD_2Cl_2) δ 8.45 (d, J = 4.9 Hz, 1H, H_4), 8.12 (s, 1H, H_1), 7.32 (d, J = 5.6 Hz, 1H, H_3), 2.49 (s, 4H, H_{Me}). ^{13}C{^{1}H} NMR (101 MHz, CD_2Cl_2) δ 157.47 (C_2), 150.76 (C_6), 150.51

(C_4), 128.62 (C_3), 124.96 (C_1), 21.55 (C_{Me}). HR-ESI MS: *m/z* calcd. for $C_{12}H_{12}N_2O_2S$: 248.0619; Found: 249.0706 $[M+H]^+$. IR (neat): $\tilde{\nu}$ (σ SO_2) 1157 and 1313 cm^{-1}.

[Ir(ppy)$_2$(DPS)][PF$_6$] (Ir-DPS)

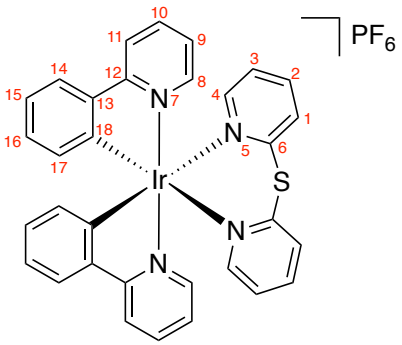

$[Ir(ppy)_2Cl]_2$ (0.111 g, 0.104 mmol, 1.0 eq.) and $AgPF_6$ (0.104 g, 0.415 mmol, 4.0 eq.) were added to a round-bottomed flask and suspended in MeOH (20 mL). The reaction mixture was stirred for 12 h at room temperature, during which AgCl formed as a grey precipitate. The reaction mixture was passed over Celite to remove the AgCl and the filtrate volume reduced. To this **DPS** (0.039 g, 0.208 mmol, 2.0 eq.) was added, the reaction mixture left to stir for 12 h at room temperature, following which the solvent was removed *in vacuo*. The crude solid was purified using column chromatography (silica, 99:1 CH_2Cl_2:MeOH) giving a yellow crystalline powder (0.080 g, 0.096 mmol, 92%). ^{1}H NMR (400 MHz, CD_2Cl_2) δ 8.17 (ddd, J = 5.9, 1.6, 0.8 Hz, 2H, H_8), 8.13 (ddd, J = 5.7, 1.8, 0.7 Hz, 2H, H_4), 8.03 (dd, J = 8.0, 1.2 Hz, 2H, H_{11}), 8.01 – 7.89 (m, 4H, $H_{1,10}$), 7.88 (td, J = 7.7, 1.8 Hz, 2H, H_2), 7.72 (dd, J = 7.7, 1.3 Hz, 2H, H_{14}), 7.23 – 7.14 (m, 4H, $H_{3,9}$), 7.07 (td, J = 7.5, 1.2 Hz, 2H, H_{15}), 6.93 (td, J = 7.5, 1.4 Hz, 2H, H_{16}), 6.24 (dd, J = 7.6, 1.1 Hz, 2H, H_{17}). $^{13}C\{^1H\}$ NMR (101 MHz, CD_2Cl_2) δ 168.12 (C_{13}), 154.34 (C_6), 154.20 (C_4), 151.49 (C_8), 147.48 (C_{18}), 144.39 (C_{12}), 139.95 (C_2), 139.14 (C_{10}), 132.03 (C_{17}), 130.91 (C_{16}), 129.57 (C_1), 126.26 (C_3), 125.32 (C_{14}), 123.51 (C_{15}), 123.09 (C_9), 120.50 (C_{11}). HR-ESI MS: *m/z* calcd. for $C_{32}H_{24}IrN_4S$: 689.1351; Found: 689.1316 $[M-PF_6]^+$.

[Ir(ppy)$_2$(DPSO)][PF$_6$] (Ir-DPSO)

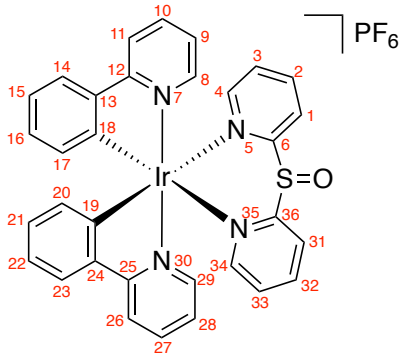

[Ir(ppy)$_2$Cl]$_2$ (0.111g, 0.104 mmol, 1.0 eq.) and AgPF$_6$ (0.110 g, 0.435 mmol, 4.0 eq.) were suspended in MeOH (20 mL) and the reaction mixture stirred for 12 h at room temperature. AgCl was removed by filtration over Celite and then the filtrate dried under reduced pressure. The resulting solid was re-dissolved in EtOH (20 mL) and **DPSO** (0.042 g, 0.207 mmol, 2.0 eq.) added, following which the solution was stirred at room temperature for 12 h. EtOH was removed *in vacuo,* the crude solid purified using column chromatography (silica, 99:1 CH_2Cl_2:MeOH) and the eluted product precipitated with hexanes giving a yellow crystalline solid (0.037 g, 0.044 mmol, 42%). ^{1}H NMR (850 MHz, CD_2Cl_2) δ 8.83 (ddd, J = 5.9, 1.5, 0.8 Hz, 1H, H_8), 8.59 (ddd, J = 5.6, 1.6, 0.7 Hz, 1H, H_4), 8.38 (ddd, J = 8.0, 1.5, 0.7 Hz, 1H, H_{31}), 8.27 (ddd, J = 8.0, 1.5, 0.7 Hz, 1H, H_1), 8.22 – 8.20 (m, 3H, $H_{2,,28,32}$), 7.96 (ddd, J = 8.3, 7.4, 1.5 Hz, 1H, H_{27}), 7.92 – 7.85 (m, 3H, $H_{10,11,23}$), 7.68 (ddd, J = 5.5, 1.6, 0.7 Hz, 1H, H_{34}), 7.56 (ddt, J = 7.7, 1.4, 0.5 Hz, 1H, H_{14}), 7.52 (ddd, J = 7.5, 5.6, 1.5 Hz, 1H, H_3), 7.28 (ddd, J = 7.4, 5.9, 1.6 Hz, 1H, H_9), 7.27 – 7.22 (m, 2H, H_{33}), 7.11 (ddd, J = 7.8, 7.2, 1.1 Hz, 1H, H_{22}), 7.04 (ddd, J = 7.7, 7.3, 1.2 Hz, 1H, H_{15}), 7.03 – 6.98 (m, 1H, H_{16}), 6.93 (ddd, J = 5.9, 1.5, 0.8 Hz, 1H, H_{29}), 6.91 (ddd, J = 7.8, 7.2, 1.4 Hz, 1H, H_{21}), 6.27 (ddd, J = 7.8, 1.2, 0.5 Hz, 1H, H_{20}), 6.19 (ddd, J = 7.6, 1.2, 0.5 Hz, 1H, H_{17}). ^{13}C{^{1}H} NMR (101 MHz, CD_2Cl_2) δ 169.10 (C_{12}), 167.69 (C_{25}), 164.38 (C_6), 161.96 (C_{36}), 154.60 (C_4), 154.35 (C_8), 152.87 (C_{34}), 148.75 (C_{29}), 145.52 (C_{18}), 145.09 (C_{13}), 144.81 (C_{19}), 144.11 (C_{24}), 141.55 (C_{32}), 141.36 (C_{28}), 139.90 (C_{27}), 139.73 (C_{10}), 132.59 (C_{17}), 131.73 (C_{20}), 131.68 (C_{16}), 131.06 (C_{21}), 128.93 (C_3), 128.51 (C_{33}), 126.23 (C_{23}), 125.03 (C_{14}), 124.51 (C_{15}), 124.23 (C_{22}), 124.17 (C_2), 123.76 (C_{31}), 123.33 (C_9), 123.24 (C_1),

121.58 (C_{26}), 120.56 (C_{11}). HR-ESI MS: *m/z* calcd. for $C_{32}H_{24}IrN_4OS$: 705.1300; Found: 705.1277 $[M-PF_6]^+$

[Ir(ppy)$_2$(DPSO$_2$)][PF$_6$] (Ir-DPSO$_2$)

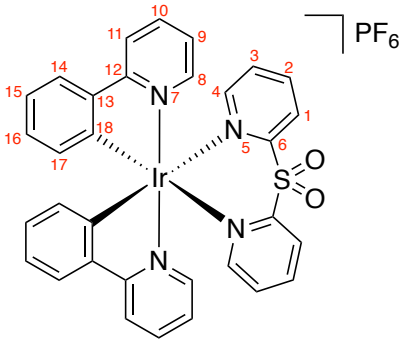

$[Ir(ppy)_2Cl]_2$ (0.090 g, 0.084 mmol, 1.0 eq.) and $AgPF_6$ (0.104 g, 0.415 mmol, 4.0 eq.) were suspended in MeOH (20 mL). The reaction mixture was stirred for 12 h at room temperature, during which time AgCl formed as a precipitate. This was removed by filtration over Celite, followed by evaporation of the solvent. The resulting solid was re-dissolved in EtOH (20 mL) and **DPSO$_2$** (0.037 g, 0.168 mmol, 2.0 eq.) was added. The reaction mixture was left to stir overnight at room temperature, following which the EtOH was removed under reduced pressure and the crude solid dissolved in CH_2Cl_2. This mixture was passed over Celite three times and the product precipitated with hexanes, yielding a yellow powder (0.020 g, 0.023 mmol, 28%). ^{1}H NMR (400 MHz, CD_2Cl_2) δ 8.72 (d, *J* = 7.8 Hz, 2H, H_1), 8.36 – 8.31 (m, 2H, H_4), 8.29 – 8.24 (m, 2H, H_2), 7.99 – 7.94 (m, 2H, H_8), 7.87 (td, *J* = 7.8, 1.5 Hz, 2H, H_{10}), 7.75 – 7.69 (m, 2H, H_{14}), 7.61 (d, *J* = 5.8 Hz, 2H, H_{11}), 7.52 (m, 2H, H_3), 7.13 – 7.05 (m, 4H, $H_{9,15}$), 6.94 (td, *J* = 7.5, 1.4 Hz, 2H, H_{16}), 6.13 (dd, *J* = 7.7, 1.2 Hz, 2H, H_{17}). ^{13}C{^{1}H} NMR (101 MHz, CD_2Cl_2) δ 167.11 (C_{12}), 155.41 (C_4), 155.05 (C_6), 152.09 (C_{11}), 144.98 (C_{13}), 142.52 (C_{18}), 141.89 (C_2), 139.51 (C_{10}), 132.22 (C_{17}), 131.71 (C_3), 131.25 (C_{16}), 127.54 (C_1), 125.59 (C_{14}), 124.52 (C_{15}), 123.62 (C_9), 120.36 (C_8). HR-ESI MS: *m/z* calcd. for $C_{32}H_{24}IrN_4O_2S$: 721.1249; Found: 721.1232 $[M-PF_6]^+$.

Synthesis of [Ir(ppy)$_2$(4,4'-Me-DPS)][PF$_6$] (Ir-4,4'-Me-DPS)

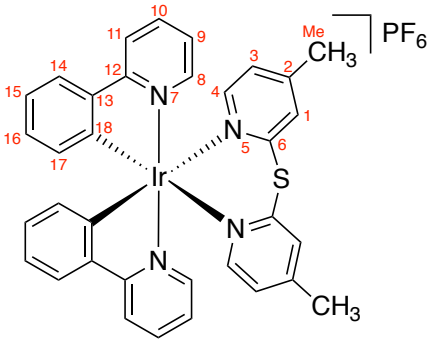

[Ir(ppy)$_2$Cl]$_2$ (0.107 g, 0.099 mmol, 1.0 eq.) and AgPF$_6$ (0.101 g, 0.400 mmol, 4.0 eq.) were suspended in MeOH (20 mL) and stirred for 12 h at room temperature. Precipitated AgCl was removed by filtration over Celite and the dried filtrate redissolved in EtOH (20 mL) and **4,4'-Me-DPS** (0.050 g, 0.199 mmol, 2.0 eq.) added. The reaction mixture was stirred at room temperature for 12 h. The filtrate was purified using column chromatography (silica, 100% CH$_3$CN, followed by 97:3:1, CH$_3$CN:H$_2$O:KNO$_3$ (sat.)) to yield a yellow crystalline solid (0.080 g, 0.093 mmol, 94%). ^{1}H NMR (400 MHz, CD$_2$Cl$_2$) δ 8.13 (ddd, J = 5.9, 1.5, 0.7 Hz, 2H, H$_{14}$), 8.00 – 7.95 (m, 2H, H$_{17}$), 7.92 – 7.86 (m, 4H, H$_{4,16}$), 7.72 (t, J = 1.5 Hz, 2H, H$_1$), 7.67 (dd, J = 7.8, 1.3 Hz, 2H, H$_{11}$), 7.13 (ddd, J = 7.4, 5.9, 1.5 Hz, 2H, H$_{15}$), 7.01 (td, J = 7.5, 1.2 Hz, 2H, H$_{10}$), 6.92 (ddd, J = 5.8, 2.0, 0.8 Hz, 2H, H$_3$), 6.88 (td, J = 7.5, 1.4 Hz, 2H, H$_9$), 6.20 (dd, J = 7.7, 1.2 Hz, 2H, H$_8$), 2.35 (s, 6H, H$_{Me}$). ^{13}C{^{1}H} NMR (101 MHz, CD$_2$Cl$_2$) δ 168.35 (C$_{18}$), 153.86 (C$_6$), 153.48 (C$_4$), 152.81 (C$_2$), 151.59 (C$_{14}$), 148.17 (C$_{12}$), 144.58 (C$_{13}$), 139.14 (C$_{16}$), 132.21 (C$_8$), 131.00 (C$_9$), 130.09 (C$_1$), 127.32 (C$_3$), 125.41 (C$_{11}$), 123.50 (C$_{10}$), 123.12 (C$_{15}$), 120.53 (C$_{17}$), 21.21 (C$_{Me}$). HR-ESI MS: *m/z* calcd. for C$_{34}$H$_{28}$IrN$_4$S: 717.1664; Found: 717.1727 [M−PF$_6$]$^+$.

[Ir(ppy)$_2$(4,4'-Me-DPSO)][PF$_6$] (Ir-4,4'-Me-DPSO)

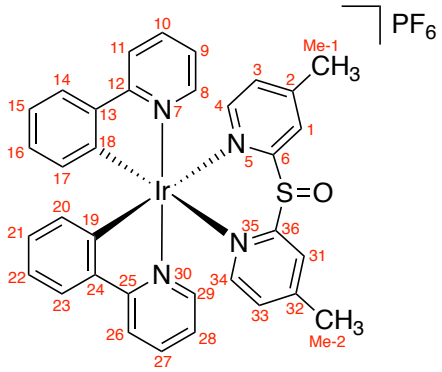

[Ir(ppy)$_2$Cl]$_2$ (0.076 g, 0.073 mmol, 1.0 eq.) was suspended in MeOH (25 mL) along with AgPF$_6$ (0.056 g, 0.220 mmol, 3.0 eq.) and stirred at room temperature for 12 h. The reaction mixture was passed over Celite to remove precipitated AgCl, and **4,4'-Me-DPSO** (0.034 g, 0.146 mmol, 2.0 eq.) was added to the filtrate, after which the solution was left to stir for 12 h at room temperature. The product precipitated out of solution and was filtered, giving a yellow powder that required no further purification (0.041 g, 0.047 mmol, 61%). ^{1}H NMR (850 MHz, CD$_2$Cl$_2$) δ 8.82 (ddd, J = 5.9, 1.5, 0.8 Hz, 1H, H$_8$), 8.37 (d, J = 5.8 Hz, 1H, H$_4$), 8.18 – 8.15 (m, 1H, H$_{26}$), 8.14 (dq, J = 2.0, 0.6 Hz, 1H, H$_{31}$), 8.04 (dt, J = 2.0, 0.6 Hz, 1H, H$_1$), 7.95 (ddd, J = 8.3, 7.4, 1.5 Hz, 1H, H$_{27}$), 7.89 – 7.84 (m, 3H, H$_{10,11,23}$), 7.55 (ddt, J = 7.7, 1.3, 0.5 Hz, 1H, H$_{14}$), 7.48 – 7.46 (m, 1H, H$_{34}$), 7.29 (ddt, J = 5.8, 2.0, 0.7 Hz, 1H, H$_3$), 7.26 (ddd, J = 7.4, 5.9, 1.7 Hz, 1H, H$_9$), 7.08 (ddd, J = 7.9, 7.2, 1.2 Hz, 1H, H$_{22}$), 7.05 – 7.03 (m, 1H, H$_{15}$), 7.02 – 7.00 (m, 2H, H$_{28,33}$), 6.98 – 6.96 (m, 2H, H$_{16,29}$), 6.89 (ddd, J = 7.8, 7.2, 1.4 Hz, 1H, H$_1$), 6.26 (ddd, J = 7.8, 1.2, 0.5 Hz, 1H, H$_{20}$), 6.19 (ddd, J = 7.6, 1.2, 0.5 Hz, 1H, H$_{17}$), 2.52 (d, J = 0.7 Hz, 3H, H$_{Me-1}$), 2.47 (d, J = 0.7 Hz, 3H, H$_{Me-2}$). ^{13}C{^{1}H} NMR (101 MHz, CD$_2$Cl$_2$) δ 169.09 (C$_{12}$), 167.67 (C$_{25}$), 163.55 (C$_6$), 161.13 (C$_{36}$), 154.86 (C$_2$), 154.61 (C$_{32}$), 154.24 (C$_8$), 153.78 (C$_4$), 152.06 (C$_{34}$), 148.82 (C$_{29}$), 146.07 (C$_{18}$), 145.34 (C$_{19}$), 145.07 (C$_{13}$), 144.16 (C$_{24}$), 139.72 (C$_{27}$), 139.52 (C$_{10}$), 132.61 (C$_{17}$), 131.67 (C$_{20}$), 131.54 (C$_{16}$), 130.90 (C$_{21}$), 129.65 (C$_3$), 129.14 (C$_{28}$), 126.11 (C$_{23}$), 124.90 (C$_{14}$), 124.25 (C$_{15}$), 124.11 (C$_{31,33}$), 123.91 (C$_{22}$), 123.57 (C$_1$), 123.19 (C$_9$), 121.38 (C$_{26}$), 120.39 (C$_{11}$), 21.97 (C$_{Me-1,Me-2}$). HR-ESI MS: *m/z* calcd. for C$_{34}$H$_{28}$IrN$_4$OS: 733.1613; Found: 733.1542 [M−PF$_6$]$^+$.

[Ir(ppy)$_2$(4,4'-Me-DPSO$_2$)][PF$_6$] (Ir-4,4'-Me-DPSO$_2$)

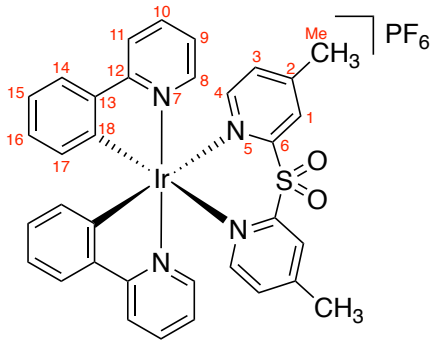

[Ir(ppy)$_2$Cl]$_2$ (0.092 g, 0.086 mmol, 1.0 eq.) and AgPF$_6$ (0.090 g, 0.356 mmol, 4.1 eq.) were suspended in MeOH (15 mL) and the reaction mixture stirred for 12 h at room temperature. AgCl precipitated out of the solution, the mixture was filtered over Celite and the filtrate dried under reduced pressure. The resulting solid was re-dissolved in EtOH (20 mL) and **4,4'-Me-DPSO$_2$** (0.043 g, 0.172 mmol, 2.0 eq.) added, following which the solution was stirred at room temperature for 12 h. The EtOH was then removed *in vacuo* and the crude mixture re-dissolved in CH_2Cl_2, following which the solution was filtered over Celite two times to remove a brown impurity. The resulting product was then precipitated out of solution with hexanes, yielding a yellow solid (0.025 g, 0.028 mmol, 33%). ^{1}H NMR (400 MHz, CD_2Cl_2) δ 8.51 (d, J = 2.0 Hz, 2H, H_1), 8.12 (d, J = 5.7 Hz, 2H, H_4), 7.97 – 7.94 (m, 2H, H_8), 7.89 – 7.83 (m, 2H, H_{10}), 7.70 (dd, J = 7.8, 1.4 Hz, 2H, H_{14}), 7.61 (d, J = 5.9 Hz, 2H, H_{11}), 7.27 (ddd, J = 5.7, 2.1, 0.9 Hz, 2H, H_3), 7.11 – 7.04 (m, 4H, $H_{9,15}$), 6.92 (td, J = 7.5, 1.4 Hz, 2H, H_{16}), 6.13 (dd, J = 7.7, 1.1 Hz, 2H, H_{17}), 2.53 (s, 6H, H_{Me}). ^{13}C{^{1}H} NMR (101 MHz, CD_2Cl_2) δ 167.16 (C_{12}), 155.22 (C_2), 154.65 (C_4), 154.41 (C_6), 152.09 (C_{11}), 145.01 (C_{13}), 143.14 (C_{18}), 139.36 (C_{10}), 132.21 (C_3), 132.12 (C_{17}), 131.14 (C_{16}), 128.11 (C_1), 125.49 (C_{14}), 124.30 (C_{15}), 123.53 (C_9), 120.24 (C_8), 21.91 (C_{Me}). HR-ESI MS: *m/z* calcd. for $C_{34}H_{28}IrN_4O_2S$: 749.1562; Found: $[M-PF_6]^+$.

CHAPTER 3: Substituent and Oxidation State Influence on Sulfur-Bridged Luminescent Copper(I) Complexes Showing Delayed Fluorescence

3.1 Introduction

Luminescent materials based on transition metal complexes have long afforded substantial research efforts due to their ability to be implemented in a range of technologies. These include solar applications,[6] photocatalysis[18] and, in particular, lighting technologies such as organic light-emitting diodes (OLEDs)[10] or light-emitting electrochemical cells (LEECs).[11] Often these applications are dominated by the use of second- and third-row transition metals such as Ir,[13,14] Ru[131] and Pt[132] due to their high degrees of colour tuneability, efficiencies and stabilities. These metals, however, are expensive and limited by low abundancies in the Earth's crust, and as such efforts are being made to find more cost-effective alternatives. In particular, coinage metals with a d^{10} configuration such as Cu(I), Ag(I) and Au(I) are promising candidates, with copper(I) especially attracting considerable interest from the research community in the past decade.[71,133,134]

Emissive copper(I) complexes have been shown to adopt a diverse range of structures. These range from homo- or heteroleptic mononuclear species containing diimine (N^N), diphosphine (P^P) or imine-phosphine (N^P) ligands,[57,58,135] to polynuclear species that can be bridged by the aforementioned ligands[136] or halide atoms,[137] to tetranuclear cubane structures.[54] This ability for copper(I) to accept a variety of structures allows for an array of different photophysical properties.[138]

The photophysics of copper(I) complexes have been extensively studied in solution, in the solid state and in polymer environments.[139] In the ground-state, the Cu(I) center is of a d^{10}

configuration adopting a pseudotetrahedral (D_{2d}) geometry, which on photoexcitation undergoes a metal-to-ligand charge transfer (MLCT) formally oxidizing the metal center to a d^9 Cu(II) configuration. Once in this excited-state, the complex undergoes a fast (<1 ps) Jahn-Teller distortion to a more flattened geometry, opening up nonradiative decay pathways such as exciplex formation with coordinating species. This distorted geometry is preserved until relaxation to the ground-state. Structural modification of the ligands has been shown to inhibit this distortion through rational design aimed at introducing constraints to maintain a tetrahedral geometry, thus increasing the lifetime of the excited-state and the quantum efficiency of the complex.[65] Furthermore, Cu(I) species can undergo an additional radiative decay pathway *via* thermally activated delayed fluorescence (TADF), whereby otherwise non-emissive triplet states can be converted to singlet states, resulting in higher emission quantum yields.[71] In order to satisfy the demands of TADF a small S_1–T_1 energy gap (<0.42 eV) must exist for reverse intersystem crossing (RISC) to be viable.[9,21]

In Chapter 2: it was shown that on increasing the oxidation state at the sulfur from sulfide (S), to sulfoxide (SO), to sulfone (SO_2) it was possible to switch from a blue-green emissive state of mainly ^{3}LC character (in the case of S and SO) to one of ^{3}MLCT/^{3}LLCT character giving yellow emission (for SO_2). The sulfur-bridged dipyridyl ligands were also found to adopt a larger bite angle than their bipyridine counterparts, which in conjunction with additional possible oxygen binding sites for the sulfoxide and sulfone analogues can lead to interesting binding modes.

In this chapter the synthesis and characterization of a series of four new heteroleptic Cu(I) species utilizing sulfur-bridged dipyridyl ligands in either sulfide or sulfone oxidation state as the N^N component, and bis[2-(diphenylphosphino)-phenyl]ether (POP) as the P^P component are

discussed. It is shown that subtle steric changes at the 6- and 6'-positions of the N^N ligand can influence the formation of bridged dinuclear complexes.

3.2 Ligand Synthesis and Characterization

Scheme 3-1 Synthesis of Cu(I) Complexes

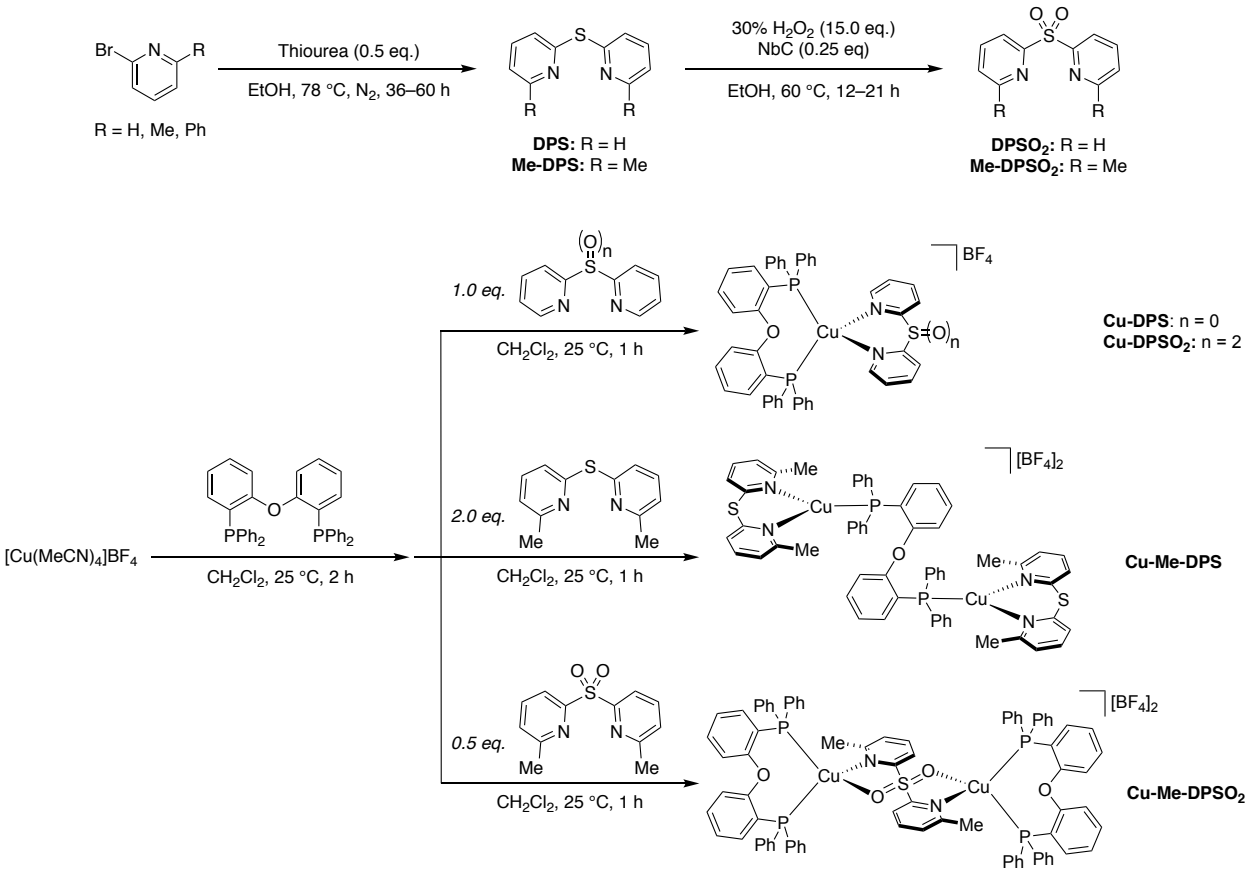

The sulfide-bridged compounds **DPS** and **Me-DPS** were synthesized *via* nucleophilic aromatic substitution of thiourea with 2-bromopyridine and 2-bromo-6-methylpyridine, respectively (Scheme 3-1). Desired sulfone species **DPSO$_2$** and **Me-DPSO$_2$** were obtained through

oxidation of the appropriate diaryl sulfide pro-ligand with 30% H_2O_2 using a niobium carbide (NbC) catalyst. High yields were attained, and the four pro-ligands were characterized using NMR spectroscopy, mass spectrometry and infrared spectroscopy. ^{1}H and ^{13}C signals were assigned using COSY, HSQC and HMBC experiments.

3.3 Synthesis and Characterization of Cu(I) Complexes

The four copper(I) complexes were prepared using the synthetic methods described by Linfoot *et al.*[140] (Scheme 3-1). To a stirring solution of $[Cu(MeCN)_4][BF_4]$ in CH_2Cl_2 at 25 ˚C was added the desired molar ratio of POP followed by the desired molar ratio of the N^N pro-ligand (N^N = **DPS**, **DPSO$_2$**, **Me-DPS** or **Me-DPSO$_2$**). Following precipitation from solution using Et_2O, the species were all isolated in high yields as off-white to yellow powders that required no further purification. ^{1}H, ^{13}C and ^{31}P NMR spectra were collected and assigned using COSY, HSQC and HMBC experiments, with the broad ^{31}P signals that are observed attributed to quadrupole coupling with the copper atom. Complexes **Cu-DPS** and **Cu-DPSO$_2$** were synthesized using equimolar ratios of $[Cu(MeCN)_4][BF_4]$, POP and the appropriate **DPS** or **DPSO$_2$** ligand and isolated as monometallic species. HR-ESI mass spectra show a product peak corresponding to $[M–BF_4]^+$ and exhibit a characteristic copper isotope pattern. Elemental analyses agree with the expected values for the assigned complexes.

3.3.1 Nuclear Magnetic Resonance (NMR) Spectroscopy

Interestingly, on increasing steric bulk through addition of methyl groups in the 6- and 6'-positions on the dipyridyl ligand (**Me-DPS** and **Me-DPSO$_2$**) bimetallic complexes **Cu-Me-DPS**

and **Cu-Me-DPSO$_2$** were isolated (Scheme 3-1). While analogous complex [Cu(POP)(tmbpy)][BF$_4$] (tmbpy = 4,4',6,6'-tetramethyl-2,2′-bipyridine) is monometallic,[76] the larger bite angle afforded by the addition of a sulfur atom between the two pyridyl rings coupled with the added bulk of the methyl substituents presumably causes the steric constraints to be too great to form the typical *P,P* and *N,N*-bound four-coordinate species.

NMR experiments for **Cu-Me-DPS** show a bimetallic complex with each discrete Cu(I) complexed with the **Me-DPS** ligand, and the two metal centres bridged by the POP ligand. This bridged binding mode for the POP ligand has not been reported before. The ^{1}H NMR spectrum of **Cu-Me-DPS** shows sharp signals for the POP ligand, but broad signals attributed to the **Me-DPS** ligand, likely caused by fluxional behavior on the NMR timescale. The use of low-temperature NMR experiments was unable to elucidate a defined structure. **Cu-Me-DPSO$_2$** was found to also exist as a bimetallic species; however, instead of POP acting as a bridging ligand, **Me-DPSO$_2$** connects the two copper(I) atoms with each discrete metal center bound in a *N,O* fashion through one pyridyl ring and one of the sulfone oxygen atoms. Four-coordinate geometry about each Cu(I) is completed by a POP ligand. Syntheses of **Cu-Me-DPS** and **Cu-Me-DPSO$_2$** were also conducted using equimolar equivalents of [Cu(MeCN)$_4$][BF$_4$], diphosphine and diimine ligands but the bridged, bimetallic structures still preferentially formed.

3.3.2 Single Crystal X-ray Diffraction

Single crystals of **Cu-DPS**, **Cu-DPSO$_2$**, **Cu-Me-DPS** and **Cu-Me-DPSO$_2$** were grown by vapor diffusion of Et$_2$O into CH$_2$Cl$_2$ solutions of the complexes. Steric factors strongly affect the coordination chemistry of copper(I) when complexed with POP ligands. POP is a bulky bidentate

component and it has been shown that when two POP ligands coordinate to copper(I), the metal adopts a trigonal geometry to reduce steric hindrance. In $[Cu(POP)_2][BF_4]$ it has been shown that only one POP is able to behave as a chelating unit, while the second ligand can only bind through one phosphorus atom forming a trigonal species.[141] In contrast, copper(I) forms tetrahedral complexes in less sterically hindered systems, for example when one POP is present together with smaller ligands.[142-144]

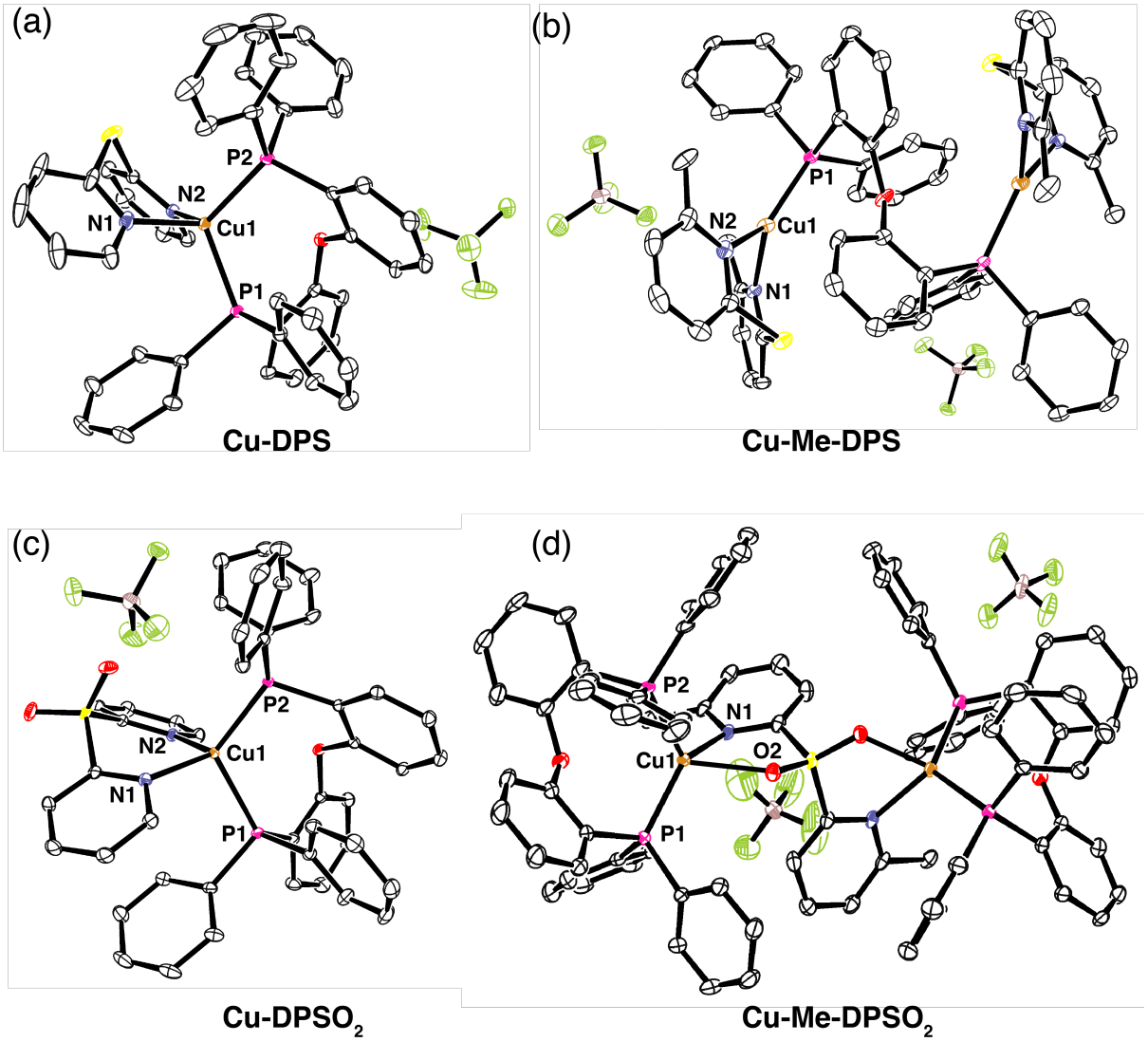

Figure 3-1 ORTEP representations of single crystal structures of (a) **Cu-DPS**; (b) **Cu-Me-DPS**; (c) **Cu-DPSO$_2$**; (d) **Cu-Me-DPSO$_2$**. Ellipsoids are plotted at the 50% probability level. Hydrogen atoms and solvent molecules are removed for clarity.

The four aforementioned copper(I) complexes were structurally characterized (Figure 3-1), with the data corroborating the NMR spectral observations. The four dipyridyl ligands each differ in both steric bulk and binding modes. **DPS** and **Me-DPS** are both bidentate ligands which coordinate to copper through the pyridyl nitrogen atoms, with **Me-DPS** possessing a larger steric bulk due to the presence of methyl groups in 6- and 6'-positions. **DPSO$_2$** and **Me-DPSO$_2$** each

have two different binding modes, either through the pyridyl nitrogen atoms (*N,N*), or through one nitrogen and one sulfone oxygen (*N,O*). These ligands can therefore adopt a preferential coordination mode in order to reduce steric tension within the complex. The result is that in the presence of methyl groups the complexes crystalize as dimers where either POP or **Me-DPSO$_2$** bridge two copper atoms.

Cu-DPS (Figure 3-1(a)) and **Cu-DPSO$_2$** (Figure 3-1(c)) both crystalize as monomers with the copper center presenting a distorted tetrahedral geometry, and in both cases the dipyridyl ligand binds in an *N,N* fashion. **Cu-Me-DPS** (Figure 3-1(b)) crystalizes as a dimer in which the POP bridges two copper atoms with a distorted trigonal geometry. **Cu-Me-DPSO$_2$** (Figure 3-1(d)) also crystalizes as a dimer, but differently from **Cu-Me-DPS**. In this case the Cu(I) atoms have tetrahedral geometry with the bridging ligand **Me-DPSO$_2$** ligand binding with *N,O* coordination modes to the two metal centers.

Selected bond lengths and angles for the four complexes are reported in Table 3-1. All the complexes exhibit a distorted geometry. This is not surprising because **DPS** and **DPSO$_2$** ligands are more rigid compared to POP and as a result the N–Cu–N bite angles are expected to be smaller than the P–Cu–P bite angles. In addition, the P–Cu–P angles are anticipated to be quite large due to the presence of the bulky PPh_3 groups. Structural studies show that in all the tetrahedral complexes the P–Cu–P bite angles are in the range of 113–117˚, and the N–Cu–N bite angles are between 93–97˚. The N–Cu–O angle in **Cu-Me-DPSO$_2$** is even smaller at 79.35˚. The trigonal **Cu-Me-DPS** complex also has a distorted structure, with a N–Cu–N angle of 96.47˚ and a P–Cu–N angle of 129.53˚. The Cu–P and Cu–N bond lengths are all similar within the series reported here and to other mononuclear copper(I) complexes in the literature.[136]

Table 3-1 Selected bond lengths (Å) and angles (˚) of **Cu-DPS**, **Cu-DPSO$_2$**, **Cu-Me-DPS**, and **Cu-Me-DPSO$_2$**.

	Cu-DPS	**Cu-DPSO$_2$**	**Cu-Me-DPS**	**Cu-Me-DPSO$_2$**
Cu1–N1	2.0804(14)	2.1186(10)	2.038(3)	2.0480(16)
Cu1–N2	2.0691(13)	2.1163(10)	2.040(3)	–
Cu1–O1	–	–	–	2.4134(13)
Cu1–P1	2.2463(4)	2.3052(3)	2.2131(10)	2.2719(5)
Cu1–P2	2.2659(4)	2.2508(3)	–	2.2292(5)
N1–Cu1–N2	93.89(6)	97.03(4)	96.47(12)	–
N1–Cu1–O1	–	–	–	79.35(5)
P1–Cu1–P2	113.268(16)	114.029(12)	–	117.12(2)
P1–Cu1–N1	117.94(4)	99.95(3)	129.52(8)	108.44(4)

3.4 Electrochemical Properties

The electrochemical behavior of the Cu(I) complexes was investigated using cyclic voltammetry (CV) of CH_2Cl_2 solutions *vs*. Fc/Fc^+ and the data summarized in Table 3-2. Two oxidative features are seen for each complex, with the first attributed to the Cu^+/Cu^{2+} oxidation.[142] In comparing the mononuclear species, on oxidizing **Cu-DPS** to **Cu-DPSO$_2$** an increase in oxidation potential is seen (+1.03 V to +1.17 V) owing to the electron-withdrawing effect of the oxygen atoms of the sulfone-bridged ligand on the coordinating nitrogen atoms. These potentials are higher than those seen for the model complex [Cu(POP)(bpy)][PF_6] which has an unsubstituted bpy ligand (+0.72 V).[145]

Table 3-2 Electrochemical data of Cu(I) complexes in CH_2Cl_2 solutions.

	$E_{(ox)}$ (V)	$E_{(red)}$ (V)	E_{HOMO} (eV) [a]	E_{LUMO} (eV) [a]	ΔE_{redox} (V)
Cu-DPS	1.03 [b]	–0.93 [b]	–6.13	–4.17	1.96
	1.64 [b]				
Cu-DPSO$_2$	1.17 [b]	–1.01 [b]	–6.27	–4.09	2.18
	1.74 [b]				
Cu-Me-DPS	1.08 [b]	–1.01 [b]	–6.18	–4.09	2.09
	1.67 [b]				
Cu-Me-DPSO$_2$	1.13 [b]	–0.99 [b]	–6.23	–4.11	2.12
	1.73 [b]				

Measurements were carried in CH_2Cl_2 at a scan rate of 50 mVs^{-1} with Fc/Fc+ employed as an internal standard, with data reported *vs.* SCE (Fc/Fc+ = 0.46 V in CH_2Cl_2).[146] [a] HOMO and LUMO energies were calculated following $E_{HOMO} = -[E^{ox\ vs.\ Fc/Fc+} + 5.1]$ eV, $E_{LUMO} = -[E^{red\ vs.\ Fc/Fc+} + 5.1]$ eV.[147] [b] Irreversible redox wave.

In comparing the two bimetallic species an increase in oxidative potential is again observed for the sulfone vs sulfide complex (+1.08 V for **Cu-Me-DPS** and +1.13 V for **Cu-Me-DPSO$_2$**) which can be attributed to electronic differences (as above), but possibly also to due to steric effects. It is known that by increasing the stabilization of the tetrahedral geometry about the copper center the Cu^+/Cu^{2+} oxidation potential is raised,[53] and so by adding substituents in the 6,6′-positions at the diimine ligand the flattening distortion is reduced. Additionally, in going from three-coordinate **Cu-Me-DPS** to four-coordinate **Cu-Me-DPSO$_2$** the stabilization of the tetrahedral geometry is further increased. Irreversible redox waves are seen for all four complexes, which is typical for transition metal complexes.[145]

3.5 Solution-state Photophysical Properties

3.5.1 Absorption Spectroscopy

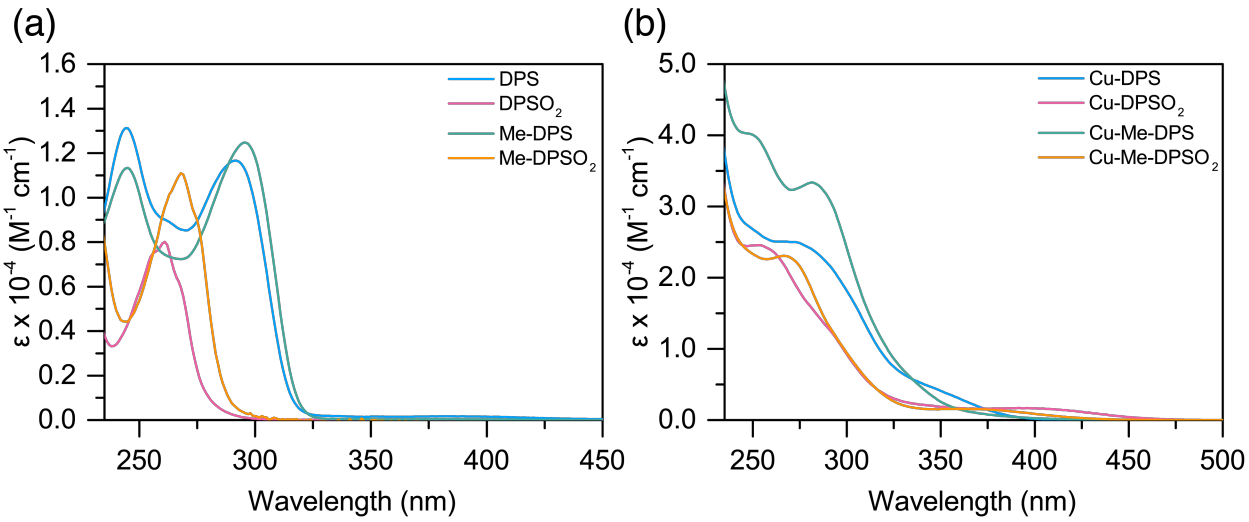

Figure 3-2 Absorption spectra of (a) pro-ligands and (b) Cu(I) complexes in CH_2Cl_2 solutions. All spectra were recorded in ~ 2×10^{-5} M CH_2Cl_2 solutions at room temperature.

The absorption spectra of sulfide and sulfone pro-ligands **DPS**, **DPSO₂**, **Me-DPS** and **Me-DPSO₂** in CH_2Cl_2 solutions are shown in Figure 3-2(a). Features at energies higher than 380 nm are attributed to π–π* transitions, and absorptions in **Me-DPS** and **Me-DPSO₂** are red-shifted relative to those of their unsubstituted counterparts due to the electron-donating nature of the methyl substituents. Absorption spectra of the four Cu(I) complexes in CH_2Cl_2 solutions are shown in Figure 3-2(b). All show intense high energy bands assigned to ligand-based transitions and broad, lower energy bands in the range 325–450 nm due to metal-to-ligand charge transfer (MLCT) transitions, typical of $[Cu(P^\wedge P)(N^\wedge N)]^+$ complexes,[148] with the sulfone derivatives red-shifted compared to those of the sulfide.

3.5.2 Photoluminescence Spectroscopy

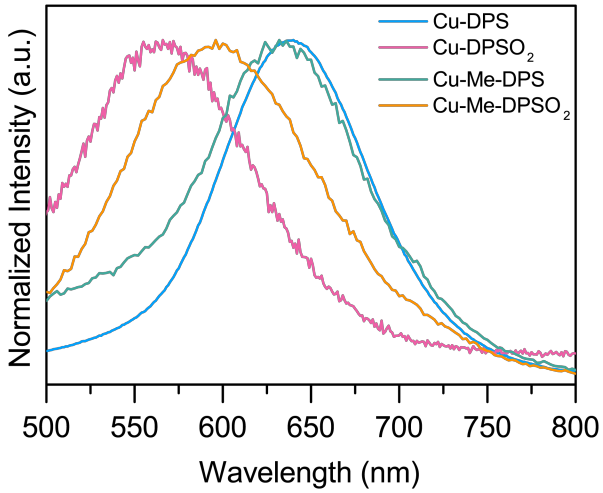

Figure 3-3 Emission spectra of Cu(I) complexes in CH_2Cl_2 solutions at room temperature. Concentrations ~ 2×10^{-5} M. λ_{ex} = 370 nm.

The photoluminescence spectra of **Cu-DPS**, **Cu-DPSO$_2$**, **Cu-Me-DPS** and **Cu-Me-DPSO$_2$** were collected in deaerated CH_2Cl_2 solutions (Figure 3-3). All complexes were found to be poorly emissive in solution presumably due to Jahn-Teller distortions in the excited-state leading to a quenching of the emission. The relative emission energies can be explained using steric and electronic arguments. As discussed in Section 1.3.5, Cu(I) complexes undergo a significant structural relaxation in the excited-state leaving a stabilized T_1 state. While the absorption occurs at the optimal equilibrium geometry of S_0, the emission occurs at the relaxed T_1 geometry and therefore determines to a large extent the energy of the radiative decay.

Unsubstituted complex **Cu-DPS** is expected to show the largest geometrical change and therefore the greatest stabilization of the T_1 energy and thus has the lowest energy emission (640 nm) of the four species. On oxidizing the ligand to **Cu-DPSO$_2$** the emission undergoes a large hypsochromic shift to 566 nm. Of the methyl-substituted species, **Cu-Me-DPS** exhibits the lowest

emission energy (632 nm) due to the distorted trigonal geometry about the copper centre, while the excited-state of **Cu-Me-DPSO$_2$** can be stabilized by the methyl groups in the 6,6′-positions of the bridging diimine ligand giving emission at 596 nm.

3.6 Solid state Photophysical Properties

3.6.1 Thin Film Photoluminescence

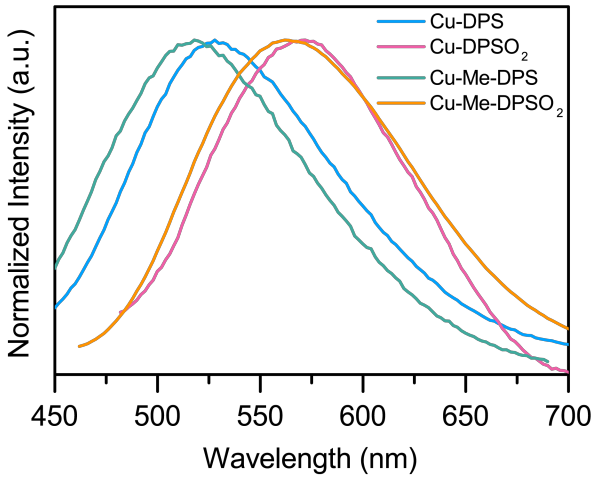

Figure 3-4 Solid state emission spectra of Cu(I) complexes as thin films drop-cast from MeOH on quartz. λ_{ex} = 370 nm.

In the solid state at room temperature, **Cu-DPS**, **Cu-DPSO$_2$**, **Cu-Me-DPS** and **Cu-Me-DPSO$_2$** show much higher emission intensities in addition to a blue-shift when compared to their dissolved counterparts. This is characteristic of [Cu(P^P)(N^N)]$^+$ complexes and is attributed to the more rigid environment severely restricting the degree of excited-state Jahn-Teller distortions. The photoluminescence spectra of the four Cu(I) complexes as thin films are shown in Figure 3-4 and their photophysical properties summarized in Table 3-3. In both the monometallic (**Cu-DPS**, λ_{max} = 525 nm; **Cu-DPSO$_2$**, λ_{max} = 560 nm) and bimetallic (**Cu-Me-DPS**, λ_{max} = 518 nm; **Cu-Me-**

DPSO$_2$, λ_{max} = 557 nm) species, oxidation to the sulfone results in a bathochromic shift of the emission wavelength. Functionalizing the diimine ligand with electron-withdrawing oxygen atoms at the sulfur reduces the electron density at the nitrogen atoms, which in turn reduces the ligands σ-donating and increases their π-accepting abilities. This destabilizes the LUMO, reducing the HOMO–LUMO gap and resulting in a lower energy emission.

Table 3-3 Solid state photophysical properties of Cu(I) complexes as neat thin films at room temperature in air.

Complex [a]	λ_{max} [nm] [b]	PLQY [b]	τ_{em} [ns] [b][c]
Cu-DPS	525	0.04	66.3 (8%), 451 (23%), 3720 (69%)
Cu-DPSO$_2$	560	<0.01	31.2 (11%), 218 (34%), 1930 (55%)
Cu-Me-DPS	518	0.06	83.4 (9%), 467 (24%), 2810 (67%)
Cu-Me-DPSO$_2$	557	0.14	90.0 (3%), 546 (27%), 2280 (70%)

[a] All samples drop-cast on to quartz from MeOH. [b] λ_{ex} = 370 nm. [c] Lifetimes collected over both a 50 ns and 5 µs time regime in order to retain accuracy for the short and long components. Percentage contributions relate to 5 µs regime.

3.6.2 Thin Film Photoluminescence Quantum Yields (PLQY)

Photoluminescence quantum yields (Table 3-3) follow a general trend of increasing as the environment about the copper becomes more constrained, likely due to improved stabilization of the tetrahedral geometry. **Cu-Me-DPSO$_2$** has the highest PLQY of 0.14, however this is lower than other POP-containing complexes that feature methyl groups in the 6,6′-positions of the diimine ligand (e.g. PLQY is 0.74 for [Cu(POP)(tmbpy)][BF$_4$]).[76] This could be due to the flexibility about the sulfur center providing additional non-radiative decay pathways when compared to bpy-based N^N ligands. **Cu-DPSO$_2$** is an outlier in this trend and is practically non-

emissive. In addition to the lack of steric bulk at the diimine, the electron-withdrawing oxygen atoms reduce the Cu–N bond strength enabling a greater stabilization of the T_1 excited-state. Single crystal structures (Section 3.3.2) show that the Cu–N bond distances are longer for **Cu-DPSO$_2$** (2.116 and 2.119 Å) than for **Cu-DPS** (2.069 and 2.080 Å).

3.6.3 Low Temperature Thin Film Photoluminescence

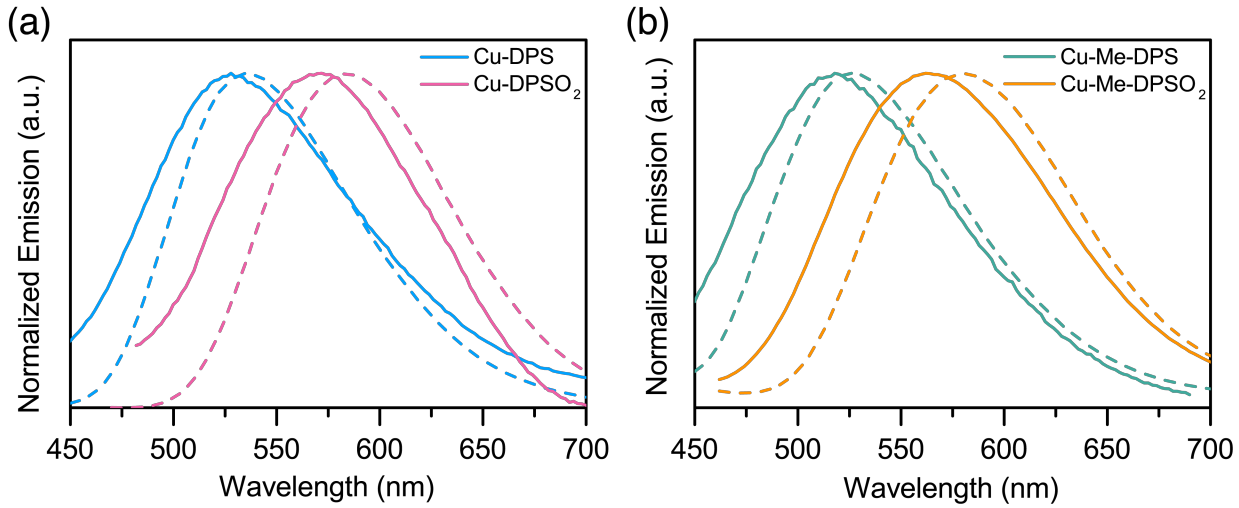

Figure 3-5 Solid state emission spectra of (a) **Cu-DPS** and **Cu-DPSO$_2$**; (b) **Cu-Me-DPS** and **Cu-Me-DPSO$_2$** at room temperature (solid line) and 77 K (dashed line). Thin films drop-cast from MeOH on quartz. λ_{ex} = 370 nm.

As discussed in Section 1.3.6, TADF occurs when the S_1–T_1 energy gap is <0.43 eV and that for practical applications this energy gap should be no more than 0.12 eV. This energy gap can be determined experimentally for Cu(I) complexes using variable-temperature steady-state emission spectroscopy. At ambient temperature, the emission originates from the S_1 state, but on cooling to 77 K the emission is from the T_1, as observed by a red-shift in the emission spectrum due to the triplet state residing at a lower energy. An estimation of $\Delta E(S_1–T_1)$ can be made by taking the difference between the λ_{max} emission at room temperature and 77 K. The emission

spectra of the four copper(I) complexes were therefore collected at room temperature and 77 K (Figure 3-5) and the $\Delta E(S_1–T_1)$ calculated (Table 3-4).

Table 3-4 $\Delta E(S_1–T_1)$ of Cu(I) complexes calculated from variable temperature solid state emission data.

Complex [a]	λ_{max} [nm] [b] Room Temperature	77 K	$\Delta E(S_1–T_1)$ [eV]
Cu-DPS	525	536	0.04
Cu-DPSO$_2$	560	584	0.05
Cu-Me-DPS	518	528	0.05
Cu-Me-DPSO$_2$	557	578	0.08

[a] All samples drop-cast on to quartz from MeOH. [b] λ_{ex} = 370 nm.

In all instances for **Cu-DPS**, **Cu-DPSO$_2$**, **Cu-Me-DPS** and **Cu-Me-DPSO$_2$** the $S_1–T_1$ energy gap was found to be less than the 0.12 eV required for the RISC process, indicating that the four complexes are candidates as TADF emitters.

3.6.4 Thin Film Photoluminescence Lifetimes

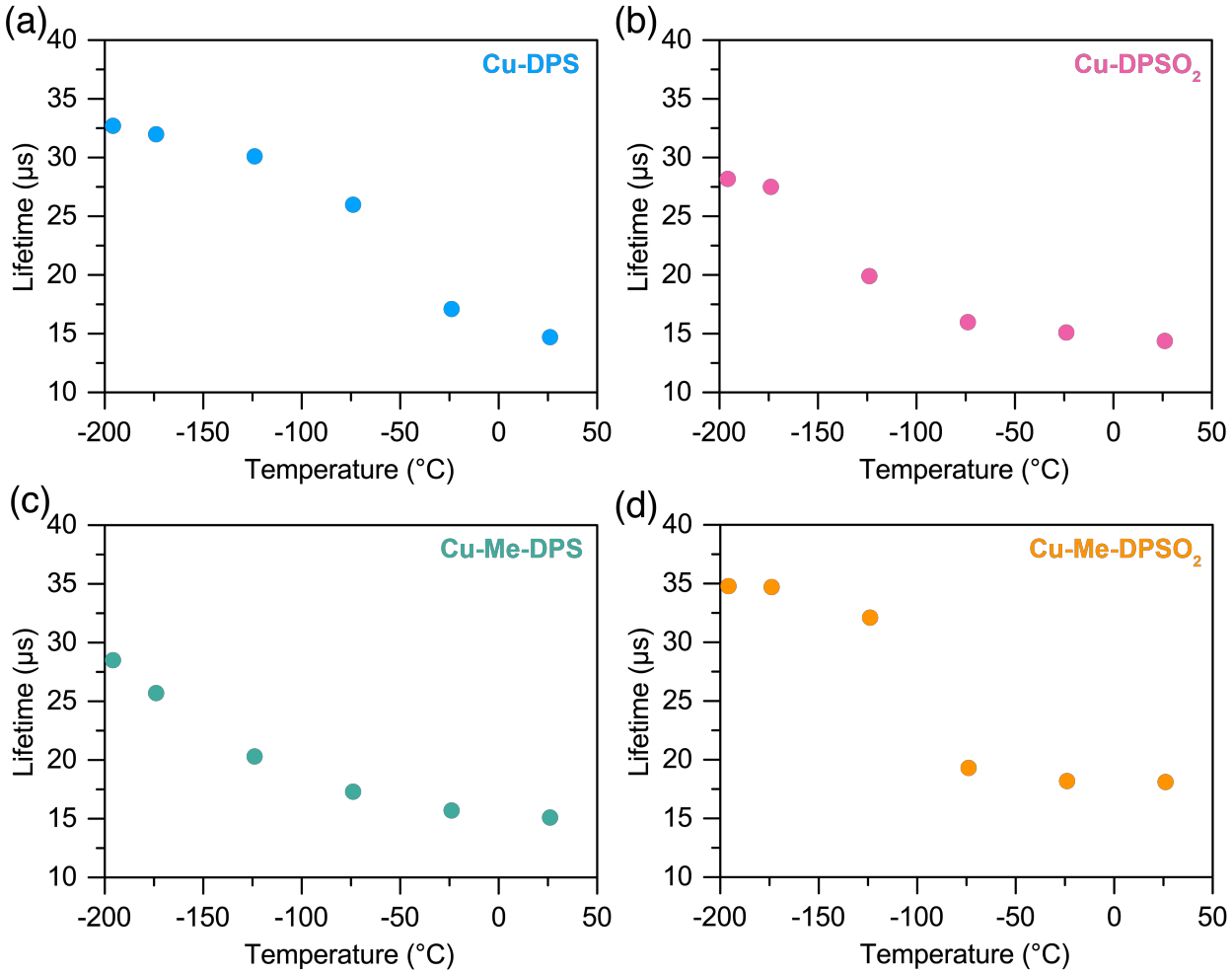

Figure 3-6 Emission lifetime measurements displaying the long lifetime component of thin films (a) **Cu-DPS**; (b) **Cu-DPSO$_2$**; (c) **Cu-Me-DPS** and (d) **Cu-Me-DPSO$_2$** are plotted. NanoLED excitation source (λ_{ex} = 370 nm).

Excited-state lifetimes of thin films of **Cu-DPS**, **Cu-DPSO$_2$**, **Cu-Me-DPS** and **Cu-Me-DPSO$_2$** were measured in air (Table 3-3) by time correlated single photon counting (TCSPC). All four complexes exhibited multi-exponential decay profiles which can be typical of Cu(I) complexes that display TADF, however the decay could also contain a mix of fluorescence and phosphorescence, or a combination of all three.[10,71] In order to discern the radiative mechanism,

variable temperature emission lifetimes were collected over a temperature range of –196 to 28 °C (Figure 3-6 and Appendix Chapter 6:Listing B.5). As discussed in Section 1.3.6, at low temperatures a prompt fluorescence is not detected, instead a very bright, long-lived phosphorescence is seen. Upon increasing the temperature, the S_1 state can be populated, resulting in an activation of the thermally delayed radiative pathway coupled with a drastic decrease in the emission lifetime and a blue-shift of the emission spectrum. The decay time of a system with thermally equilibrated excited state is determined by a Boltzmann-type relationship, and thus variable temperature excited-state lifetime experiments of copper(I) species displaying TADF show a sigmoidal curve.[71] All species exhibit multi-exponential decay profiles, and when plotting the long lifetime components (which correspond to the thermalized emission of the triplet state), complexes **Cu-DPS**, **Cu-DPSO$_2$** and **Cu-Me-DPSO$_2$** exhibit a sigmoidal profile, indicating the TADF nature of their radiative mechanism. **Cu-Me-DPS** does not show this same pattern, however –196 °C is not always sufficient to isolate only the T_1 emission (for that liquid helium temperatures are required) and so emission at low temperature in this instance is likely due to a mix of phosphorescence and TADF.

3.7 Time-resolved Photophysical Properties

As discussed in Sections 1.3.7 and 3.6.3, luminescence from the T_1 state can occur at 77 K, and $\Delta E(S_1–T_1)$ can be estimated from the emission spectra at low temperature and room temperature. The λ_{max} value, however, is the most probable transition and therefore a more accurate determination for $\Delta E(S_1–T_1)$ can be performed if the zero–zero energy ($E_{0–0}$) for each excited-state is calculated. $E_{0–0}$ is the energy difference between the ground and excited-state, each taken at their zero vibrational levels.[149] For copper(I) species, time-resolved photoluminescence spectroscopy

can be employed. Through monitoring emission at 77 K using different time regimes, the emission profiles of the fluorescence (ns, from S_1 state) and phosphorescence (μs, from T_1 state) can be collected. By using the onset values for each excited-state at 77 K, $\Delta E(S_1–T_1)$ can be more accurately determined.[150]

In conjunction with the Zysman-Colman and Samuel groups at the University of St. Andrews, Scotland, time-resolved photoluminescence spectroscopy was used to determine the $\Delta E(S_1–T_1)$ of **Cu-DPS**, **Cu-DPSO$_2$**, **Cu-Me-DPS** and **Cu-Me-DPSO$_2$** (Figure 3-7). Samples were prepared as neat powders and cooled to 77 K, following which the emission profiles at ns and μs regimes were collected. Time-resolved spectra in the time window of 100–200 ns (**Cu-DPS**, **Cu-DPSO$_2$** and **Cu-Me-DPS**) and 100–600 ns (**Cu-Me-DPSO$_2$**) give the photoluminescence spectra for transitions emanating from the S_1 state (grey traces), while spectra in the time windows 100–200 μs (**Cu-Me-DPS**) and 400–500 μs (**Cu-DPS**, **Cu-DPSO$_2$** and **Cu-Me-DPSO$_2$**) give the photoluminescence spectra for $T_1 \rightarrow S_0$ transitions. In all instances a shift to lower energy is seen when monitoring the longer time component, indicative of emission from a lower-energy state.

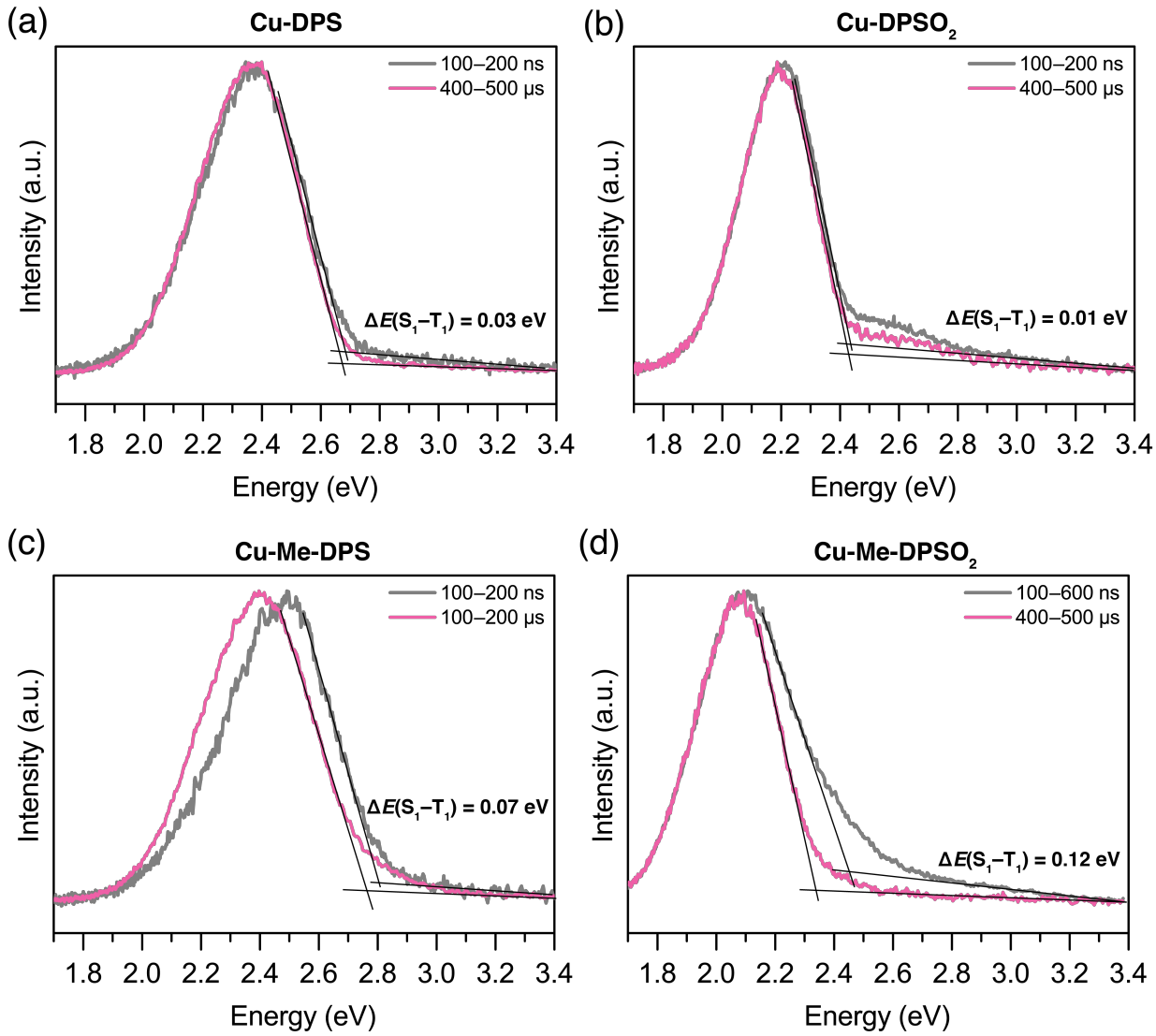

Figure 3-7 Time-resolved solid state photoluminescence spectra of (a) **Cu-DPS**; (b) **Cu-DPSO$_2$**; (c) **Cu-Me-DPS**; (d) **Cu-Me-DPSO$_2$** at 77 K. Grey traces represent emission from the S_1 state, and pink traces emission from the T_1 state. Black lines indicate the determination of $E_{0\text{–}0}$. Samples prepared as neat powders.

By determining $E_{0\text{–}0}$ of each excited-state transition (represented by the black lines in Figure 3-7), $\Delta E(S_1\text{–}T_1)$ was calculated for each complex. **Cu-DPS** (0.03 eV), **Cu-DPSO$_2$** (0.01 eV), **Cu-Me-DPS** (0.07 eV) and **Cu-Me-DPSO$_2$** (0.12 eV) all have S_1–T_1 energy gaps far less than the 0.43 eV limit for RISC, and so at least one of the long-lived time components in the room

temperature emission lifetime data (**Error! Reference source not found.**) is likely due to a TADF m echanism. Comparisons of the time-resolved data to the steady-state data are presented in Table 3-5. All $\Delta E(S_1–T_1)$ values are close and, with the exception of **Cu-DPSO**, the trend remains the same whereby the energy gap becomes larger when functionalizing the slightly electron-donating methyl groups to the pyridyl rings. This shows that using λ_{max} emission values from variable temperature steady-state emission data can give a good estimation as the $S_1–T_1$ energy gap.

Table 3-5 $S_1–T_1$ energy gaps of Cu(I) complexes as calculated using low temperature steady-state emission and low temperature time-resolved emission spectra.

Complex	$\Delta E(S_1–T_1)$ [eV]	
	Steady-State [a]	Time-Resolved [b]
Cu-DPS	0.04	0.03
Cu-DPSO$_2$	0.05	0.01
Cu-Me-DPS	0.05	0.07
Cu-Me-DPSO$_2$	0.08	0.12

[a] Calculated using λ_{max} emission at room temperature and 77 K. All samples drop-cast on to quartz from MeOH. [b] $E_{0–0}$ at room temperature and 77 K determined from emission onset, with $\Delta E(S_1–T_1)$ determined from $E_{0–0}$ values. Samples prepared as neat powders.

3.8 Theoretical Calculations

DFT and TD-DFT calculations were performed in order to elucidate the ground- and excited-states of the Cu(I) complexes and the character of the electronic transitions. The crystal structures discussed in Section 3.3.2 were used as starting points in the ground-state geometry

optimization. Calculated energy levels, oscillator strength (*f*) and orbital transitions are summarized in Table 3-6.

Table 3-6 TD-DFT calculated energy levels, oscillator strength and orbital transitions for Cu(I) complexes.

	S_1				T_1			
	f	***E*** **[eV]**	**Contribution [H–L]**	**Assignment**	***E*** **[eV]**	**Contribution [H–L]**	**Assignment**	**$\Delta E(S_1–T_1)$ [eV]**
Cu-DPS	0.0125	2.15	97.2%	MLCT/LLCT	2.02	94.8%	MLCT/LLCT	0.13
Cu-DPSO$_2$	0.0012	1.06	97.6%	MLCT/LLCT	0.98	98.4%	MLCT/LLCT	0.08
Cu-Me-DPS	0.0160	2.72	93.3%	MLCT/LLCT	2.59	88.8%	MLCT/LLCT	0.13
Cu-Me-DPSO$_2$	0.0071	1.33	99.1%	MLCT/LLCT	1.31	96.7%	MLCT/LLCT	0.02

For monometallic species **Cu-DPS** and **Cu-DPSO$_2$**, the HOMO is largely located on the 3d orbital of the copper(I) center and the coordinating phosphorus ligand, while the LUMO is mainly distributed over the sulfur-bridged dipyridyl ligand. In the bimetallic complex **Cu-Me-DPS**, the HOMO is distributed over the 3d orbital of the copper(I) atom and the bridging POP ligand, with the LUMO located on the two dipyrdyl ligands, separated by the copper(I) atoms and the POP ligand. In the **Cu-Me-DPSO$_2$** dyad, the HOMO is again located across the copper(I) centre and POP ligand, with the LUMO distributed mainly over the bridging **Me-DPSO$_2$** ligand. The HOMO–LUMO transition can be assigned as metal-to-ligand charge transfer (MLCT).

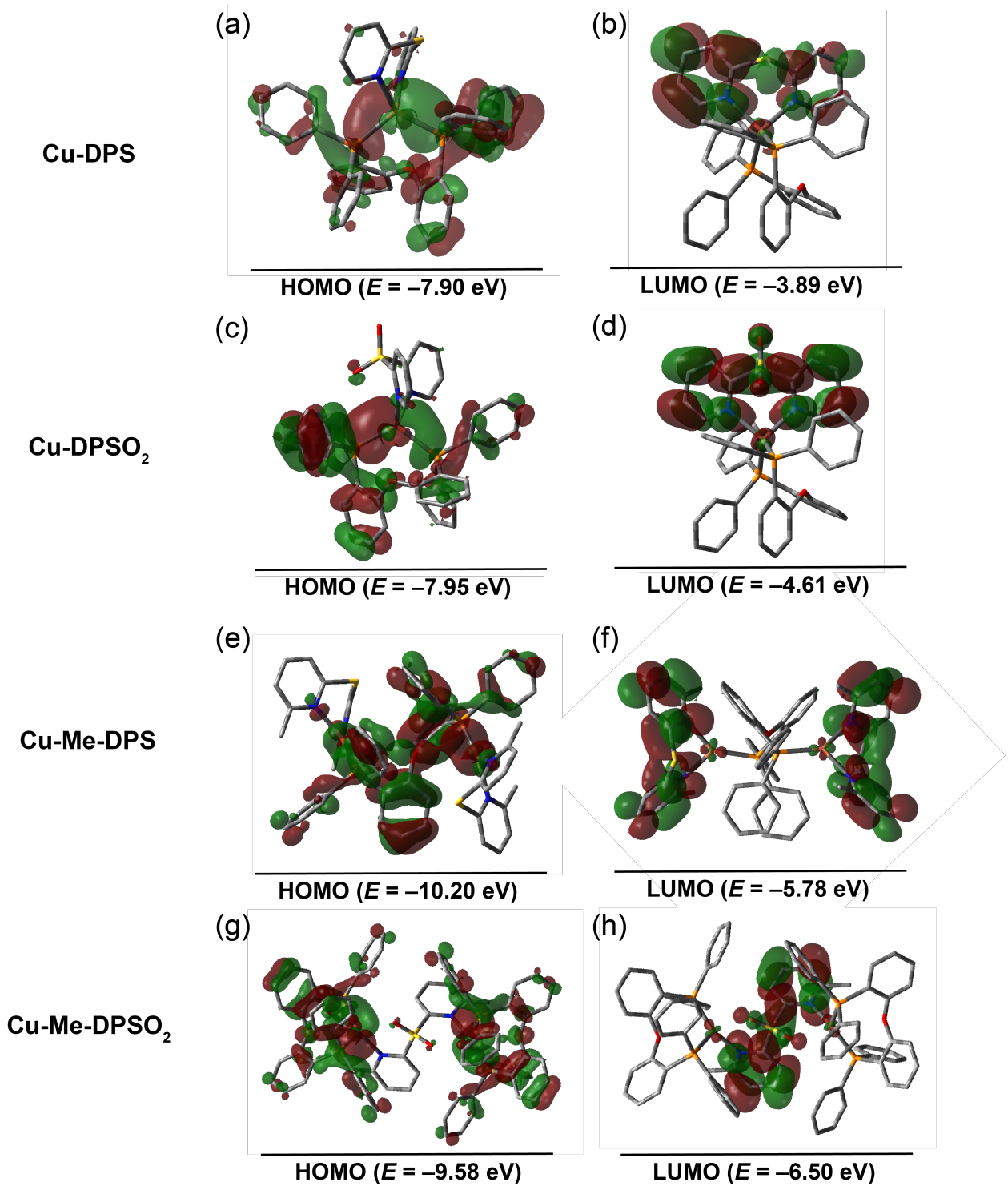

Figure 3-8 Frontier orbital plots illustrating the HOMO and LUMO distributions for Cu(I) complexes.

The spatial separation of HOMO and LUMO is distinct, so a relatively small singlet–triplet energy gap $\Delta E(S_1–T_1)$ can be predicted, indicative of TADF. Indeed, TD-DFT calculations using the B3LYP method in singlet and triplet state optimized geometries give relatively small values of $\Delta E(S_1–T_1)$ (Table 3-6), much smaller than the critical value for TADF of 0.43 eV. The major transitions of singlet and triplet excited states can be assigned as HOMO–LUMO transitions.

Pronounced MLCT electronic transitions result in significant changes of nuclear coordinates in excited states.[151,152] From the oscillator strength data in Table 3-6, **Cu-DPSO$_2$** has the smallest value (f = 0.0012), suggesting that this complex undergoes the most significant geometry distortion and therefore contributes to the low luminescence quantum yield observed.

Additionally, calculations were performed using the wb97xd functional with effective core potential SDD for copper and 6-31G(d,p) for all other atoms. This method is regarded as being more sophisticated than those used above, however the results were not satisfying. For complexes **Cu-DPS** and **Cu-Me-DPS** $\Delta E(S_1–T_1)$ were both around 0.30 eV, with the emission energies of **Cu-DPS** under-estimated (S_1: 2.75 ev; T_1: 2.38 eV) and the emission energies of **Cu-Me-DPS** over-estimated (S_1: 2.75 ev; T_1: 2.38 eV) compared to the experimental data. The optimization of the singlet excited-state for **Cu-DPSO$_2$** and both the singlet and triplet excited-states for **Cu-Me-DPSO$_2$** did not converge. For these reasons the B3LYP calculations were used.

3.9 Conclusions

Four heteroleptic Cu(I) complexes of the class [Cu(POP)(N^N)][BF_4] are reported where N^N = sulfur-bridged dipyridyl ligands functionalized either with or without methyl substituents in the 6,6′-positions of the pyridyl rings and sulfide or sulfone oxidation states at the sulfur center. Single crystal structures of **Cu-DPS** and **Cu-DPSO$_2$** confirm that the complexes are coordinated

in a distorted tetrahedral geometry. However upon introducing additional bulk with methyl groups the steric constraints about the copper center become too great and dimers are formed. **Cu-Me-DPS** is a bimetallic species which adopts a trigonal geometry with a bridging POP ligand, whereas **Cu-Me-DPSO$_2$** (with additional binding sites at the sulfone oxygen atoms) forms a bimetallic species with the diimine moiety acting as a bridging ligand linking the two copper atoms. These structures are retained when the complexes are dissolved in solution.

The complexes were all weakly emissive in solution, but luminance improved in the solid state, with PLQYs up to 0.14 for the most sterically constrained complex, **Cu-Me-DPSO$_2$**. The sulfone complexes (**Cu-DPSO$_2$** and **Cu-Me-DPSO$_2$**) both show a red-shifted emission profile when compared to their sulfide counterparts (**Cu-DPS** and **Cu-Me-DPS**) due to the electron-withdrawing nature of the oxygen atoms at the sulfur of the diimine ligand. All four complexes showed multiexponential decay profiles consisting of a prompt emission in the nanosecond regime, followed by longer components up to microseconds in length. Through the use of low-temperature time-resolved photoluminescence spectroscopy, in addition to computational methods, the S_1–T_1 energy gaps for each complex was determined and it was found that the decay profile is likely due to a TADF mechanism.

Here we have shown that with changes in steric constraints and sulfur oxidation state a variety of different complex geometries can be obtained. **Cu-Me-DPS** represents the first examples of a dimetallic Cu(I) species bridged by a POP ligand, and **Cu-Me-DPSO$_2$** represents the first example of a sulfone-based N^O-bound diimine ligand. **Cu-Me-DPSO$_2$** could show promise for application in LEECs, and the novel binding modes seen in the complex could open avenues towards interesting, luminescent coordination polymers.

3.10 Experimental Details

3.10.1 General

All experiments were conducted in atmospheric conditions unless otherwise stated. Solvents used for synthesis were of reagent grade and were used without any further purification. HPLC grade solvents were used for spectroscopic studies. 2-bromo-6-methylpyridine and niobium carbide were purcashed from Alfa Aesar, $[Cu(MeCN)_4][BF_4]$ and 30% H_2O_2 solutions were purchased from Sigma-Aldrich, and thiourea from TCI. All reagents were used as received. Bis(pyridin-2-yl)sulfane (**DPS**) and 2,2′-sulfonyldipyridine (**DPSO$_2$**) were synthesized using the methods described in Chapter 1:.

3.10.2 Spectroscopy

^{1}H, ^{13}C{^{1}H}, ^{31}P{^{1}H}, COSY, NOESY, HSQC and HMBC NMR spectra were collected using a Bruker AV-400 spectrometer and referenced first to TMS and then to the residual protonated solvent peak. NMR solvents (Aldrich or Cambridge Isotope Laboratories) were used as received. Electrospray ionization mass spectrometry data was obtained using a Bruker Esquire LC ion trap mass spectrometer and elemental analysis determined using a Thermo Flash 2000 Elemental Analyzer. Infrared spectroscopy was performed on an attenuated total reflection (ATR) crystal using a Perkin-Elmer Frontier FT-IR spectrometer. UV-vis absorption spectra were recorded on a Varian-Cary 5000 UV-Vis-near-IR spectrophotometer. Fluorescence data were collected on a Photon Technology International (PTI) QuantaMaster 50 fluorimeter fitted with an integrating sphere, double excitation monochrometer and utilizing a 75 W Xe arc lamp as the source. Emission lifetime data were collected using a Horiba Yvon Fluorocube TCSPC apparatus. A 370 nm NanoLED was used as the excitation source, pulsing at a repetition rate of 100 kHz and

with a lifetime of 1.2 ns. Broadband emission was monitored by a CCD detector at the desired wavelengths using appropriate low pass filters. The lifetime data were fitted using the DAS6 Data Analysis software package. Solution spectra were collected using 1 cm^2 quartz cells (Starna Cells) and spectra of the neat solids were collected by drop-casting from MeOH on to quartz slides (Ted Pella, Inc.).

3.10.3 X-Ray Crystallography

SCXRD raw data were collected on a Bruker APEX DUO diffractometer using graphite monochromated MoKα radiation (λ = 0.71073) at 90 K and to a resolution of 0.77 Å. The data elaboration was performed with the software APEX2.[153] Structures were solved using SUPERFLIP[154] and refined using full-matrix least-squares on F^2 within the CRYSTALS[155] suite. Hydrogen atoms were initially refined with restraints on bond lengths and angles, after which the positions were used as the basis for a riding model.[156] All non-hydrogen atoms were refined anisotropically.

3.10.4 Computational Details

Density functional theory (DFT) calculations were carried out using the Gaussian 16 Rev.A03 suite of programs. The B3LYP functional[123,124,157] with 6-31G** basis set (for C, H, S N P and O atoms) and the LANL2DZ effective-core pseudopotential (for Cu)[125] was employed to optimize the geometry of the ground-states (S_0) of all complexes with input structures extracted from the X-ray crystallographic data. Time-dependent DFT (TD-DFT) calculations were also performed to understand the nature of first singlet (S_1) and triplet excited states (T_1).[128,129,158]

3.10.5 Synthesis

bis(6-methylpyridin-2-yl)sulfane (Me-DPS)

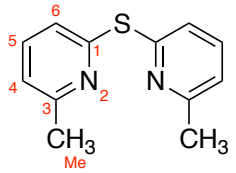

2-Bromo-6-methylpyridine (0.66 mL, 5.81 mmol, 1.0 eq.) was added to a solution of thiourea (0.21 g, 2.76 mmol, 0.48 eq.) in 100 mL of EtOH under an N_2 atmosphere and heated to reflux for 36 h. The reaction mixture was cooled to room temperature, the solvent removed under reduced pressure and the resultant residue dissolved in CH_2Cl_2 (20 mL) and washed with water (3 × 20 mL) and brine (1 × 50 mL). The organic layer was dried with $MgSO_4$, filtered and the CH_2Cl_2 removed *in vacuo*. The crude product was purified over silica gel using a solvent gradient from 1:0 CH_2Cl_2:MeOH to 9:1 CH_2Cl_2:MeOH, yielding a brown oil (0.558 g, 2.72 mmol, 99%). ^{1}H NMR (400 MHz, CD_2Cl_2) δ 7.50 (t, J = 7.7 Hz, 2H, H_5), 7.19 (dt, J = 7.9, 0.8 Hz, 2H, H_6), 7.02 (ddd, J = 7.6, 0.9, 0.5 Hz, 2H, H_4), 2.50 (s, 6H, H_{Me}). ^{13}C{^{1}H} NMR (CD_2Cl_2, 100 MHz) δ 159.82 (C_1), 156.80 (C_3), 137.69 (C_5), 123.05 (C_6), 121.67 (C_4), 24.62 (C_{Me}). ESI-HR MS: Calcd. for $C_{12}H_{13}N_2S$: 217.0799; Found: 217.0798 $[M+H]^+$

6,6'-sulfonylbis(2-methylpyridine (Me-DPSO$_2$)

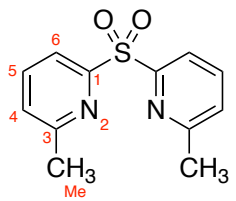

A round-bottomed flask was charged with **Me-DPS** (0.167 g, 0.772 mmol, 1.0 eq.) and NbC (0.020 g, 0.193 mmol, 0.25 eq.). 10 mL EtOH and 30% aqueous solution of H_2O_2 (1.09 mL, 11.6 mmol, 15.0 eq.) were added and the reaction mixture was heated to 60 ºC for 12 h. The mixture was cooled to room temperature, diluted with saturated $Na_2S_2O_3$ (10 mL) and extracted with CH_2Cl_2 (3 × 10 mL). The combined organics were dried over $MgSO_4$, filtered and the solvent removed *in vacuo* yielding a white powder that required no further purification (0.190 g, 0.765 mmol, 99%). ^{1}H NMR (400 MHz, CD_2Cl_2) δ 8.07 (d, J = 7.7 Hz, 2H, H_6), 7.85 (t, J = 7.8 Hz, 2H, H_5), 7.36 (d, J = 7.8 Hz, 2H, H_4), 2.51 (s, 6H, H_{Me}).

$^{13}C\{^1H\}$ NMR (101 MHz, CD_2Cl_2) δ 160.67 (C_1), 156.90 (C_3), 138.43 (C_5), 127.71 (C_4), 121.54 (C_6), 24.53 (C_{Me}). IR (solid): $\tilde{\nu}$ (σ SO_2) 1450, 1313 cm^{-1}. ESI-HR MS: Calcd. for $C_{12}H_{12}N_2O_2SNa$: 271.0517; Found: 271.0520 $[M+Na]^+$.

[Cu(POP)(DPS)][BF$_4$] (Cu-DPS)

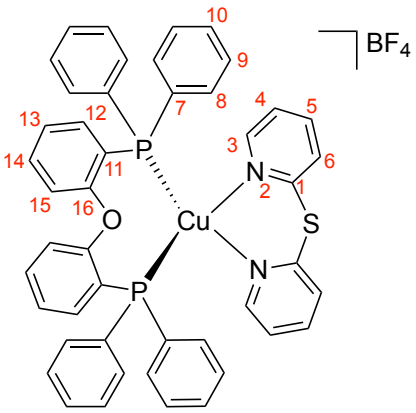

[Cu(MeCN)$_4$]BF$_4$ (0.092 g, 0.292 mmol, 1.0 eq.) and POP (0.158 g, 0.292 mmol, 1.0 eq.) were dissolved in 12 mL CH_2Cl_2 and stirred at room temperature for 2 h, after which **DPS** (0.055 g, 0.292 mmol, 1.0 eq.) was added and the solution left to stir for a further 1 h. The reaction mixture was then concentrated *in vacuo*, the product precipitated with Et_2O, filtered and washed with Et_2O, yielding an off-white powder that required no further purification (0.214 g, 0.244 mmol, 84%). ^1H NMR (400 MHz, CD_3OD) δ 8.16 – 8.10 (m, 2H, H_6), 7.90 – 7.81 (m, 4H, $H_{3,5}$), 7.39 – 7.19 (m, 22H, $H_{8,9,10,14}$), 7.14 – 7.08 (m, 2H, H_4), 7.05 (td, J = 7.6, 1.1 Hz, 2H, H_{13}), 6.99 (dtd, J = 8.2, 2.5, 1.0 Hz, 2H, H_{15}), 6.82 (dtd, J = 7.8, 4.0, 1.6 Hz, 2H, H_{12}). $^{13}C\{^1H\}$ NMR (101 MHz, CD_3OD) δ 159.11 (C_{16}), 154.90 (C_1), 152.31 (C_6), 140.64 (C_5), 135.02 (C_{12}), 134.74 (t, J = 8.1 Hz, C_8), 133.41 (C_{14}), 132.22 (t, J = 16.5 Hz, C_7), 131.47 (C_{10}), 130.29 (C_3), 129.98 (C_9), 126.30 (C_{13}), 125.92 (t, J = 14.4 Hz, C_{11}), 125.41 (C_4), 121.69 (C_{15}). $^{31}P\{^1H\}$ NMR (162 MHz, CD_3OD) δ –14.20. ESI-HR MS Calcd. for $C_{46}H_{36}N_2OP_2S^{63}Cu$: 789.1320; Found: 789.1323 $[M–BF_4]^+$. Elemental Analysis: Calcd. $C_{46}H_{36}BF_4N_2OP_2SCu$: C, 62.99; H, 4.14; N, 3.19; S, 3.65. Found: C, 62.71; H, 4.26; N, 3.15; S, 3.64.

[Cu(POP)(DPSO$_2$)][BF$_4$] (Cu-DPSO$_2$)

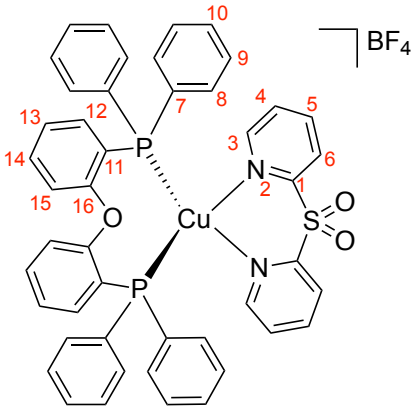

A solution of [Cu(MeCN)$_4$]BF$_4$ (0.079 g, 0.250 mmol, 1.0 eq.) and POP (0.134 g, 0.250 mmol, 1.0 eq.) in 12 mL CH_2Cl_2 was stirred at room temperature for 2 h, after which **DPSO$_2$** (0.055 g, 0.250 mmol, 1.0 eq.) was added and the solution left to stir for a further 1 h. The reaction mixture was then concentrated under reduced pressure, the product precipitated with Et_2O, filtered and washed with Et_2O, giving a yellow powder (0.210 g, 0.231 mmol, 92%). ^{1}H NMR (400 MHz, CD_3OD) δ 8.52 (d, J = 4.8 Hz, 2H, H_6), 8.36 (d, J = 7.9 Hz, 2H, H_3), 8.14 (td, J = 7.8, 1.6 Hz, 2H, H_5), 7.54 (ddd, J = 7.7, 4.9, 1.2 Hz, 2H, H_4), 7.46 – 7.37 (m, 4H, H_{10}), 7.31 (ddt, J = 10.2, 7.3, 2.7 Hz, 18H, $H_{8,9,14}$), 7.02 (td, J = 7.6, 1.1 Hz, 2H, H_{13}), 6.97 (dtd, J = 8.2, 2.5, 1.0 Hz, 2H, H_{15}), 6.75 (dtd, J = 7.9, 4.1, 1.6 Hz, 2H, H_{12}). ^{13}C{^{1}H} NMR (101 MHz, CD_3OD) δ 159.13 (t, J = 5.9 Hz, C_{16}), 157.31 (C_1), 152.08 (C_6), 140.67 (C_5), 135.28 (C_{12}), 134.81 (t, J = 8.3 Hz, C_8), 133.31 (C_{14}), 132.00 (t, J = 17.2 Hz, C_7), 131.53 (C_{10}), 130.02 (t, J = 4.9 Hz, C_9), 129.64 (C_4), 126.13 (C_{13}), 125.54 (C_3), 125.31 (t, C_{11}), 121.44 (C_{15}). ^{31}P{^{1}H} NMR (162 MHz, CD_3OD) δ –17.56. ESI-HR MS Calcd. for $C_{46}H_{36}N_2O_3P_2S^{63}Cu$: 821.1225; Found: 821.12183 $[M–BF_4]^+$. Elemental Analysis: Calcd. $C_{46}H_{36}BF_4N_2O_3P_2SCu$: C, 60.77; H, 3.99; N, 3.08; S, 3.53. Found: C, 60.44; H, 4.24; N, 2.76; S, 3.41.

[(Me-DPS)Cu(POP)Cu(Me-DPS)][BF$_4$]$_2$ (Cu-Me-DPS)

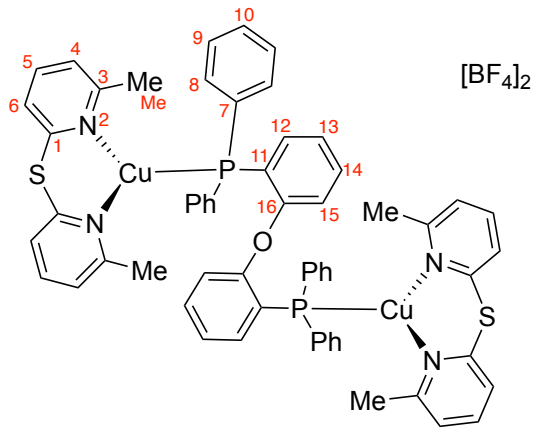

[Cu(MeCN)$_4$]BF$_4$ (0.176 g, 0.559 mmol, 2.0 eq.) and POP (0.140 g, 0.278 mmol, 1.0 eq.) were dissolved in 15 mL CH_2Cl_2 and stirred at room temperature for 2 h, after which **Me-DPS** (0.121 g, 0.559 mmol, 2.0 eq.) was added and the solution left to stir for a further 1 h. The reaction mixture was then concentrated *in vacuo*, the product precipitated with Et_2O, filtered and washed with Et_2O, yielding an off-white powder that required no further purification (0.290 g, 0.228 mmol, 82%). ^{1}H NMR (400 MHz, CD_3OD) δ 7.91 (br s, 8H, $H_{4,5}$), 7.51 (br m, 2H, H_6) 7.39 (m, 8H, $H_{10,14}$), 7.28 (t, J = 7.5 Hz, 8H, H_9), 7.14 (m, 10H, $H_{8,15}$), 7.02 (t, J = 7.5 Hz, 2H, H_{13}), 6.64 (dtd, J = 5.9, 4.1, 1.5 Hz, 2H, H_{12}), 2.21 (br s, 12H, H_{Me}). ^{13}C{^{1}H} NMR (101 MHz, CD_3OD) δ 159.33 (C_{16}), 135.54 (C_{12}), 134.44 (t, C_8), 133.63 (C_{14}), 131.74 (C_{10}), 131.30 (t, J = 19.6 Hz, C_7), 130.14 (t, J = 5.0 Hz, C_9), 126.31 (C_{13}), 124.36 (C_{11}), 121.40 (C_5). ^{31}P{^{1}H} NMR (162 MHz, CD_3OD) δ –15.83. Elemental Analysis: Calcd. $C_{60}H_{52}B_2F_8N_4OP_2S_2Cu_2$: C, 56.66; H, 4.12; N, 4.41; S, 5.04. Found: C, 56.64; H, 4.12; N, 4.40; S, 5.10.

[(POP)Cu(Me-DPSO$_2$)Cu(POP)][BF$_4$]$_2$ (Cu-Me-DPSO$_2$)

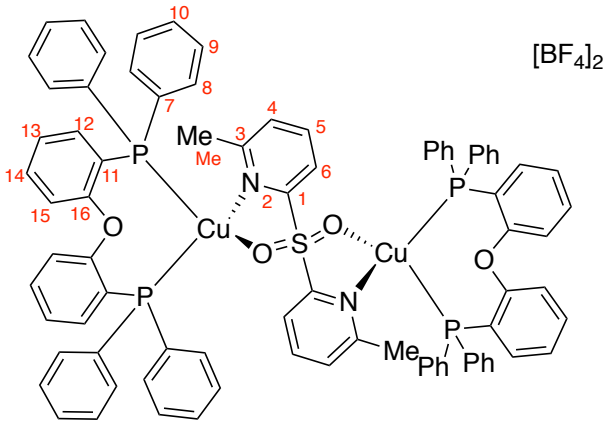

[Cu(MeCN)$_4$]BF$_4$ (0.064 g, 0.202 mmol, 2.0 eq.) and POP (0.109 g, 0.202 mmol, 1.0 eq.) were dissolved in 10 mL CH_2Cl_2 and stirred at room temperature for 2 h, after which **Me-DPSO$_2$** (0.025 g, 0.101 mmol, 1.0 eq.) was added and the solution left to stir for a further 1 h. The reaction mixture was then concentrated *in vacuo*, the product precipitated with Et_2O, filtered and washed with Et_2O, yielding a yellow powder that required no further purification (0.157 g, 0.097 mmol, 96%). ^{1}H NMR (400 MHz, CD_3OD) δ 8.00 (d, J = 7.5 Hz, 4H, $H_{4,5}$), 7.53 (d, J = 7.2 Hz, 2H, H_6), 7.47 – 7.40 (m, 8H, H_{10}), 7.39 – 7.27 (m, 36H, $H_{8,9,14}$), 7.00 (t, J = 7.4 Hz, 8H, $H_{13,15}$), 6.69 (dtd, J = 8.0, 4.0, 1.6 Hz, 4H, H_{12}), 2.26 (s, 6H, H_{Me}). ^{13}C{^{1}H} NMR (101 MHz, CD_3OD) δ ^{13}C{^{1}H} NMR (101 MHz, CD_3OD) δ 161.65 (C_1), 159.34 (t, C_{16}), 140.50 (C_5), 135.41 (C_{12}), 134.77 (t, J = 8.3 Hz, C_8), 133.25 (C_{14}), 132.20 (t, J = 17.6 Hz, C_7), 131.58 (C_{10}), 130.02 (t, J = 4.9 Hz, $C_{3,6,9}$), 126.02 (C_{13}), 124.96 (t, J = 15.5 Hz, C_{11}), 122.78 (C_4), 121.45 (C_{15}), 24.28 (C_{Me}). ^{31}P{^{1}H} NMR (162 MHz, CD_3OD) δ –18.44. Elemental Analysis: Calcd. $C_{84}H_{68}B_2F_8N_2O_4P_4SCu$: C, 62.04; H, 4.22; N, 1.72; S, 1.97. Found: C, 62.02; H, 4.55; N, 1.60; S, 1.93.

CHAPTER 4: Thermochromic Solid state Emission of Dipyridyl Sulfoxide Copper(I) Complexes

4.1 Introduction

Luminescent materials have seen a surge of interest within the last two decades for their use in a broad range of applications such as biological labelling,[159] sensing,[160,161] lighting and displays.[26,162] These applications often involve emission in the solid state, with organic light-emitting diodes (OLEDs) and light-emitting electrochemical cells (LECs) being two of the more common implementations. It has been shown that the emissive properties (such as colour, emission lifetime etc.) in these devices can be manipulated, and for metal complexes this can be achieved through ligand design[27,88,89,163] or *via* intermolecular interactions.[164-168]

Copper(I) complexes have been shown to be excellent candidates for low-cost, solid state emitters due to their high Earth-abundance and low cost, coupled with their ability to luminesce brightly at room temperature,[71] resulting in complexes with interesting photophysical characteristics. Nishihara et al. have reported that stimuli-responsive ring rotation in copper(I) complexes can be used to switch physical properties, including a dual luminescence.[169,170] In addition, copper(I) complexes have shown emissive thermochromic properties as clusters,[54,171-175] in coordination polymers[176] and in trinuclear species[177] with a high sensitivity to temperature, their environment and the rigidity of their medium.[171]

The photophysics of [Cu(disphosphine)(diimine)]$^+$ complexes have received considerable attention. These complexes exhibit an absorption in the visible light region due to a metal-to-ligand charge transfer (MLCT) transition resulting in an intense luminescence.[148,178-183] In particular,

Cu(I) complexes with an (oxydi-2,1-phenylene)bis(diphenylphosphine) (POP) diphosphine ligand have been extensively researched, and the introduction of a bulky diimine ligand into the coordination sphere has been shown to increase the excited state lifetime of the complex by preventing structural relaxation from tetrahedral to square-planar geometry and inhibiting solvent coordination.

The Wolf group has shown that the degree of sulfur oxidation can have significant effects on the electronic properties of a system, both in conjugated organic molecules[77-80] and inorganic complexes (Chapter 1:. In this work, sulfur-bridged diimine ligands based on di(pyridine-2-yl)sulfanes are used to probe how ligand binding mode and intermolecular interactions affect emission behaviour in Cu(I) complexes. Similar to 2,2'-bipyridine, sulfur-bridged diimine ligands can bear differing substituents at the pyridyl rings. However, the addition of the sulfur bridge in the 2,2' positions both increases the bite angle of the chelator and gives an additional site for further electronic tuning. On oxidizing the sulfur to sulfoxide, a third binding site becomes available leading to a variety of binding modes, which, when coupled with the tetrahedral geometry of the bridge and the electron-withdrawing nature of the S=O bond, gives flexibility to the ligand allowing coordination changes at copper.

Herein, we report two heteroleptic Cu(I) complexes **Cu-DPSO** and **Cu-Me-DPSO** containing sulfoxide ligands based on di(pyridine-2-yl)sulfanes (**DPSO** and **Me-DPSO**). The structural properties of the complexes were characterized using NMR experiments, X-ray crystallography, mass spectrometry and elemental analysis, and the photophysical behavior was studied as a function of temperature. **Cu-Me-DPSO** was found to luminesce either yellow or orange depending on morphology and temperature. This behavior is attributed to a change in

excited state coordination geometry, fundamentally differing from thermochromism in other copper complexes involving emission from Cu–Cu states.

4.2 Ligand Synthesis and Characterization

Scheme 4-1 Synthesis of Cu(I) species **Cu-DPSO** and **Cu-Me-DPSO**.

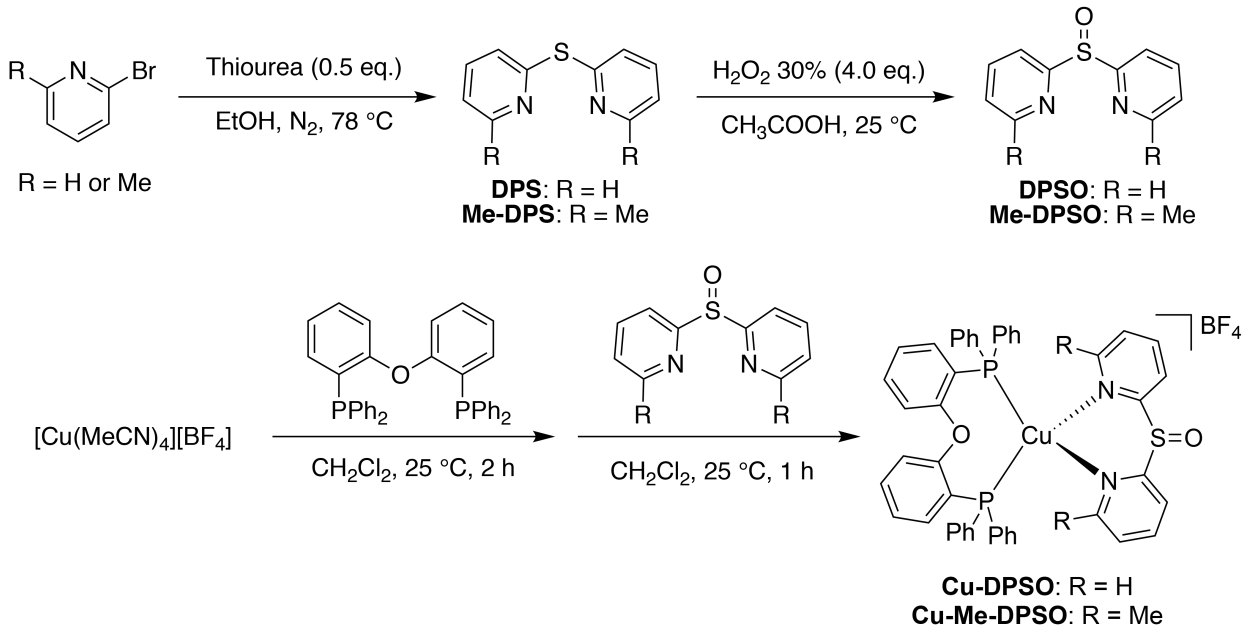

The diimine sulfide precursors **DPS** and **Me-DPS** were prepared *via* a nucleophilic aromatic substitution of 2-bromopyridine or 2-bromo-6-methylpyridine using thiourea (Scheme 4-1).[96] The desired sulfoxide proligands (**DPSO** and **Me-DPSO**) were then synthesized by oxidizing the appropriate sulfide compound with 30% H_2O_2 in the presence of glacial CH_3COOH and purified using column chromatography.[97] Structural characterization was performed using ^1H and ^{13}C NMR spectroscopy (including COSY, HSQC and HMBC experiments), infrared spectroscopy and high resolution mass spectrometry.

4.3 Synthesis and Characterization of [Cu(P^P)(N^N)[BF_4] Complexes

Cu(I) complexes (**Cu-DPSO** and **Cu-Me-DPSO**) were prepared *via* reaction of [Cu(MeCN)$_4$][BF_4] with POP, followed by the addition of the appropriate dipyridyl sulfoxide proligand.[76,141] The products both precipitated with diethyl ether yielding yellow powders that required no further purification (Scheme 4-1). All complexes were characterized using ^{1}H, ^{13}C{^{1}H} and ^{31}P{^{1}H} NMR spectroscopy, high resolution mass spectrometry, X-ray crystallography, powder XRD and elemental analysis. HR-ESI spectra show peaks corresponding to [M–BF_4]$^+$ and exhibit a characteristic copper isotope splitting pattern. ^{1}H and ^{13}C signals were assigned using COSY, NOESY, HSQC and HMBC NMR experiments.

4.3.1 Nuclear Magnetic Resonance (NMR)

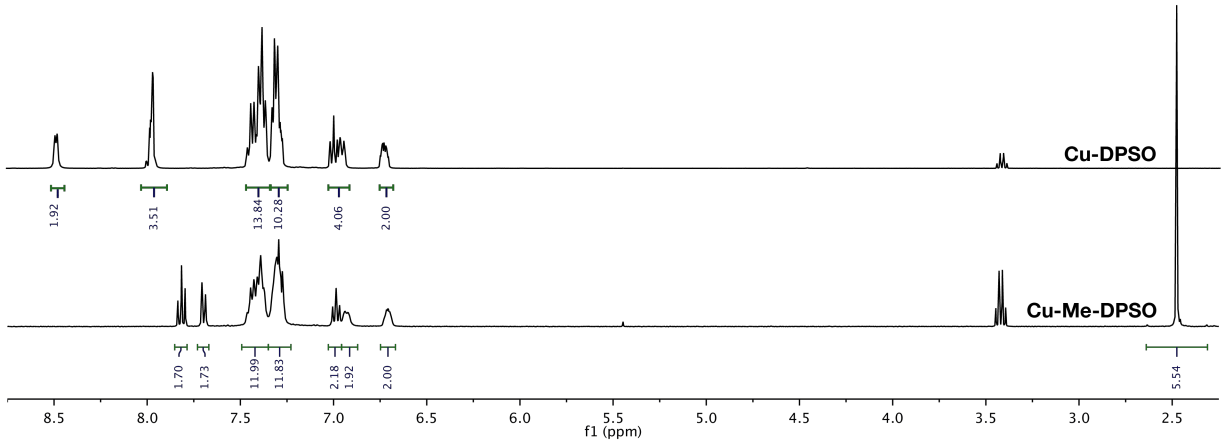

Figure 4-1 ^{1}H NMR spectra of **Cu-DPSO** and **Cu-Me-DPSO** in CD_3CN at 25 ºC (400 MHz).

The room-temperature NMR spectra of both **Cu-DPSO** and **Cu-Me-DPSO** show clear, defined signals with no evidence for exchange or dissociation occurring in CD_3CN (Figure 4-1). Sulfoxide ligands **DPSO** and **Me-DPSO** can bind to metals in three possible binding modes: in a

bidentate fashion *via* either both pyridyl rings (*N,N*), through one pyridyl ring and one oxygen (*N,O*) or through a pyridyl ring and the sulfur lone pair (*N,S*). For both **Cu-DPSO** and **Cu-Me-DPSO**, the NMR spectra are consistent with a symmetric *N,N* bound species with equivalent pyridyl rings. The POP ligand is bound in the usual bidentate fashion chelating *via* the phosphorus groups in both complexes, with a single peak in each case in the $^{31}P\{^{1}H\}$ NMR spectrum, with quadrupolar broadening attributed to the copper atoms. On cooling a CD_3CN solution of **Cu-Me-DPSO** to –40 ºC no change in the ^{1}H NMR spectrum was observed (Figure 4-2), indicating that over this temperature range the complex is either in fast equilibrium or present only as a single structure.

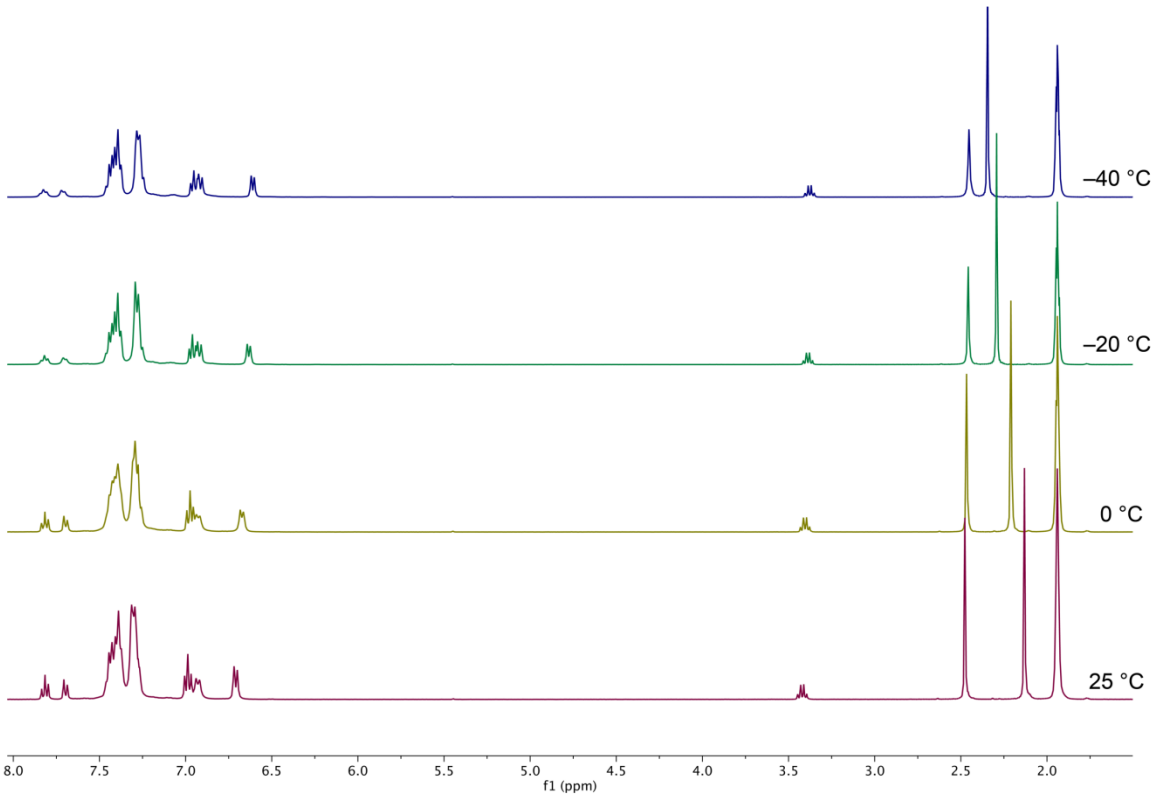

Figure 4-2 Low temperature ^{1}H NMR spectra of **Cu-Me-DPSO** in CD_3CN from 25 ºC to –40 ºC (400 MHz).

4.3.2 Single Crystal X-Ray Diffraction

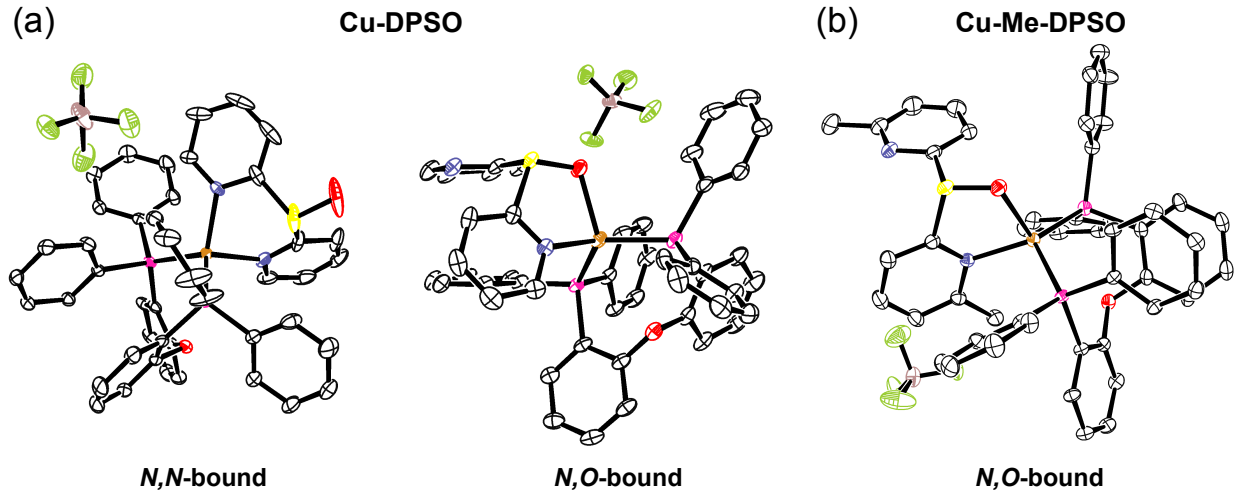

Figure 4-3 Solid state structures of (a) **Cu-DPSO** (*N,N* and *N,O* coordination modes, same unit cell). (b) **Cu-Me-DPSO** (*N,O* coordination mode). Ellipsoids are plotted at the 50% probability level. Hydrogen atoms and solvent molecules are removed for clarity.

X-ray quality crystals of each complex were obtained through the slow diffusion of Et_2O into a CH_2Cl_2 solution (Figure 4-3). Structural studies show the binding mode in these mononuclear copper(I) complexes in the solid state in the presence of the bulky POP chelating ligand. **Cu-DPSO** comprises the less bulky **DPSO** ligand and crystallizes in the space group P-1 with the asymmetric unit containing two distinct Cu(I) complexes, each with a different coordination mode for the **DPSO** ligand (Figure 4-3(a); *N,N* and *N,O* binding modes). The packing is stabilized by intermolecular hydrogen bonding between the sulfoxide oxygen of **Cu-DPSO** (*N,N*) and the α-proton of the non-bound pyridyl ring of **Cu-DPSO** (*N,O*), with a bond distance of 2.442 Å.

Table 4-1 Selected bond lengths (Å) and angles (º) of **Cu-DPSO** (*N,N*-bound), **Cu-DPSO** (*N,O*-bound) and **Cu-Me-DPSO** (*N,O*-bound).

	Cu-DPSO (*N,N*-bound)	**Cu-DPSO (*N,O*-bound)**	**Cu-Me-DPSO (*N,O*-bound)**
Cu1–N1	2.092(2) [a]	2.066(2)	2.0687(18)
Cu1–N12	2.092(2)	–	–
Cu1–O1	–	2.1777(18)	2.1975(17)
Cu1–P1	2.2643(7) [b]	2.2478(7)	2.2380(6)
Cu1–P2	2.2753(7) [c]	2.2851(7)	2.2809(5)
N11–Cu1–N12	91.82(8)	–	–
N1–Cu1–O1	–	81.16(8)	83.81(7)
P1–Cu1–P2	112.42(2) [d]	116.14(3)	114.73(2)

[a] Cu11–N11. [b] Cu11–P11. [c] Cu11–P12. [d] P11–Cu11–P12.

Only the *N,O* binding mode is found in the crystal structure of **Cu-Me-DPSO** (Figure 4-3(b)). In this conformation one of the pyridyl rings of **Me-DPSO** is rotated, orienting the methyl group away from the copper center. **Cu-Me-DPSO** contains a diimine ligand with methyl groups in the 6,6'-positions, resulting in greater steric strain near the metal center; in the *N,N* binding mode the two methyl groups will point towards the phenyl groups of the POP ligand. Binding through both pyridyl nitrogen atoms therefore appears to be disfavored in the crystal. This *N,O*-bound structure is not consistent with the solution structure determined by NMR spectroscopy; the presence of two different structures in the solution and solid state suggests that the energy difference between *N,N* and *N,O* binding modes is relatively small. The *N,S* binding mode was not observed with either **DPSO** or **Me-DPSO** ligands in the solid state or in solution, presumably due to the greater strain that would result from an acute N–Cu–S bond angle.

Selected bond lengths and angles are reported in Table 4-1. Structural analysis shows that the copper(I) complexes have a d^{10} tetrahedral structure and avoid mutual repulsion of the POP and diamine ligands by adopting a distorted tetrahedral geometry.[184] The P–Cu–P bite angle was anticipated to be quite large due to the presence of the bulky PPh_3 groups, whereas the N–Cu–N and N–Cu–O angles were expected to be smaller due to the higher steric constraints of the diimine ligands. Structural studies reveal that in all the complexes the P–Cu–P angles are in the range 112–116º while the N–Cu–N angle is 91.82º in *N,N*-bound **Cu-DPSO** and N–Cu–O angles are 81.16º and 83.81º for *N,O*-bound **Cu-DPSO** and **Cu-Me-DPSO** respectively. The three structures observed have similar Cu–P, Cu–N and Cu–O bond lengths, which are comparable to those measured in other related mononuclear copper(I) complexes.[75,76,136,185] The shortest inter-complex Cu(I)–Cu(I) bond distances were found to be 9.733 Å and 10.872 Å for **Cu-DPSO** and **Cu-Me-DPSO**, respectively. These values exceed the sum of the van der Waals radius of copper(I) (2.80 Å)[186] and thus metal–metal interactions are not seen.

4.3.3 Powder X-Ray Diffraction (pXRD)

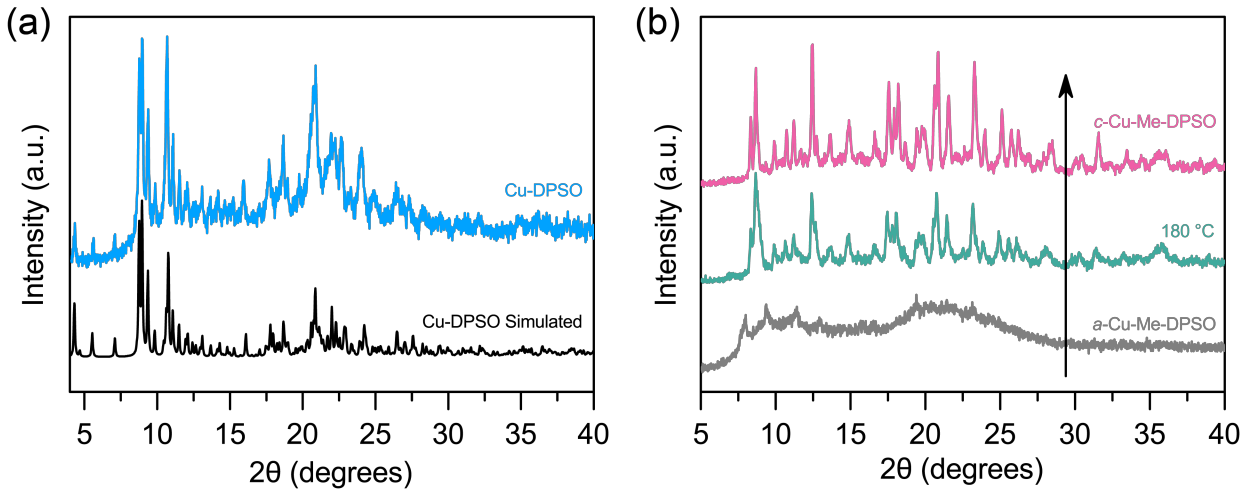

Figure 4-4 (a) pXRD of **Cu-DPSO** compared to the simulated powder pattern generated from the single crystal structure (*N,N* and *N,O* bound). (b) pXRD spectra of amorphous ***a*-Cu-Me-DPSO** (grey) heated to 180 ºC (teal) and then cooled to room temperature, retaining crystalline species ***c*-Cu-Me-DPSO** (pink)

Powder X-ray diffraction (pXRD) scans were recorded for both complexes at room temperature, with all powders isolated *via* rapid precipitation through addition of Et_2O to a concentrated CH_2Cl_2 solution of the complex. **Cu-DPSO** shows crystallinity with diffraction peaks matching those calculated from the diffraction data of the single crystal X-ray structure (Figure 4-4(a)), confirming that the isolated powder contains a mixture of complexes bound both *N,N* and *N,O* through the diimine ligand. The isolated methyl-substituted complex, however, is amorphous as isolated at room temperature (***a*-Cu-Me-DPSO**, Figure 4-4(b)).

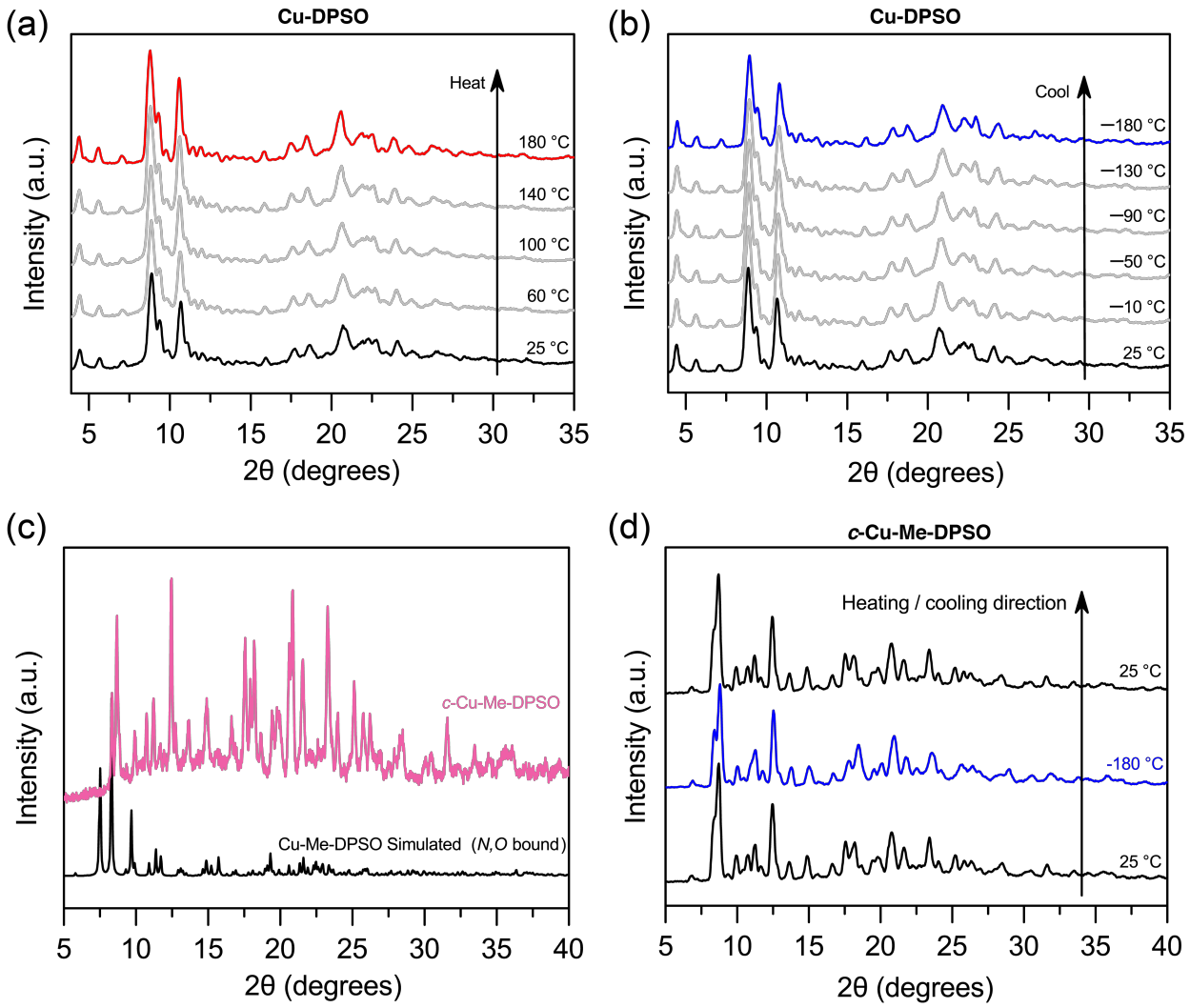

Figure 4-5 (a) pXRD of **Cu-DPSO** during heating to 180 ºC. (b) pXRD of **Cu-DPSO** during cooling to –180 ºC. (c) pXRD comparing ***c*-Cu-Me-DPSO** (pink) to the diffraction pattern generated from the single crystal data of *N,O*-bound **Cu-Me-DPSO** (black). ***a*-Cu-Me-DPSO**: amorphous state. ***c*-Cu-Me-DPSO**: crystalline state. (d) pXRD cycle of ***c*-Cu-Me-DPSO** cooled from room temperature to –180 ºC and back to room temperature.

The yellow powdered sample of **Cu-DPSO** was first heated to 180 ºC, then cooled to –180 ºC, and heated back to room temperature with no appreciable changes in the diffractogram (Figure 4-5(a) and Figure 4-5(b) respectively), indicating the structure was retained throughout this treatment. On heating ***a*-Cu-Me-DPSO** to 180 ºC however, the sample crystallized and the

crystallinity was maintained on cooling back to room temperature (***c*-Cu-Me-DPSO**, Figure 4-4(b)) giving a yellow-orange powder. The diffraction peaks observed for this sample do not match those predicted from the single crystal X-ray structure data, indicating that this structure does not contain ligand **Me-DPSO** bound in the *N,O* form (Figure 4-5(c)). On cooling ***c*-Cu-Me-DPSO** to –180 ºC a small shift in the diffraction pattern is observed indicating a change in the crystalline lattice (Figure 4-5(d)). The change could be a contraction in the unit cell as on warming to room temperature the diffraction pattern returned to that originally seen. NMR studies showed that both ***a*-Cu-Me-DPSO** and ***c*-Cu-Me-DPSO** exhibit identical ^{1}H NMR spectra when dissolved in CD_3CN or non-coordinating CD_2Cl_2, indicating that in solution only one state is preferred and that no reactions occur during the heating process.

4.3.4 Differential Scanning Calorimetry (DSC)

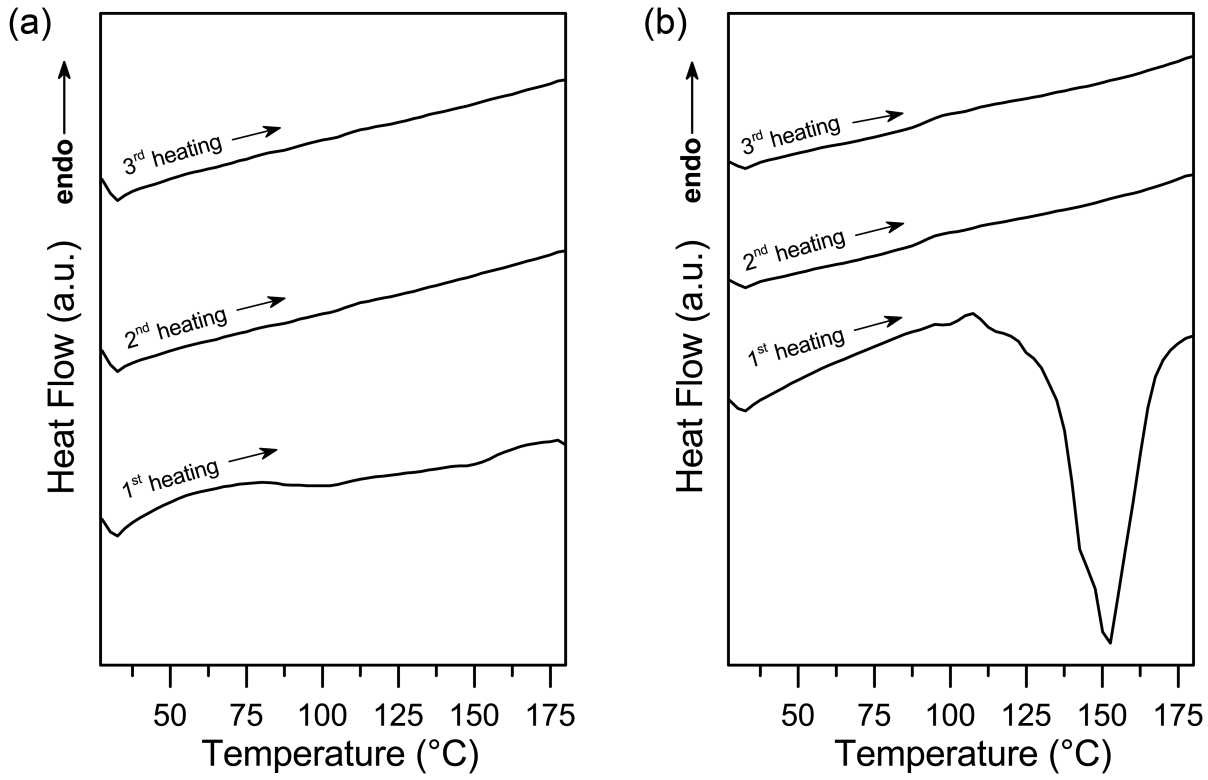

Figure 4-6 DSC data of (a) **Cu-DPSO** and (b) **Cu-Me-DPSO**. Both samples were scanned over a temperature range of 25–180 ºC with three cycles.

Differential scanning calorimetry (DSC) of **Cu-DPSO** over a temperature range of 25–180 ºC (Figure 4-6(a)) shows no marked change over each of three scans, however ***a*-Cu-Me-DPSO** over the same temperature range shows a strong endothermic feature in the first heating scan with an onset at 110 ºC which is attributed to the crystallization of ***a*-Cu-Me-DPSO** to ***c*-Cu-Me-DPSO** (Figure 4-6(b)). Once crystallized, ***c*-Cu-Me-DPSO** exhibits a glass transition (T_g ~100 ºC) on further heating cycles. The crystallization may be due to a flattening distortion of the complex towards a pseudo-tetrahedral geometry, as it has been noted that a slight red-shift in the absorption

of ground-state Cu(I) complexes accompanies changes of this type,[187,188] consistent with the slight change in colour of **Cu-Me-DPSO** from yellow to yellow-orange.

4.3.5 Fourier Transform Infrared Spectroscopy (FT-IR)

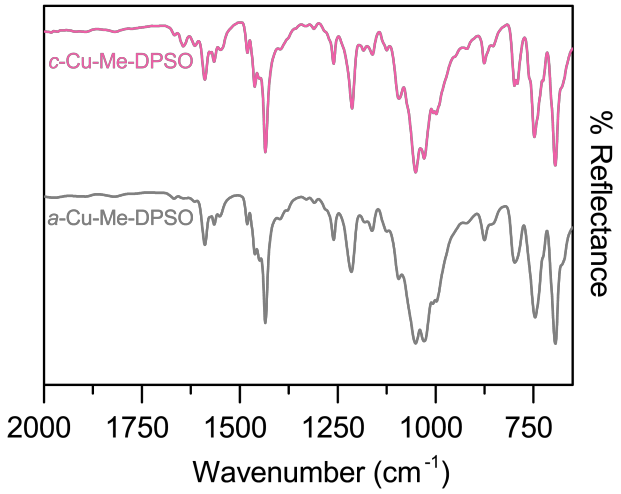

Figure 4-7 FT-IR spectra of ***a*-Cu-Me-DPSO** (grey) and ***c*-Cu-Me-DPSO** (pink) as neat solids at 25 ºC.

Infrared spectroscopy provides a useful handle for elucidating the structural transformation as the sulfoxide functional group has a strong stretching band. If the binding mode were changed from *N*,*N* to *N*,*O* upon crystallization, the SO stretch would be expected to shift to a lower frequency upon coordination to the metal center. However in comparing the spectra of ***a*-Cu-Me-DPSO** to ***c*-Cu-Me-DPSO** (Figure 4-7) the sulfoxide stretching band (1050 cm^{-1}) does not shift, therefore it is concluded that the complex maintains the *N*,*N* binding motif on crystallization.

4.4 Solution-state Photophysical Properties

4.4.1 Pro-ligand Photophysical Properties

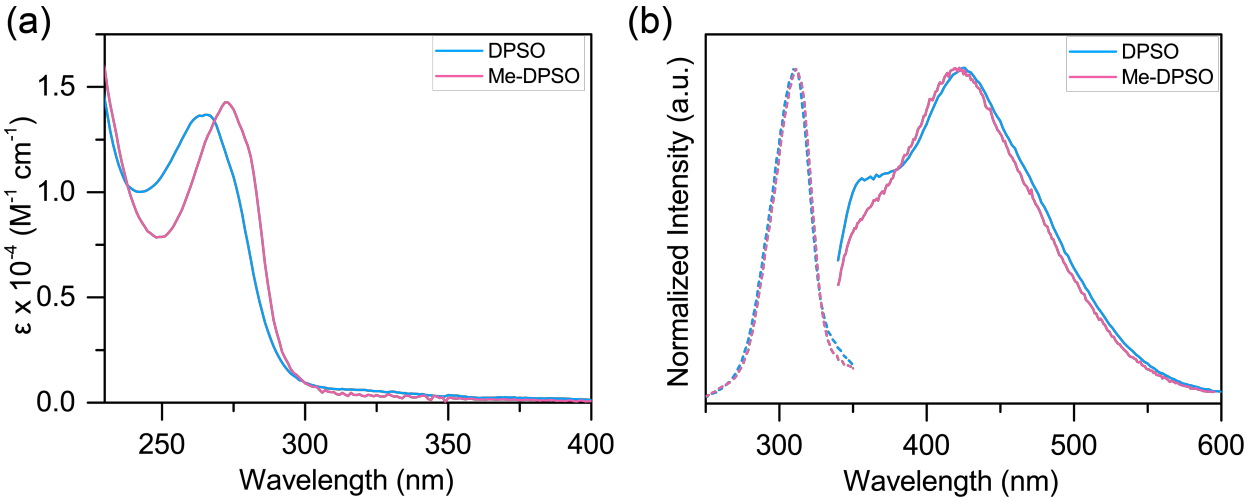

Figure 4-8 (a) UV-vis absorption spectra of **DPSO** (blue trace) and **Me-DPSO** (pink trace). (b) Normalized excitation (dashed line) and emission (solid line) spectra of **DPSO** (blue trace) and **Me-DPSO** (pink trace). λ_{ex} = 310 nm. Solutions of CH_2Cl_2 at 25 ºC, concentrations ~1 × 10^{-5} M.

The absorption spectra of sulfoxide pro-ligands **DPSO** and **Me-DPSO** were recorded in ~1 × 10^{-5} M solutions of CH_2Cl_2 (Figure 4-8(a) and Table 4-2) with features at energies higher than 300 nm corresponding to π–π* transitions. Both compounds exhibit blue fluorescence with λ_{max} = 426 and 422 nm for **DPSO** and **Me-DPSO**, respectively, with each compound also displaying a higher energy shoulder in the near-UV (Figure 4-8(b)). The excitation spectra of both pro-ligands shows that the emission stems from a π–π* transition with λ_{max} = 311 nm.

4.4.2 Cu(I) Complex Photophysical Properties

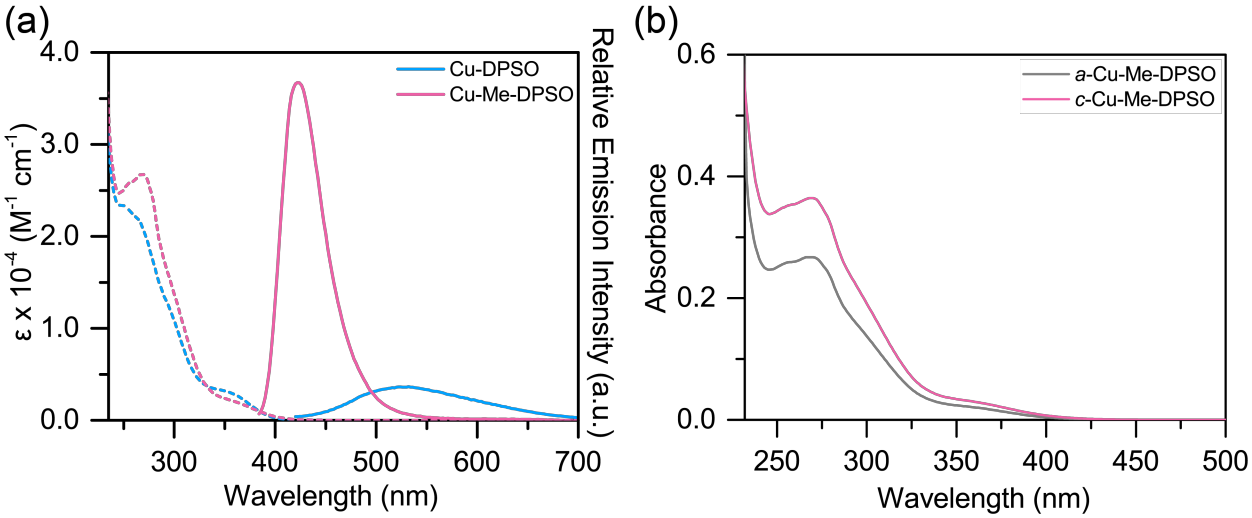

Figure 4-9 (a) Absorption and emission spectra of **Cu-DPSO** (blue) and **Cu-Me-DPSO** (pink) in sparged (Ar) CH_2Cl_2 solutions (concentrations ~3 × 10^{-5} M). Emission spectra are corrected for absorbance at the excitation wavelength (λ_{ex} = 380 nm). (b) Absorption spectra of ***a*-Cu-Me-DPSO** (grey) and ***c*-Cu-Me-DPSO** (pink) in CH_2Cl_2 at 25 ºC (concentrations ~5 × 10^{-5} M).

Absorption spectra of **Cu-DPSO** and **Cu-Me-DPSO** in CH_2Cl_2 are shown in Figure 4-9(a) and the photophysical data for the copper(I) complexes are summarized in Table 4-2. In CH_2Cl_2, **Cu-DPSO** and **Cu-Me-DPSO** both show intense absorption bands below 300 nm which are assigned to π–π* ligand centered (LC) transitions of the diimine ligands and the POP ligand. Additional shoulders between 300–400 nm not observed in the free ligands are assigned to d(Cu)–π*(*N,N*) metal-to-ligand charge-transfer (MLCT) transitions mixed with π(PP)–π*(*N,N*) ligand-to-ligand charge-transfer (LLCT) transitions,[148] and the lack of features near 450 nm indicates that the bis-diimine complex is not present in solution. The absorptions of ***a*-Cu-Me-DPSO** and ***c*-Cu-Me-DPSO** in CH_2Cl_2 were compared and found to be identical (Figure 4-9(b)) indicating that the ground state structure of both complexes reverts to the same geometry in solution.

Table 4-2 Photophysical data for compounds in CH_2Cl_2 (~1 × 10^{-5} M).

Compound	Absorption		Emission		
	λ_{max} (nm)	ε (M^{-1} cm^{-1})	λ_{em} (nm)	PLQY	τ_{em} [c]
DPSO	266	1.3 × 10^4	426 [a]	–	N/A [d]
Me-DPSO	272	1.4 × 10^4	422 [a]	–	N/A [d]
Cu-DPSO	250, 355	2.3 × 10^4, 3.0 × 10^3	532 [b]	<0.01	3 ns (63%), 11 ns (37%)
Cu-Me-DPSO	271, 365	2.7 × 10^4, 1.9 × 10^3	422 [b]	0.09	4 ns

[a] λ_{ex} = 310 nm. [b] λ_{ex} = 380 nm. [c] λ_{ex} = 370 nm. [d] Reliable emission lifetimes of the pro-ligands could not be collected due to lack of absorption at 370 nm.

Emission spectra of both complexes were recorded in CH_2Cl_2 after sparging with Ar for 30 min. **Cu-DPSO** displays a very weak, broad yellow emission when excited at 380 nm (λ_{max} = 532 nm, PLQY < 0.01) indicative of a MLCT-based transition (Figure 4-9(a)). The low intensity in solution is attributed to a flattening distortion in the vibrationally relaxed state, typical of copper(I) complexes of this type.[180] **Cu-Me-DPSO** shows a stronger blue emission upon excitation at 380 nm (λ_{max} = 422 nm, PLQY = 0.09), significantly blue-shifted from that of **Cu-DPSO**. The more intense emission is due to the steric bulk afforded by the methyl groups on the diimine ligand hindering the Jahn-Teller distortion and reducing the level of quenching. This emission profile is similar to that of pro-ligand **Me-DPSO** in solution, and may therefore be due to an inter-ligand charge transfer (ILCT) state. Both complexes have emission lifetimes consistent with fluorescence, and no change was observed in the photophysical properties before and after sparging with Ar.

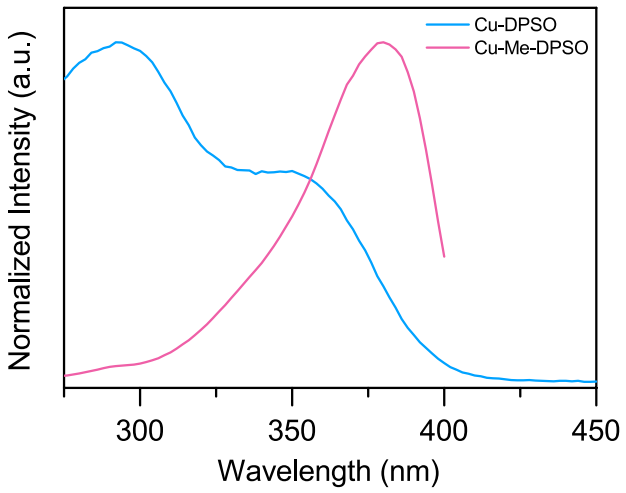

Figure 4-10 Excitation spectra of **Cu-DPSO** and **Cu-Me-DPSO** in CH_2Cl_2 at 25 ºC (concentrations ~3 × 10^{-5} M).

$[Cu(PP)(NN)]^+$ complexes are known to be labile in solution[141] so it is possible that the emission seen in **Cu-Me-DPSO** could be from the formation of $[Cu(POP)_2]^+$, however this homoleptic complex emits at ~480 nm in CH_2Cl_2,[144] 60 nm red-shifted from the emission of **Cu-Me-DPSO**. $[Cu(POP)_2]^+$ also does not display absorption at energies lower than 350 nm in CH_2Cl_2, while **Cu-Me-DPSO** shows a strong MLCT band centered at 365 nm. The excitation spectrum of **Cu-DPSO** contains both ligand-based (λ_{max} = 292 nm) and MLCT-based (λ_{max} = 350 nm) contributions, while the spectrum of **Cu-Me-DPSO** contains primarily one MLCT transition, with λ_{max} = 380 nm and a small shoulder at ~335 nm (Figure 4-10).

4.5 Cu(I) Complex Solid state Photophysical Properties

4.5.1 Photoluminescence Spectroscopy

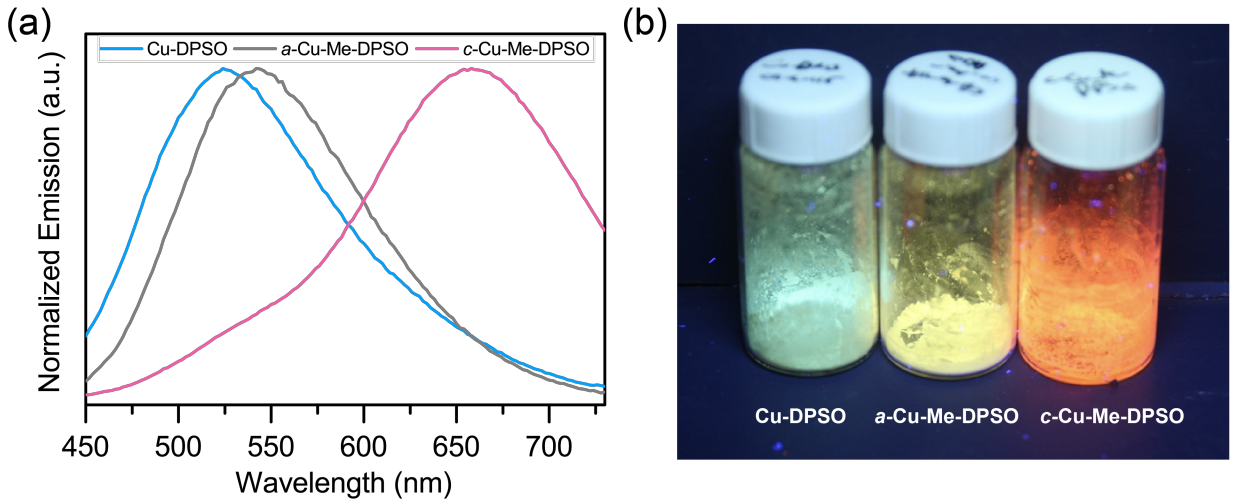

Figure 4-11 (a) Room temperature solid state emission of **Cu-DPSO** (blue), ***a*-Cu-Me-DPSO** (grey) and ***c*-Cu-Me-DPSO** (pink) drop-cast from MeOH on quartz. (λ_{ex} = 380 nm); (b) Photograph of the three complexes under UV hand lamp irradiation. (λ_{ex} = 365 nm)

Thin films of the neat powders were prepared by drop-casting onto quartz from MeOH. When irradiated with UV light (λ_{ex} = 380 nm) **Cu-DPSO** gives green-yellow luminescence (λ_{em} = 524) and ***a*-Cu-Me-DPSO** gives yellow luminescence (λ_{em} = 542 nm at 25 ºC) with broad, unstructured emission bands attributed to a MLCT (Figure 4-11(a) and Table 4-3).[71,182,189] However, when a thin film of the crystallized sample ***c*-Cu-Me-DPSO** was irradiated, it showed a pronounced bathochromic shift in emission with λ_{em} = 658 nm upon excitation. A large N-Cu-N bite angle (in comparison to that in $[Cu(POP)(bpy)]^+$ systems[76]) coupled with the additional steric constraints of methyl groups in the 6- and 6'-positions on the diimine ligand of **Cu-Me-DPSO** creates a bulky environment in conjunction with the POP ligand, which when rapidly precipitated from solution results in amorphous ***a*-Cu-Me-DPSO** being isolated. Due to the similar emission

energy of this compound when compared to **Cu-DPSO**, it is likely that the Cu(I) center in ***a*-Cu-Me-DPSO** possesses a tetrahedral environment aided by the bulky methyl groups on the diimine ligand. However, once heated above ~100 ºC a structural change occurs which triggers a red-shift in the emission wavelength. ***c*-Cu-Me-DPSO** likely acquires a more flattened distortion about the metal center as it is known that a bathochromic shift in the emission of Cu(I) result from pseudo-Jahn-Teller distortions.[190]

Table 4-3 Solid state emission data for thin films of **Cu-DPSO**, ***a*-Cu-Me-DPSO** and ***c*-Cu-Me-DPSO**.

	Solid state Emission [a]	
	λ_{em} at 25 ºC (nm)	**λ_{em} at –196 ºC (nm)**
Cu-DPSO	524	534
***a*-Cu-Me-DPSO**	542	558
***c*-Cu-Me-DPSO**	658	556

[a] Thin films drop-cast from MeOH on to quartz. (λ_{ex} = 380 nm)

4.5.2 Low-Temperature Photophysical Properties

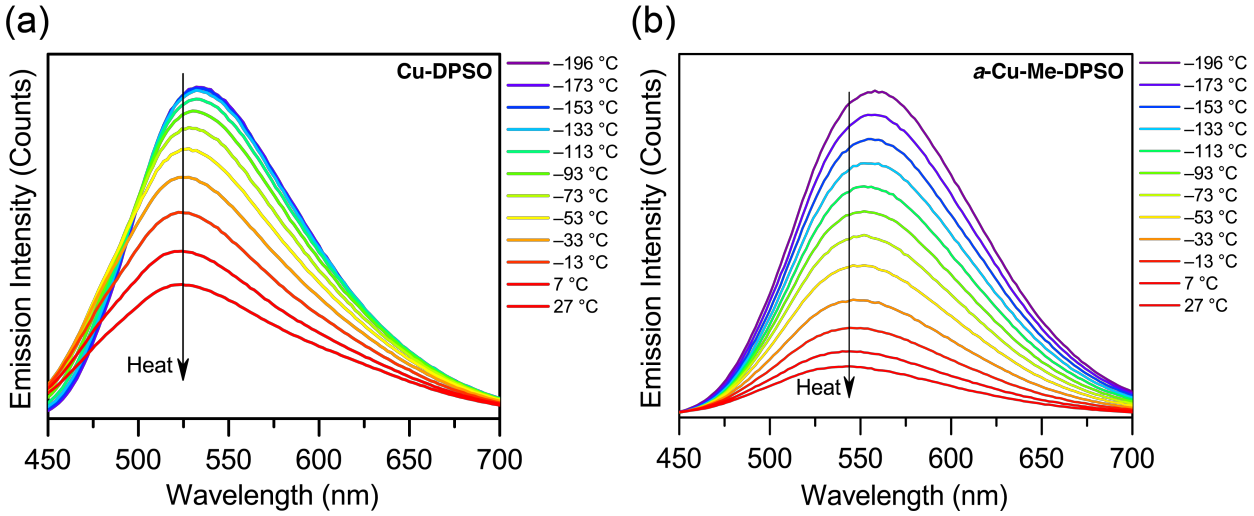

Figure 4-12 Variable-temperature solid state emission spectra of (a) **Cu-DPSO** and (b) ***a*-Cu-Me-DPSO** from –196 to 27 ºC. Thin films dropcast on quartz from MeOH. (λ_{ex} = 380 nm)

Low-temperature solid state emission data helps elucidate the cause of the large red-shift in emission from ***a*-Cu-Me-DPSO** to ***c*-Cu-Me-DPSO**. The solid state emission spectra of a thin film of **Cu-DPSO** drop-cast from MeOH on a quartz slide were collected from –196 to 25 ºC (Figure 4-12(a)). The emission intensity decreased and a blue-shift in λ_{max} from 534 to 524 nm was observed on warming from –196 ºC to room temperature. Cu(I) complexes are known to often have a small $\Delta E(S_1–T_1)$ and the T_1 state can be populated even at liquid nitrogen temperatures.[10] The observed blue-shift is therefore a consequence of thermal activation of the energetically higher-lying S_1 state and is typical of the behavior of $[Cu(PP)(NN)]^+$ complexes, with a $\Delta E(S_1–T_1)$ of 0.04 eV seen for **Cu-DPSO**.

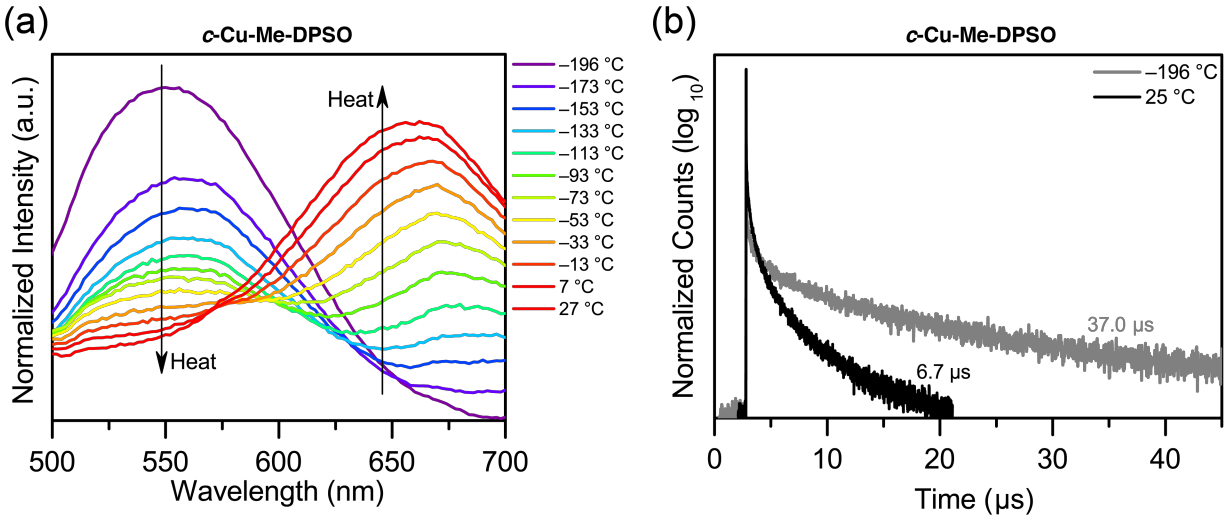

Figure 4-13 (a) Variable temperature solid state emission spectra of ***c*-Cu-Me-DPSO** from –196 to 27 ºC (λ_{ex} = 380 nm). (b) Variable temperature, solid state emission lifetimes of ***c*-Cu-Me-DPSO** at –196 and 25 ºC. To maintain accuracy, a 50 µs time range was used for –196 ºC and 20 µs for 25 ºC. Longest time component for each complex reported (λ_{ex} = 370 nm). Thin films dropcast on quartz from MeOH.

Emission spectra of a thin film of ***a*-Cu-Me-DPSO** were collected from –196 ºC to 25 ºC and a blue-shift of 558 to 542 nm observed, similar to the results for **Cu-DPSO** (Figure 4-12(b)). In contrast, ***c*-Cu-Me-DPSO** in the solid state exhibited significant emission thermochromism on warming from –196 ºC to 25 ºC (Figure 4-13(a)), with a red-shift of 102 nm from a high energy (HE) band at 556 nm to a low energy (LE) band at 658 nm. This thermochromic emission behavior was found to be reversible and rapid. As a thin film cooled in liquid nitrogen, ***c*-Cu-Me-DPSO** gives a bright yellow emission when irradiated with a handheld UV lamp, and then when heated (either rapidly with a Varitemp heat gun or left to slowly warm to room temperature) gives orange emission. This process can be repeatedly cycled with no noticeable change to the emission colour thus demonstrating reversible thermochromism. Similar behavior has been observed in transition metal complexes where a bathochromic shift accompanies occupancy of an energetically lower-lying state (such as a T_1 state) that reduces the HOMO–LUMO energy gap. However, variable-temperature emission lifetime data for ***c*-Cu-Me-DPSO** exhibited an increase in lifetime on cooling, with a long-lived component ranging from 6.7 μs at 25 ºC, to 37.0 μs at –196 ºC (Figure 4-13(b)). While the emission lifetime increases at low temperature, the higher energy emission indicated that yellow emission band is not due to a of population of a lower-energy phosphorescent state.

Based on these results, we propose that the observed thermochromism is the result of a structural change about the copper center. The dynamics of $[Cu(PP)(NN)]^+$ complexes after photoexcitation have been well documented.[181,191] The ground state d^{10} electronic configuration of these complexes favors a pseudo-tetrahedral geometry, which alters to a tetragonally distorted environment on excitation to the MLCT excited state as the Cu(I) is formally oxidized to a d^9 Cu(II) center.[59] Following this, the complex undergoes a pseudo-Jahn-Teller distortion on a sub-

picosecond timescale, resulting in a flattening distortion of the molecular geometry.[60] These classical Cu(I) dynamics are consistent with the observations in **Cu-DPSO**.

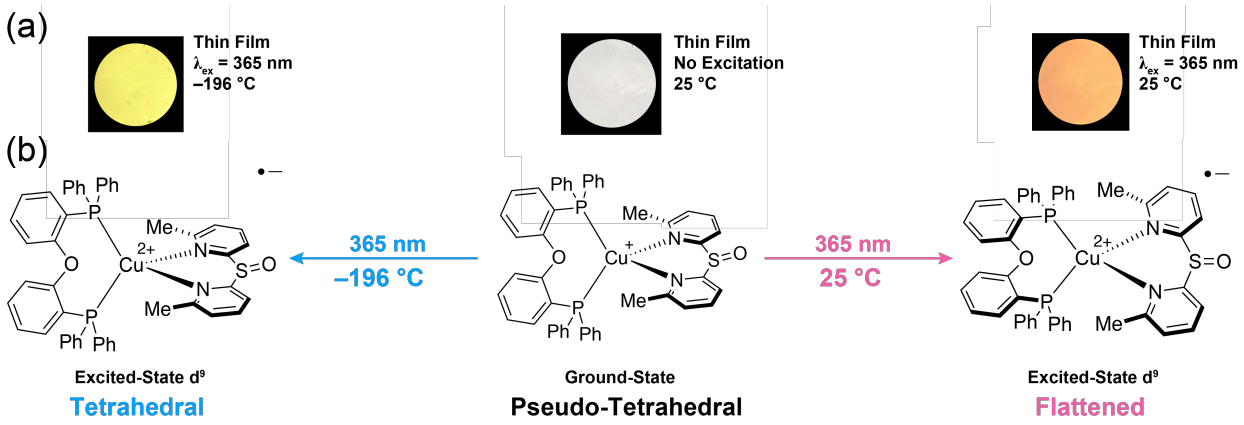

Figure 4-14 (a) Photographs showing the thermochromic behaviour of thin films of ***c*-Cu-Me-DPSO** in the ground-state and under UV lamp excitation (λ_{ex} = 365 nm) at different temperatures. (b) The proposed excited-state conformational change for the thermochromic emission of ***c*-Cu-Me-DPSO**.

It has been known for some time, however, that Cu(II) bis-diimine complexes can undergo a thermochromic distortion in the ground-state, whereby a blue-shift in colour is seen on cooling which results from a square-planar to tetrahedral distortion.[192-194] We believe that this phenomenon is occurring in the excited, Cu(II)-like state of ***c*-Cu-Me-DPSO** (Figure 4-14). When the complex is in the ground-state, ***c*-Cu-Me-DPSO** resides in a pseudo-tetrahedral geometry. On irradiating at room temperature the complex undergoes a Jahn-Teller distortion and an orange emission is observed. However when the complex is excited in a cooled state, a distortion towards a geometry closer to tetrahedral about the now-Cu(II) metal center is preferred, resulting in a diminishing of the orange emissive LE band and the growth of a yellow emissive HE band. The methyl groups in the 6- and 6'-positions on the diimine ligand help stabilize this transition, which explains why the

thermochromism is not observed in **Cu-DPSO**. It is postulated that the yellow emission in ***a*-Cu-Me-DPSO** is due to the less rigid environment of the amorphous powder allowing a more tetrahedral geometry to be achieved.

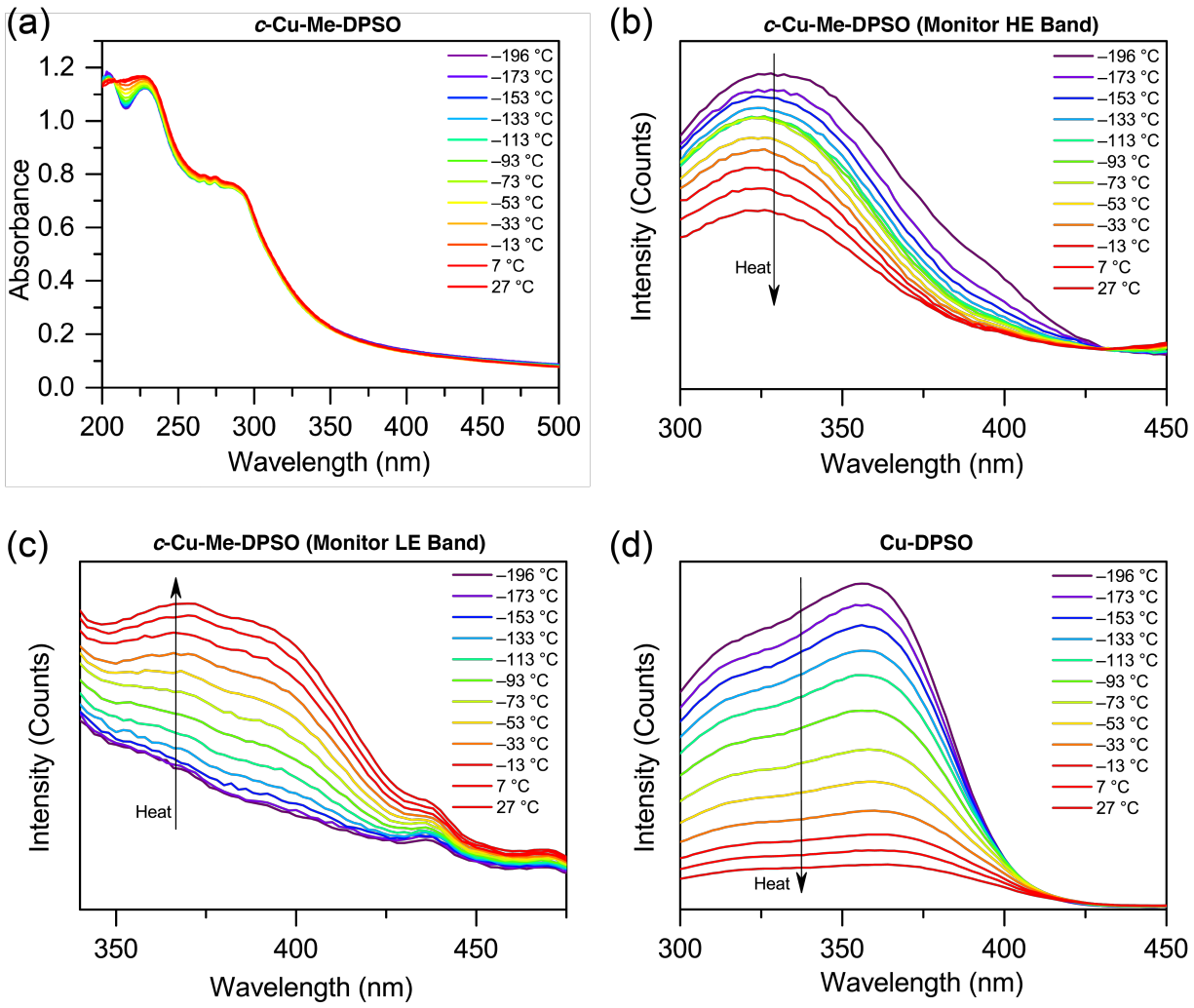

Figure 4-15 (a) Variable temperature UV-vis absorption spectra of ***c*-Cu-Me-DPSO** from –196 to 27 ºC. (b) Variable temperature excitation spectra of ***c*-Cu-Me-DPSO** measuring the HE emission at 556 nm. (c) Variable temperature excitation spectra of ***c*-Cu-Me-DPSO** measuring the LE emission at 658 nm. (d) Variable temperature excitation spectra of **Cu-DPSO** measuring the emission at 524 nm. Thin films dropcast on quartz from MeOH.

Further evidence for the thermochromism being related to the excited-state is found in the variable temperature UV-vis absorption and excitation spectra. On warming a thin film of ***c*-Cu-Me-DPSO** from –196 ºC to 25 ºC no change is observed in the lower energy MLCT region of the spectrum (Figure 4-15(a)), however a pronounced change in seen in the excitation spectra. On monitoring the HE emission band, a transition is seen in the excitation spectrum at $\lambda_{max} \approx 325$ nm (Figure 4-15(b)). This transition is strongest at –196 ºC and diminishes on warming to room temperature. Conversely, when monitoring the LE emission band minimal transitions are seen at –196 ºC, but on warming an excitation feature at $\lambda_{max} \approx 390$ nm grows in (Figure 4-15(c)). The excitation wavelength ($\lambda_{ex} = 380$ nm) for the emission experiments traverses the overlap of these two excitation bands giving "full" yellow character at liquid nitrogen temperatures and "full" orange character at room temperature, with a mix of the two states present at intermediate temperatures. There is no evidence of an excitation growing in at energies lower than 450 nm, indicating that the orange emission is not caused by the formation of a [Cu(**Me-DPSO**)$_2$][BF_4] complex. The spectrum of **Cu-DPSO** shows no shift in the excitation band, merely a diminishing in intensity on warming (Figure 4-15(d)).

The emissive behavior during the crystallization transition from ***a*-Cu-Me-DPSO** to ***c*-Cu-Me-DPSO** was also monitored to help elucidate the origin of the thermochromic emission. ***a*-Cu-Me-DPSO** was drop-cast from MeOH onto a quartz slide, heated in a cryostat and the emission spectra monitored (Figure 4-16). At temperatures up to 87 ºC no change in the HE emission band are seen, however at 107 ºC the LE orange emission begins to grow in, and monitoring at this temperature over a period of 30 minutes shows the HE band diminishing and the LE band growing in. If the thermochromism were due to temperature-dependent population of a different electronic state, it would be anticipated that growth of the LE orange emission band would occur in seconds

or quicker, and not on the timescales observed. The temperature range in which the colour-change occurs agrees with the temperature required for onset of crystallization as observed by DSC. These data give further evidence towards a thermochromic emission caused by a structural change.

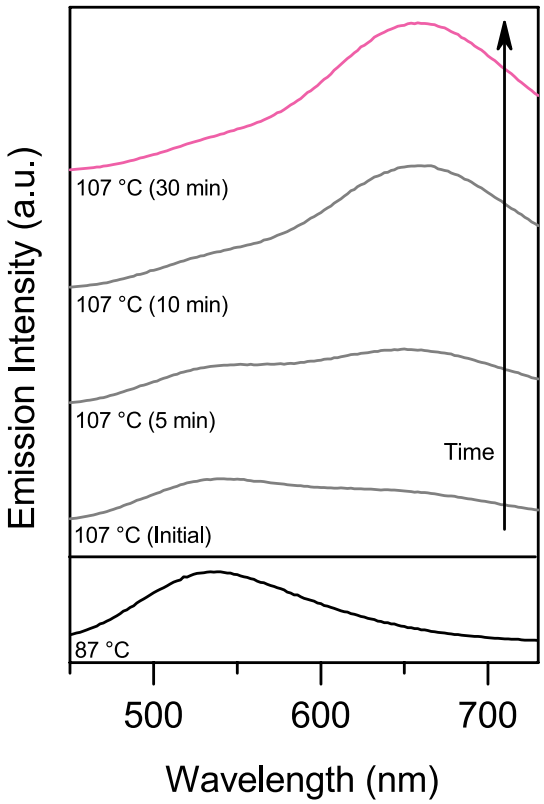

Figure 4-16 Solid state emission spectra of the crystallization process from ***a*-Cu-Me-DPSO** to ***c*-Cu-Me-DPSO**. At 87 ºC (black trace) the thin film shows HE emission, and at 107 ºC (initial) the LE band has already started to grow in. Over the next 30 min the HE band diminishes and the LE band increases in intensity (pink trace).

4.6 Conclusions

The ability to control or tune photoluminescence properties is advantageous in the design of photofunctional materials, particularly those which react to an external stimulus. While there have been other examples of thermochromic emission behavior in copper(I) systems, those were

in halide clusters only where Cu–Cu interactions play a role. In this work we have developed two new [Cu(disphosphine)(diimine)]$^+$ complexes, **Cu-DPSO** and **Cu-Me-DPSO**, where sulfoxide-bridged diimine ligands are present. **Cu-DPSO** displayed photophysical properties typical of other Cu(I) complexes. However, on addition of methyl substituents in the 6- and 6′-positions of the diimine ligand to give complex **Cu-Me-DPSO**, we were able to access a variety of different photophysical properties. **Cu-Me-DPSO** is initially isolated as an amorphous solid (***a*-Cu-Me-DPSO**) which under UV irradiation gives a yellow emission. Upon heating to 180 ºC, ***a*-Cu-Me-DPSO** forms a crystalline species which is retained on cooling to room temperature (***c*-Cu-Me-DPSO**). This crystalline species gives markedly bathochromically shifted (>100 nm) orange emission, which is attributed to a flattening conformational change during the crystallization process due to the increased bulk at the diimine ligand. Low-temperature solid state emission experiments revealed a small red-shift in emission colour for **Cu-DPSO**, typical for Cu(I) complexes. On the other hand, reversible thermochromic emission was observed in ***c*-Cu-Me-DPSO**, whereby the complex undergoes a large colour change from orange at room temperature to yellow at –196 ºC. It is inferred that this hypsochromic shift is not due to the population of a lower energy triplet state at low temperatures (as is often the case in copper(I) complexes), but is instead attributed to a geometric distortion in the excited-state. At room temperature the excited ***c*-Cu-Me-DPSO** complex exists in a more flattened state giving an orange emission, however at –196 ºC the complex prefers to adopt a pseudo-tetrahedral geometry giving rise to a yellow emission.

We show that subtle changes in the properties of the diimine ligand in [Cu(disphosphine)(diimine)]$^+$ complexes can have a dramatic impact on the properties of the complex. In utilizing a sulfur-bridged dipyridyl ligand it is not only possible to alter the steric and

electronic properties through substitution at the pyridyl rings, but also alter the degree of oxidation at the sulfur atom with addition of electron-withdrawing oxygen atoms. This gives an additional level of control over the electronics, allowing for finely-tuned electronic properties in these ligands.

In showing that a copper(I) complex can exhibit reversible thermochromism, avenues that were inaccessible due to the limitations of thermochromic copper halide clusters can now be realized. For example, inexpensive copper(I) metallopolymers that offer a response to thermal stimuli could be fabricated. The simple synthetic procedures to the complexes reported, coupled with the absence of toxic heavy metals, give avenues towards practical applications in optoelectronics, including light-emitting diodes, display technologies and chemical and biological sensors.

4.7 Experimental Details

4.7.1 General

All experiments were conducted under an inert nitrogen atmosphere using standard Schlenk-line techniques, unless otherwise stated. 2-Bromopyridine, 2-bromo-6-methylpyridine and tetrakis(acetonitrile)copper(I) tetrafluoroborate were purchased from Aldrich. POP was purchased from Strem and thiourea obtained from TCI. All compounds were used as received. All other solvents were obtained from commercial sources and used without any further purification.

4.7.2 Spectroscopy

^{1}H NMR, ^{13}C NMR and ^{31}P NMR spectra were collected using a Bruker AV-400 spectrometer and referenced to the residual protonated solvent peak. NMR solvents (from either

Cambridge Isotope Laboratories or Aldrich) were used as received. Electrospray ionization mass spectrometry data were obtained using a Bruker Esquire LC ion trap mass spectrometer and elemental analysis determined using a Thermo Flash 2000 Elemental Analyzer. Infrared spectra were collected using a Perkin Elmer Frontier FT-IR spectrometer and DSC data collected using a Netzsch DSC 216 Polyma. Electronic absorption spectra were recorded on a Varian-Cary 5000 UV−vis−near-IR spectrophotometer. Fluorescence data were collected on a Photon Technology International (PTI) QuantaMaster 50 fluorimeter fitted with an integrating sphere, double excitation monochrometer and utilizing a 75 W Xe arc lamp as the source. Emission lifetime data were collected using a Horiba Yvon Fluorocube TCSPC apparatus. A 370 nm NanoLED source pulsing at a repetition rate of 100−1000 kHz was used for excitation. Broad-band emission was monitored by a CCD detector at wavelengths >450 nm using a low-pass filter. Data were fitted using the DAS6 Data Analysis software package. Samples for low temperature emission were cooled using an Oxford Instruments Optistat DN. Solution spectra were collected using 1 cm^2 quartz cells (Starna Cells) and spectra of the neat solids were collected by drop-casting from MeOH on to quartz slides (Ted Pella, Inc.).

4.7.3 X-Ray Crystallography

Single crystal X-ray data were collected using a Bruker APEX DUO diffractometer with graphite monochromated Mo Kα radiation (λ = 0.71073 Å) at 90 K. Raw frame data were processed using APEX2.[195] Structure solution was performed using SUPERFLIP and refinement was carried out using full-matrix least-squares on *F* within the CRYSTALS suite.[154,155] All non-hydrogen atoms were refined with anisotropic displacement parameters. The positions of the hydrogen atoms were calculated using the Fourier difference map and were initially refined with

restraints on bond lengths and angles, after which the positions were used as the basis for the riding model.[156] Powder X-ray diffraction patterns were collected using a Bruker D8 Advance Powder Diffractometer and data analyzed using Bruker DiffracPlus EVA software.

4.7.4 Synthesis

di(pyridin-2-yl)sulfane (DPS)

Using a procedure adapted from Khan *et al.*[96] a two-necked round-bottomed flask was charged with thiourea (5.86 g, 77.0 mmol, 0.5 eq.), placed under an N_2 atmosphere and dissolved in 500 mL EtOH. To this, 2-bromopyridine (15.0 mL, 154 mmol, 1.0 eq.) was added and the reaction mixture heated to reflux for 36 h, after which the flask was cooled to room temperature and the solvent removed *in vacuo*. The crude product was dissolved in CH_2Cl_2 (50 mL), washed with water (3 × 50 mL) then brine (1 × 100 mL) and the organic layer dried with $MgSO_4$, filtered and the solvent evaporated under reduced pressure. Following purification using a silica gel column and a solvent gradient from 1:0 CH_2Cl_2:MeOH to 9:1 CH_2Cl_2:MeOH, a yellow-brown oil was isolated (13.5 g, 92%). The spectroscopic data matched that of the literature.[196]

bis(6-methylpyridin-2-yl)sulfane (Me-DPS)

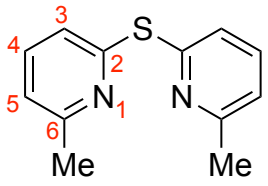

2-bromo-6-methylpyridine (0.66 mL, 5.81 mmol, 1.0 eq.) was added to a solution of thiourea (0.210 g, 2.76 mmol, 0.48 eq.) in 100 mL of EtOH under an N_2 atmosphere and heated to reflux for 36 h. The reaction mixture was cooled to room temperature the solvent removed and the resultant residue dissolved in CH_2Cl_2 (20 mL) and washed with water (3 × 20 mL) and brine (1 × 50 mL). The organic layer was dried with $MgSO_4$, filtered and the CH_2Cl_2 removed *in vacuo*. The crude product was purified by column

chromatography on silica gel using a solvent gradient from 1:0 CH_2Cl_2:MeOH to 9:1 CH_2Cl_2:MeOH, yielding a brown oil (0.558 g, 2.58 mmol, 94%). ^{1}H NMR (400 MHz, CD_2Cl_2) δ 7.50 (t, J = 7.7 Hz, 2H, H_4), 7.19 (dt, J = 7.9, 0.8 Hz, 2H, H_3), 7.02 (ddd, J = 7.6, 0.9, 0.5 Hz, 2H, H_5), 2.50 (s, 6H, H_{Me}). ^{13}C{^{1}H} NMR (CD_2Cl_2, 101 MHz) δ 159.82 (C_2), 156.80 (C_6), 137.69 (C_4), 123.05 (C_3), 121.67 (C_5), 24.62 (C_{Me}). HR-ESI MS: Calcd for $C_{10}H_8N_2OSNa$: 227.0255; Found: 227.0255 $[M+Na]^+$.

2,2'-sulfinyldipyridine (DPSO)

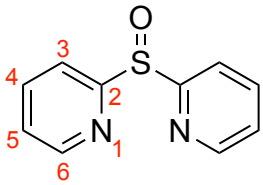

DPS (0.173 g, 0.919 mmol, 1.0 eq.) was dissolved in 2 mL glacial acetic acid, to which a 30% solution of H_2O_2 (0.35 mL, 3.68 mmol, 4.0 eq.) was added dropwise. The reaction mixture was stirred at 25 ºC for 42.5 h, following which 6 M NaOH was added until basic, forming a yellow suspension which turned white after stirring for 30 min. Brine (50 mL) was added and the crude product extracted with CH_2Cl_2 (3 × 10 mL) followed by drying of the combined organics over $MgSO_4$ and removal of the CH_2Cl_2 *in vacuo*. Purification over a silica gel column using a 95:5 CH_2Cl_2:MeOH solvent system resulted in an off-white powder (0.107 g, 0.524 mmol, 57%). ^{1}H NMR (400 MHz, CD_2Cl_2) δ 8.57 (d, J = 4.6 Hz, 2H, H_4), 7.97 (d, J = 7.9 Hz, 2H, H_1), 7.88 (td, J = 7.7, 1.6 Hz, 2H, H_2), 7.39 – 7.31 (m, 2H, H_3). ^{13}C{^{1}H} NMR (CD_2Cl_2, 100 MHz) δ 164.84 (C_6), 150.23 (C_4), 138.40 (C_2), 125.47 (C_3), 119.96 (C_1). HR-ESI MS: *m/z* calcd. for $C_{10}H_8N_2ONaS$: 227.0255; Found: 227.0255 $[M+Na]^+$. IR (neat): $\tilde{\nu}$ (σ SO) 1037 cm^{-1}.

6,6'-sulfinylbis(2-methylpyridine) (Me-DPSO)

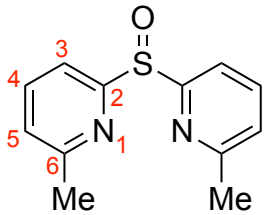

Me-DPS (0.199 g, 0.920 mmol, 1.0 eq.) was dissolved in 12 mL glacial acetic acid and heated to 25 ºC. To this, 30% H_2O_2 (0.35 mL, 2.68 mmol, 4.0 eq.) was added dropwise, and the solution left to stir for 23 h. The reaction mixture was cooled, basified using 6 M NaOH and the crude product extracted using CH_2Cl_2 (3 × 15 mL). The combined organics were dried over $MgSO_4$, filtered and the solvent removed *in vacuo*. Column chromatography on silica gel utilizing a 95:5 CH_2Cl_2:MeOH solvent system gave an off-white powder (0.100 g, 0.431 mmol, 47%). ^{1}H NMR (CD_2Cl_2, 400 MHz): δ 7.77 – 7.70 (m, 4H, $H_{3,4}$), 7.21 – 7.15 (m, 2H, H_5), 2.53 (s, 6H, H_{Me}). $^{13}C\{^1H\}$ NMR (CD_2Cl_2, 101 MHz) δ 164.40 (C_2), 159.91 (C_6), 138.47 (C_4), 125.29 (C_5), 117.21 (C_3), 24.48 (C_{Me}). IR (solid): (σ SO) 1037 cm^{-1}. HR-ESI MS: Calcd for $C_{12}H_{12}N_2OSNa$: 255.0568; Found: 255.0569 $[M+Na]^+$

[Cu(POP)(DPSO)][BF$_4$] (Cu-DPSO)

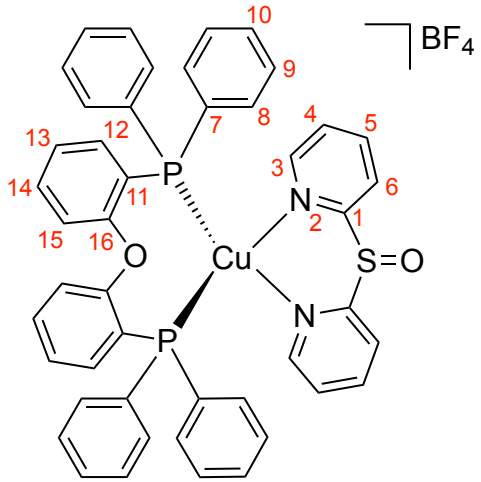

$[Cu(MeCN)_4]BF_4$ (0.077 g, 0.245 mmol, 1.0 eq.) and POP (0.132 g, 0.245 mmol, 1.0 eq.) were dissolved in CH_2Cl_2 and stirred at room temperature for 2 h, after which **DPSO** (0.050 g, 0.245 mmol, 1.0 eq.) was added and the solution left to stir for a further 1 h. The reaction mixture was then concentrated *in vacuo*, the product precipitated with Et_2O, filtered and washed with Et_2O, giving a yellow-white powder (0.194 g, 0.217 mmol, 89%). ^{1}H NMR (CD_3CN, 400 MHz): δ 8.48 (d, J = 4.8 Hz, 2H, H_6), 8.01 – 7.94 (m, 4H, $H_{3,5}$), 7.47 – 7.34 (m, 14H, $H_{4,9,10}$), 7.34 – 7.25 (m, 10H, $H_{8,14}$), 7.00 (td, J =

7.6, 1.1 Hz, 2H, H_{13}), 6.98 – 6.92 (m, 2H, H_{15}), 6.73 (ddt, J = 6.2, 4.0, 2.4 Hz, 2H, H_{12}). $^{13}C\{^1H\}$ NMR (CD_3CN, 101 MHz) δ 164.85 (C_1), 158.81 (C_{16}), 151.06 (C_6), 139.76 (C_5), 135.02 (C_{12}), 134.47 (t, C_8), 132.99 (C_{14}), 131.99 (t, C_7), 131.22 (C_{10}), 129.84 (t, C_9), 126.60 (C_4), 125.77 (C_{13}), 124.47 (t, C_{11}), 121.12 (C_{15}), 120.87 (C_3). $^{31}P\{^1H\}$ NMR (CD_3CN, 161 MHz): δ –14.1. HR-ESI MS: Calcd for $C_{46}H_{36}N_2O_2P_2SCu$: 805.1269; Found: 805.1276 $[M–BF]^+$. Anal. Calcd for $C_{46}H_{36}BF_4N_2O_2P_2SCu$: C, 61.86; H, 4.06; N, 3.14; S, 3.59. Found: C, 61.82; H, 4.23; N, 2.98; S, 3.47.

[Cu(POP)(Me-DPSO)][BF$_4$] (Cu-Me-DPSO)

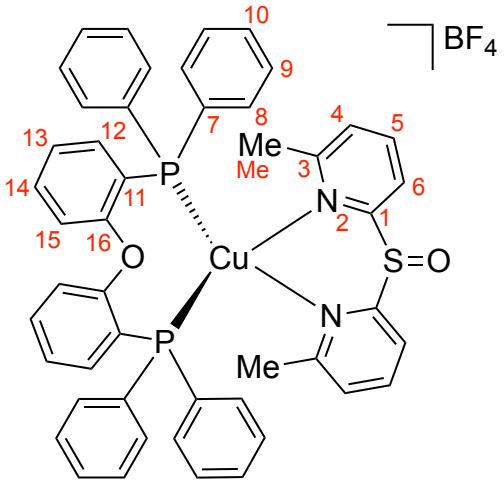

$[Cu(MeCN)_4]BF_4$ (0.068 g, 0.215 mmol, 1.0 eq.) and POP (0.116 g, 0.215 mmol, 1.0 eq.) were dissolved in CH_2Cl_2 and stirred at room temperature for 2 h, after which **Me-DPSO** (0.050 g, 0.215 mmol, 1.0 eq.) was added and the solution left to stir for a further 1 h. The reaction mixture was then concentrated *in vacuo*, the product precipitated with Et_2O, filtered and washed with Et_2O, giving a yellow-white powder (0.151 g, 0.164 mmol, 76%). ^1H NMR (CD_3CN, 400 MHz): δ 7.82 (t, J = 7.7 Hz, 2H, H_5), 7.70 (d, J = 7.7 Hz, 2H, H_4), 7.41 (dt, J = 13.6, 6.8 Hz, 12H, $H_{8,9}$), 7.35 – 7.23 (m, 12H, $H_{8,14,16}$), 6.99 (t, J = 7.5 Hz, 2H, H_{13}), 6.93 (d, J = 8.0 Hz, 2H, H_{15}), 6.71 (dt, J = 7.2, 3.3 Hz, 2H, H_{12}), 2.48 (s, 6H, H_{Me}). $^{13}C\{^1H\}$ NMR (CD_3CN, 101 MHz) δ 164.69 (C_1), 160.36 (C_3), 158.91 (C_{16}), 139.40 (C_5), 135.11 (C_{12}), 134.49 (t, C_8), 132.93 (C_{14}), 132.21 (t, C_7), 131.18 (C_{10}), 129.82 (t, C_9), 126.07 (C_6), 125.71 (C_{13}), 124.44 (C_{11}), 121.05 (C_{15}), 117.87 (C_4), 24.19 (C_{Me}). $^{31}P\{^1H\}$ NMR (CD_3CN, 161 MHz): δ –14.6. HR-ESI MS: Calcd for

$C_{48}H_{40}N_2O_2P_2SCu$: 833.1582; Found: 833.1600 $[M–BF_4]^+$. Anal. Calcd for $C_{48}H_{40}BF_4N_2O_2P_2SCu$: C, 62.85; H, 4.38; N, 3.04; S, 3.48. Found: C, 62.41; H, 4.41; N, 2.85; S, 3.40.

CHAPTER 5: Sulfur-Bridged Bimetallic Ru(II)-Re(I) Systems – Modulating CO_2 Reduction with Sulfur Oxidation State

5.1 Introduction

Global energy consumption is rapidly increasing, driven by a population boom and industrialization. In 2001, global energy consumption was 4.3×10^{20} J[197] with this usage projected to triple by 2050.[198] The majority of this energy is obtained from fossil resources: oil, coal and natural gas. When burned, these fuels generate a significant amount of CO_2 which is then released into the atmosphere, and this increase in atmospheric CO_2 concentration results in global warming. Additionally, fossil fuels are a finite resource and are not just an energy source, but also a feedstock for many chemical starting materials. It is therefore of great importance to reduce the volume of CO_2 released in to the atmosphere, but also to convert this otherwise wasted by-product into something more industrially useful.

5.1.1 Photocatalytic CO_2 Reduction

With more efficient methods required to convert solar energy to useable chemical energy, researchers have taken inspiration from Nature in a bid to mimic photosynthesis and ultimately harness this solar radiation through storage of energy in chemical bonds and reactive chemical species.[199,200] Photocatalytic reduction is a technique in which CO_2 is converted into useful higher energy components such as CO or formic acid, and various metal complexes have been reported which are catalytically active for this process.[201] Photochemical CO_2 reduction involves two

components: a redox photosensitizer (PS) that absorbs light in the visible region; and a catalytic center at which the reduction occurs. The scope of this work will focus on Ru(II) as the PS unit, and Re(I) as the catalyst.

Since the first reported example of luminescence from tris-2,2′-bipyridine ruthenium(II) by Paris and Brandt nearly 60 years ago,[202] a significant number of members of the coordination chemistry community have focused their research on ruthenium(II) complexes. While expensive, ruthenium has proven itself a useful tool through modification of its transition metal complexes, giving rise to a wealth of tunable spectroscopic and redox properties, stemming from a low-lying, intense Ru(dπ) to ligand(π*) metal-to-ligand charge transfer (MLCT) transition. These properties have helped establish ruthenium(II) complexes as viable candidates for solar energy conversion, as molecular devices, in the medical field towards new therapeutics and bio-probes, and for use in photocatalysis.[203] Ruthenium(II) complexes with polypyridyl ligands are ideal for use as photosensitizers[204] due to their long excited-state lifetimes, redox properties, chemical stability, and excited-state reactivity.[205]

The catalytic center in light-driven CO_2 reduction systems has predominantly been based on *fac*-Re(bpy)$(CO)_3$X (X = Cl^- and Br^-) due to the stability, high product selectivity and efficiencies of these complexes.[201] The use of Re(I) complexes as monometallic units for CO_2 reduction was first demonstrated by Lehn, Ziessel and Hawecker in 1983.[206] It has been shown, however, that supramolecular photocatalytic systems – whereby the PS and catalytic units are conjoined – can greatly increase the reduction efficiency.[207]

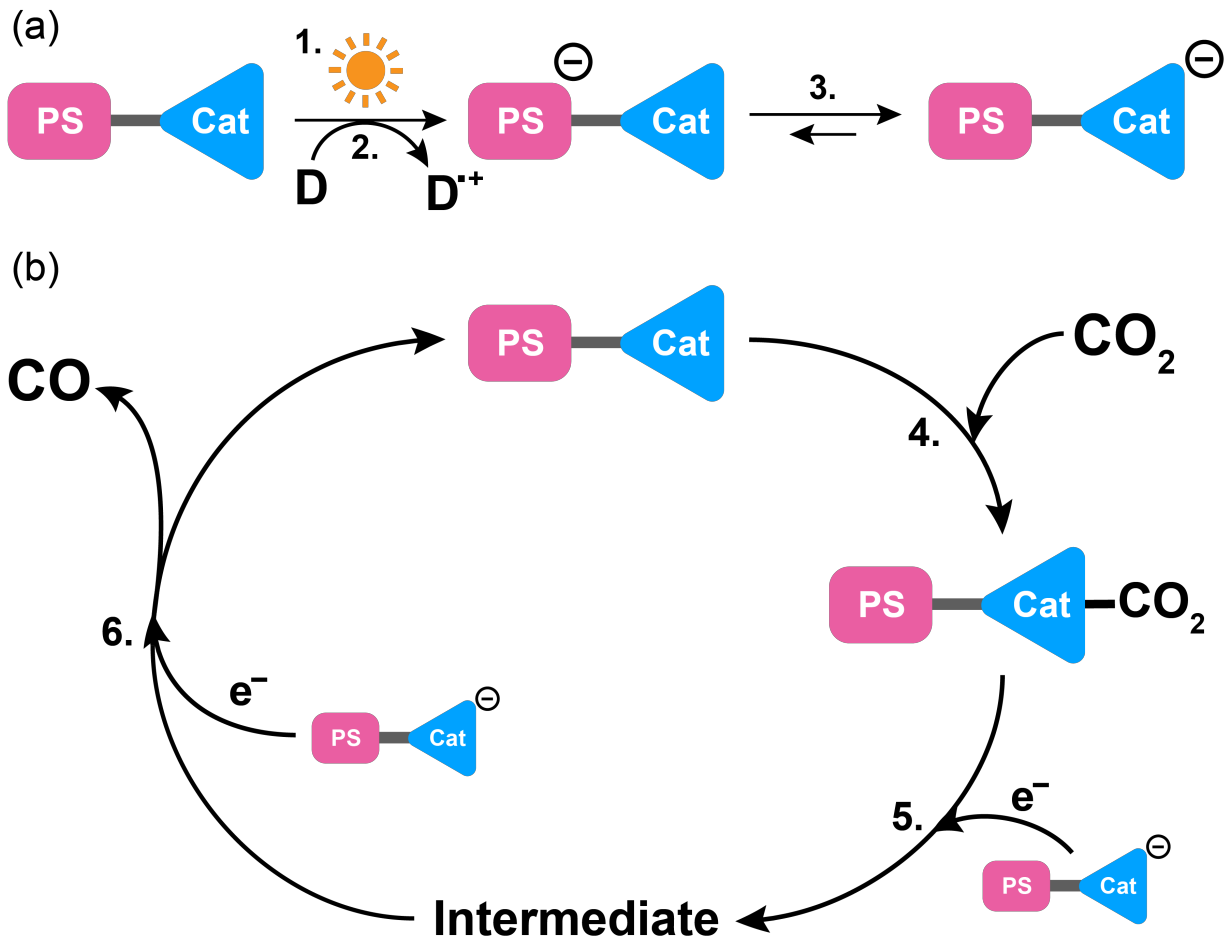

Figure 5-1 Depiction of a supramolecular photocatalyst assembly for CO_2 reduction, where (a) illustrates the generation of the one electron reduced species (OERS) of the photocatalyst, and (b) illustrates the catalytic cycle for CO_2 reduction.

A supramolecular photocatalyst consists of a visible-light absorbing PS unit and a catalytic unit bound together *via* a bridging ligand (Figure 5-1). The electron transfer between the PS and the catalyst is accelerated when compared to relying on intermolecular interactions for a solution containing free PS and free catalyst. This enhances the durability of the system as the unstable redox states can be consumed more rapidly, helping improve the efficiency of the system.[208] The reaction mechanism can be broken into two sections, the first being the generation of the one

electron reduced species (OERS) of the photocatalyst (Figure 5-1(a)), and the second being the catalytic cycle for the production of CO (Figure 5-1(b)). The mechanism proceeds as follows:

1. Irradiation of the metallic PS gives the ^{3}MLCT excited-state.
2. The excited PS unit is quenched by a sacrificial electron donor (D), generating the one electron reduced species (OERS) of the PS.
3. A rapid intramolecular electron transfer from the OERS of the PS to the catalytic center (Cat).
4. CO_2 binds to the photocatalyst.
5. Additional OERS of the PS–Cat remaining in solution functions as a redox photosensitizer and supplies an electron, forming an intermediate.
6. The electron for the second reduction process is supplied again by remaining OERS of PS-Cat, resulting in the formation of CO and the regeneration of PS–Cat.

5.1.2 Ru(II)-Re(I) Supramolecular Photocatalytic Systems

In 2005, Ishitani and co-workers demonstrated the first successful Ru(II)-Re(I) supramolecular photocatalyst for CO_2 reduction (**24**, Figure 5-2) consisting of a $[Ru(N^\wedge N)]^{2+}$ PS unit and a *fac*-$Re(N^\wedge N)(CO)_3Cl$ catalyst bridged by two 4-methyl-bpy ligands connected with a -$CH_2CH(OH)CH_2$- chain.[209] When irradiating with visible light (> 500 nm) and using 1-benzyl-1,4-dihydronicotinamide (BNAH) as a sacrificial electron donor, CO was found to be produced with a high efficiency and selectivity (Φ_{CO} = 0.12, TON_{CO} = 170). These Ru(II)-Re(I) systems have since garnered considerable research and it has been shown that the bridging ligand plays a major role in the efficiency of the systems, a selection of which are found in Figure 5-2.

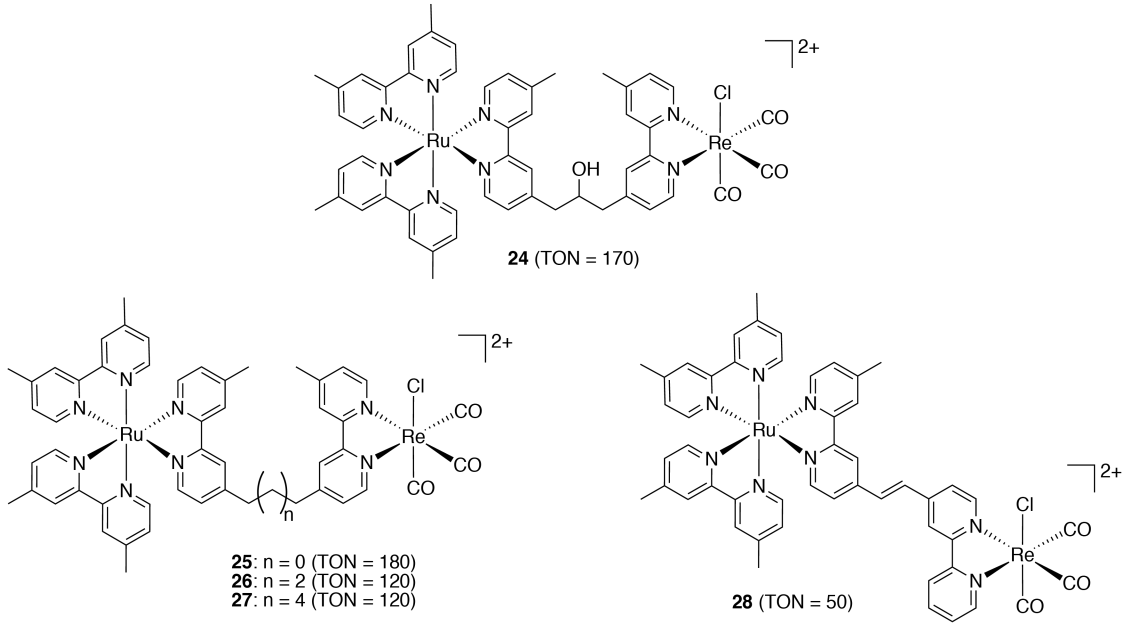

Figure 5-2 Selected Ru(II)-Re(I) systems.[209-211]

It was found that the length of the alkyl chain linking the Ru(II) and Re(I) centers impacted the efficiency of the supramolecular catalyst.[210] When the alkyl linker bridging the species increased in length the efficiency decreased. For **25** containing an ethyl linked bridge, $\Phi_{CO} = 0.13$ and $TON_{CO} = 180$. However on increasing the length to a butylene (**26**) or hexylene (**27**) chain, the catalytic activity diminished ($\Phi_{CO} = 0.11$ and $TON_{CO} = 120$) with similar properties seen between the two species with longer bridges. An electronic interaction between the two metal centers in the excited state was only observed in **25** and not in the **26** or **27** dyads. This causes a higher reductive quenching efficiency of the ^{3}MLCT state by BNAH in **25**, leading to increased reduction of CO_2.

The electronics at the bridge also affect the performance of the photocatalysts.[208] **28** is structured with the two bipyridyl moieties of the bridge joined by a carbon-carbon double bond,[211]

which is comparable to **25** that is connected *via* the saturated analogue. **25** displays a significant enhancement in efficiency over **28** (TON = 180 and 50, respectively). Extended conjugation at the bridging ligand lowers the reducing power of the OERS of rhenium which can inhibit its reductive catalytic activity. It has been reported that a threshold for the photocatalytic activity of mononuclear Re complexes exists at $E_{1/2}^{red}$ = –1.4 V, and it is this occurrence that explains the difference in activity: $E_{1/2}^{red}$ of **28** was –1.34 V, while **25** was –1.77 V.

In this work we investigate how the oxidation state at sulfur affects the CO_2 reductive properties of two new Ru(II)-Re(I) supramolecular catalysts. A sulfur-bridged bisphenanthroline is utilized as the connector between the two metal units, allowing us to maintain almost-identical geometric structures between the sulfide and sulfone oxidation states.

5.2 Ligand Synthesis and Characterization

The series of ligands described in this work was prepared using modifications of previously reported procedures (Scheme 1). Ligand **PSP** was prepared in a one-pot synthesis through reaction of Li_2S with commercially available 5,6-epoxy-5,6-dihydro-1,10-phenanthroline in refluxing *tert*-butanol.[212] This pro-ligand was then oxidized to the sulfone (**PSO_2P**) analogue with 30% H_2O_2 in the presence of a NbC catalyst.[99] Both bridging pro-ligands were isolated in moderate to high yields and structural characterization performed using ^{1}H, ^{13}C{^{1}H}, COSY, HSQC and HMBC NMR experiments, in addition to mass spectrometry and infrared spectroscopy.

Scheme 5-1 Synthesis of Ru(II)-Re(I) complexes **Ru-PSP-Re** and **Ru-PSO₂P-Re**.

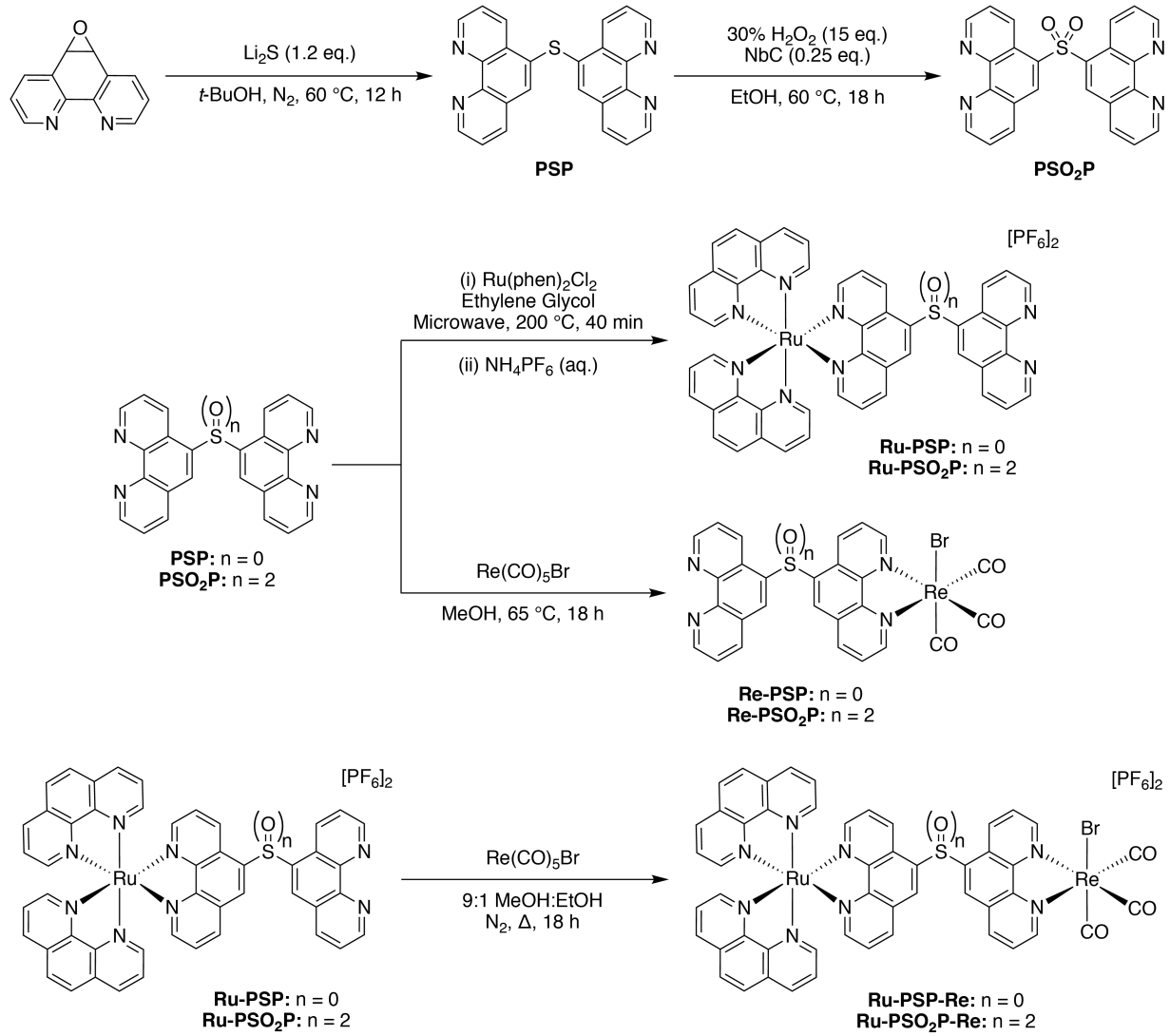

5.3 Synthesis and Characterization of Ru(II) Complexes

cis-Ru(phen)$_2$Cl$_2$ was synthesized as per the literature.[213] Monometallic Ru(II) complexes **Ru-PSP** and **Ru-PSO₂P** were prepared using an adapted procedure from Johansson *et al*. utilizing a microwave synthesizer.[214] *cis*-Ru(phen)$_2$Cl$_2$ was reacted with an excess of the desired pro-ligand (Scheme 1) and the crude products purified *via* column chromatography over silica gel (F60) using

$CH_3CN:H_2O:KNO_3$ (aq) as the eluting solvent. The pure products were isolated as hexafluorophosphate salts through the addition of a saturated aqueous NH_4PF_6 solution that resulted in the formation of precipitates that were orange in colour in all cases. Monometallic rhenium complexes **Re-PSP** and **Re-PSO$_2$P** were synthesized by reaction of the desired pro-ligand with $Re(CO)_5Br$ in MeOH heated to reflux in the dark. Purification occurred by purification with column chromatography using silica gel (F60) using first CH_3CN then 98:2 CH_2Cl_2:MeOH as the eluting solvents. Bridged Ru(II)-Re(I) species were prepared through reaction of **Ru-PSP** or **Ru-PSO$_2$P** with $Re(CO)_5Br$ under a nitrogen atmosphere in the dark followed by purification over silica gel in a similar manner to the monometallic Ru(II) species. ^{1}H and ^{13}C NMR spectra were assigned using ^{1}H, ^{13}C{^{1}H}, COSY, ROESY, HSQC and HMBC experiments. The HR-MS spectra show product peaks corresponding to $[M-PF_6]^+$ exhibiting characteristic ruthenium and rhenium isotope patterns.

Both **Ru-PSP-Re** and **Ru-PSO$_2$P-Re** exist as diastereomers due to chirality at both the ruthenium and rhenium centers. This unfortunately made full assignment of the complexes difficult, even with a field strength of 20 T in the NMR spectrometer; however through analysis of the bridge protons in **Ru-PSO$_2$P-Re** it was possible to observe two different species (Figure 5-3(a)). The protons in the 6- and 6′-positions on the **PSO$_2$P** bridge are singlets in ^{1}H NMR with signals at $\delta = 9.50$ and $\delta = 8.23$ for the phenanthroline moieties bound at Ru and Re, respectively. ROESY experiments observing through-space correlations between the bridge and the phen ligands bound to the Ru center were used to determine the binding of **PSO$_2$P**. The singlet seen at each position is in fact two overlapping signals (for the two diastereomers) as determined from HSQC experiments (Figure 5-3(b)) indicating that the proton signal corresponds to two separate

carbon environments. From COSY, ROESY, HSQC, HMBC and $^{13}C\{^{1}H\}$ experiments it was possible to distinguish the bridging ligands of the two distinct isomers.

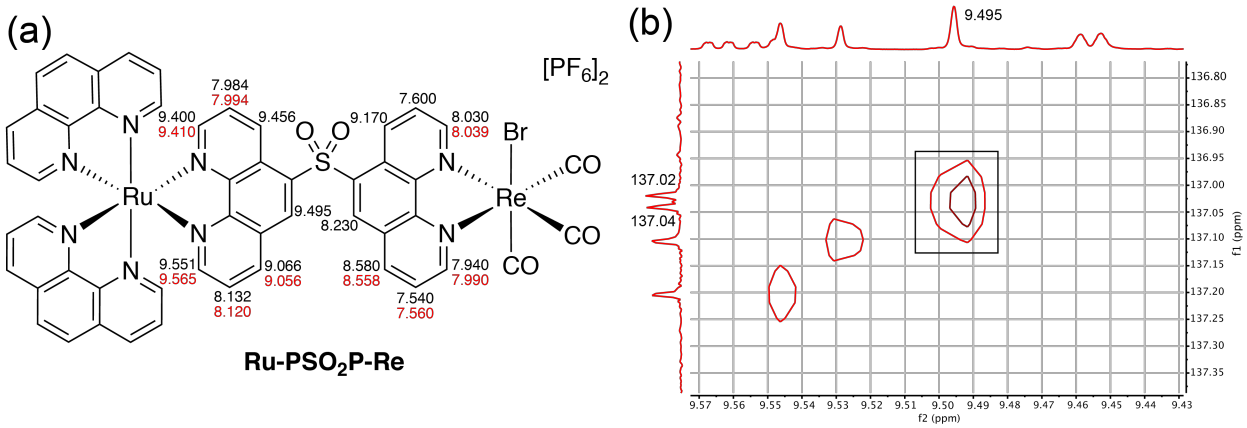

Figure 5-3 (a) ^{1}H NMR shifts for the bridging ligand in **Ru-PSO$_2$P-Re**. Black text designates signals from one diastereotopic species, red text for the other. Chemical shifts with only one number indicates overlapping, indistinguishable species. (b) HSQC NMR spectrum (CD_3CN, 850 MHz, 25 ºC) showing two diastereotopic carbon signals correlating to one broad singlet.

5.4 Electrochemical Properties

The electrochemical behavior of each monometallic and bimetallic species was determined using cyclic voltammetry (CV) and square wave voltammetry (SWV) referenced to a Fc/Fc^{+} standard. CVs were collected at a scan rate of 0.1 Vs^{-1} and a 25 Hz wave form was applied in SWV.

From CV data (Figure 5-4 and Table 5-1), both ruthenium monometallic complexes (**Ru-PSP** and **Ru-PSO$_2$P**) display a quasi-reversible anodic event at ~1.0 V which is consistent with a Ru(II)/Ru(III) couple. Oxidation of the sulfur bridge to **Ru-PSO$_2$P** was found to be accompanied by a +40 mV shift in anodic peak potential with no significant change in ΔE_p and is taken to be a

result of the greater electron-withdrawing character of the sulfone group. The rhenium monometallic species (**Re-PSP** and **Re-PSO$_2$P**) are oxidized irreversibly at potentials between 50 and 100 mV positive of the analogous ruthenium complexes. Sulfur oxidation state appears to impose a greater effect on the Re(I)/Re(II) couple, where the wave was found to shift positively by 100 mV with a change from a sulfide to sulfone bridging group.

The corresponding oxidative wave for the bimetallic species (**Ru-PSP-Re** and **Ru-PSO$_2$P-Re**) occurs at an intermediate potential between the corresponding Ru and Re analogues, and the current response appears as a superposition of the two monometallic complexes. However, the change in peak potential as function of sulfur oxidation state is nearly equivalent to that observed for the Ru subunit.

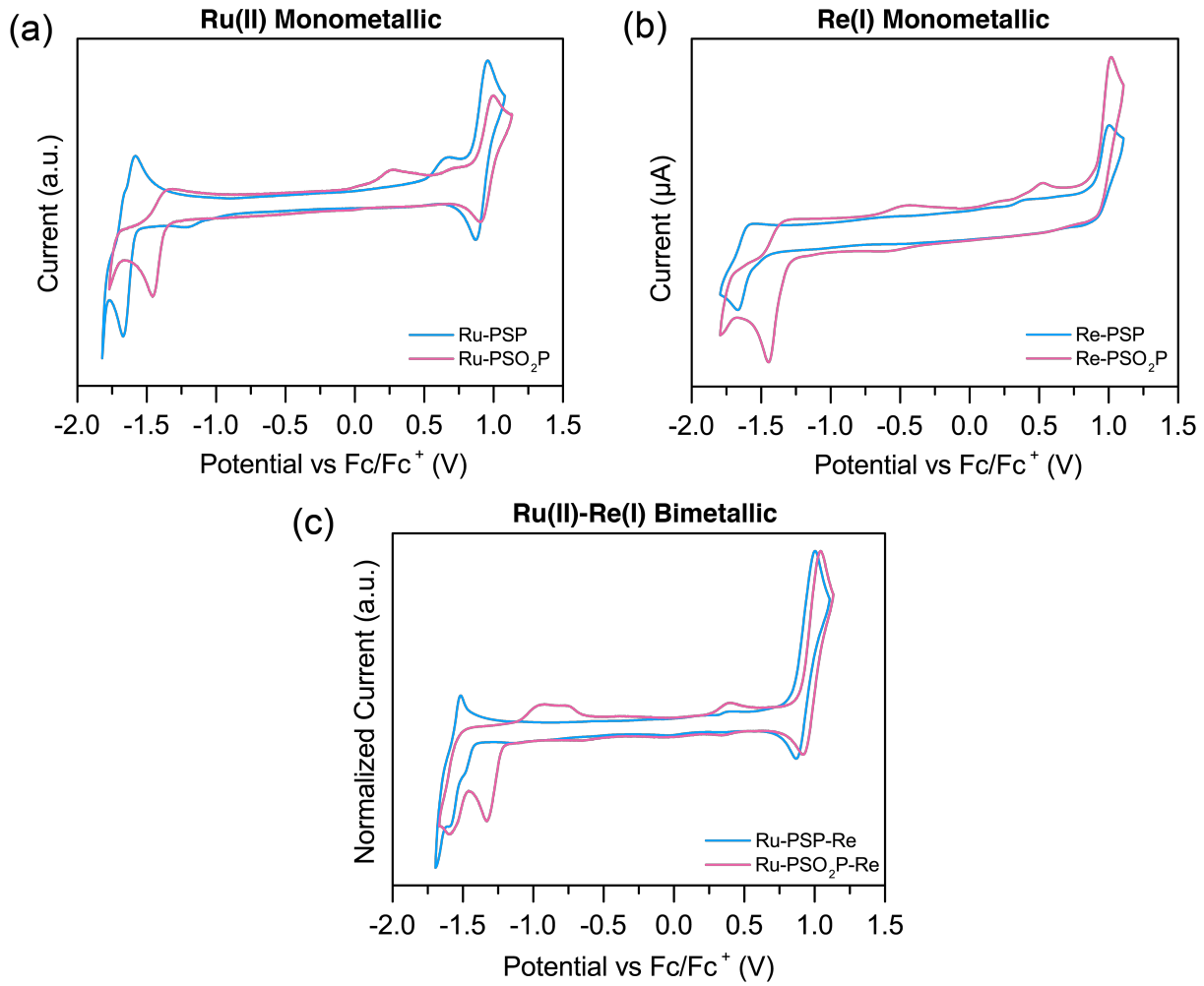

Figure 5-4 Cyclic voltammograms of (a) Ru(II) monometallic complexes; (b) Re(I) monometallic complexes; (c) Ru(II)-Re(I) bimetallic species. All spectra taken in dry, N_2-sparged CH_3CN solutions at room temperature.

Due to overlapping peaks in the CV, the cathodic response from each complex was determined with SWV (Table 5-1). The most positive reduction potential of the monometallic species is generally assigned to a ligand-based reduction and was found to occur at potentials between –1.41 and –1.65 V for these complexes. The separation in peak potential between analogous Re and Ru subunits was found to be much smaller for this wave than the metal-based couples, where E_{pc1} (peak cathodic potential) was found to be less than 12 mV negative for the Ru

complexes. In contrast, oxidation of the sulfur bridge from sulfide to sulfone resulted in a 220 mV negative shift in E_{pc1} for both cases. This result supports the assignment of E_{pc1} to a ligand-based reduction and indicates that the oxidation state of the linking sulfur bears a larger influence on redox properties of the bridging ligand than on the metal center. Additionally, the slightly higher reduction potentials measured for **Re-PSP** (–1.63 V) and **Re-PSO$_2$P** (–1.41 V) suggests that downhill electron transfer can occur from Ru to Re in the dyads, with a limited loss of energy.

Table 5-1 Electrochemical data of Ru and Re mono- and bimetallic species.

	$E_{(ox)}$ [V] [a]	$E_{(red)}$ [V] [b]
Ru-PSP	0.96 [c]	–1.64
Ru-PSO$_2$P	1.00 [c]	–1.42
Re-PSP	1.00 [d]	–1.63
Re-PSO$_2$P	1.11 [d]	–1.41
Ru-PSP-Re	1.00 [c]	–1.56
Ru-PSO$_2$P-Re	1.04 [c]	–1.30

[a] Cyclic voltammetry. [b] Square-wave voltammetry. [c] Quasi-reversible wave. [d] Irreversible wave. All experiments conducted in dry CH_3CN solutions sparged with N_2.

The first reduction event for the S and SO_2 linked bimetallic complexes (**Ru-PSP-Re** and **Ru-PSO$_2$P-Re**) occurred at significantly less negative potentials (–1.56 and –1.30 V, respectively) than that of either of their monometallic analogues, with **Ru-PSO$_2$P-Re** affected to a greater extent. The lower reduction potential for the sulfone species in comparison to the sulfide is due to the additional conjugation in the bridging ligand reducing the π^*-orbital energy of the phenanthroline unit at the rhenium(I).[215] The positive change in E_{p1} between the mono- and

bimetallic bridging ligand may be explained by added electron withdrawing character brought on by coordination to the electropositive Re center.

5.5 Photophysical Properties

5.5.1 Absorption Spectroscopy

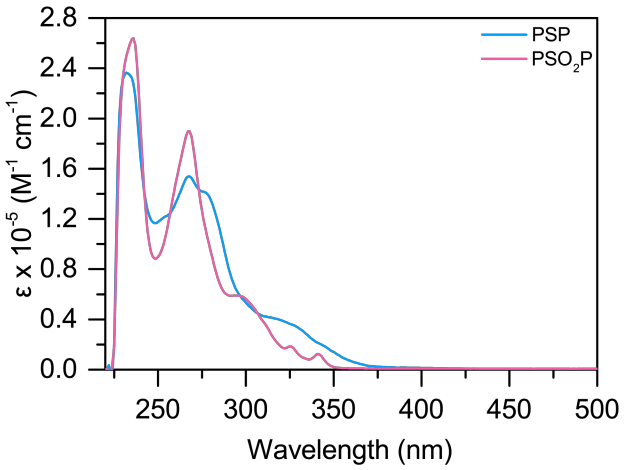

Figure 5-5 Absorption spectra of **PSP** and **PSO₂P** in CH_2Cl_2 solutions at room temperature.

Figure 5-5 shows the UV-vis absorption spectra of pro-ligands **PSP** and **PSO₂P** measured in CH_2Cl_2 at room temperature. Both compounds contain strong features at energies higher than 300 nm are attributed to π–π* transition on the phenanthroline rings, analogous to those observed in 1,10-phenanthroline.[216] Both compounds also exhibit lower energy features tailing to 380 nm and 345 nm for **PSP** and **PSO₂P**, respectively, that are attributed to the introduction of the sulfur bridge. This low energy band is broader for the sulfide relative to the sulfone species. In the sulfide-bridged compound it is possible to achieve multiple conformations about the sulfur leading to differing degrees of interaction between the phenanthroline rings, contributing to a broadness in the band. In the sulfone, however, the absence of lone pairs on the sulfur prevents these interactions

and results in a more structured absorption. This has been seen in calculations of poly-*p*-phenyl sulfide[217] and in oligo- and polythienyl sulfur-bridged compounds by our group.[80]

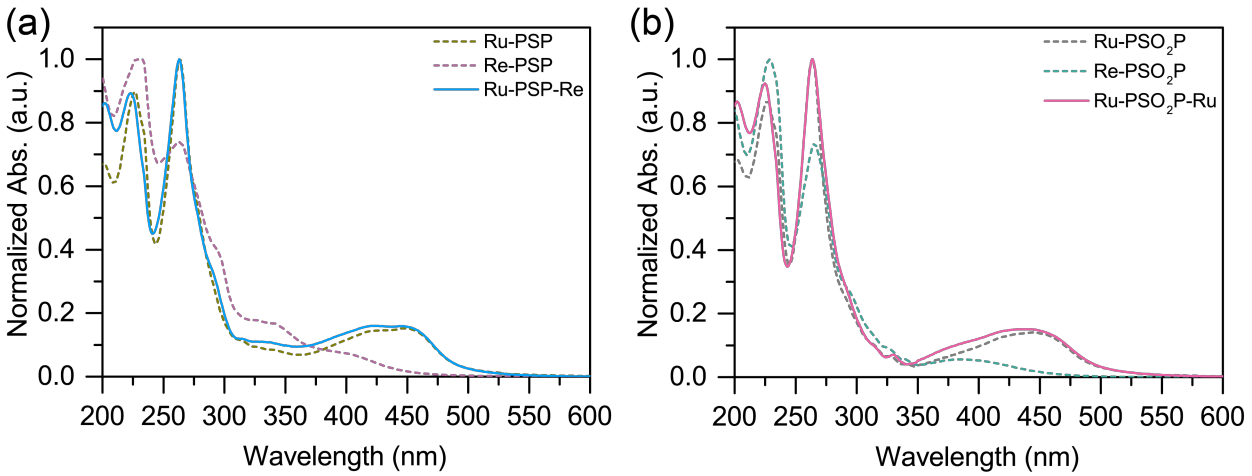

Figure 5-6 Absorption spectra of (a) **Ru-PSP-Re** (blue) and its monometallic model complexes **Ru-PSP** (grey) and **Re-PSP** (purple). (b) **Ru-PSO₂P-Re** (pink) and model complexes **Ru-PSO₂P** (grey) and **Re-PSO₂P** (teal). CH_3CN solutions of concentration ~3×10^{-6} M at room temperature.

Figure 5-6(a) shows the UV-vis absorption spectrum of **Ru-PSP-Re** and its model mononuclear complexes **Ru-PSP** and **Re-PSP**, and Figure 5-6(b) shows **Ru-PSO₂P-Re** and the model species **Ru-PSO₂P** and **Re-PSO₂P**. In both dyads, broad absorptions between 380–500 nm are due to a ^{1}MLCT at the ruthenium, and those between 350–440 nm contain contributions from ^{1}MLCT absorption of both the ruthenium and rhenium metals, however as with other Ru(II)-Re(I) systems the ^{1}MLCT of the Re is often obscured.[209] Strong absorptions from 200–300 nm are due to π–π^* transitions at the diimine ligands.

5.5.2 Photoluminescence Spectroscopy

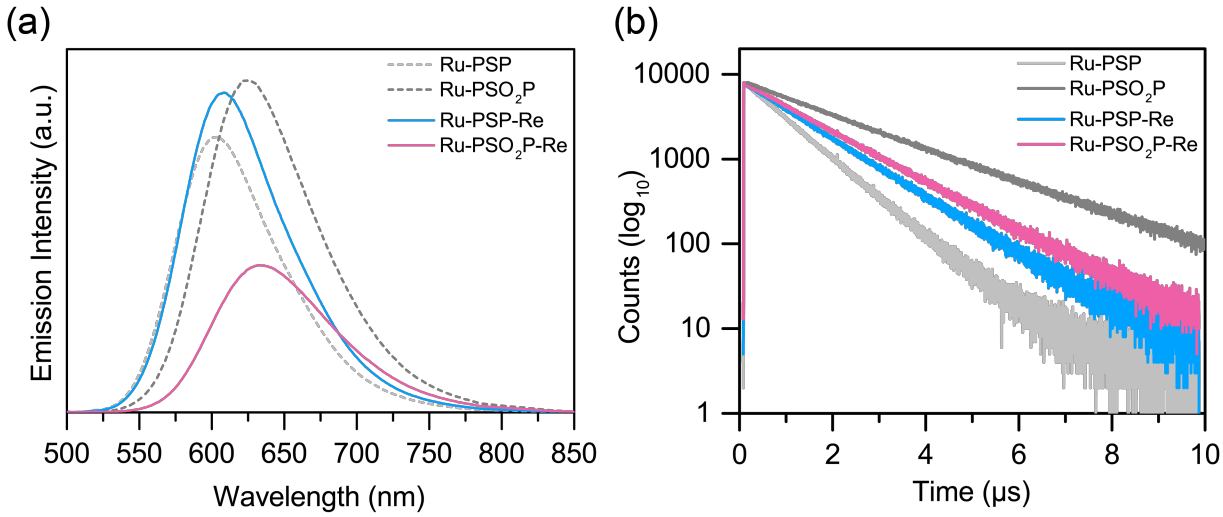

Figure 5-7 (a) Emission spectra of **Ru-PSP** (light grey), **Ru-PSO₂P** (dark grey), **Ru-PSP-Re** (blue) and **Ru-PSO₂P-Re** (pink). Spectra were normalized to the absorbance at the excitation wavelength (λ_{ex} = 450 nm). (b) TCSPC data for Ru-containing monometallic and bimetallic species (λ_{ex} = 453 nm). CH_3CN solutions of concentration ~3 × 10^{-6} M at room temperature.

The photoluminescence spectra of **Ru-PSP-Re**, **Ru-PSO₂P-Re** and their Ru monometallic counterparts were measured in CH_3CN solutions and are shown in Figure 5-7 and presented in Table 5-2(a). Emission spectra were normalized for absorbance at the excitation wavelength (450 nm) Following irradiation, all ruthenium-containing complexes exhibited a broad, featureless emission profile indicative of radiative decay from a Ru-based ^{3}MLCT excited-state.[40] The dyads were each slightly (5–8 nm) red-shifted of their monometallic Ru counterparts indicating that there is a weak electronic interaction between the two metal centers.[210] However, when comparing the two bimetallic species, the emission maximum of **Ru-PSO₂P-Re** was red-shifted 24 nm compared to **Ru-PSP-Re**, which in addition to the quenching of emission intensity, suggests that increasing the oxidation at the sulfur bridge in turn increases the electronic communication between the Ru

and Re centers. While a decrease in excited-state lifetime would be expected in concert with a reduction in emission intensity, in Figure 5-7(b) and Table 5-2 it is shown that τ_{em} increases for **Ru-PSO$_2$P-Re** (1.46 μs) over **Ru-PSP-Re** (1.27 μs). This could be explained by increased delocalization of the excited electron at the sulfone unit compared to the sulfide, as seen in the monometallic Ru species (**Ru-PSP** = 0.93 μs; **Ru-PSO$_2$P** = 2.20 μs).

Table 5-2 Photophysical properties of **Ru-PSP-Re**, **Ru-PSO$_2$P-Re** and their respective monometallic model complexes.[a]

Complex	λ_{max} (nm) [b]	τ_{em} (μs) [c]
Ru-PSP	603	0.93 [d]
Ru-PSO$_2$P	625	2.20 [e]
Ru-PSP-Re	608	1.27 [d]
Ru-PSO$_2$P-Re	632	1.46 [d]

[a] Measured in CH_3CN at 25 ºC. Samples were sparged with Ar for 30 min prior to irradiation and left under a blanket of Ar for the duration of the studies. [b] Excitation wavelength was 450 nm. [c] Excitation wavelength was 453 nm. [d] Collected over a 10 μs time window. [e] Collected over a 20 μs time window.

5.6 Preliminary Photocatalytic Studies

For the photocatalytic reaction, a CH_3CN-triethanolamine (TEOA) (5:1, v/v) solution was prepared containing either **Ru-PSP-Re** or **Ru-PSO$_2$P-Re** (0.05 mM) and BNAH (0.1 M) as the sacrificial reductant. The sample was saturated with CO_2 and irradiated with a 500 nm LED setup (2.7×10^{-8} einstein s^{-1}, FWHM = 30 nm). This emission source was chosen as it selectively excites only the Ru unit, and not into the Re directly.

Ru(II)-Re(I) supramolecular CO_2 photocatalysts typically form CO as the major product, with H_2 and HCOOH as by-products.[208] After irradiation for 24 h, TON_{CO} values were found to

be very low for **Ru-PSP-Re** and **Ru-PSO$_2$P-Re** (0.8 and 0.9, respectively) which was surprising as for both complexes bubbling was observed in the solution during the photocatalysis, to the point of having pressurized the sealed cell after just 1 h. In both studies GC data shows that H_2 is not evolved, and solvent suppressed ^{1}H NMR experiments show that no HCOOH is observed. The GC traces for **Ru-PSP-Re** (Figure 5-8(a)) and **Ru-PSO$_2$P-Re** (Figure 5-8(b)) each show a significant peak overlapping with that for CO_2, however this peak is due to volatized CH_3CN produced during the CO_2 sparging.

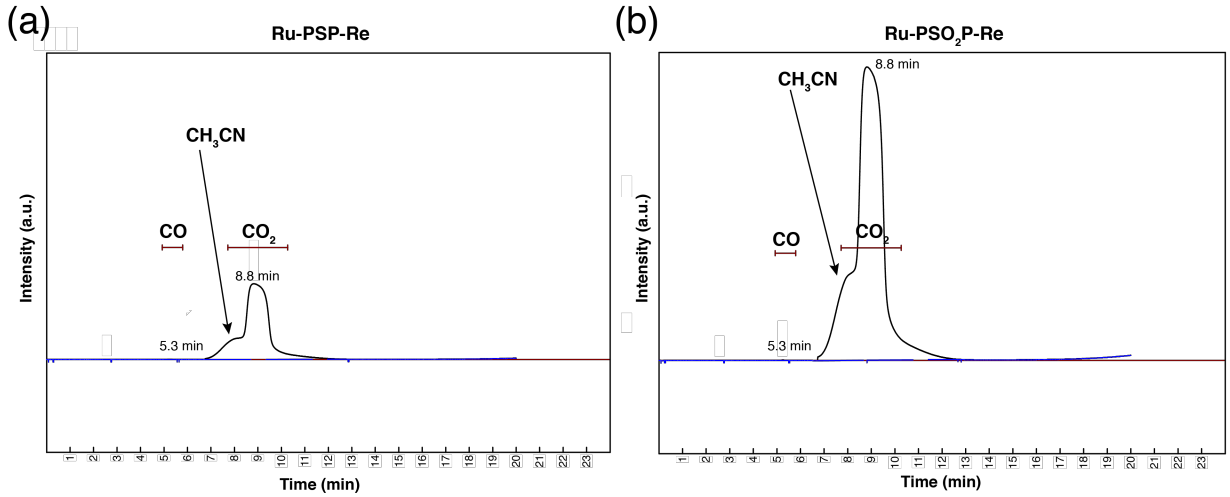

Figure 5-8 Gas chromatograms of (a) **Ru-PSP-Re** and (b) **Ru-PSO$_2$P-Re**.

Further experiments are required to elucidate the gas being evolved. While not seen for Re(I) photocatalyic CO_2 reduction, possible volatile reduction products include methane, ethane and ethylene. Atmospheric mass spectrometry will be employed to give an online detection over a mass range of 0–100 m/z. While a number of gases have the same m/z (CO_2, N_2 and C_2H_6 with m/z = 28), the study will be crucial in monitoring if any sulfur-containing volatiles are produced

from decomposition of the Ru(II)-Re(I) catalyst. Additionally, GC-MS will be conducted for further analysis of the gas produced.

5.7 Conclusions and Future Work

Two new Ru(II)-Re(I) dyads have been synthesized with their metal centers tethered by a sulfur-bridged bisphenanthroline bridging ligand with a view for use as supramolecular photocatalysts for CO_2 reduction. In changing the oxidation state at the sulfur center from sulfide to sulfone it is hoped that the degree of electron transfer from the Ru(II) photosensitizer to the Re(I) catalytic center can be modulated. Electrochemical data indicates that **Ru-PSP-Re** should be the more efficient catalyst of the two due to its lower reduction potential; however, photophysical data suggests **Ru-PSO$_2$P-Re** has a greater degree of electronic communication between the two metals due to a red-shift and quenching of emission observed in the photoluminescence spectra.

Preliminary photocatalytic data show that both complexes show poor efficiency for generation of CO with $TON_{CO} < 1$. GC and solvent suppression ^{1}H NMR data show that neither H_2 nor HCOOH are produced as by-products, but a substantial peak overlapping with the CO_2 signal is seen in the GC trace, corresponding to an unidentified compound. Further studies involving atmospheric-MS and GC-MS must be performed in order to elucidate the unknown volatile species.

5.8 Experimental Details

5.8.1 General

All experiments were conducted under air unless otherwise stated. Solvents used for synthesis were of reagent grade and were used without any further purification. HPLC grade solvents were used for spectroscopic studies. Microwave reactions were performed in a Biotage Initiator 2.5 microwave synthesizer. 5,6-epoxy-5,6-dihydro-[1,10]-phenanthroline, ruthenium(III) chloride and 30% H_2O_2 solutions were purchased from Sigma-Aldrich. Niobium carbide was purchased from Alfa Aesar. All reagents were used as received. *cis*-Ru(phen)$_2$Cl$_2$ was prepared as per the literature.[213]

5.8.2 Spectroscopy

^{1}H, ^{13}C{^{1}H}, COSY, ROESY, HSQC and HMBC NMR spectra were collected using Bruker NMR spectrometers and referenced first to TMS and then to the residual protonated solvent peak. Pro-ligand spectra were collected on a Bruker AV-400 spectrometer, spectra of the monometallic species on a Bruker AV-600 spectrometer, and spectra of the mixed-metal systems on a Bruker AV-850 spectrometer. NMR solvents (from Aldrich) were used as received. Electrospray ionization mass spectrometry data was obtained using a Bruker Esquire LC ion trap mass spectrometer. Infrared spectroscopy was performed on an attenuated total reflection (ATR) crystal using a Perkin-Elmer Frontier FT-IR spectrometer. UV-vis absorption spectra were recorded on a Varian-Cary 5000 UV-Vis-near-IR spectrophotometer. Fluorescence data were collected on a Photon Technology International (PTI) QuantaMaster 50 fluorimeter fitted with an integrating sphere, double excitation monochrometer and utilizing a 75 W Xe arc lamp as the source. Emission lifetime data were collected using a Horiba Yvon Fluorocube TCSPC apparatus.

A 453 nm NanoLED was used as the excitation source, pulsing at a repetition rate of 100 kHz. Broadband emission was monitored by a CCD detector at wavelengths >550 nm using a low pass filter. Data were fitted using the DAS6 Data Analysis software package. Sample solutions were first sparged with Ar for 30 min and then maintained under a blanket of Ar for the duration of the measurements in 1 cm^2 quartz cells (Starna Cells) fitted with a rubber septum.

5.8.3 Electrochemistry

All electrochemical measurements were performed using a Metrohm Autolab PGSTAT12 in an air tight single compartment cell with the use of an $Ag/AgNO_3$ pseudo reference electrode. A 7 mm^2 glassy carbon disc and a platinum mesh were used as the working and counter electrodes, respectively. Each experiment was referenced to a Fc/Fc^+ couple and carried out in a N_2 sparged CH_3CN solution with analytically pure 0.1 M *n*-Bu_4NPF_6 as the supporting electrolyte. The working electrode was regenerated and cleaned between measurements by polishing with alumina paste and sonicating in H_2O and acetone, successively. Measurements were performed at a 1 mM concentration of analyte except in the case of the Re monometallic species which were run at lower concentration due to limited solubilities in acetonitrile.

5.8.4 Photocatalytic Setup

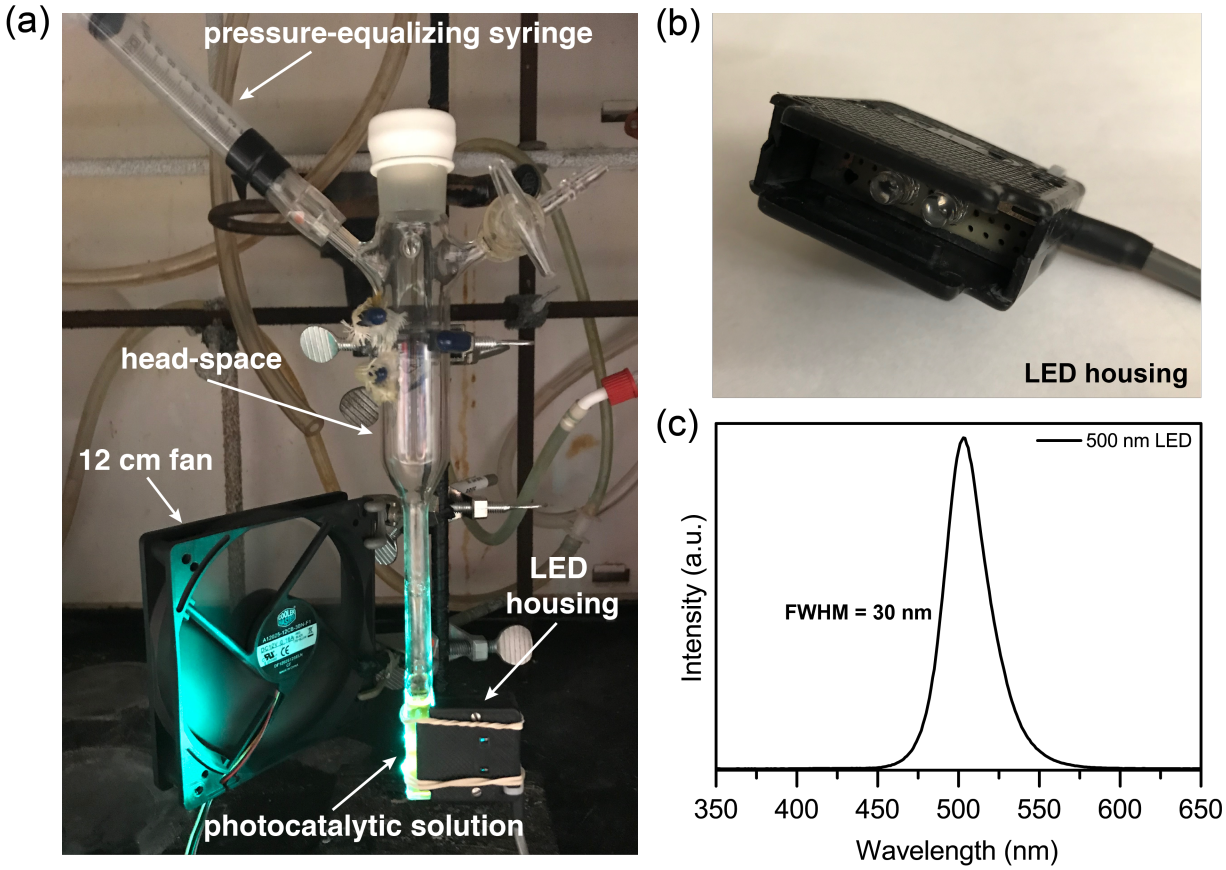

Figure 5-9 (a) Photocatalytic setup under irradiation. (b) LED housing used for photocatalytic experiments. (c) Emission profile of the LED source (peak wavelength = 503 nm, FWHM = 30 nm).

Figure 5-9(a) shows the photocatalytic setup used, consisting of a custom-made housing (Figure 5-9(b)) utilizing two LUMEX "Emerald Green" LEDs (SSL-LX5095UEGC, peak wavelength = 503 nm, FWHM = 30 nm, Figure 5-9(c)) wired in series and driven by an AC adaptor (YHi 898-1015-U12S) giving a continuous DC supply of 12.31 V. The housing was attached to a borosilicate cuvette (0.8 cm pathlength) which itself is fused to a Schlenk flask giving a total volume of 74 mL, from which headspace analysis could be conducted. During photocatalysis a 12 cm fan (CoolerMaster A12025-12CB-3BN-F1) running with an input of 9 V was used to maintain

cuvette temperature. A discussion on the determination of the incident light intensity using an Aberchrome 670 actinometer can be found in Chapter 6:Listing D.1.

5.8.5 Synthesis

di(1,10-phenanthrolin-5-yl)sulfane (PSP)

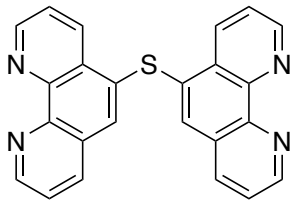

While under an N_2 atmosphere, a solution of Li_2S (0.591 g, 12.8 mmol, 1.2 eq.) in *tert*-butanol (250 mL) was added dropwise to a suspension of 5,6-epoxy-5,6-dihydro-[1,10]-phenanthroline (2.10 g, 10.7 mmol, 1.0 eq.) in *tert*-butanol (60 mL) at 60 ºC over a 40 minute period. The reaction was monitored by TLC (silica gel; EtOAc:MeOH:NH_4OH 10:1:0.5) and subsequently stirred for 18 h at 60 ºC, following which the solvent was removed under reduced pressure and the crude product dissolved in $CHCl_3$ (300 mL) and washed with sat. NH_4Cl (40 mL). The aqueous layer was then further extracted with $CHCl_3$ (3 × 100 mL) and the combined organics washed with brine (2 × 100 mL). The organic layer was dried with $MgSO_4$, filtered and the solvent removed *in vacuo*. The resulting crude solid was recrystallized from MeOH:H_2O (2:1) giving off-white needles (2.72 g, 6.95 mmol, 65%). The spectroscopic and spectrometric data matches that of the literature.[212] ^{1}H NMR (400 MHz, $CDCl_3$) δ 9.30 (dd, J = 4.4, 1.6 Hz, 2H), 9.23 (dd, J = 4.4, 1.7 Hz, 2H), 8.79 (dd, J = 8.4, 1.6 Hz, 2H), 8.05 (dd, J = 8.2, 1.7 Hz, 2H), 7.74 – 7.68 (m, 4H), 7.64 (dd, J = 8.1, 4.4 Hz, 2H). HR-ESI MS: *m/z* calcd. for $C_{24}H_{15}N_4S$: 391.1017; Found: 391.1015 $[M+H]^+$.

5,5´-sulfonylbis(1,10-pheananthroline) (PSO_2P)

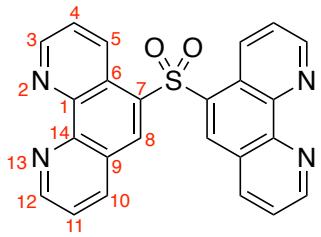

To EtOH (50 mL) was added **PSP** (0.496 g, 1.27 mmol, 1.0 eq.), NbC (0.033 g, 0.320 mmol, 0.25 eq.) and 30% H_2O_2 solution (1.90 mL, 19.1 mmol, 15.0 eq.). The reaction mixture was then heated to 60 ºC for 18 h. After cooling to room temperature, sat. $Na_2S_2O_3$ solution (25 mL) was added, followed by H_2O (75 mL), forming a white precipitate which was extracted with EtOAc (3 × 30 mL). The combined organics were washed with H_2O (30 mL) and brine (30 mL), dried over $MgSO_4$, filtered and the solvent removed under reduced pressure to give a white solid that required no further purification (0.510 g, 1.21 mmol, 95%). ^{1}H NMR (400 MHz, $CDCl_3$*d*) δ 9.37 (dd, *J* = 4.4, 1.7 Hz, 2H, H_3), 9.21 (dd, *J* = 4.3, 1.6 Hz, 2H, H_{12}), 9.05 (dd, *J* = 8.6, 1.6 Hz, 2H, H_{10}), 8.90 (s, 2H, H_8), 8.46 (dd, *J* = 8.1, 1.7 Hz, 2H, H_5), 7.81 (dd, *J* = 8.1, 4.4 Hz, 2H, H_4), 7.63 (dd, *J* = 8.6, 4.3 Hz, 2H, H_{11}). ^{13}C{^{1}H} NMR (101 MHz, $CDCl_3$) δ 153.86 (C_3), 151.37 (C_{12}), 148.14 (C_1), 146.58 (C_{14}), 138.00 (C_5), 134.83 (C_8), 133.06 (C_{10}), 131.98 (C_7), 125.94 (C_6), 124.41 (C_4), 123.80 (C_{11}), 123.59 (C_9). IR (neat): $\tilde{\nu}$ (σ SO_2) 1288 and 1126 cm^{-1}. HR-EI MS: *m/z* calcd. for $C_{24}H_{14}N_4O_2S$: 422.0837; Found: 422.0834 [M]$^+$.

[Ru(phen)$_2$(PSP)][PF$_6$]$_2$ (Ru-PSP)

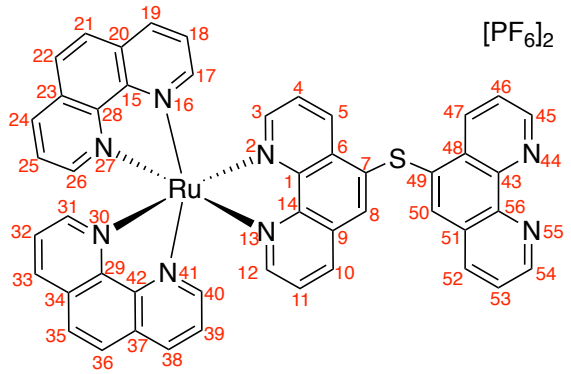

To a microwave vial was added Ru(phen)$_2$Cl$_2$ (0.470 g, 0.883 mmol, 1.0 eq.), and **PSP** (0.383 g, 0.981 mmol, 1.11 eq.) and ethylene glycol (11 mL). The suspension was reacted in a microwave for 40 min at 200 ºC and cooled to room temperature, following which the solvent was diluted with H_2O

(80 mL) and NH_4PF_6 added to precipitate the crude compound. The resulting orange precipitate was filtered and washed with H_2O and Et_2O and then purified over silica gel (F60) using CH_3CN:H_2O:KNO_3 (aq.) (88:8:10) as the eluting solvent. The first major orange band was collected. After an ion exchange with NH_4PF_6 the pure product was isolated as an orange solid (0.439 g, 0.385 mmol, 44%). ^{1}H NMR (600 MHz, CD_3CN) δ 9.20 (dd, *J* = 4.3, 1.7 Hz, 1H, H_{12}), 9.18 (dd, *J* = 4.4, 1.6 Hz, 1H, H_3), 8.97 (dd, *J* = 8.5, 1.2 Hz, 1H, H_{47}), 8.74 (dd, *J* = 8.2, 1.7 Hz, 1H, H_5), 8.59 (tdd, *J* = 15.9, 8.3, 1.3 Hz, 4H, $H_{19,24,33,38}$), 8.37 (dd, *J* = 8.0, 1.7 Hz, 1H, H_{10}), 8.35 (s, 1H, H_8), 8.26 (d, *J* = 0.7 Hz, 2H, $H_{35,36}$), 8.23 (d, *J* = 2.1 Hz, 2H, $H_{21,22}$), 8.12 (dd, *J* = 8.4, 1.2 Hz, 1H, H_{52}), 8.09 (dd, *J* = 5.3, 1.2 Hz, 1H, H_{45}), 8.07 (dd, *J* = 5.2, 1.3 Hz, 1H, H_{17}), 8.04 (dd, *J* = 5.2, 1.2 Hz, 1H, H_{40}), 8.01 (dd, *J* = 5.2, 1.3 Hz, 1H, H_{31}), 7.98 (dd, *J* = 5.4, 1.3 Hz, 1H, H_{26}), 7.90 (dd, *J* = 5.3, 1.3 Hz, 1H, H_{54}), 7.78 (dd, *J* = 8.1, 4.3 Hz, 1H, H_{11}), 7.72 – 7.64 (m, 5H, $H_{4,18,39,46,50}$), 7.62 (dd, *J* = 8.2, 5.2 Hz, 1H, H_{32}), 7.59 (dd, *J* = 8.2, 5.3 Hz, 1H, H_{25}), 7.42 (dd, *J* = 8.4, 5.2 Hz, 1H, H_{53}). ^{13}C{^{1}H} NMR (151 MHz, CD_3CN) δ 154.47 (C_{45}), 154.10 (C_{40}), 154.04 (C_{17}), 153.92 (C_{31}), 153.86 (C_{26}), 153.45 (C_{54}), 152.41 (C_{12}), 151.61 (C_3), 149.38 (C_{43}), 148.81 ($C_{15,28,29,42}$), 148.11 ($C_{1,56}$), 147.79 (C_{14}), 137.78 ($C_{19,24,33,38}$), 137.22 (C_{10}), 136.56 (C_8), 136.41 (C_{52}), 134.82 (C_5), 134.40 (C_{47}), 131.95 ($C_{20,23,34,37}$), 131.58 (C_{51}), 130.48 (C_{49}), 129.60 (C_9), 129.18 ($C_{6,48}$), 129.01 ($C_{35,36}$), 128.98 ($C_{21,22}$), 127.55 (C_{50}), 127.43 (C_7), 127.13 (C_{53}), 126.95 (C_{46}), 126.83 ($C_{18,39}$), 126.80 ($C_{25,32}$), 124.90 (C_{11}), 124.76 (C_4). MALDI-TOF MS: *m/z* calcd. for $C_{48}H_{30}F_6N_8PRuS$: 991.1028; Found: 991.1032 $[M–PF_6]^+$.

[Ru(phen)$_2$(PSO$_2$P)][PF$_6$]$_2$ (Ru-PSO$_2$P)

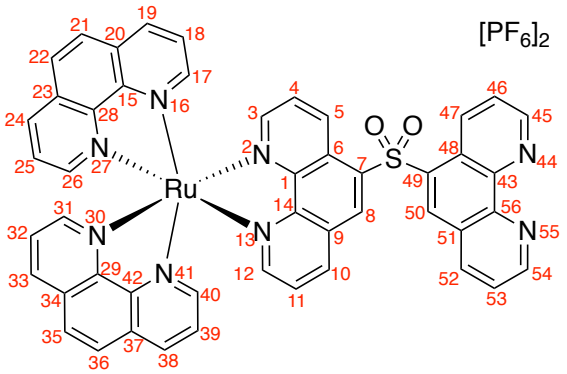

Ru(phen)$_2$Cl$_2$ (0.284 g, 0.533 mmol, 1.0 eq.) and **PSO$_2$P** (0.250 g, 0.591 mmol, 1.1 eq.) and ethylene glycol (15 mL) were heated in a microwave at 200 ºC for 40 min. The reaction was cooled to room temperature and the ethylene glycol diluted with H_2O (80 mL). NH_4PF_6 was added to a stirred solution of the reaction mixture, following which the precipitate was filtered and washed with H_2O and Et_2O. The crude product was purified over a silica gel column (F60) using CH_3CN:H_2O:KNO_3 (aq.) (88:8:10) as the eluting solvent where the first major orange band was collected, which after anion exchange with NH_4PF_6 yielded the pure complex as an orange powder (0.130 g, 0.111 mmol, 21%). ^{1}H NMR (600 MHz, CD_3CN) δ 9.39 (s, 1H, H_8), 9.25 (d, J = 4.4 Hz, 2H, $H_{50,54}$), 9.19 (dd, J = 8.8, 1.2 Hz, 1H, H_{47}), 9.14 – 9.11 (m, 2H, $H_{3,5}$), 8.81 (dd, J = 8.3, 1.3 Hz, 1H, H_{10}), 8.72 (dd, J = 8.2, 1.8 Hz, 1H, H_{52}), 8.60 – 8.52 (m, 4H, $H_{19,24,32,38}$), 8.22 (s, 2H, $H_{21,36}$), 8.20 (s, 2H, $H_{22,35}$), 8.14 (dd, J = 5.4, 1.3 Hz, 1H, H_{12}), 7.99 (dd, J = 5.4, 1.2 Hz, 1H, H_{45}), 7.93 (ddd, J = 6.9, 5.2, 1.3 Hz, 3H, $H_{17,31,40}$), 7.91 (dd, J = 5.3, 1.3 Hz, 1H, H_{26}), 7.87 (dd, J = 8.1, 4.3 Hz, 1H), H_{53}, 7.71 (m, 2H, $H_{4,11}$), 7.59 (dd, J = 8.4, 5.4 Hz, 1H, H_{39}), 7.57 – 7.53 (m, 3H, $H_{25,32,46}$), 7.51 (dd, J = 8.3, 5.2 Hz, 1H, H_{18}). ^{13}C{^{1}H} NMR (151 MHz, CD_3CN) δ 156.95 (C_{12}), 154.90 (C_{45}), 154.70 (C_{54}), 154.21 (C_{17}), 154.19 (C_{40}), 153.86 (C_{31}), 153.77 (C_{26}), 151.85 (C_3), 151.14 (C_{14}), 149.87 (C_{43}), 148.92 (C_{56}), 148.70 ($C_{15,42}$), 148.64 ($C_{28,29}$), 147.33 (C_1), 139.70 (C_{52}), 139.31 (C_{10}), 137.91 ($C_{19,38}$), 137.88 (C_{24}), 137.85 (C_{33}), 137.73 (C_{49}), 135.00 (C_{50}), 134.56 (C_{47}), 134.40 (C_8), 134.05 (C_5), 131.96 ($C_{30,37}$), 131.90 ($C_{23,34}$), 129.61 (C_9), 128.99 ($C_{21,36}$), 128.97 ($C_{22,35}$), 127.84 (C_{11}), 127.39 (C_{46}), 127.25 (C_{48}), 127.19 (C_{51}), 126.82 (C_{32}), 126.80 (C_{25}), 126.69 (C_{34}), 126.66 (C_{18}),

125.46 (C_{53}), 124.83 (C_4), 124.41 (C_7). IR (neat): $\tilde{\nu}$ (σ SO_2) 1312 and 1136 cm^{-1}. MALDI-TOF MS: *m/z* calcd. for $C_{48}H_{30}F_6N_8O_2PRuS$: 1023.0930; Found: 1023.0928 $[M–PF_6]^+$.

Re(PSP)(CO)$_3$Br (Re-PSP)

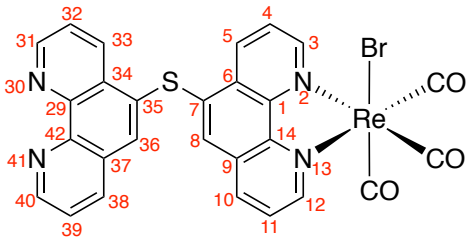

PSP (0.231 g, 0.599 mmol, 1.32 eq.) was dissolved in refluxing MeOH (250 mL), to which $Re(CO)_5Br$ (0.185 g, 0.455 mmol, 1.0 eq.) in 90 mL MeOH was added dropwise. The solution left to reflux for 18 h in the dark, following which the reaction mixture was cooled to room temperature and the solvent removed *via* rotary evaporation. The crude powder was purified using column chromatography (silica, F60) first using CH_3CN, followed by 98:2 CH_2Cl_2:MeOH, giving a yellow solid. (0.149 g, 0.201 mmol, 44%). ^1H NMR (600 MHz, $CDCl_3$) δ 9.50 (ddd, J = 8.3, 5.1, 1.3 Hz, 1H, H_3), 9.33 (dd, J = 4.4, 1.7 Hz, 1H, H_{12}), 9.30 (dd, J = 4.3, 1.6 Hz, 1H, H_{31}), 9.27 (ddd, J = 7.1, 5.0, 1.4 Hz, 1H, H_{40}), 9.07 (ddd, J = 8.5, 5.6, 1.4 Hz, 1H, H_5), 8.69 (ddd, J = 8.4, 6.7, 1.7 Hz, 1H, H_{33}), 8.29 (dd, J = 8.1, 1.7 Hz, 1H, H_{10}), 8.25 (s, 1H, H_8), 8.05 (td, J = 8.4, 1.4 Hz, 1H, H_{38}), 7.98 (ddd, J = 8.4, 5.1, 3.2 Hz, 1H, H_4), 7.75 (dd, J = 8.0, 4.4 Hz, 1H, H_{11}), 7.70 (ddd, J = 8.4, 6.0, 4.5 Hz, 2H, $H_{32,39}$), 7.24 (s, 1H, H_{36}). $^{13}C\{^1H\}$ NMR (151 MHz, $CDCl_3$) δ 153.86 (C_3), 152.83 (C_{40}), 152.08 (C_{12}), 151.54 (C_{31}), 147.44 (C_1), 146.82 (C_{14}), 146.70 (C_{29}), 146.06 (C_{38}), 136.83 (C_{42}), 136.66 (C_{10}), 136.11 (C_8), 134.90 (C_3), 134.24 (C_{33}), 130.42 (C_{37}), 129.49 (C_7), 128.44 (C_{35}), 128.41 (C_9), 126.36 (C_{39}), 126.10 (C_4), 125.28 (C_{3g}), 124.44 (C_{31}), 124.20 (C_{11}). IR (neat): $\tilde{\nu}$ (σ CO) 2019, 1884 and 1866 cm^{-1}. HR-EI MS: *m/z* calcd. for $C_{27}H_{15}BrN_4O_3ReS$: 738.9578; Found: 738.9575 $[M]^+$.

Re(PSO$_2$P)(CO)$_3$Br (Re-PSO$_2$P)

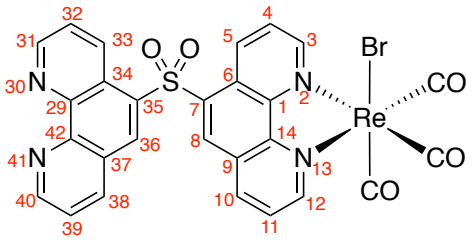

To a MeOH (250 mL) solution heated to reflux of **PSO$_2$P** (0.239 g, 0.566 mmol, 1.48 eq.) was added dropwise a MeOH (90 mL) solution of Re(CO)$_5$Br (0.155 g, 0.382 mmol, 1.0 eq.). The reaction was heated at reflux for 18 h in the absence of light, following which the solution was cooled to room temperature and the solvent removed *in vacuo*. The crude solid was then purified over silica gel (F60) using first CH_3CN followed by 98:2 CH_2Cl_2:MeOH as the eluting solvents, yielding an orange powder. (0.145 g, 0.188 mmol, 49%). ^{1}H NMR (600 MHz, $CDCl_3$) δ 9.53 (ddd, J = 8.6, 5.2, 1.4 Hz, 1H, H_{12}), 9.48 – 9.44 (m, 1H, H_3), 9.43 – 9.39 (m, 2H, $H_{5,40}$), 9.28 (dd, J = 4.3, 1.6 Hz, 1H, H_{31}), 9.04 (ddd, J = 8.6, 3.4, 1.6 Hz, 1H, H_{33}), 8.97 (d, J = 2.3 Hz, 1H, H_{36}), 8.81 (d, J = 1.3 Hz, 1H, H_8), 8.65 (ddd, J = 8.2, 6.3, 1.4 Hz, 1H, H_{10}), 8.53 (dt, J = 8.2, 1.8 Hz, 1H, H_{38}), 7.98 (ddd, J = 8.4, 5.1, 3.7 Hz, 1H, H_{11}), 7.92 (ddd, J = 8.7, 5.1, 4.0 Hz, 1H, H_4), 7.85 (dd, J = 8.1, 4.4 Hz, 1H, H_{39}), 7.72 (ddd, J = 8.6, 4.3, 1.5 Hz, 1H, H_{32}). ^{13}C{^{1}H} NMR (151 MHz, $CDCl_3$) δ 156.07 (C_{12}), 154.47 (C_{40}), 154.43 (C_3), 151.82 (C_{31}), 148.83 (C_{14}), 148.26 (C_{42}), 147.73 (C_1), 139.59 (C_{10}), 138.43 (C_{38}), 137.68 (C_7), 135.71 (C_5), 133.36 (C_{36}), 133.29 (C_{33}), 133.16 (C_{35}), 131.22 (C_8), 128.24 (C_9), 127.11 (C_{11}), 126.80 (C_4), 126.37 (C_6), 125.97 (C_{37}), 124.81 (C_{39}), 124.38 (C_{32}), 123.64 (C_{34}). IR (neat): $\tilde{\nu}$ (σ SO_2) 1304 and 1126 cm^{-1}; $\tilde{\nu}$ (σ CO) 2016, 1884 and 1865 cm^{-1}. HR-EI MS: *m/z* calcd. for $C_{27}H_{15}BrN_4O_5ReS$: 770.9476; Found: 770.9484 [M]$^+$.

[Ru(phen)$_2$(PSP)Re(CO)$_3$Br][PF$_6$]$_2$ (Ru-PSP-Re)

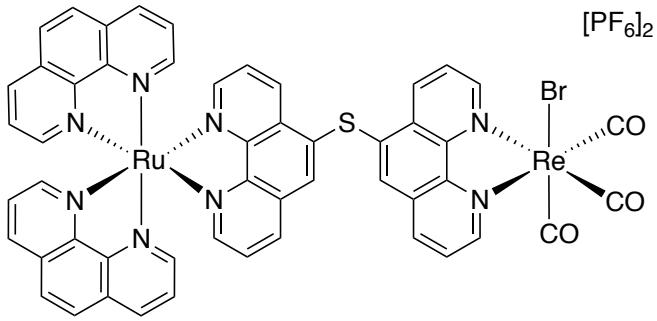

A round-bottomed flask was charged with **Ru-PSP** (0.426 g, 0.373 mmol, 1.0 eq.) and Re(CO)$_5$Br (0.181 g, 0.448 mmol, 1.2 eq.) and placed under an N_2 atmosphere. A 9:1 MeOH:EtOH (500 mL) solution was added and the reaction mixture refluxed for 18 h in the dark then cooled to room temperature, following which the solvent was removed *in vacuo*. The crude product was purified over silica gel (F60) with a CH_3CN:H_2O:KNO_3 (aq.) (95:5:5) solvent system. The nitrate salt of the complex underwent a salt metathesis with NH_4PF_6 and was filtered, yielding an orange powder. (0.466 g, 0.299 mmol, 80%). ^{1}H NMR (850 MHz, CD_3CN) δ 9.49 (dddd, *J* = 16.1, 10.8, 5.0, 1.3 Hz, 2H), 9.43 (dddd, *J* = 11.6, 8.0, 5.0, 1.4 Hz, 2H), 9.19 – 9.06 (m, 2H), 8.96 – 8.89 (m, 2H), 8.70 – 8.52 (m, 11H), 8.37 – 8.25 (m, 10H), 8.21 (s, 1H), 8.19 (s, 1H), 8.14 – 8.07 (m, 7H), 8.05 – 7.96 (m, 10H), 7.72 – 7.68 (m, 4H), 7.68 – 7.62 (m, 6H), 7.57 (dddd, *J* = 14.2, 9.3, 5.6, 1.2 Hz, 2H). ^{13}C{^{1}H} NMR (214 MHz, CD_3CN) δ 156.28, 156.27, 155.11, 155.10, 155.02, 154.95, 154.93, 154.87, 154.73, 154.68, 154.66, 149.81, 149.75, 149.08, 148.88, 148.87, 148.86, 148.85, 148.66, 148.63, 148.62, 148.27, 148.25, 147.91, 147.85, 147.83, 140.56, 140.53, 139.60, 139.57, 139.52, 139.47, 138.50, 138.48, 137.89, 137.88, 137.86, 137.85, 137.84, 137.52, 137.47, 137.44, 137.38, 136.98, 136.90, 136.88, 135.05, 134.96, 134.87, 133.83, 133.77, 133.75, 133.69, 133.64, 133.61, 133.36, 133.29, 133.28, 133.22, 133.16, 132.68, 132.59, 132.53, 132.45, 132.42, 132.38, 132.19, 132.16, 132.07, 132.06, 132.04, 132.02, 132.01, 131.69, 131.59, 131.56, 131.51, 131.49, 131.45, 131.43, 131.29, 131.21, 131.16, 131.08, 130.92, 129.10, 129.08, 129.05, 128.20, 128.20, 128.10, 128.09, 127.78, 127.75, 127.72, 127.66, 127.64, 127.63, 127.60, 127.41, 127.39, 127.37, 127.28, 127.26, 127.24, 126.91,

126.90, 126.88, 126.85. IR (neat): $\tilde{\nu}$ (σ CO) 2022, 1913 and 1894 cm^{-1}. MALDI-TOF MS: *m/z* calcd. for $C_{51}H_{30}BrF_6N_8O_3PRuReS$: 1346.9588; Found: 1346.9583 $[M–PF_6]^+$.

$[Ru(phen)_2(PSO_2P)Re(CO)_3Br][PF_6]_2$ (Ru-PSO$_2$P-Re)

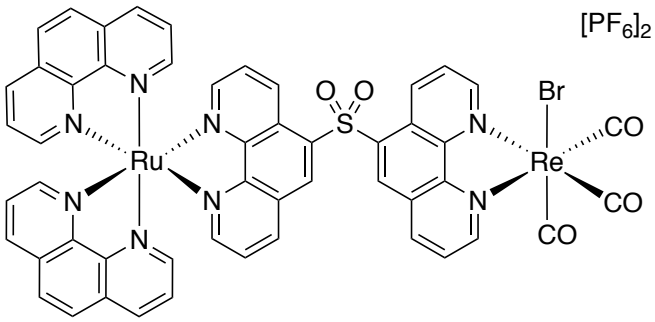

Under an N_2 atmosphere, and in the absence of light, **Ru-PSO$_2$P** (0.127 g, 0.108 mmol, 1.0 eq.) and $Re(CO)_5Br$ (0.053 g, 0.130 mmol, 1.2 eq.) were heated to reflux for 18 h in a 9:1 MeOH:EtOH (500 mL) solution. Following cooling, the solvents were removed under reduced pressure and the crude residue purified using column chromatography over silica gel (F60) with CH_3CN:H_2O:KNO_3 (aq.) (95:5:5) as the eluting solvent. The product was converted to the hexafluorophosphate salt through addition of NH_4PF_6 (aq.) and then filtered, yielding an orange solid. (0.129 g, 0.105 mmol, 97%). ^{1}H NMR (850 MHz, CD_3CN) δ 9.56 (dt, *J* = 5.2, 0.9 Hz, 1H), 9.56 – 9.54 (m, 2H), 9.53 (s, 1H), 9.50 (s, 2H), 9.46 (dt, *J* = 5.1, 1.0 Hz, 2H), 9.40 (tt, *J* = 7.7, 1.1 Hz, 2H), 9.17 (dt, *J* = 8.9, 0.9 Hz, 2H), 9.06 (td, *J* = 8.7, 1.4 Hz, 2H), 8.88 (dt, *J* = 8.4, 1.6 Hz, 2H), 8.62 – 8.60 (m, 3H), 8.58 (dddd, *J* = 6.6, 4.7, 3.3, 1.1 Hz, 4H), 8.57 – 8.55 (m, 1H), 8.26 (d, *J* = 0.6 Hz, 2H), 8.25 (s, 2H), 8.23 (d, *J* = 0.8 Hz, 2H), 8.22 – 8.18 (m, 4H), 8.14 – 8.13 (m, 1H), 8.13 – 8.11 (m, 1H), 8.03 (ddd, *J* = 7.0, 5.2, 1.1 Hz, 2H), 8.01 – 7.98 (m, 3H), 7.97 (td, *J* = 5.3, 1.5 Hz, 3H), 7.95 – 7.93 (m, 4H), 7.77 (d, *J* = 5.5 Hz, 1H), 7.76 (d, *J* = 5.4 Hz, 1H), 7.64 – 7.59 (m, 7H), 7.59 – 7.57 (m, 1H), 7.57 – 7.55 (m, 1H), 7.55 – 7.53 (m, 1H). $^{13}C\{^1H\}$ NMR (214 MHz, CD_3CN) δ 159.32, 158.88, 157.06, 157.05, 156.70, 156.68, 155.88, 155.85, 155.81, 155.77, 155.53, 155.49, 155.46, 155.45, 153.10, 153.07, 151.62, 151.43, 150.37, 150.35, 150.34, 150.32, 150.31, 150.29, 150.15, 143.84, 143.80,

141.15, 139.65, 139.62, 139.59, 139.58, 139.55, 139.54, 138.57, 138.55, 138.51, 138.50, 138.44, 138.06, 138.05, 137.21, 137.10, 137.04, 137.02, 136.12, 136.04, 135.99, 133.65, 133.63, 133.62, 133.58, 131.31, 131.29, 131.06, 131.04, 130.67, 130.66, 130.63, 130.57, 129.98, 129.95, 129.61, 129.59, 129.56, 129.54, 129.26, 129.20, 128.85, 128.84, 128.71, 128.67, 128.50, 128.48, 128.47, 128.38, 128.37, 128.32, 128.28. IR (neat): $\tilde{\nu}$ (σ SO_2) 1322 and 1140 cm^{-1}; $\tilde{\nu}$ (σ CO) 2022, 1914 and 1889 cm^{-1}. MALDI-TOF MS: *m/z* calcd. for $C_{51}H_{30}BrF_6N_8O_5PRuReS$: 1373.9474; Found: 1373.9476 $[M–PF_6]^+$.

CHAPTER 6: Conclusions and Future Work

The oxidation of sulfur atoms can be achieved simply and safely by a variety of methods with the use of low-cost, commercially available reagents. While at face value this appears to be a subtle structural change, in actuality the effect on the electronic properties is far from small. It is hoped that through this thesis other scientists are inspired to probe and manipulate this versatile sulfur atom in order to tailor new materials for a variety of photophysical applications.

In **Chapter 2** six new cyclometalated iridium(III) complexes bearing sulfur-bridged dipyridyl ligands were synthesized and characterized. In changing the sulfur center from sulfide (S), to sulfoxide (SO) to sulfone (SO_2) it was revealed that this oxidation can serve as a switch to alter the emission of the complex from that of blue/green to yellow. This leads to a new class of ligand capable of a "two-level" tuning of the photoluminescence colour, whereby a combination of substituents at the pyridyl rings and sulfur oxidation state can be used to finely modify the electronics. While the PLQY for the complexes was found to be low, thereby limiting use in emissive devices, the additional degree of control over the excited-state properties is expected to be advantageous for applications in photoredox catalysis. The colour-tuning ability could be a useful property for fluorescence microscopy applications probing oxidative pathways, whereby the sulfide (with blue-green emission) is oxidized to the sulfone *in vitro* to give a yellow emissive species allowing the determination of oxygen-rich and oxygen-poor cell environments.

With a view to creating lower-cost emitters, in **Chapter 3** heteroleptic copper(I) complexes bearing POP diphosphine ligands and sulfur-bridged diimine ligands were prepared.

The sulfur-bridged dipyridyl ligands were functionalized either with or without methyl substituents in the 6,6′-positions of the pyridyl rings and sulfide or sulfone oxidation states at the sulfur center. Ligands without methyl functionalization formed monometallic species, but once the bulky substituents were introduced bimetallic adducts were isolated due to steric constraints about the copper. For the sulfide (**Cu-Me-DPS**), a bimetallic species consisting of a bridging POP ligand is seen, but the sulfone (**Cu-Me-DPSO$_2$**) forms a bimetallic species with the diimine moiety acting as a bridging ligand linking the two copper atoms due to the additional binding sites at the sulfone oxygen atoms. These arrangements were observed in solution and as single crystal structures. PLQYs were modest, up to 0.14 for the most sterically constrained complex, **Cu-Me-DPSO$_2$**, Through the use of low-temperature time-resolved photoluminescence spectroscopy, in addition to computational methods, the emissive pathway was determined to be due to a TADF mechanism. **Cu-Me-DPSO$_2$** could show promise as an emissive material in a LEEC device, and further structural modifications at the 6- and 6′-positions of the diimine ligand could be of interest to see if PLQYs can be increased through additional steric constraints about the copper(I) atom.

The ability to control or tune photoluminescence properties is advantageous in the design of photofunctional materials, particularly those which react to an external stimulus. Further illustrating subtle alterations can result in dramatic changes in properties, in **Chapter 4**, two new [Cu(diphosphine)(diimine)]$^+$ complexes bearing sulfoxide-bridged diimine ligands are presented. **Cu-DPSO** displayed photophysical properties typical of other Cu(I) complexes. However, on addition of methyl substituents in the 6- and 6′-positions of the diimine ligand to give complex **Cu-Me-DPSO**, we were able to access a variety of different photophysical properties. **Cu-Me-DPSO** is initially isolated as an amorphous solid which under UV irradiation gives a yellow emission, but upon heating to 180 ºC, a crystalline species (***c*-Cu-Me-DPSO**) is formed which

gives orange emission due to a flattening conformational change during the crystallization process. ***c*-Cu-Me-DPSO** was also shown to exhibit reversible thermochromic emission, whereby the complex undergoes a large colour change from orange at room temperature to yellow at –196 ºC. Based on data from solid state variable-temperature excitation and absorption spectra this phenomenon is attributed to a change in coordination geometry about the copper atom in the excited state. At low temperatures, a pseudo-tetrahedral geometry is preferred, giving higher energy emission, while at higher temperatures a flattened geometry dominates giving a lower energy emission under UV irradiation. In showing that a copper(I) complex can exhibit reversible thermochromism, avenues that were inaccessible due to the limitations of thermochromic copper halide clusters can now be realized. For example, inexpensive copper(I) metallopolymers that offer a response to thermal stimuli could be fabricated. The simple synthetic procedures to the complexes reported, coupled with the absence of toxic heavy metals required, lends itself to practical applications in optoelectronics, including light-emitting diodes, display technologies and chemical and biological sensors.

In **Chapter 5** the use of supramolecular ruthenium(II)-rhenium(I) species as photocatalysts for CO_2 reduction is introduced. In these systems the Ru(II) moiety acts as a visible-light absorbing photosensitizer (PS) unit, and the Re(I) as the catalytic center. The reaction mechanism proceeds by the selective photoexcitation of a one-electron reduced species (OERS) at the Ru(II) center which then proceeds *via* an intramolecular electron transfer to the Re(I) catalytic center, where CO_2 reduction then occurs. When the two metal centers are tethered together the electron transfer is accelerated. Previous research in the Wolf group has shown that sulfur oxidation state can vary the nature of charge transfer in sulfur-bridged organic chromophores, and

so this project was designed to probe the degree of electron transfer in a tethered Ru(II)-Re(I) photocatalytic system and thus the impact on CO_2 reduction.

In using a sulfur-bridged bisphenanthroline ligand to connect the two metal centers, two new Ru(II)-Re(I) supramolecular photocatalysts were prepared with sulfide (**Ru-PSP-Re**) and sulfone (**Ru-PSO$_2$P-Re**) oxidation states at the sulfur, in addition to their monometallic Ru(II) and Re(I) analogues. Electrochemical data were used to indicate the suitability of each dyad towards CO_2 reduction. It has been reported that a threshold for the photocatalytic activity of mononuclear Re complexes exists at $E_{1/2}^{red} = -1.4$ V, and this translates to Ru(II)-Re(I) supramolecular catalysts with far lower efficiencies for catalysts at potentials more positive than this value. Reduction potentials for **Ru-PSP-Re** (–1.56 V) and **Ru-PSO$_2$P-Re** (–1.30 V) suggest that the sulfide species is a better candidate for the photocatalysis. However, on analysis of the photophysical data, a bathochromic shift of 25 nm and a decrease in emission intensity is observed on going from **Ru-PSP-Re** to **Ru-PSO$_2$P-Re** indicating a greater degree of electronic communication between the two metal centers for the sulfone species, which could aid in the efficiency of the electron transfer of the OERS. PLQYs are required to quantify the degree of emission quenching, and transient absorption measurements could aid in elucidating the nature of the excited-state.

While the TON of both complexes for formation of CO was found to be very low, significant bubbling was observed from the solution under irradiation to the point of pressurizing the sealed vessel. From GC data it is seen that this gas is not CO or H_2, the two volatile products typically produced in these systems, and from solvent suppression ^{1}H NMR studies no formic acid was produced either. In order to probe whether the gas formed is a decomposition product of the catalyst, atmospheric MS will be performed in real-time, scanning 0–100 m/z to see if any volatile sulfur-containing species are evolved. Atmospheric-MS can also help identify other possible low

mass products, such as ethane or ethylene. Additionally, GC-MS will be conducted for further analysis of the gas produced.

Overall, the work discussed in this thesis illustrates that through altering the oxidation state at sulfur can change the photophysical properties of a variety of metals, with copper, iridium, rhenium and ruthenium highlighted in this body of work, and as a consequence the complexes reported have the potential to be used in a wide variety of applications, from light-emitting applications such as OLEDs and LEECs, to photocatalytic reduction of CO_2, to photocatalysis and uses in bioimaging. This work expands on the library of sulfur-bridged chromophores studied, and hopefully opens a new avenue of ligand tuning for photophysical coordination compounds.

REFERENCES

(1) Benson, J. L. *Greek Colour Theory and the Four Elements*; University of Massachusetts Amherst Libraries: Amherst, Massachusetts, 2000.

(2) Bailey, C.; Lucretius, C. T. *Lucretius on the Nature of Things*; Oxford: Clarendon Press: New York,, 1948.

(3) Al-Khalili, J. *Nature* **2015**, *518*, 164–165.

(4) Sabra, A. I.; Stork, D. G. *Phys. Today* **2008**, *36*, 71–72.

(5) Scharbach, P. N. *Physics Bulletin* **1983**, *34*, 522–522.

(6) Hagfeldt, A.; Boschloo, G.; Sun, L.; Kloo, L.; Pettersson, H. *Chem. Rev.* **2010**, *110*, 6595–6663.

(7) Wolfbeis, O. S. *Chem. Soc. Rev.* **2015**, *44*, 4743–4768.

(8) Kok, P.; Munro, W. J.; Nemoto, K.; Ralph, T. C.; Dowling, J. P.; Milburn, G. J. *Rev. Mod. Phys.* **2007**, *79*, 135–174.

(9) Mentley, D. E. *Proc. IEEE* **2002**, *90*, 453–459.

(10) Yersin, H.; Rausch, A. F.; Czerwieniec, R.; Hofbeck, T.; Fischer, T. *Coord. Chem. Rev.* **2011**, *255*, 2622–2652.

(11) Ertl, C. D.; Momblona, C.; Pertegás, A.; Junquera-Hernández, J. M.; La-Placa, M.-G.; Prescimone, A.; Ortí, E.; Housecroft, C. E.; Constable, E. C.; Bolink, H. J. *J. Am. Chem. Soc.* **2017**, *139*, 3237–3248.

(12) *OLED Market worth 48.41 Billion USD by 2023*; https://www.marketsandmarkets.com/PressReleases/global-OLED-market.asp (accessed July 18, 2018)

(13) Costa, R. D.; Ortí, E.; Bolink, H. J.; Graber, S.; Schaffner, S.; Neuburger, M.; Housecroft, C. E.; Constable, E. C. *Adv. Funct. Mater.* **2009**, *19*, 3456–3463.

(14) Xu, H.; Chen, R.; Sun, Q.; Lai, W.; Su, Q.; Huang, W.; Liu, X. *Chem. Soc. Rev.* **2014**, *43*, 3259–3302.

(15) Jablonski, A. *Nature* **1933**, *131*, 839–840.

(16) Jaffe, H. H.; Miller, A. L. *J. Chem. Educ.* **1966**, *43*, 469.

(17) Wardle, B. *Principles and Applications of Photochemistry*; John Wiley & Sons: London, 2009; pp 1–267.

(18) Prier, C. K.; Rankic, D. A.; MacMillan, D. W. C. *Chem. Rev.* **2013**, *113*, 5322–5363.

(19) Xiang, D.; Wang, X.; Jia, C.; Lee, T.; Guo, X. *Chem. Rev.* **2016**, *116*, 4318–4440.

(20) Thorp-Greenwood, F. L. *Organometallics* **2012**, *31*, 5686–5692.

(21) Housecroft, C. E.; Sharpe, A. G. *Inorganic Chemistry*, Fourth. Pearson Education Limited: Edinburgh, 2012; pp 1–1257.

(22) Demas, J. N.; DeGraff, B. A. *Coord. Chem. Rev* **2001**, *211*, 317–351.

(23) Caspar, J. V.; Kober, E. M.; Sullivan, B. P.; Meyer, T. J. *J. Am. Chem. Soc.* **1982**, *104*, 630–632.

(24) Evans, R. C.; Douglas, P.; Winscom, C. J. *Coord. Chem. Rev.* **2006**, *250*, 2093–2126.

(25) King, K. A.; Spellane, P. J.; Watts, R. J. *J. Am. Chem. Soc.* **1985**, *107*, 1431–1432.

(26) Baldo, M. A.; Lamansky, S.; Burrows, P. E.; Thompson, M. E.; Forrest, S. R. *Appl. Phys. Lett.* **1999**, *75*, 4–6.

(27) Ma, D.; Tsuboi, T.; Qiu, Y.; Duan, L. *Adv. Mater.* **2017**, *29*, 1603253.

(28) Tsuboyama, A.; Iwawaki, H.; Furugori, M.; Mukaide, T.; Kamatani, J.; Igawa, S.; Moriyama, T.; Miura, S.; Takiguchi, T.; Okada, S.; Hoshino, M.; Ueno, K. *J. Am. Chem. Soc.* **2003**, *125*, 12971–12979.

(29) Costa, R. D.; Ortí, E.; Bolink, H. J. *Pure Appl. Chem.* **2011**, *83*, 2115–2128.

(30) Park, B.; Huh, Y. H.; Jeon, H. G.; Park, C. H.; Kang, T. K.; Kim, B. H.; Park, J. *J. Appl. Phys.* **2010**, *108*, 094506–094507.

(31) Hasan, K.; Bansal, A. K.; Samuel, I. D. W.; Roldán-Carmona, C.; Bolink, H. J.; Zysman-Colman, E. *Sci. Rep.* **2015**, *5*, 12325.

(32) Nazeeruddin, M. K.; Wegh, R. T.; Zhou, Z.; Klein, C.; Wang, Q.; De Angelis, F.; Fantacci, S.; Gratzel, M. *Inorg. Chem.* **2006**, *45*, 9245–9250.

(33) Rodríguez-Redondo, J. L.; Costa, R. D.; Ortí, E.; Sastre-Santos, A.; Bolink, H. J.; Fernández-Lázaro, F. *Dalton Trans.* **2009**, *44*, 9787–9793.

(34) Simon, J. A.; Curry, S. L.; Schmehl, R. H.; Schatz, T. R.; Piotrowiak, P.; Jin, X.; Thummel, R. P. *J. Am. Chem. Soc.* **1997**, *119*, 11012–11022.

(35) Winkler, J. R.; Gray, H. B. *Chem. Rev.* **1992**, *92*, 369–379.

(36) Poynton, F. E.; Bright, S. A.; Blasco, S.; Williams, D. C.; Kelly, J. M.; Gunnlaugsson, T. *Chem. Soc. Rev.* **2017**, *46*, 7706–7756.

(37) Mari, C.; Pierroz, V.; Ferrari, S.; Gasser, G. *Chem. Sci.* **2015**, *6*, 2660–2686.

(38) Bomben, P. G.; Robson, K. C. D.; Koivisto, B. D.; Berlinguette, C. P. *Coord. Chem. Rev.* **2012**, *256*, 1438–1450.

(39) Kalyanasundaram, K. *Coord. Chem. Rev.* **1982**, *46*, 159–244.

(40) Juris, A.; Balzani, V.; Barigelletti, F.; Campagna, S.; Belser, P.; Zelewsky, von, A. *Coord. Chem. Rev.* **1988**, *84*, 85–277.

(41) Myrick, M. L.; Blakley, R. L.; DeArmond, M. K.; Arthur, M. L. *J. Am. Chem. Soc.* **1988**, *110*, 1325–1336.

(42) Yeh, A.; Shank, C.; McCusker, J. *Science* **2000**, *289*, 935–938.

(43) Damrauer, N. H.; Cerullo, G.; Yeh, A.; Boussie, T. R.; Shank, C. V.; McCusker, J. K. *Science* **1997**, *275*, 54–57.

(44) Caspar, J. V.; Meyer, T. J. *J. Am. Chem. Soc.* **1983**, *105*, 5583–5590.

(45) Ashford, D. L.; Glasson, C. R. K.; Norris, M. R.; Concepcion, J. J.; Keinan, S.; Brennaman, M. K.; Templeton, J. L.; Meyer, T. J. *Inorg. Chem.* **2014**, *53*, 5637–5646.

(46) Danielson, E.; Elliott, C. M.; Merkert, J. W.; Meyer, T. J. *J. Am. Chem. Soc.* **1987**, *109*, 2519–2520.

(47) Treadway, J. A.; Chen, P.; Rutherford, T. J.; Keene, F. R.; Meyer, T. J. *J. Phys. Chem. A* **1997**, *101*, 6824–6826.

(48) Falkenström, M.; Johansson, O.; Hammarström, L. *Inorganica Chim. Acta* **2007**, *360*, 741–750.

(49) Wenger, O. S. *Coord. Chem. Rev.* **2009**, *253*, 1439–1457.

(50) McMillin, D. R.; Buckner, M. T.; Ahn, B. T. *Inorg. Chem.* **1977**, *16*, 943–945.

(51) Lavie-Cambot, A.; Cantuel, M.; Leydet, Y.; Jonusauskas, G.; Bassani, D.; McClenaghan, N. *Coord. Chem. Rev.* **2008**, *252*, 2572–2584.

(52) Adachi, C. *Jpn. J. Appl. Phys.* **2014**, *53*, 060101.

(53) Keller, S.; Prescimone, A.; Bolink, H.; Sessolo, M.; Longo, G.; Martínez-Sarti, L.; Junquera-Hernández, J. M.; Constable, E. C.; Ortí, E.; Housecroft, C. E. *Dalton Trans.* **2018**, *124*, 4918–14.

(54) Perruchas, S.; Le Goff, X. F.; Maron, S.; Maurin, I.; Guillen, F.; Garcia, A.; Gacoin, T.; Boilot, J.-P. *J. Am. Chem. Soc.* **2010**, *132*, 10967–10969.

(55) Paria, S.; Reiser, O. *ChemCatChem* **2014**, *6*, 2477–2483.

(56) Ichinaga, A. K.; Kirchhoff, J. R.; McMillin, D. R.; Dietrich-Buchecker, C. O.; Marnot, P. A.; Sauvage, J.-P. *Inorg. Chem.* **1987**, *26*, 4290–4292.

(57) Mara, M. W.; Fransted, K. A.; Chen, L. X. *Coord. Chem. Rev.* **2015**, *282-283*, 2–18.

(58) Armaroli, N. *Chem. Soc. Rev.* **2001**, *30*, 113–124.

(59) McMillin, D. R.; Kirchhoff, J. R.; Goodwin, K. V. *Coord. Chem. Rev.* **1985**, *64*, 83–92.

(60) Siddique, Z. A.; Yamamoto, Y.; Ohno, T.; Nozaki, K. *Inorg. Chem.* **2003**, *42*, 6366–6378.

(61) Garakyaraghi, S.; Danilov, E. O.; McCusker, C. E.; Castellano, F. N. *J. Phys. Chem. A* **2015**, *119*, 3181–3193.

(62) Palmer, C. E. A.; McMillin, D. R.; Kirmaier, C.; Holten, D. *Inorg. Chem.* **1987**, *26*, 3167–3170.

(63) Everly, R. M.; McMillin, D. R. *Photochem. Photobiol.* **1989**, *50*, 711–716.

(64) Stacy, E. M.; McMillin, D. R. *Inorg. Chem.* **1990**, *29*, 393–396.

(65) Eggleston, M. K.; McMillin, D. R.; Koenig, K. S.; Pallenberg, A. J. *Inorg. Chem.* **1997**, *36*, 172–176.

(66) Lockard, J. V.; Kabehie, S.; Zink, J. I.; Smolentsev, G.; Soldatov, A.; Chen, L. X. *J. Phys. Chem. B* **2010**, *114*, 14521–14527.

(67) Khnayzer, R. S.; McCusker, C. E.; Olaiya, B. S.; Castellano, F. N. *J. Am. Chem. Soc.* **2013**, *135*, 14068–14070.

(68) Baldo, M. A.; O'brien, D. F.; You, Y.; Shoustikov, A.; Sibley, S.; Thompson, M. E.; Forrest, S. R. *Nature* **1998**, *395*, 151–154.

(69) Volz, D.; Wallesch, M.; Fléchon, C.; Danz, M.; Verma, A.; Navarro, J. M.; Zink, D. M.; Bräse, S.; Baumann, T. *Green Chem.* **2015**, *17*, 1988–2011.

(70) Schmidbauer, S.; Hohenleutner, A.; König, B. *Adv. Mater.* **2013**, *25*, 2114–2129.

(71) Czerwieniec, R.; Leitl, M. J.; Homeier, H. H. H.; Yersin, H. *Coord. Chem. Rev.* **2016**, *325*, 2–28.

(72) Iwamura, M.; Watanabe, H.; Ishii, K.; Takeuchi, S.; Tahara, T. *J. Am. Chem. Soc.* **2011**, *133*, 7728–7736.

(73) Leitl, M. J.; Krylova, V. A.; Djurovich, P. I.; Thompson, M. E.; Yersin, H. *J. Am. Chem. Soc.* **2014**, *136*, 16032–16038.

(74) Parker, C. A.; Hatchard, C. G. *J. Phys. Chem.* **1962**, *66*, 2506–2511.

(75) Czerwieniec, R.; Yu, J.; Yersin, H. *Inorg. Chem.* **2011**, *50*, 8293–8301.

(76) Linfoot, C. L.; Leitl, M. J.; Richardson, P.; Rausch, A. F.; Chepelin, O.; White, F. J.; Yersin, H.; Robertson, N. *Inorg. Chem.* **2014**, *53*, 10854–10861.

(77) Christensen, P. R.; Nagle, J. K.; Bhatti, A.; Wolf, M. O. *J. Am. Chem. Soc.* **2013**, *135*, 8109–8112.

(78) Cruz, C. D.; Christensen, P. R.; Chronister, E. L.; Casanova, D.; Wolf, M. O.; Bardeen, C. J. *J. Am. Chem. Soc.* **2015**, *137*, 12552–12564.

(79) Pahlavanlu, P.; Christensen, P. R.; Therrien, J. A.; Wolf, M. O. *J. Phys. Chem. C* **2015**, *120*, 70–77.

(80) Caron, E.; Wolf, M. O. *Macromolecules* **2017**, *50*, 7543–7549.

(81) *Light's Labour's Lost*; Energy Efficiency Policy Profiles; OECD Publishing, 2006.

(82) Armaroli, N.; Balzani, V. *Energy Environ. Sci.* **2011**, *4*, 3193–3222.

(83) Humphreys, C. J. *MRS Bulletin* **2008**, *33*, 459–470.

(84) Tang, C. W.; VanSlyke, S. A. *Appl. Phys. Lett.* **1987**, *51*, 913–915.

(85) Burroughes, J. H.; Bradley, D.; Brown, A. R.; Marks, R. N. *Nature* **1990**, *348*, 352–352.

(86) Pei, Q.; Yu, G.; Zhang, C.; Yang, Y.; Heeger, A. J. *Science* **1995**, *269*, 1086–1088.

(87) Flamigni, L.; Barbieri, A.; Sabatini, C.; Ventura, B.; Barigelletti, F. In *Photochemistry and Photophysics of Coordination Compounds II*; Springer Berlin Heidelberg, 2007; pp 143–203.

(88) Chi, Y.; Chou, P.-T. *Chem. Soc. Rev.* **2010**, *39*, 638–655.

(89) Chou, P.-T.; Chi, Y.; Chung, M.-W.; Lin, C.-C. *Coord. Chem. Rev.* **2011**, *255*, 2653–2665.

(90) Powell, B. J. *Coord. Chem. Rev.* **2015**, *295*, 46–79.

(91) Karolyn M Maness; Roger H Terrill; Thomas J Meyer; Royce W Murray, A.; Wightman, R. M. *J. Am. Chem. Soc.* **1996**, *118*, 10609–10616.

(92) Slinker, J. D.; Rivnay, J.; Moskowitz, J. S.; Parker, J. B.; Bernhard, S.; Abruña, H. D.; Malliaras, G. G. *J. Mater. Chem.* **2007**, *17*, 2976–2988.

(93) Sun, Q.; Li, Y.; Pei, Q. *J. Display Technol.* **2007**, *3*, 211–224.

(94) Costa, R. D.; Ortí, E.; Bolink, H. J.; Monti, F.; Accorsi, G.; Armaroli, N. *Angew. Chem. Int. Ed.* **2012**, *51*, 8178–8211.

(95) Tordera, D.; Serrano-Pérez, J. J.; Pertegás, A.; Ort, E.; Bolink, H. J.; Baranoff, E.; Nazeeruddin, M. K.; Frey, J. *Chem. Mater.* **2013**, *25*, 3391–3397.

(96) Manivel, P.; Prabakaran, K.; Krishnakumar, V.; Nawaz Khan, F.-R.; Maiyalagan, T. *Ind. Eng. Chem. Res.* **2014**, *53*, 7866–7870.

(97) Golchoubian, H.; Hosseinpoor, F. *Molecules* **2007**, *12*, 304–311.

(98) Chun, J.-H.; Morse, C. L.; Chin, F. T.; Pike, V. W. *Chem. Commun.* **2013**, *49*, 2151–2153.

(99) Kirihara, M.; Itou, A.; Noguchi, T.; Yamamoto, J. *Synlett* **2010**, *10*, 1557–1561.

(100) Davies, D. L.; Lowe, M. P.; Ryder, K. S.; Singh, K.; Singh, S. *Dalton Trans.* **2011**, *40*, 1028–1030.

(101) Hansch, C.; Leo, A.; Taft, R. W. *Chem. Rev.* **1991**, *91*, 165–195.

(102) Spek, A. L. *Acta Crystallogr. C* **2015**, *71*, 9–18.

(103) Bruno, G.; Nicol, F.; Schiavo, Lo, S.; Sinicropi, M. S.; Tresoldi, G. *J. Chem. Soc., Dalton Trans.* **1995**, 17–24.

(104) Tresoldi, G.; Schiavo, Lo, S.; Piraino, P.; Zanello, P. *J. Chem. Soc., Dalton Trans.* **1996**, 885–892.

(105) Scopelliti, R.; Bruno, G.; Donato, C.; Tresoldi, G. *Inorganica Chim. Acta* **2001**, *313*, 43–55.

(106) Tresoldi, G.; Piraino, P.; Rotondo, E.; Faraone, F. *J. Chem. Soc., Dalton Trans.* **1991**, *0*, 425–430.

(107) Tresoldi, G.; Rotondo, E.; Piraino, P.; Lanfranchi, M.; Tiripicchio, A. *Inorganica Chim. Acta* **1992**, *194*, 233–241.

(108) Nicolò, F.; Bruno, G.; Tresoldi, G. *Acta Crystallogr. C* **1996**, *52*, 2188–2191.

(109) Geiß, B.; Lambert, C. *Chem. Commun.* **2009**, 1670–1672.

(110) Finkenzeller, W. J.; Stoessel, P.; Kulikova, M.; Yersin, H. *Proc. of SPIE* **2004**, *5214*, 356–367.

(111) Skórka, Ł.; Filapek, M.; Zur, L.; Małecki, J. G. *J. Phys. Chem. C* **2016**, *120*, 7284–7294.

(112) Costa, R. D.; Ortí, E.; Tordera, D.; Pertegás, A.; Bolink, H. J.; Graber, S.; Housecroft, C. E.; Sachno, L.; Neuburger, M.; Constable, E. C. *Adv. Energy Mater.* **2011**, *1*, 282–290.

(113) Takizawa, S.-Y.; Shimada, K.; Sato, Y.; Murata, S. *Inorg. Chem.* **2014**, *53*, 2983–2995.

(114) Takizawa, S.-Y.; Ikuta, N.; Zeng, F.; Komaru, S.; Sebata, S.; Murata, S. *Inorg. Chem.* **2016**, *55*, 8723–8735.

(115) Sprouse, S.; King, K. A.; Spellane, P. J. *J. Am. Chem. Soc.* **1984**, *106*, 6647–6653.

(116) Tamayo, A. B.; Garon, S.; Sajoto, T.; Djurovich, P. I.; Tsyba, I. M.; Bau, R.; Thompson, M. E. *Inorg. Chem.* **2005**, *44*, 8723–8732.

(117) He, L.; Duan, L.; Qiao, J.; Wang, R.; Wei, P.; Wang, L.; Qiu, Y. *Adv. Funct. Mater.* **2008**, *18*, 2123–2131.

(118) APEX2, version 2, User Manual, M86-E01078. Bruker Analytical X-ray Systems: Madison, WI, 2006.

(119) Farrugia, L. J. *J. Appl. Crystallogr.* **1999**, *32*, 1–2.

(120) Sheldrick, G. M. *SHELXS-97 Programs for Crystal Solution*; University of Göttingen, 1997.

(121) Farrugia, L. J.; IUCr. *J. Appl. Crystallogr.* **2012**, *45*, 849–854.

(122) Spek, A. L. *J. Appl. Crystallogr.* **2003**, *36*, 1–7.

(123) Becke, A. D. *J. Chem. Phys.* **1993**, *98*, 5648–5652.

(124) Lee, C.; Yang, W.; Parr, R. G. *Phys. Rev. B* **1988**, *37*, 785–789.

(125) Hay, P. J.; Wadt, W. R. *J. Chem. Phys.* **1985**, *82*, 299–310.

(126) Miertuš, S.; Scrocco, E.; Tomasi, J. *Chem. Phys.* **1981**, *55*, 117–129.

(127) Tomasi, J.; Mennucci, B.; Cammi, R. *Chem. Rev.* **2005**, *105*, 2999–3094.

(128) Casida, M. E.; Jamorski, C.; Casida, K. C.; Salahub, D. R. *J. Chem. Phys.* **1998**, *108*, 4439–4449.

(129) Jamorski, C.; Casida, M. E.; Salahub, D. R. *J. Chem. Phys.* **1996**, *104*, 5134–5147.

(130) Amiri, K.; Rostami, A.; Rostami, A. *New J. Chem.* **2016**, *40*, 7522–7528.

(131) Welter, S.; Brunner, K.; Hofstraat, J. W.; De Cola, L. *Nature* **2003**, *421*, 54–57.

(132) Zhang, J.; Xu, L.; Wong, W.-Y. *Coord. Chem. Rev.* **2018**, *355*, 180–198.

(133) Keller, S.; Camenzind, T. N.; Abraham, J.; Prescimone, A.; Häussinger, D.; Constable, E. C.; Housecroft, C. E. *Dalton Trans.* **2018**, *47*, 946–957.

(134) Kuchison, A. M.; Wolf, M. O.; Patrick, B. O. *Inorg. Chem.* **2010**, *49*, 8802–8812.

(135) Mondal, R.; Lozada, I. B.; Davis, R. L.; Williams, J. A. G.; Herbert, D. E. *Inorg. Chem.* **2018**, *57*, 4966–4978.

(136) Bergmann, L.; Braun, C.; Nieger, M.; Bräse, S. *Dalton Trans.* **2018**, *47*, 608–621.

(137) Artem'ev, A. V.; Ryzhikov, M. R.; Taidakov, I. V.; Rakhmanova, M. I.; Varaksina, E. A.; Bagryanskaya, I. Y.; Malysheva, S. F.; Belogorlova, N. A. *Dalton Trans.* **2018**, *47*, 2701–2710.

(138) Cariati, E.; Lucenti, E.; Botta, C.; Giovanella, U.; Marinotto, D.; Righetto, S. *Coord. Chem. Rev.* **2016**, *306*, 566–614.

(139) Razgoniaev, A. O.; McCusker, C. E.; Castellano, F. N.; Ostrowski, A. D. *ACS Macro Letters* **2017**, *6*, 920–924.

(140) Linfoot, C. L.; Richardson, P.; Hewat, T. E.; Moudam, O.; Forde, M. M.; Collins, A.; White, F.; Robertson, N. *Dalton Trans.* **2010**, *39*, 8945–8956.

(141) Kaeser, A.; Mohankumar, M.; Mohanraj, J.; Monti, F.; Holler, M.; Cid, J.-J.; Moudam, O.; Nierengarten, I.; Karmazin-Brelot, L.; Duhayon, C.; Delavaux-Nicot, B.; Armaroli, N.; Nierengarten, J.-F. *Inorg. Chem.* **2013**, *52*, 12140–12151.

(142) Moudam, O.; Kaeser, A.; Delavaux-Nicot, B.; Duhayon, C.; Holler, M.; Accorsi, G.; Armaroli, N.; Séguy, I.; Navarro, J.; Destruel, P.; Nierengarten, J.-F. *Chem. Commun.* **2007**, *29*, 3077–3079.

(143) Qin, L.; Zhang, Q.; Sun, W.; Wang, J.; Lu, C.; Cheng, Y.; Wang, L. *Dalton Trans.* **2009**, *280*, 9388–4.

(144) Kaeser, A.; Moudam, O.; Accorsi, G.; Séguy, I.; Navarro, J.; Belbakra, A.; Duhayon, C.; Armaroli, N.; Delavaux-Nicot, B.; Nierengarten, J.-F. *Eur. J. Inorg. Chem.* **2014**, *2014*, 1345–1355.

(145) Andrés-Tomé, I.; Fyson, J.; Dias, F. B.; Monkman, A. P.; Iacobellis, G.; Coppo, P. *Dalton Trans.* **2012**, *41*, 8669–8674.

(146) Connelly, N. G.; Geiger, W. E. *Chem. Rev.* **1996**, *96*, 877–910.

(147) Cardona, C. M.; Li, W.; Kaifer, A. E.; Stockdale, D.; Bazan, G. C. *Adv. Mater.* **2011**, *23*, 2367–2371.

(148) Yang, L.; Feng, J.-K.; Ren, A.-M.; Zhang, M.; Ma, Y.-G.; Liu, X.-D. *Eur. J. Inorg. Chem.* **2005**, *2005*, 1867–1879.

(149) Ceroni, P.; Balzani, V. In *The Exploration of Supramolecular Systems and Nanostructures by Photochemical Techniques*; Lecture Notes in Chemistry; Springer Netherlands: Dordrecht, 2011; Vol. 78, pp 1–20.

(150) Bergmann, L.; Hedley, G. J.; Baumann, T.; Bräse, S.; Samuel, I. D. W. *Sci. Adv.* **2016**, *2*, e1500889–e1500889.

(151) Endicott, J. F.; Schlegel, H. B.; Uddin, M. J.; Seniveratne, D. S. *Coord. Chem. Rev.* **2002**, *229*, 95–106.

(152) Dicke, B.; Hoffmann, A.; Stanek, J.; Rampp, M. S.; Grimm-Lebsanft, B.; Biebl, F.; Rukser, D.; Maerz, B.; Göries, D.; Naumova, M.; Biednov, M.; Neuber, G.; Wetzel, A.; Hofmann, S. M.; Roedig, P.; Meents, A.; Bielecki, J.; Andreasson, J.; Beyerlein, K. R.; Chapman, H. N.; Bressler, C.; Zinth, W.; Rübhausen, M.; Herres-Pawlis, S. *Nat. Chem.* **2018**, *10*, 355–362.

(153) Bruker, S. *Version 6.02 (includes XPREP and SADABS)*; Bruker AXS Inc., 1999.

(154) Palatinus, L.; Chapuis, G. *J. Appl. Crystallogr.* **2007**, *40*, 786–790.

(155) Betteridge, P. W.; Carruthers, J. R.; Cooper, R. I.; Prout, K.; Watkin, D. J. *J. Appl. Crystallogr.* **2003**, *36*, 1487–1487.

(156) Cooper, R. I.; Thompson, A. L.; Watkin, D. J. *J. Appl. Crystallogr.* **2010**, *43*, 1100–1107.

(157) Stephens, P. J.; Devlin, F. J.; Chabalowski, C. F.; Frisch, M. J. *J. Phys. Chem.* **1994**, *98*, 11623–11627.

(158) Petersilka, M.; Gossmann, U.; Gross, E. *Phys. Rev. Lett.* **1996**, *76*, 1212–1215.

(159) Chan, W. C.; Nie, S. *Science* **1998**, *281*, 2016–2018.

(160) Chen, B.; Wang, L.; Xiao, Y.; Fronczek, F. R.; Xue, M.; Cui, Y.; Qian, G. *Angew. Chem. Int. Ed.* **2009**, *48*, 500–503.

(161) Santos, dos, C. M. G.; Harte, A. J.; Quinn, S. J.; Gunnlaugsson, T. *Coord. Chem. Rev.* **2008**, *252*, 2512–2527.

(162) Zhang, Q.; Zhou, Q.; Cheng, Y.; Wang, L.; Ma, D.; Jing, X.; Wang, F. *Adv. Mater.* **2004**, *16*, 432–436.

(163) Montes, V. A.; Pohl, R.; Shinar, J.; Anzenbacher, P. *Chem. Eur. J.* **2006**, *12*, 4523–4535.

(164) Sagara, Y.; Kato, T. *Nat. Chem.* **2009**, *1*, 605–610.

(165) Shan, G.-G.; Li, H.-B.; Qin, J.-S.; Zhu, D.-X.; Liao, Y.; Su, Z.-M. *Dalton Trans.* **2012**, *41*, 9590–9594.

(166) Howarth, A. J.; Patia, R.; Davies, D. L.; Lelj, F.; Wolf, M. O.; Singh, K. *Eur. J. Inorg. Chem.* **2014**, *2014*, 3657–3664.

(167) Alam, P.; Climent, C.; Kaur, G.; Casanova, D.; Choudhury, A. R.; Gupta, A.; Alemany, P.; Laskar, I. R. *Cryst. Growth Des.* **2016**, *16*, 5738–5752.

(168) Ravotto, L.; Ceroni, P. *Coord. Chem. Rev.* **2017**, *346*, 62–76.

(169) Nishikawa, M.; Nomoto, K.; Kume, S.; Inoue, K.; Sakai, M.; Fujii, M.; Nishihara, H. *J. Am. Chem. Soc.* **2010**, *132*, 9579–9581.

(170) Nishikawa, M.; Kume, S.; Nishihara, H. *Phys. Chem. Chem. Phys.* **2013**, *15*, 10549–10565.

(171) Tard, C.; Perruchas, S.; Maron, S.; Le Goff, X. F.; Guillen, F.; Garcia, A.; Vigneron, J.; Etcheberry, A.; Gacoin, T.; Boilot, J.-P. *Chem. Mater.* **2008**, *20*, 7010–7016.

(172) Huitorel, B.; Benito, Q.; Fargues, A.; Garcia, A.; Gacoin, T.; Boilot, J.-P.; Perruchas, S.; Camerel, F. *Chem. Mater.* **2016**, *28*, 8190–8200.

(173) Perruchas, S.; Tard, C.; Le Goff, X. F.; Fargues, A.; Garcia, A.; Kahlal, S.; Saillard, J.-Y.; Gacoin, T.; Boilot, J.-P. *Inorg. Chem.* **2011**, *50*, 10682–10692.

(174) Yang, K.; Li, S.-L.; Zhang, F.-Q.; Zhang, X.-M. *Inorg. Chem.* **2016**, *55*, 7323–7325.

(175) Tran, D.; Ryu, C. K.; Ford, P. C. *Inorg. Chem.* **1994**, *33*, 5957–5959.

(176) Kim, T. H.; Shin, Y. W.; Jung, J. H.; Kim, J. S.; Kim, J. *Angew. Chem. Int. Ed.* **2008**, *47*, 685–688.

(177) Dias, H. V. R.; Diyabalanage, H. V. K.; Rawashdeh-Omary, M. A.; Franzman, M. A.; Omary, M. A. *J. Am. Chem. Soc.* **2003**, *125*, 12072–12073.

(178) Cuttell, D. G.; Kuang, S.-M.; Fanwick, P. E.; McMillin, D. R.; Walton, R. A. *J. Am. Chem. Soc.* **2002**, *124*, 6–7.

(179) Kuang, S.-M.; Cuttell, D. G.; McMillin, D. R.; Fanwick, P. E.; Walton, R. A. *Inorg. Chem.* **2002**, *41*, 3313–3322.

(180) Everly, R. M.; Ziessel, R.; Suffert, J.; McMillin, D. R. *Inorg. Chem.* **1991**, *30*, 559–561.

(181) Armaroli, N.; Accorsi, G.; Cardinali, F.; Listorti, A. *Top. Curr. Chem.* **2007**, 69–115.

(182) McMillin, D. R.; McNett, K. M. *Chem. Rev.* **1998**, *98*, 1201–1220.

(183) Cunningham, C. T.; Cunningham, K. L. H.; Michalec, J. F.; McMillin, D. R. *Inorg. Chem.* **1999**, *38*, 4388–4392.

(184) Ruthkosky, M.; Castellano, F. N.; Meyer, G. J. *Inorg. Chem.* **1996**, *35*, 6406–6412.

(185) Gneuß, T.; Leitl, M. J.; Finger, L. H.; Rau, N.; Yersin, H.; Sundermeyer, J. *Dalton Trans.* **2015**, *44*, 8506–8520.

(186) Bondi, A. *J. Phys. Chem.* **1964**, *68*, 441–451.

(187) Cunningham, C. T.; Moore, J. J.; Cunningham, K. L. H.; Fanwick, P. E.; McMillin, D. R. *Inorg. Chem.* **2000**, *39*, 3638–3644.

(188) Kovalevsky, A. Y.; Gembicky, M.; Novozhilova, I. V.; Coppens, P. *Inorg. Chem.* **2003**, *42*, 8794–8802.

(189) Felder, D.; Nierengarten, J.-F.; Barigelletti, F.; Ventura, B.; Armaroli, N. *J. Am. Chem. Soc.* **2001**, *123*, 6291–6299.

(190) Iwamura, M.; Takeuchi, S.; Tahara, T. *J. Am. Chem. Soc.* **2007**, *129*, 5248–5256.

(191) Ruthkosky, M.; Kelly, C. A.; Castellano, F. N.; Meyer, G. J. *Coord. Chem. Rev.* **1998**, *171*, 309–322.

(192) Lever, A. B. P.; Mantovani, E.; Donini, J. C. *Inorg. Chem.* **1971**, *10*, 2424–2427.

(193) Lever, A. B. P.; Mantovani, E. *Inorg. Chem.* **1971**, *10*, 817–826.

(194) Grenthe, I.; Paoletti, P.; Sandstroem, M.; Glikberg, S. *Inorg. Chem.* **1979**, *18*, 2687–2692.

(195) Jennifer, S. J.; Thomas Muthiah, P.; Tamilselvi, D. *Chem Cent J* **2014**, *8*, 58.

(196) Chachaty, C.; Pappalardo, G. C.; Scarlata, G. *J. Chem. Soc., Perkin Trans. 2* **1976**, 1234–1238.

(197) *Annual Energy Outlook 2018*; U.S. Energy Information Administration: Washington, DC, 2018; pp 304–317.

(198) Lewis, N. S.; Nocera, D. G. *Proc. Natl. Acad. Sci. U.S.A.* **2006**, *103*, 15729–15735.

(199) Alstrum-Acevedo, J. H.; Brennaman, M. K.; Meyer, T. J. *Inorg. Chem.* **2005**, *44*, 6802–6827.

(200) Barber, J. *Chem. Soc. Rev.* **2009**, *38*, 185–196.

(201) Kuramochi, Y.; Ishitani, O.; Ishida, H. *Coord. Chem. Rev.* **2017**, 1–24.

(202) Paris, J. P.; Brandt, W. W. *J. Am. Chem. Soc.* **1959**, *81*, 5001–5002.

(203) Nicewicz, D. A.; MacMillan, D. W. C. *Science* **2008**, *322*, 77–80.

(204) Sun, L.; Hammarström, L.; Åkermark, B.; Styring, S. *Chem. Soc. Rev.* **2001**, *30*, 36–49.

(205) Steel, P. J.; Constable, E. C. *J. Chem. Soc., Dalton Trans.* **1990**, 1389–1396.

(206) Hawecker, J.; Lehn, J.-M.; Ziessel, R. *J. Chem. Soc., Chem. Commun.* **1983**, *9*, 536–538.

(207) Elgrishi, N.; Chambers, M. B.; Wang, X.; Fontecave, M. *Chem. Soc. Rev.* **2017**, *46*, 761–796.

(208) Tamaki, Y.; Ishitani, O. *ACS Catalysis* **2017**, *7*, 3394–3409.

(209) Gholamkhass, B.; Mametsuka, H.; Koike, K.; Tanabe, T.; Furue, M.; Ishitani, O. *Inorg. Chem.* **2005**, *44*, 2326–2336.

(210) Koike, K.; Naito, S.; Sato, S.; Tamaki, Y.; Ishitani, O. *J. Photochem. Photobiol. A* **2009**, *207*, 109–114.

(211) Bian, Z.-Y.; Wang, H.; Fu, W. F.; Li, L.; Ding, A.-Z. *Polyhedron* **2012**, *32*, 78–85.

(212) Dotsenko, I. A.; Curtis, M.; Samoshina, N. M.; Samoshin, V. V. *Tetrahedron* **2011**, *67*, 7470–7478.

(213) Sullivan, B. P.; Salmon, D. J.; Meyer, T. J. *Inorg. Chem.* **1978**, *17*, 3334–3341.

(214) Jäger, M.; Kumar, R. J.; Görls, H.; Bergquist, J.; Johansson, O. *Inorg. Chem.* **2009**, *48*, 3228–3238.

(215) Sahara, G.; Ishitani, O. *Inorg. Chem.* **2015**, *54*, 5096–5104.

(216) Armaroli, N.; De Cola, L.; Balzani, V.; Sauvage, J.-P.; Dietrich-Buchecker, C. O.; Kern, J.-M. *Faraday Trans.* **1992**, *88*, 553–556.

(217) Brédas, J. L.; Chance, R. R.; Silbey, R.; Nicolas, G.; Durand, P. *J. Chem. Phys.* **1982**, *77*, 371–378.

(218) Glaze, A. P.; Heller, H. G.; Whittall, J. *J. Chem. Soc., Perkin Trans. 2* **1992**, *4*, 591.

(219) Herder, M.; Schmidt, B. M.; Grubert, L.; Pätzel, M.; Schwarz, J.; Hecht, S. *J. Am. Chem. Soc.* **2015**, *137*, 2738–2747.

APPENDIX

Appendix A: Tunable Emission of Iridium(III) Complexes Bearing Sulfur-Bridged Dipyridyl Ligands

Listing A.1 Frontier orbital diagrams for **Ir-DPS**, **Ir-DPSO** and **Ir-DPSO$_2$**.

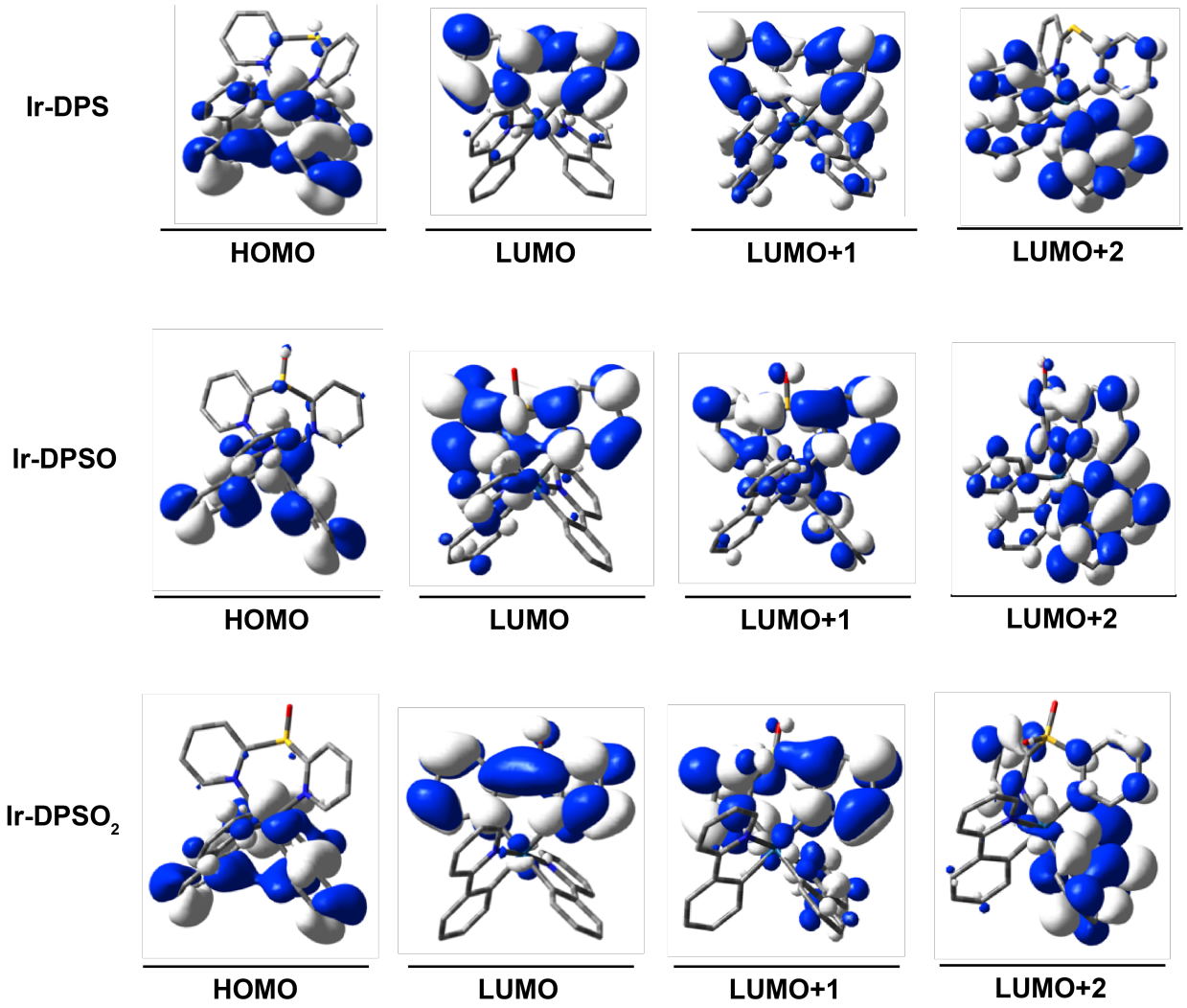

Listing A.2 Frontier orbital diagrams for **Ir-4,4'-Me-DPS**, **Ir-4,4'-Me-DPSO** and **Ir-4,4'-Me-DPSO$_2$**.

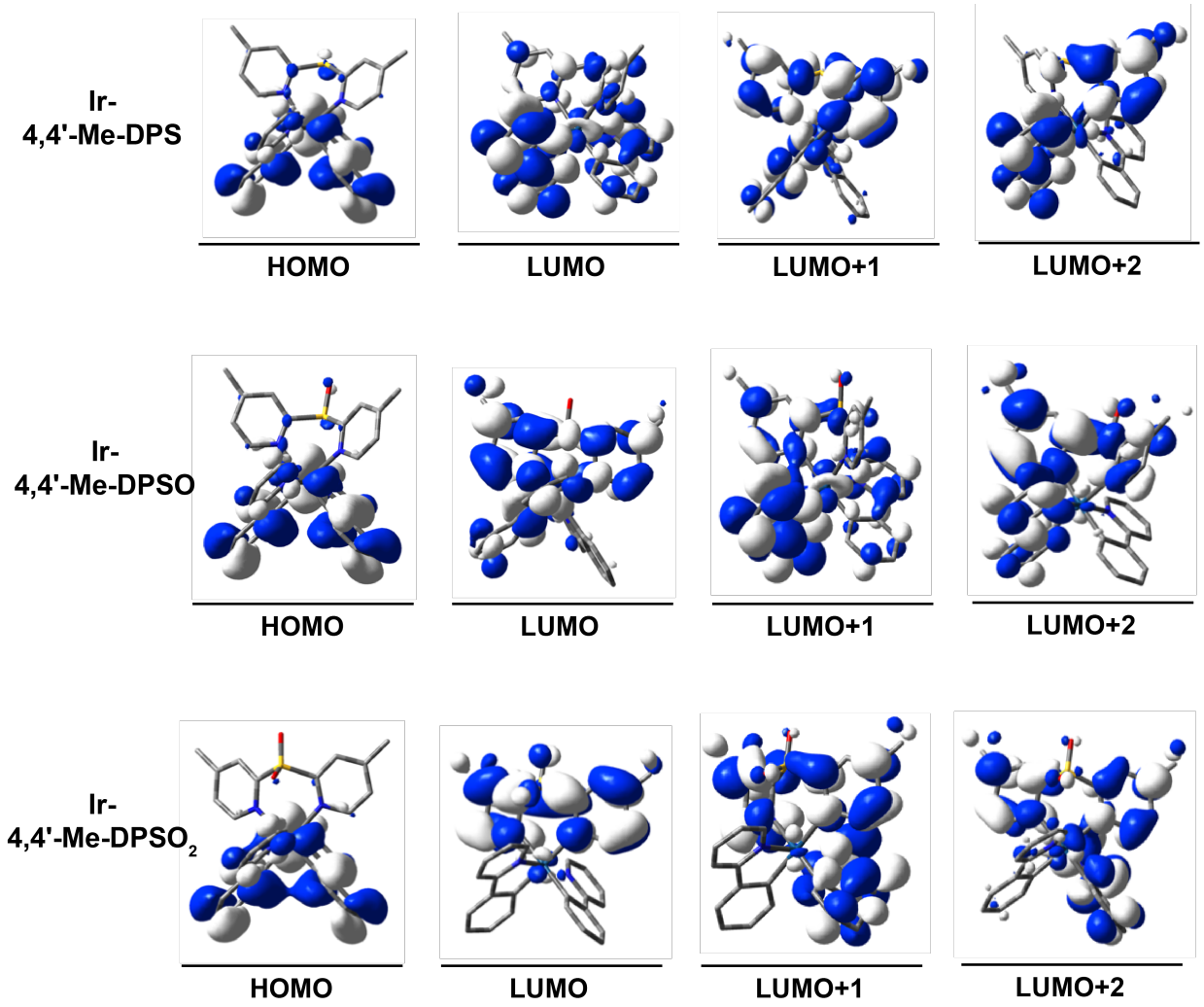

Listing A.3 Unpaired-electron spin density contours for Ir(III) complexes.

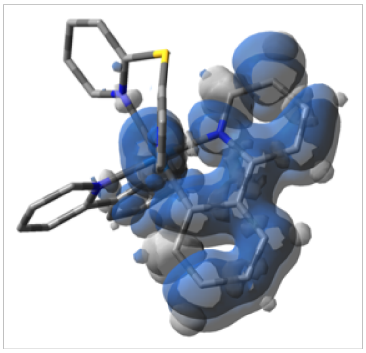

Ir-DPS

ppy: 1.75 e^-
Ir: 0.22 e^-

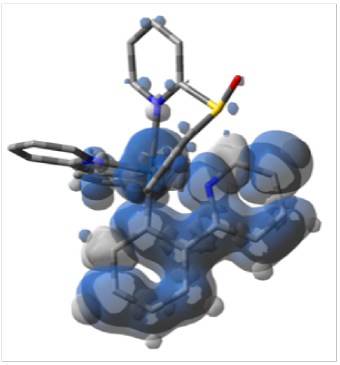

Ir-DPSO

ppy: 1.55 e^-
Ir: 0.33 e^-

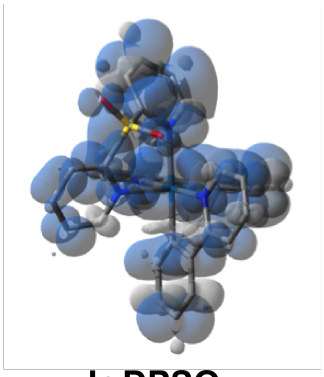

Ir-DPSO$_2$

ppy: 0.47 e^-
Ir: 0.56 e^-
DPSO$_2$: 0.97 e^-

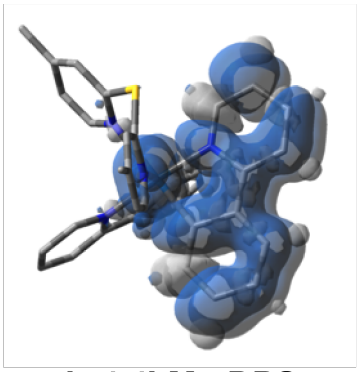

Ir-4,4'-Me-DPS

ppy: 1.44 e^-
Ir: 0.52 e^-

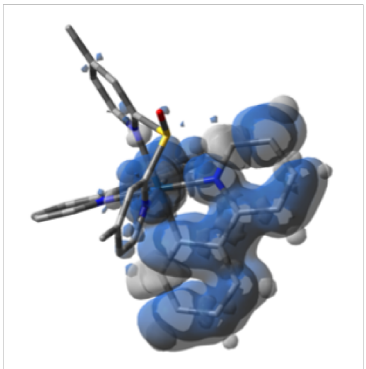

Ir-4,4'-Me-DPSO

ppy: 1.60 e^-
Ir: 0.33 e^-

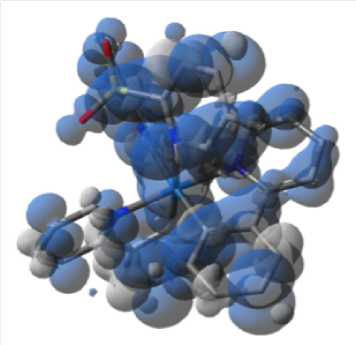

Ir-4,4'-Me-DPSO$_2$

ppy: 0.60 e^-
Ir: 0.33 e^-
4,4'-Me-DPSO$_2$: 1.00 e^-

Listing A.4 Lowest triplet excited states calculated at the TD-DFT B3LYP/(6-31G**+LANL2DZ) level. Vertical excitation energies (E), dominant monoexcitations with contributions (within parentheses) greater than 15%, nature of the electronic transition and description of the excited state are summarized for Ir(III) complexes.

	Monoexcitation	**Energy**	**Nature**	**Description**
Ir-DPS	H→ L+2 (55 %)	2.76 eV	$\mathbf{d}_{\pi}(\mathrm{Ir}) + \boldsymbol{\pi}_{\mathrm{ppy}} \rightarrow \boldsymbol{\pi}^{*}_{\mathrm{ppy}}$	^{3}LC/ ^{3}MLCT
Ir-DPSO	H→ L+2 (26 %)	2.77 eV	$\mathbf{d}_{\pi}(\mathrm{Ir}) + \boldsymbol{\pi}_{\mathrm{ppy}} \rightarrow \boldsymbol{\pi}^{*}_{\mathrm{ppy}}$	^{3}LC/ ^{3}MLCT
Ir-DPSO$_2$	H→ L (90 %)	2.65 eV	$\mathbf{d}_{\pi}(\mathrm{Ir}) + \boldsymbol{\pi}_{\mathrm{ppy}} \rightarrow \boldsymbol{\pi}^{*}_{\mathbf{anc}}$	^{3}MLCT/ ^{3}LLCT
Ir-4,4'-Me-DPS	H→ L (54 %)	2.76 eV	$\mathbf{d}_{\pi}(\mathrm{Ir}) + \boldsymbol{\pi}_{\mathrm{ppy}} \rightarrow \boldsymbol{\pi}^{*}_{\mathbf{ppy}}$	^{3}LC/ ^{3}MLCT
Ir-4,4'-Me-DPSO	H→L +1 (46 %)	2.76 eV	$\mathbf{d}_{\pi}(\mathrm{Ir}) + \boldsymbol{\pi}_{\mathrm{ppy}} \rightarrow \boldsymbol{\pi}^{*}_{\mathbf{ppy}}$	^{3}LC/ ^{3}MLCT
Ir-4,4'-Me-DPSO$_2$	H→ L (42 %)	2.74 eV	$\mathbf{d}_{\pi}(\mathrm{Ir}) + \boldsymbol{\pi}_{\mathrm{ppy}} \rightarrow \boldsymbol{\pi}^{*}_{\mathbf{anc}}$	^{3}MLCT/ ^{3}LLCT

Listing A.5 Summary of crystallographic data for **Ir-DPS**.

Compound	**Ir-DPS**	
Empirical formula	$C_{16}H_{12}F_3Ir_{0.50}N_2P_{0.50}S_{0.50}$	
Formula weight	416.89	
Temperature	173(2) K	
Wavelength	0.71073 Å	
Crystal system	Triclinic	
Space group	P -1	
Unit cell dimensions	a = 14.7218(16) Å	α= 67.320(5)º.
	b = 15.0655(17) Å	β= 76.875(5)º.
	c = 16.9581(19) Å	γ = 73.592(5)º.
Volume	3299.2(7) $Å^3$	
Z	8	
Density (calculated)	1.679 Mg/m^3	
Absorption coefficient	4.221 mm^{-1}	
F(000)	1624	
Crystal size	0.302 x 0.100 x 0.020 mm^3	
Theta range for data collection	1.313 to 26.482º.	
Index ranges	-18<=h<=17, -18<=k<=18, -21<=l<=17	
Reflections collected	46631	
Independent reflections	13136 [R(int) = 0.0269]	
Completeness to theta = 25.242º	96.7 %	
Refinement method	Full-matrix least-squares on F^2	
Data / restraints / parameters	13136 / 0 / 835	

Goodness-of-fit on F^2	1.055
Final R indices [I>2sigma(I)]	R1 = 0.0351, wR2 = 0.0887
R indices (all data)	R1 = 0.0433, wR2 = 0.0945
Extinction coefficient	n/a
Largest diff. peak and hole	2.791 and -1.682 e.$Å^{-3}$

Appendix B:

Listing B.1 Summary of crystallographic data for **Cu-DPS**

Compound	**Cu-DPS**
Chemical formula	$C_{46}H_{36}CuN_2OP_2SBF_4$
Formula weight	877.13
a (Å)	17.6927(7)
b (Å)	13.6703(5)
c (Å)	17.7523(7)
α (deg)	90
β (deg)	105.7929(10)
γ (deg)	90
Unit cell volume (Å^3)	4131.6(3)
Temperature (K)	90
Crystal system	Monoclinic
Space group	P 2_1/n
Z	4
Absorption coefficient (μ/mm^{-1})	0.713
Total number of reflections	72233
Unique reflections	12659
Final R_1 values ($I > 2\sigma(I)$)	0.0351
Final wR(F^2) values (all data)	0.0941

Listing B.2 Summary of crystallographic data for **Cu-DPSO$_2$**.

Compound	**Cu-DPSO$_2$**
Chemical formula	$C_{46}H_{36}CuN_2O_3P_2S$, BF_4
Formula weight	909.13
a (Å)	11.9139(4)
b (Å)	13.1490(5)
c (Å)	15.6199(6)
α (deg)	96.3361(9)
β (deg)	112.0557(11)
γ (deg)	93.6302(9)
Unit cell volume (Å^3)	2239.40(14)
Temperature (K)	90
Crystal system	Triclinic
Space group	P -1
Z	2
Absorption coefficient (μ/mm^{-1})	0.664
Total number of reflections	33113
Unique reflections	13668
Final R_1 values ($I > 2\sigma(I)$)	0.0295
Final wR(F^2) values (all data)	0.0767

Listing B.3 Summary of crystallographic data for **Cu-Me-DPS**.

Compound	**Cu-Me-DPS**
Chemical formula	$C_{60}H_{52}Cu_2N_4OP_2S_2$, 2($BF_4$), 2($CH_2Cl_2$)
Formula weight	1441.69
a (Å)	16.8444(16)
b (Å)	13.7286(13)
c (Å)	27.057(2)
α (deg)	90
β (deg)	90
γ (deg)	90
Unit cell volume (Å^3)	6256.9(10)
Temperature (K)	90
Crystal system	Orthorhombic
Space group	P b c n
Z	4
Absorption coefficient (μ/mm^{-1})	1.038
Total number of reflections	13008
Unique reflections	7149
Final R_1 values ($I > 2\sigma(I)$)	0.0475
Final wR(F^2) values (all data)	0.1141

Listing B.4 Summary of crystallographic data for **Cu-Me-DPSO$_2$**.

Compound	**Cu-Me-DPSO$_2$**
Chemical formula	$C_{84}H_{68}Cu_2N_2O_4P_4S$, 2($BF_4$)
Formula weight	1626.06
a (Å)	23.1483(9)
b (Å)	27.8735(11)
c (Å)	14.5524(6)
α (deg)	90
β (deg)	91.3552(9)
γ (deg)	90
Unit cell volume (Å^3)	9386.9(6)
Temperature (K)	90
Crystal system	Monoclinic
Space group	C 2/c
Z	4
Absorption coefficient (μ/mm^{-1})	0.602
Total number of reflections	56010
Unique reflections	10825
Final R_1 values ($I > 2\sigma(I)$)	0.0401
Final wR(F^2) values (all data)	0.1103

Listing B.5 Variable temperature emission lifetime plots for **Cu-DPS**, **Cu-DPSO$_2$**, **Cu-Me-DPS** and **Cu-Me-DPSO$_2$** from –196 to 28 °C.

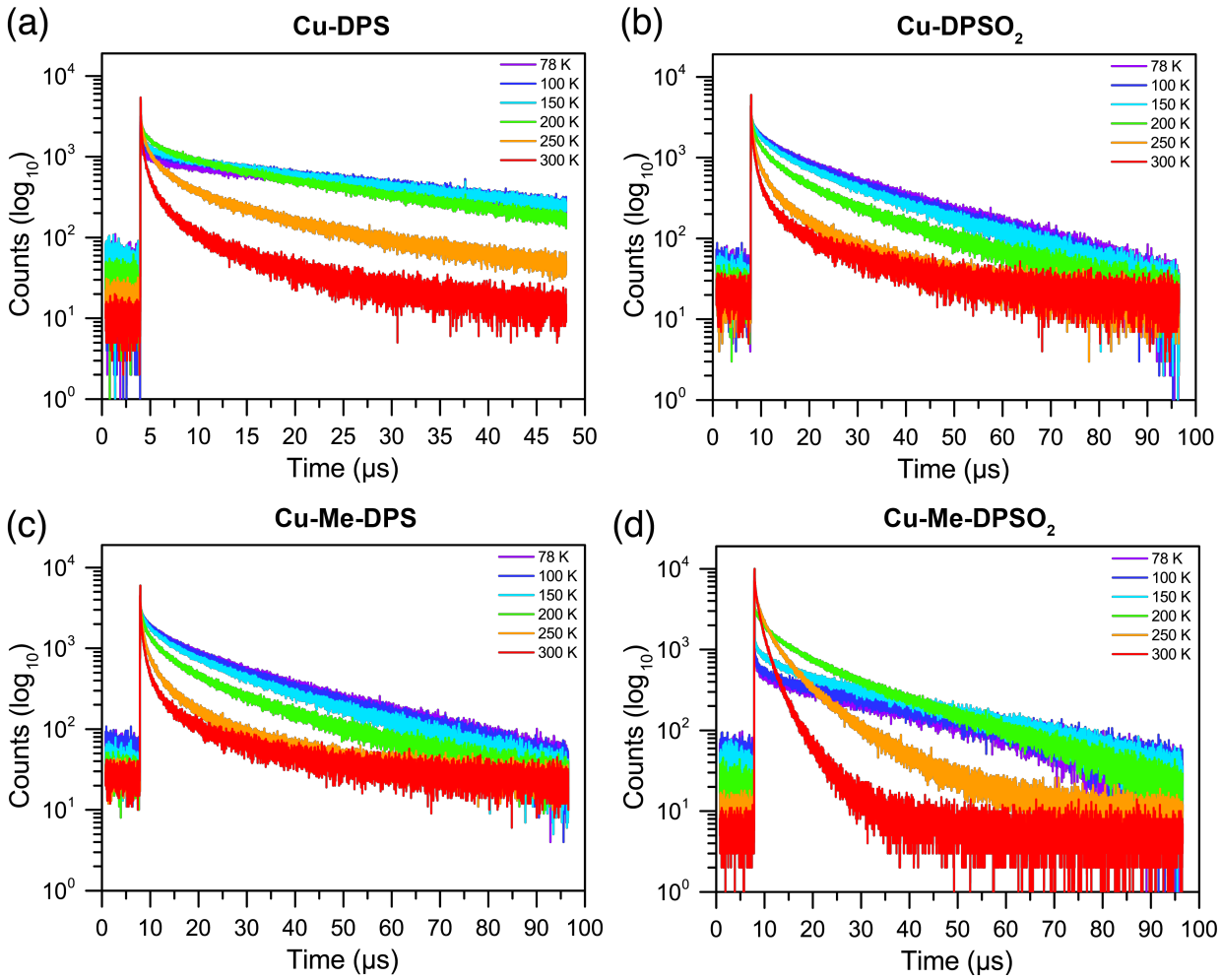

All samples drop-cast from MeOH on to quartz slides. Excitation with a NanoLED source (370 nm) with a pulse width of 1.2 ns repeating at a rate of 10 kHz.

Appendix C: Thermochromic Solid state Emission of Dipyridyl Sulfoxide Copper(I) Complexes

Listing C.1 Summary of crystallographic data for **Cu-DPSO**.

Compound	**Cu-DPSO**
Chemical formula	$2(C_{46}H_{36}CuN_2O_2P_2S)$, $2(BF_4)$
Formula weight	1786.34
a (Å)	10.2401(7)
b (Å)	19.7604(14)
c (Å)	21.4189(15)
α (deg)	101.9908(16)
β (deg)	99.5004(16)
γ (deg)	99.8941(15)
Unit cell volume ($Å^3$)	4084.8(5)
Temperature (K)	90
Crystal system	Triclinic
Space group	P -1
Z	2
Absorption coefficient (μ/mm^{-1})	0.725
Total number of reflections	36823
Unique reflections	18738
Final R_1 values ($I > 2\sigma(I)$)	0.0413
Final $wR(F^2)$ values (all data)	0.1013

Listing C.2 Summary of crystallographic data for **Cu-Me-DPSO**.

Compound	**Cu-Me-DPSO**
Chemical formula	$C_{48}H_{40}CuN_2O_2P_2S$, BF_4, CH_2Cl_2
Formula weight	1006.15
a (Å)	12.4822(11)
b (Å)	14.5739(14)
c (Å)	15.8204(14)
α (deg)	74.485(2)
β (deg)	88.104(2)
γ (deg)	72.284(2)
Unit cell volume ($Å^3$)	2637.9(4)
Temperature (K)	90
Crystal system	Triclinic
Space group	P -1
Z	2
Absorption coefficient (μ/mm^{-1})	0.667
Total number of reflections	48576
Unique reflections	22839
Final R_1 values ($I > 2\sigma(I)$)	0.0662
Final $wR(F^2)$ values (all data)	0.2034

Appendix D: Sulfur-Bridged Bimetallic Ru(II)-Re(I) Systems – Modulating CO_2 Reduction with Sulfur Oxidation State

Listing D.1 Actinometry for the photocatalytic LED setup.

Light intensities at 503 nm were determined using the commercial furyl fulgide Aberchrome 670[218] (TCI) following the procedure of Herder *et al.* [219] A toluene solution of Aberchrome 670 (4 mL, 1.4×10^{-4} M) was irradiated in a quartz cell (Starna Cells, 1 cm path length) for 5 min using a 365 nm hand lamp. Irradiation at 503 nm using the LED housing was conducted in 6 steps with 4 s irradiation times. I_0 is calculated from the depletion of Aberchrome 670 absorbance at 519 nm:

$$I_0 = -\frac{\Delta A^{519\,nm}}{\Delta t} \times \frac{V}{1000 \times \Phi^{503\,nm} \times \varepsilon^{519\,nm} \times \mathrm{L} \times (1 - 10^{-A'})}$$

$\Delta A^{519\,\mathrm{nm}}$	=	change in absorbance at 519 nm
Δt	=	change in time
V	=	volume of Aberchrome 670 solution (mL)
$\Phi^{503\,\mathrm{nm}}$	=	0.30
$\varepsilon^{519\,\mathrm{nm}}$	=	7760 $\mathrm{M^{-1}\,cm^{-1}}$
L	=	Path length of cuvette (cm)
A'	=	Initial absorbance at the irradiation wavelength (503 nm)